# Advanced Mechanistic 3D Spatial Modeling and Analysis Methods to Accurately Represent Nuclear Facility External Event Scenarios

## (NEUP-13-5142)

Final Project Report

Submitted:
December 29, 2017

**Research team:**
H. Sezen (PI)*
T. Aldemir (Co-PI)**
R. Denning (Co-PI in the original proposal, consultant)**
N. Vaidya (Co-PI)***

F. Alemdar (engineering director, researcher)***
E. Althoff (Masters student; graduated in May 2017)*
B. Cohn (graduate student)**
J. Fan (PhD student; graduated in December 2017)*
A. Guler (PhD student; graduated in December 2015)**
J. Hur (senior researcher)*
Z. Jankovsky (graduate student)**
M. Kose (senior researcher, until December 2015)*
C. Thyen (Masters student; graduated in May 2015)*
S. Uwizerimana (Masters student; graduated in December 2015)*

*Department of Civil, Environmental and Geodetic Engineering
**Nuclear Engineering Program, Department of Mechanical and Aerospace Engineering
College of Engineering
The Ohio State University, Columbus, Ohio

and

***Rizzo Associates, Pittsburgh, Pennsylvania

**Table of Contents**

# 1. RESEARCH OVERVIEW

## 1.1 Project Objectives and Progress

The objective of this project was to develop a set of tools for the dynamic seismic probabilistic risk assessment (DSPRA) of nuclear power plants which will consider seismically induced events, such as internal floods, and a methodology for the integration of seismic PRA (SPRA) into traditional internal events PRA including aftershocks and remedial actions. The time evolution of all events, their potential impacts on plant equipment and the associated uncertainties will be modeled using dynamic event trees (DETs).

The project involves four major analysis steps: 1) seismic hazard analysis and development of hazard curves considering earthquake frequency and site characteristics, 2) structural model development for structures, systems, and components (SSCs) at a nuclear power plant (NPP) site, 3) calculation of probability of failure of SSCs at the NPP site (including potential internal flooding) due to seismic input determined in Step 1, and 4) system analysis to calculate the frequency of core damage using the results from Steps 1 and 2, including the spatial dependency of equipment failures.

In this project, case studies are being used to support the development and demonstration of analysis tools. Work has progressed on two case studies during the reporting period. In commercial practice, a formalized approach to uncertainty analysis is used, the Separation of Variables (SOV) approach, in which sources of uncertainty are treated as multiplicative factors characterized by log normal uncertainty distributions. Case study 2 involves a best estimate plus uncertainty (BEPU) analysis treatment of uncertainty, using Risk-Informed Safety Margins Characterization (RISMC) tools. This case examines the common cause failure of essentially identical components at two levels of an auxiliary building. The fragility curve for the components is assumed to be based on experiment. For the load analysis, uncertainty distributions are developed for input parameters from which samples are drawn. The Case 2 study (see Chapter 8) is an integrated demonstration of the tools under development including a preliminary dynamic event tree (DET) analysis. The case examined involves structural failure of Condensate Storage Tank (CST), flooding of rooms, different types of common cause failures, a time-dependent evaluation of recovery actions and assessment of core damage frequency.

Several commercially available software packages have been used to model and analyze NPP structures and their components with varying degrees of complexity and accuracy. Surrogate structural models are being developed for computational feasibility in quantifying impacts of uncertainties on risk metrics and the results are being compared to those from commercial software.

## 1.2 Project Tasks

The project consisted of four major tasks. Table 1 indicates the schedule for the various activities. Major research activities that have been completed since the start of the project are listed below. Details of these activities are described and research results are briefly presented in the following sections.

The project was initiated on January 29, 2014. This is the final project report.

Table 1.1. Research Schedule (included in the proposal)

| **Task** | **Definition** | **Month** | | | | | | | | | | | | | | | | | |
|---|---|---|---|---|---|---|---|---|---|---|---|---|---|---|---|---|---|---|---|
| | | 2 | 4 | 6 | 8 | 10 | 12 | 14 | 16 | 18 | 20 | 22 | 24 | 26 | 28 | 30 | 32 | 34 | 36 |
| 1. | Definition of High-level System Specifications | ♦ | ♦ | ♦ | | | | | | | | | | | | | | | |
| 2. | Module Development, Testing and Validation | ♦ | ♦ | ♦ | ♦ | ♦ | ♦ | ♦ | ♦ | ♦ | ♦ | ♦ | ♦ | | | | | | |
| 2.1. | DINOSAUR framework development | ♦ | ♦ | ♦ | | | | | | | | | | | | | | | |
| 2.2. | Tool development, verification, and validation | | ♦ | ♦ | ♦ | ♦ | ♦ | ♦ | ♦ | ♦ | ♦ | ♦ | ♦ | ♦ | | | | | |
| 3. | Integral System Demonstration and Testing | ♦ | ♦ | ♦ | ♦ | ♦ | ♦ | ♦ | ♦ | ♦ | ♦ | ♦ | ♦ | ♦ | ♦ | ♦ | ♦ | ♦ | |
| 3.1. | Pseudo-plant design | | ♦ | ♦ | ♦ | ♦ | ♦ | | | | | | | | | | | | |
| 3.2. | Interim integral testing | | | | | | ♦ | ♦ | ♦ | ♦ | ♦ | | | | | | | | |
| 3.3. | System demonstration | | | | | | | | | | | | ♦ | ♦ | ♦ | ♦ | ♦ | ♦ | |
| 4. | Toolset documentation | | | | | | | | | | | | | | | ♦ | ♦ | ♦ | ♦ |
| | **Final Project Report** | | | | | | | | | | | | | | | | | ♦ | ♦ |

## 2. PUBLICATIONS AND PRESENTATIONS

All published papers, presentation, and abstracts are listed below and recent publications are included in Appendix A.

Three papers are being prepared to be submitted soon to peer reviewed technical journals.

1. Hur J., Althoff E., Sezen H., Denning R., and Aldemir T. 2017. “Seismic Assessment and Performance of Nonstructural Components Affected by Structural Modeling” *Nuclear Engineering Technology*, Vol. 49, No. 2, 387-394
2. Sezen H., Hur J., Kose M. M., Denning R. S., and Aldemir T. August 10-14, 2015. “Mechanistic and Probabilistic Seismic Assessment of Structures and Components in Nuclear Power Plants.” *SMIRT-23 Conference (Structural Mechanics in Reactor Technology),* Manchester, United Kingdom
3. Sezen H., Aldemir T., and Denning R. October 4-8, 2015. “Simulation of Performance of Structural Materials under Extreme Conditions.” MS&T15 Material Science and Technology Conference, Columbus, Ohio (abstract and oral presentation)
4. Hur J., Guler A., Sezen H., Aldemir T., and Denning R. S. April 17-20, 2016. “Assessing the Degree of Conservatism in the Separation of Variables Approach to Seismic PRA.” *ICAPP 2016 International Conference on Advances in Nuclear Power Plants,* San Francisco, CA
5. Guler A., Hur J., Jankovsky Z., Sezen H., Aldemir T., and Denning R. S. April 17-20, 2016. “A Dynamic Treatment of Common Cause Failure in Seismic Events.” *ICAPP 2016 International Conference on Advances in Nuclear Power Plants,* San Francisco, CA
6. Uwizerimana S., Kose M. M., Sezen H., Denning R., Hur J., and Aldemir T. April 17-20, 2016. “Computational Simulation of Dynamic Response and Failure of Structures in Seismic Events.” *ICAPP 2016 International Conference on Advances in Nuclear Power Plants,* San Francisco, CA
7. Hur J., Sezen H., Denning R., and Aldemir T. October 2-7, 2016. “Assessment of the Effect of Structural Model Fidelity on the Failure Probability of Nonstructural Components.” *PSAM13 13th International Conference Probabilistic Safety Assessment and Management,* Seoul, Korea
8. Guler A., Hur J., Denning R., Aldemir T., and Sezen H. October 2-7, 2016. “Aging Effects on Safety Margins of Passive Components in Seismic Events.” *PSAM13 13th International Conference Probabilistic Safety Assessment and Management,* Seoul, Korea
9. Hur J., Kose M., Sezen H., Denning R., and Aldemir T. October 2-7, 2016. “Development of Seismic Response Models of a Condensate Storage Tank.” *PSAM13 13th International Conference Probabilistic Safety Assessment and Management,* Seoul, Korea
10. Jankovsky Z., Denning R., Aldemir T., Sezen H., and Hur J. October 2-7, 2016. “Application of Dynamic Probabilistic Risk Assessment to a Seismically Induced Internal Flood Event.” *PSAM13 13th International Conference Probabilistic Safety Assessment and Management,* Seoul, Korea
11. Sezen H., Aldemir T., Denning R. S., Hur J., and Smith C. L. October 2016. “Advanced Three-Dimensional Spatial Modeling and Analysis to Accurately Represent Nuclear Facility External Event Scenarios.” LWRS Newsletter, Issue 22, pp. 6-9

12. Cohn B., Denning R., Aldemir T., Hur J., and Sezen H. June 18-22, 2017. “Implementation of Surrogate Models within RAVEN to Support SPRA Uncertainty Analysis.” ESREL 2017 European Safety and Reliability Conference, Portoroz, Slovenia
13. Althoff A., Hur J., Sezen H., Denning R., and Aldemir T. August 20-25, 2017. “Seismic Evaluation of Reduced-Order Models for Auxiliary Buildings.” *SMIRT-24 Conference (Structural Mechanics in Reactor Technology),* Busan, Korea
14. Hur J., Cohn B., Aldemir T., Denning R., and Sezen H. August 20-25, 2017. “Uncertainty Quantification in the Assessment of Seismic Failure Probability of Nonstructural Components Using Surrogate Models.” *SMIRT-24 Conference (Structural Mechanics in Reactor Technology),* Busan, Korea
15. Fan J., Sezen H., Hur J., Althoff A., Denning R., and Aldemir T. August 20-25, 2017. “Structural Modeling and Seismic Analysis of Condensate Storage Tanks.” *SMIRT-24 Conference (Structural Mechanics in Reactor Technology),* Busan, Korea
16. Cohn B., Denning R., Aldemir T., Hur J., and Sezen H. September 25-27, 2017 “Surrogate Model Selection in RAVEN for Seismic Dynamic PRA/PSA.” *PSA 2017 International Topical Meeting on Probabilistic Safety Assessment and Analysis*, Pittsburgh, PA
17. Hur J., Althoff E., Sezen H., Aldemir T., and Denning R. S. “Seismic Evaluation of Auxiliary Buildings and Effects of 3D Locational Dynamic Response in SPRA.” *PSA 2017 International Topical Meeting on Probabilistic Safety Assessment and Analysis*, Pittsburgh, PA, September 24-28, 2017.

# 3. FRAMEWORK TO COUPLE PROBABILISTIC AND MECHANISTIC MODELS OF SPRA

## 3.1 Introduction

The objective of this report is to describe the framework that has been developed for coupling the deterministic and probabilistic aspects of seismic probabilistic risk assessment (SPRA) within the context of a Risk-Informed Safety Margin Characterization (RISMC) approach.[1] In this section we will discuss the evolution of the historical deterministic basis for regulatory safety analysis, its transition from conservative models to a best-estimate plus uncertainty analysis approach to the treatment of uncertainties, and the emergence of risk-informed regulatory analysis as an augmentation of a deterministic regulatory approach. This section also describes the approaches to SPRA currently being used by the nuclear industry. Section 2 describes the framework for the RISMC-based approach to SPRA developed and tested in this NEUP project. Section 3 provides greater detail of the steps to be undertaken when a dynamic event tree (DET) analysis is warranted. Section 4 summarizes the status of development and testing of the framework.

With few exceptions, the computer codes that are used in the performance of safety analyses, such as transient thermal-hydraulic analyses or structural response analyses, are deterministic in nature. Given a set of inputs, specific values of output variables are obtained. For example, in analyzing the peak clad temperature that would result from a loss of coolant accident, a RELAP 7 calculation can be performed, which for a given set of inputs will result in one value for peak clad temperature. This value can then be compared with the regulatory criterion of 2200 F to determine whether the design of the emergency core cooling system is acceptable. Historically, in the time period of the 1970s when these evaluations were originally being performed, the modeling uncertainties were recognized to be large. To account for these uncertainties conservative assumptions were made in what were referred to as "regulatory models."[2] This type of regulatory analysis, based on deterministic models, is called a deterministic safety analysis. With time, it was recognized that this approach to regulatory analysis had drawbacks and instead a best-estimate plus uncertainty analysis approach was developed.[3] Two types of uncertainty are considered in this type of analysis: epistemic uncertainties (state of knowledge uncertainty) and aleatory uncertainty (stochastic uncertainty or variability). In this approach to safety analysis, rather than comparing a single output value with the regulatory limit, a probability of exceeding the limit is determined at a specified confidence level (referred to as a 95:95 criterion). Best-estimate plus uncertainty analysis is still considered to be a deterministic safety analysis approach, even though there is a probabilistic aspect to the treatment of uncertainty, because it is conditioned on the occurrence of the accident event.

In contrast to deterministic safety analysis, probabilistic risk analysis assesses the probability per year of an event occurring in addition to the consequences of the event. For example, if core

---

[1] Szilard R, Smith C, and Youngblood, R. (2014). "RISMC Advanced Safety Analysis Project Plan, FY 2015 – FY 2019, Light Water Reactor Sustainability Program," *INL/EXT-14-33186*.

[2] US NRC, (1974). "ECCS Evaluation Models," *Title 10 Code of Federal Regulations, Part 50, Appendix K.*

[3] Boyack, B. et al., (1989). "Quantifying Reactor Safety Margins, Application of Code Scaling, Applicability, and Uncertainty Evaluation Methodology to a Large-break Loss-of-Coolant Accident," *NUREG/CR-5249*.

damage is the consequence of concern, the risk is described in terms of core damage frequency (CDF). Thus, the frequency of accident initiating events is included as consideration in the regulatory acceptance of the output of the analysis. Although following the performance of the first major reactor risk study, WASH-1400,[4] the Nuclear Regulatory Commission (NRC) was reluctant to base regulatory requirements on the results PRA, as more experience was obtained with PRA, the NRC commissioners informed the staff to risk-inform the regulatory process.[5]

Development of the methods of PRA was originally focused on the risk initiated by internal events (such as failure of a valve) rather than external events, such as earthquakes. In the Individual Plant Examination External Events (IPEEE)[6] program mandated by the NRC, all plants either performed a seismic probabilistic risk assessment (SPRA) or seismic margins study. Following the Fukushima accident, all plants were required to revisit their analysis of seismic risk.[7] There are two SPRA methodologies currently in use by the industry, the Separation of Variables Approach[8] and the Conservative Deterministic Failure Margin approach[9]. These approaches have been developed by the Electric Power Research Institute (EPRI). Both approaches incorporate considerable conservatism and expert judgment in the analysis. The objective of the NEUP program undertaken by The Ohio State University (OSU) in collaboration with its subcontractor, P. Rizzo and Associates, was to develop an advanced approach to SPRA more firmly based on first principles and best estimate plus uncertainty analysis. This approach has been built around the methods under development in the Risk Informed Safety Margins Characterization program (RISMC) within the DOE Light Water Reactor Sustainability Program[10]. In particular, the framework developed for this advanced SPRA approach was to include the capability to consider the dynamic aspects of plant response to a seismic event associated with the recovery of plant equipment damaged in the seismic event and common cause failures of equipment including the effects of seismically initiated fires and floods. The output of the analysis would be an assessment of CDF and large early release frequency (LERF), which are the risk measures commonly employed in risk-informed regulation[11].

### 3.2 RISMC–Based SPRA Framework

Figure 1 illustrates the overall SPRA framework developed at OSU for a RISMC-based SPRA. This framework enables a multi-physics solution using MOOSE[12] as a finite-element equation solver.

---

[4] US NRC, "Reactor Safety Study, An Assessment of Accident Risks in U.S. Commercial Nuclear Power Plants," *WASH-1400 (NUREG 75/014)*, October 1975.

[5] US NRC, "Use of Probabilistic Risk Assessment Methods in Nuclear Regulatory Activities: Final Policy Statement," 60FR42622, August 16, 1995.

[6] US NRC, "Perspectives Gained from the Individual Plant Examination of External Events (IPEEE) Program," *NUREG-1742*, April 2002.

[7] US NRC, "Recommendations for Enhancing Reactor Safety in the 21st Century, The Near-Term Task Force Review of Insights from the Fukushima Dai-Ichi Accident," July 2011.

[8] EPRI, (1994). "Methodology for Developing Seismic Fragilities," *EPRI TR-103959*.

[9] EPRI, (1991). "A Methodology for Assessment of Nuclear Plant Seismic Margin, Revision 1," *EPRI NP-6041-SL*.

[10] Szilard R, Smith C, and Youngblood, R. (2014). "RISMC Advanced Safety Analysis Project Plan, FY 2015 – FY 2019, Light Water Reactor Sustainability Program," *INL/EXT-14-33186*.

[11] US NRC, (2002). "An Approach for Using Probabilistic Risk Assessment in Risk-Informed Decisions on Plant-Specific Changes to the Licensing Basis," *Regulatory Guide 1.174, Rev. 1*.

[12] INL, (2015). " MOOSE Framework, Open Source Multiphysics," http://mooseframework.org.

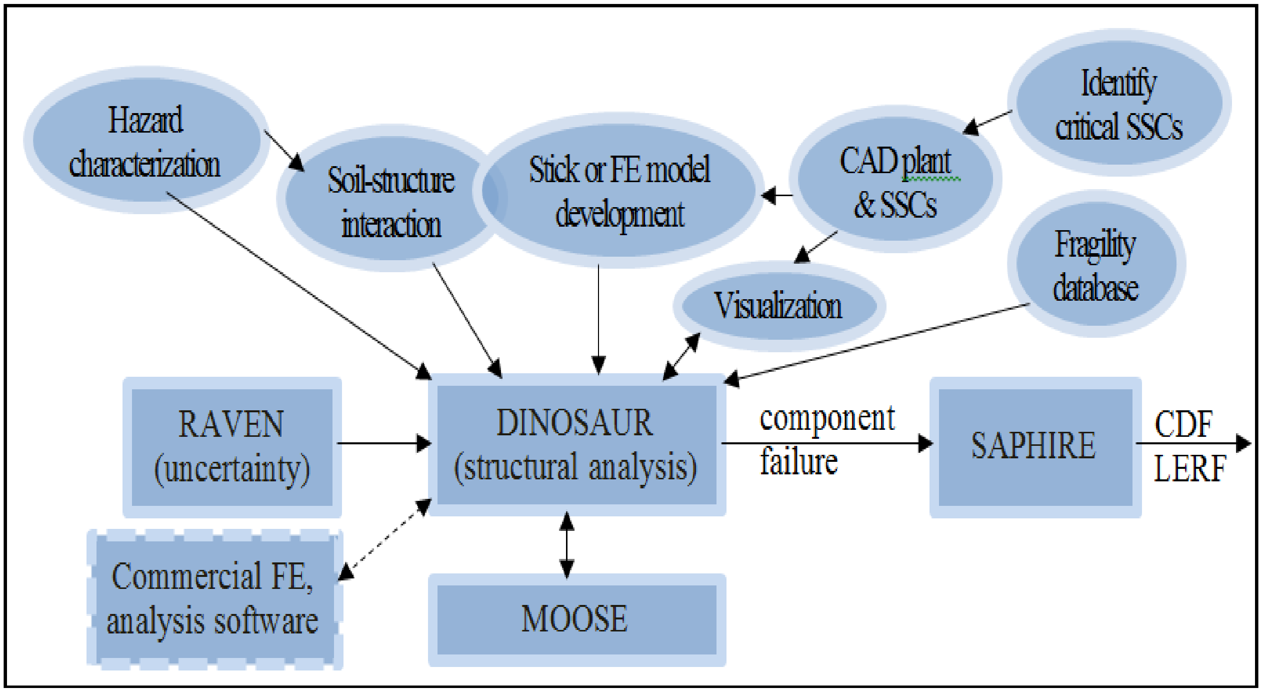

Figure 1. Framework for RISMC-Based SPRA

The DINOSAUR block represents a set of tools developed and demonstrated/used in this NEUP project including not only reduced order finite element structural models but also deterministic thermal-hydraulic models (such as MELCOR[13] or RELAP 7), which are used to assess minimum performance levels of engineered safety features required to avoid core damage or to support dynamic analyses. The RAVEN[14] code is the driver for the performance of uncertainty analysis and the DET analysis, for cases in which a dynamic analysis is warranted. The framework includes the characterization of the seismic hazard and soil structure interaction. Within the project, however, only methods for assessing the above ground impacts of seismic loads on safety-related structures were examined. The progression of seismic waves through the soil and the loads imposed on the base of the structure are being investigated by the Idaho National Laboratory (INL). The framework for SPRA is built on the internal events PRA for the plant.

In this project, the framework has been demonstrated through the performance of variations for three case studies as described below:

---

[13] Gauntt, R.O. (2006). "MELCOR Computer Code Manual, Version 1.8.5, Vol. 2, Rev.2," *NUREG/CR-6119, Sandia National Laboratory, Albuquerque, NM.*

[14] Alfonsi, A. et al., (2013). "RAVEN as a Tool for Dynamic Probabilistic Risk Assessment: Software Overview," *Proceedings of M&C 2013 International Topical Meeting on Mathematics and Computation, DC-ROM, American Nuclear Society, LaGrange Park, IL*

- Case Study 1: Uncertainty analysis, reduced order model development and assessment of marginal and joint failure probabilities of safety-related equipment in different locations of an auxiliary building as a function of building asymmetry
- Case Study 2: Dynamic uncertainty analysis including reduced order modeling of condensate storage tank failure, seismically induced flooding, aftershocks, equipment recovery and integrated assessment of core damage frequency
- Case Study 3: Uncertainty analysis, reduced order model development for containment building, and failure of the polar crane occurring while the plant is in the shutdown mode.

### 3.3 Dynamic Seismic Probabilistic Risk Assessment

In addition to the general framework for a RISMC-based approach to SPRA, a detailed set of steps has been developed for performing a dynamic SPRA (DSPRA). A DSPRA would be required to consider the dynamic aspects of seismically induced events, such as internal floods, recovery actions and aftershocks. The time evolution of all events, their potential impacts on plant equipment and the associated uncertainties are modeled using DETs[15].

The analysis involves four major analysis steps: 1) seismic hazard analysis and development of hazard curves considering earthquake frequency and site characteristics, 2) structural model development for structures, systems, and components (SSCs) at a nuclear power plant (NPP) site, 3) calculation of probability of failure of SSCs at the NPP site (including potential internal flooding) due to seismic input determined in Step 1, and 4) system analysis to calculate the frequency of core damage using the results from Steps 1 and 2, including the spatial dependency of equipment failures.

To date, SPRAs have used static event trees, as is common practice for internal event PRAs. However, seismic events are dynamic by nature. The initial earthquake is typically followed by a series of earthquakes over a period of days, including aftershocks that can be comparable in size to the initial shock. A seismic event is a major potential producer of common cause failures. The operators may be unaware that a system is not functional until it is called on or a system may initially function and subsequently fail. In the Fukushima accident, issues were encountered that affected the ability of the operator to resolve evolving threats to core damage and containment integrity. Historically, risk studies provided very little credit for the performance of emergency actions, particularly if there were no procedures available for their implementation. In the post-9/11 and post-Fukushima environment, much more attention us being given in PRAs to evaluate the effectiveness of FLEX[16] equipment and the implementation of Severe Accident Management Guidelines (SAMG). There was an extended time period in the Fukushima accident required to achieve cold shutdown (termination) of the accident at each of the units. The operating crew was required to perform tasks that involved considerable innovation under great stress. With post-Fukushima improvements in procedures, training and available equipment, greater assistance will be provided to the operating crew and Technical Support Center staff in future events. However,

---

[15] Aldemir, T., (2013) "A Survey of Dynamic Methodologies for Probabilistic Safety Assessment of Nuclear Power Plants," *Annals of Nuclear Energy, **52**, 113-124.*

[16] Nuclear Energy Institute, "Diverse and Flexible Coping Strategies (FLEX), Implementation Guide," *NEI 12-06*, Washington, D.C. 2012.

unlike Emergency Operating Procedures (EOPs), which provide detailed instructions for operator actions as long as the plant remains within design basis conditions, severe accident management guidelines (SAMGs) are guidelines not procedures. The decision makers are required to examine plant conditions and make informed decisions about the proper actions to undertake, recognizing that they may be presented with inadequate or inconsistent data and with potentially large uncertainties regarding the true plant state. DETs are required to reproduce the spectrum of scenarios that could be faced by the operating crew.

Figure 2 (from the ASME PRA Standard)[17] identifies the main steps of a SPRA. The objective of the NEUP study is to provide the capability to perform the various steps of at least a Level 2 SPRA to enable the calculation of LERF. Current practice of SPRA is based on static event trees. In order to address the dynamic aspects, some additional tools and capabilities are required.

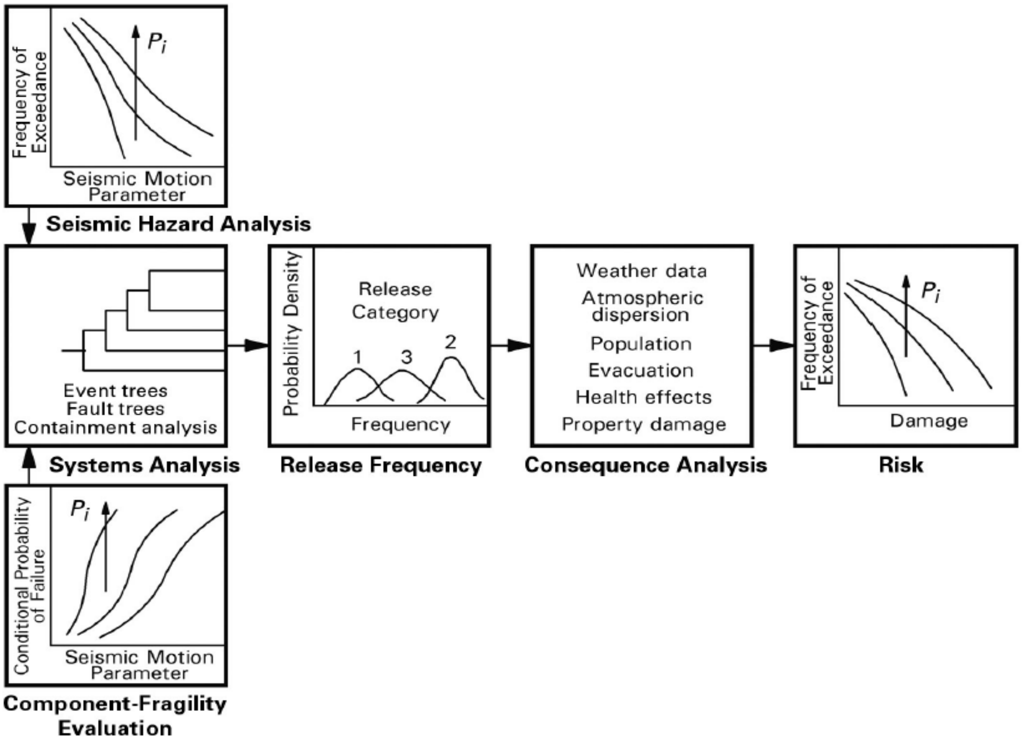

Figure 2. Principal Steps of Level 3 Traditional SPRA[7]

The following initial steps of the DSPRA process are essentially the same as for a fixed event tree SPRA as illustrated in Figure 3:

1) Determine input ground motion at the NPP site representing the dynamic seismic loads to be applied on the structural models.
2) Develop a list of SSCs included in the DSPRA model, for which seismic fragilities and spatial interactions are to be obtained.

---

[17] ASME, “Addenda to ASME/ANS RA-S-2008, Standard for Level 1/Large Early Release Frequency Probabilistic Risk Assessment for Nuclear Power plant Applications,” ASME/ANS RA-Sa-2009 (2009)

3) Develop FE models of plant SSCs and, as necessary, FE model of the global structure including the effects of soil-structure interaction.
4) Perform seismic analysis of plant structures for the input time histories developed in Step 1 above to calculate seismic forces and moments on structural components, equipment and structural system.
5) Obtain fragility parameters for the selected SSCs and assess the probabilities of failure of safety-related SSCs.
6) Use conditional failure probabilities of SSCs obtained in Step 5 with frequency of seismic levels to determine SSC failure probability as a function of seismic magnitude.
7) Combine seismic failure of SSCs with internal event PRA

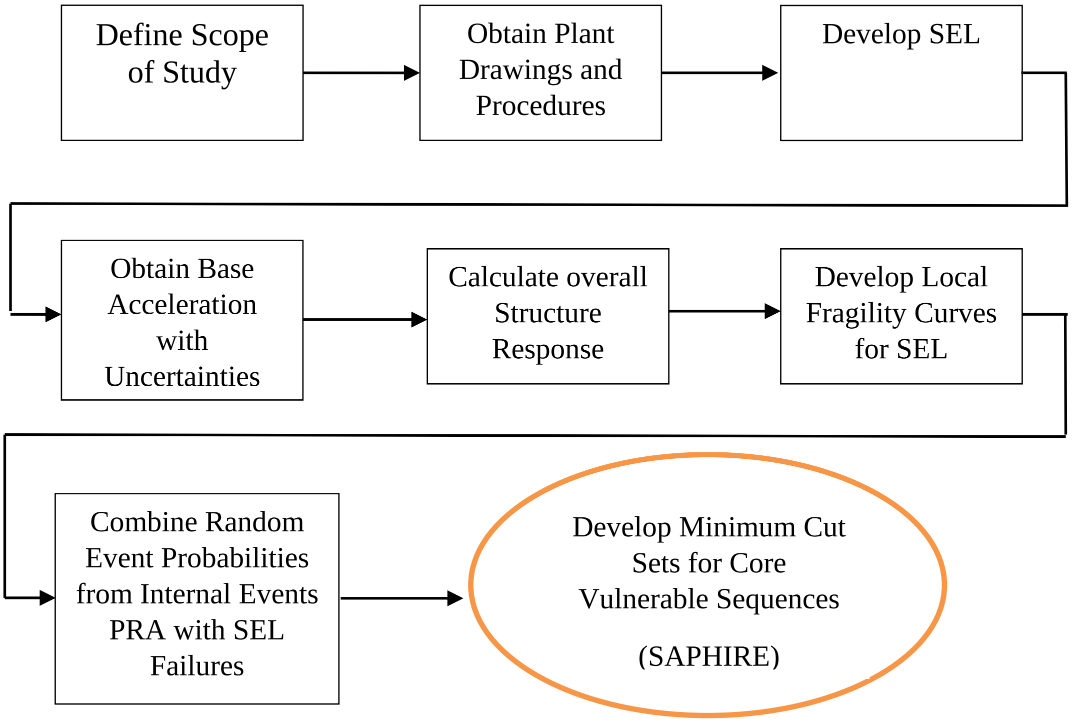

Figure 3. Identification of Event Sequences of Interest

The manner in which seismic event failure of SSCs is combined with internal events (Step 7 above) will depend on the time scope and extent of the DSPRA. Either ADAPT[18] or RAVEN would be used with the system response simulated by a transient thermal hydraulic code like RELAP 7 or the MELCOR code[19] to determine for a scenario pathway whether core damage occurs or is avoided. For a Level 2 analysis, for a scenario pathway it would also be necessary to determine whether containment failure occurs or is avoided as simulated by the MELCOR code. The probabilities of the DET pathways would then be used in combination with random (internal event)

---

[18] A. Hakobyan, T. Aldemir, et al., “Dynamic Event Tree Generation of Accident Progression Event Trees,” *Nuclear Engineering and Design*, **238**, 3457-3467 (2008)

[19] R. O. Gauntt et al "MELCOR Computer Code Manual, Version 1.8.5, Vol. 2, Rev.2," *NUREG/CR-6119*, Sandia National Laboratory, Albuquerque, NM. (2006)

faults to determine CDF and LERF. The DET pathways and probabilities can be integrated into an existing plant PRA using the approach described in NUREG/CR-6942[20]

Figure 4 shows the overall flow of the DPRA graphically. The DET branching rules will account for remedial and/or recovery actions (such as power recovery in a station blackout event). Aftershocks can be also accounted for in this dynamic framework as well.

The seismic and seismically induced events can affect many components simultaneously leading to common cause failures (CCFs). There are well established procedures to handle CCFs within the traditional internal event PRA framework[21]. External events bring a new dimension to CCF analysis not only due to the possible similarity of SSCs affected but also due to the proximity and initiating cause similarities. If these events are to be integrated within a Level 1 framework using traditional tools such as SAPHIRE, CCFs need to be accounted for to prevent underestimation through the Boolean logic. Whenever possible, U.S. NRC procedures for CCF analysis would be followed[22].

---

[20] T. Aldemir, M.P. Stovsky, J. Kirschenbaum, D. Mandelli, P. Bucci, L.A. Mangan, D.W. Miller, X. Sun, E. Ekici, S. Guarro, M. Yau, B. Johnson, C. Elks, and, S. A. Arndt, “Dynamic Reliability Modeling of Digital Instrumentation and Control Systems for Nuclear Reactor Probabilistic Risk Assessments”, NUREG/CR-6942, U. S. Nuclear Regulatory Commission, Washington, D.C. (August 2007)

[21] IAEA, “Procedures for Conducting Common Cause Failure Analysis in Probabilistic Safety Assessment,” IAEA-TECDOC-648 (1992)

[22] A. Mosleh, D. Rasmuson, and F. Marshall, “Guidelines on Modeling Common-Cause Failures in Probabilistic Risk Assessment,” NUREG/CR-5485 (1998)

## 4. DEVELOPMENT OF INPUT GROUND MOTIONS

This section summarizes the methodology to develop a set of ground motion time histories for a nuclear power plant at a Central and Eastern United States (CEUS) Rock Site (Central Illinois Site), whose response spectra match the target spectra as the rock Uniform Hazard Response Spectra (UHRS) for the Site. The adjusted time histories will be used as the ground motion input in the Soil Structure Interaction (SSI) analysis.

### 4.1 Description of Methodology

In order to develop the set of design time histories, four main steps are required:

I. Selection of target spectra
II. Selection of seed motions,
III. Spectral matching
IV. Power spectral density check

A flow chart containing a summary of the process is shown in Figure 4.1. Based on the spectral shape of the target horizontal UHRS, a set of seed motions (two horizontal and one vertical acceleration time histories) are selected. Then the seed motions are modified in order to obtain adjusted motions whose response spectra match the target spectra. The power spectral densities (PSD) of the adjusted motions are checked against the target PSD in NUREG 8000[23] to ensure there are no significant energy gaps in the frequency range of interest.

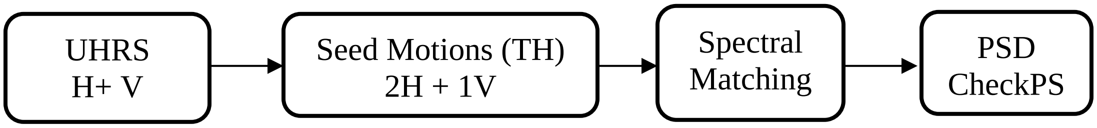

Figure 4.1. Flowchart for development of design input motion time histories.

### 4.1.1 Selection of Seed Motion

The commonly used target spectra for design time history development are scenario spectra, conditional spectra[24], uniform hazard response spectra (UHRS)[25] and performance based ground motion response spectra (GMRS) or foundation input response spectra (FIRS)[26]. The selection of appropriate target spectrum for different applications is discussed in Section 5.3 in NIST GCR 1-917-15 [27]. UHRS or performance based GMRS or FIRS are commonly used targets in nuclear industry. In this research project, the horizontal target is selected from seven test site locations

---

[23] US Nuclear Regulatory Commission, "Standard Review Plan 3.7.1, Seismic Design Parameters," Revisions 3 and 4, Washington, D.C. (March 2007, and December 2014)

[24] C.B. Haselton, A.S. Whittaker, A. Hortacsu, J.W. Baker, J. Bray, and D.N. Grant, "Selecting and Scaling Earthqake Ground Motions for Performing Response-History Analyses," 15th World Conference for Earthquake Engineering, Lisbon, (2012)

[25] Canadian Standards Association, "N289.3-10 – Design Procedures for Seismic Quantification of Nuclear Power Plants," (2010)

[26] US Nuclear Regulatory Commission, Regulatory Guide 1.208, "A Performance-Based Approach to Define the Site-Specific Earthquake Ground Motion," (March 2007)

[27] National Institute of Standards and Technology, "Selecting and Scaling Earthquake Ground Motions for Performing Repsone-History Analyses," NIST GCR 1-917-15 (November 2011)

used for demonstration hazard calculations in EPRI[28]. The selected sites are shown Figure 4.2. The 1E-4 rock UHRS for Central Illinois Site is selected as the target spectra. In Figure 4.3, the selected horizontal target spectra are compared with the spectral shape from NUREG/CR-6728[29] and the Bin Average Response Spectra for CEUS Rock Site from Table 7 in SRP 3.7.1[30].

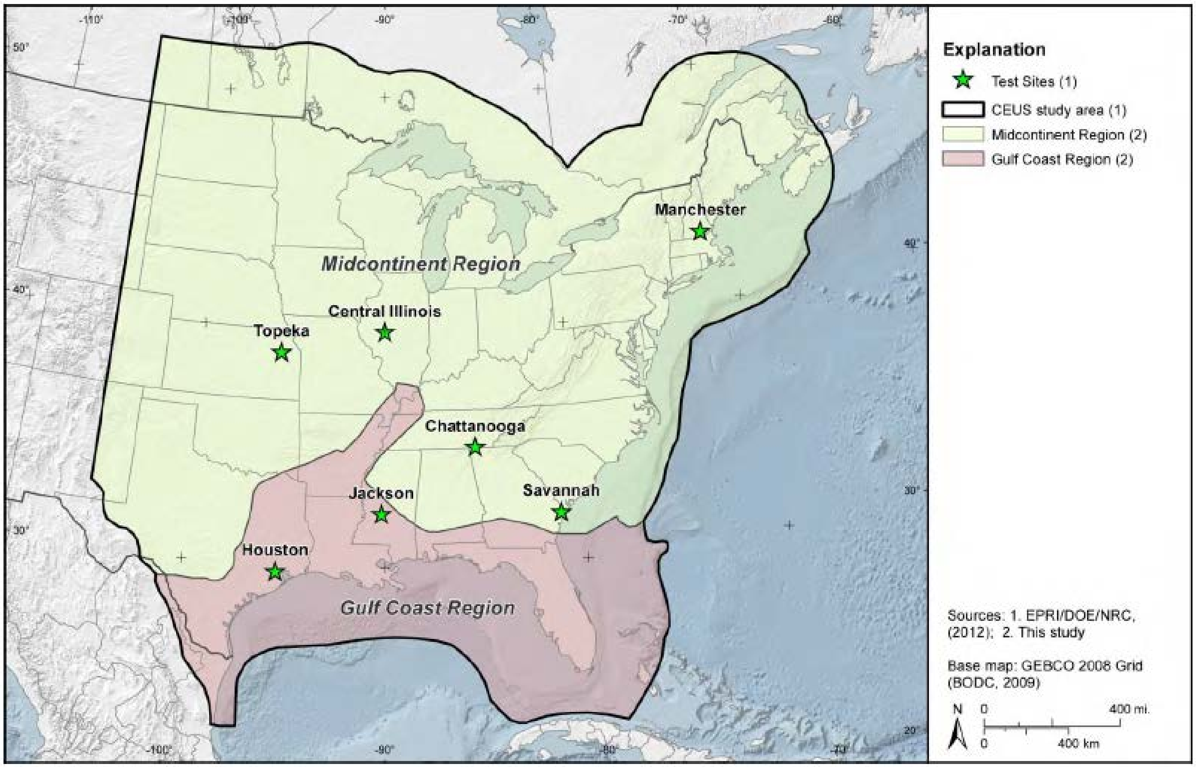

Figure 4.2. Location of the test sites for seismic hazard calculations

The vertical target spectra are developed as the horizontal spectra multiplied by the vertical-to-horizontal spectral ratio (V/H ratio) recommended in NUREG/CR-6728 for CEUS hard rock condition without any site-specific adjustment.

It should be noted that the target compatible time histories developed in this project may be appropriate for the soil-structure interaction (SSI) analysis for a structure founded on a hard rock site in CEUS, but not suitable for a structure founded on a soil site, for which a site-specific GMRS or FIRS should be used as the target for time history development.

Two ground motion databases are considered in the seed motion selection. One is the Pacific Earthquake Engineering Research Center (PEER) ground motion database for the NGA-West2 project (http://ngawest2.berkeley.edu/). The other is the ground motion database CD

---

[28] Eletric Power Research Institute, "EPRI (2004, 2006) Ground-Motion Model (GMM) Review Project", 3002000717, (June 2013)

[29] R.K. McGuire, W.J. Silva, and C.J. Costantino, "Technical basis for revision of regulatory guidance on design ground motions: hazard- and risk-consistent ground motion spectra guidelines," NUREG/CR-6728, U.S. Nuclear Regulatory Commission, (October 2001)

[30] US Nuclear Regulatory Commission, "Standard Review Plan 3.7.1, Seismic Design Parameters," Revision 4, Washington, D.C. (December 2014)

accompanying NUREG/CR-6728. The PEER database for the current NGA-East project is not considered since the number of strong ground motion records in that database is not sufficient for this study.

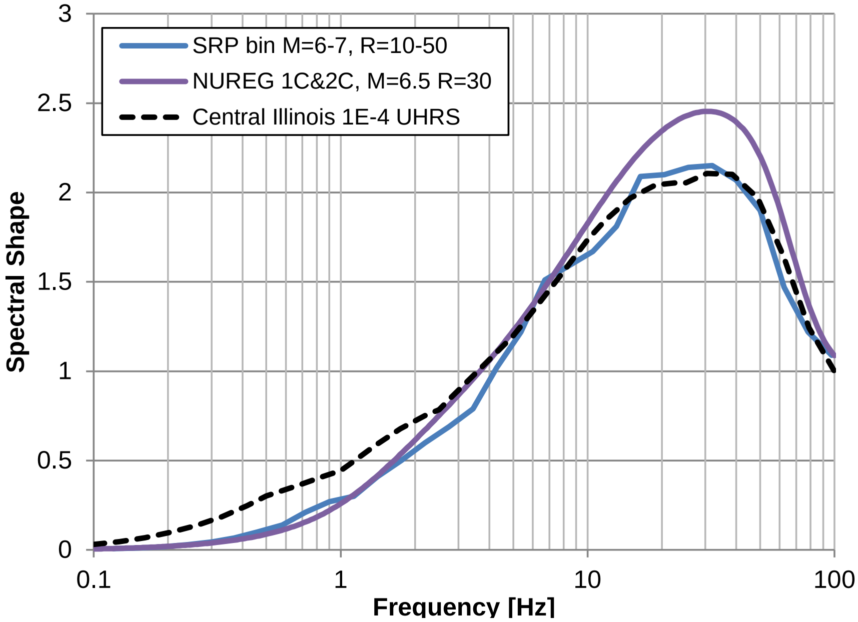

Figure 4.3. Selected target spectra and spectra from SRP 3.7.1 and NUREG/CR-6728[31]

The web-based PEER NGA-West2 ground motion database provides tools for searching, selecting and downloading ground motion data. This database includes a large set of ground motions recorded during shallow crustal earthquakes in active tectonic regions of the world. Although the target region (CEUS rock condition) is different in this report, it was shown[32] that unbiased estimates of structural response are obtained for the case in which seed motions that originate in other regions are adjusted to resemble those for a target region.

The target response spectrum (horizontal 1E-4 UHRS for Central Illinois Site) is used in NGA-West2 database under “User Defined Spectrum”. A basic criterion used by the NGA-West2 ground motion database is to select a representative acceleration time series whose response spectra provides a “good match” to the user’s target spectrum over the spectral period range of interest. Specifically, the software identifies acceleration time series whose spectral shape is similar to the spectral shape of the selected design response spectrum. The software allows the user to define the period range of interest over which the spectral shape is matched.

The quantitative measure used to evaluate how well a time series conforms to the target spectrum is the mean squared error (MSE) of the difference between the spectral accelerations of the record and the target spectrum, computed using the logarithms of spectral period and spectral acceleration.

---

[31] R.K. McGuire, W.J. Silva, and C.J. Costantino, “Technical basis for revision of regulatory guidance on design ground motions: hazard- and risk-consistent ground motion spectra guidelines,” NUREG/CR-6728, U.S. Nuclear Regulatory Commission, (October 2001)

[32] J.E. Carballo, and C.A. Cornell, “Probabilistic Seismic Demand Analysis: Spectrum Matching and Design,” Report No. RMS-41, Reliability of Marine Structures Program, Stanford University, Palo Alto, California, (July 2000)

The NGA-West2 ground motion database web-based tool searches the database for records that satisfy general acceptance criteria provided by the user and then ranks the records in order of increasing MSE, with the best-matching records having the lowest MSE.

The focus of the NGA-West2 ground motion database is on selecting "as recorded" strong ground motion acceleration time series for use in seismic analyses. The records do include the effects of processing by the supplying agency, such as filtering and baseline correction. Therefore, the tool does not provide the capability of altering the frequency content of the recordings to better match a target spectrum. However, it does provide the ability to linearly scale recorded time series to improve their match to the target spectrum and select time series that have the best spectral match.

The user has three options for scaling. One option is to apply a scale factor that minimizes the MSE over the period range of interest. This approach results in selection of records that have spectral shapes that are similar on average to the target spectra over the period range of interest, but whose spectra will oscillate about the target. The second option is to scale the records so that the spectral acceleration at a specific period matches the target spectral acceleration at that period. This provides a set of scaled time series whose spectral accelerations are all equal to the target at the specified period. A third option of not scaling is also available. The choice of scaling approach is up to the user.

For all three options, the MSEs of the records are calculated and ranked. In this research, the first method of selection is used, i.e., a scale factor is applied to minimize the MSE over the period range of interest. In this study, the period range of 0.01 sec to 10 sec is used. The period range was selected to be consistent with the period range of application for the GMRS or target spectrum.

The MSE between the target spectrum and the response spectrum of a recorded time series is computed in terms of the difference in the natural logarithm of spectral acceleration. The period range from 0.01 sec to 10 sec is subdivided into a large number of points equally-spaced in *ln* (period, $T_i$) (100 points/log cycle, therefore 301 points from 0.01 second to 10 seconds, end points included) and the target and record response spectra are interpolated to provide spectral accelerations at each period, $SA^{\text{target}}(T_i)$, and $SA^{\text{record}}(T_i)$, respectively. The MSE is then computed using Equation 4.1 over periods in the user-specified period range of interest.

$$\text{MSE} = \frac{\sum_i w(T_i)\left\{\ln[SA^{\text{target}}(T_i)] - \ln\left[SF \times SA^{\text{record}}(T_i)\right]\right\}^2}{\sum_i w(T_i)} \tag{4.1}$$

Parameter *SF* in Equation 4.1 is a linear scale factor applied to the entire response spectrum of the recording. Parameter $w(T_i)$ is a weight function that allows the user to assign relative weights to different parts of the period range of interest, providing greater flexibility in the selection of records. The simplest case is to assign equal weight to all periods in the period range of interest (i.e., $w(T_i)$ = 1), but the user may wish to emphasize the match over a narrow period range while maintaining a reasonable match over a broad period range. Arbitrary weight functions may be specified. In this project, equal weights for all periods in the period range of 0.01 sec to 10 sec is used (i.e., $w(T_i)$ = 1).

The NGA-West2 ground motion database web-based tool allows the user to select recordings for which the geometric mean of the two horizontal components provides a good match to the target spectrum. In this case the MSE is computed over both components using Equation 4.1 with the same value of *SF* applied to both components. While the NGA-West2 ground motion database tool also allows for the possibility that each horizontal component is selected independently (possibly, from different earthquakes or different recording stations), this was not selected for this application so that the two horizontal components represent the same earthquake magnitude, preserving the relative amplitude of the two horizontal components.

Minimization of the MSE as defined in Equation 4.1 is achieved by a scale factor given by the mean weighted residual in natural logarithm space between the target and the record spectra as defined in Equation 4.2.

$$ln\,SF = \frac{\sum_i w(T_i)\ln\left(SA^{\text{target}}(T_i) \big/ SA^{\text{record}}(T_i)\right)}{\sum_i w(T_i)} \qquad (4.2)$$

When record selection is based on simultaneous consideration of both horizontal components, the scale factor computed using Equation 4.2 minimizes the MSE between the target spectrum and the geometric mean of the spectra for the two horizontal components. The geometric mean (GM) of the two horizontal accelerations is given by Equation 4.3.

$$SA_{GM} = \sqrt{SA_{H1} \cdot SA_{H2}} \quad \text{or} \quad ln\,SA_{GM} = (ln\,SA_{H1} + ln\,SA_{H2})/2 \qquad (4.3)$$

Note that in NGA-West2 ground motion database users have the option to specify the ranges of parameters over which searches are to be conducted and other limits and restrictions can be applied to the searches. These may include: event name; NGA number; station name; earthquake magnitude range; type of faulting; distance range; Vs30 range (average shear wave velocity of soil within 30 m depth); significant duration range; whether records are to exclude, include, or be limited to pulse records; and limits on the scale factor *SF*.

Selected records are also checked to ensure that they meet criteria established by the SRP 3.7.1[33] regarding the adequacy of time histories. Based on SRP 3.7.1, the strong motion duration is defined as the time required for the Arias Intensity[34] to rise from 5% to 75% ($D_{5\text{-}75}$). The minimum acceptable strong motion duration should be six seconds.

To determine the strong-motion duration ($D_{5\text{-}75}$) the normalized Arias Intensity, $AI_N(\mathrm{t})$, is defined in Equation 4.4.

$$AI_N(\mathrm{t}) = \frac{\int_0^{\mathrm{t}} [\mathrm{a(t)}]^2 \mathrm{dt}}{\int_0^{\mathrm{t_{dur}}} [\mathrm{a(t)}]^2 \mathrm{dt}} \qquad (4.4)$$

---

[33] US Nuclear Regulatory Commission, "Standard Review Plan 3.7.1, Seismic Design Parameters," Revision 4, Washington, D.C. (December 2014)

[34] Arias A., "A Measure of Earthquake Intensity," In *Seismic Design for Nuclear Power Plants*, Ed. R.J. Hansen, MIT Press, Cambridge, Massachusetts. (1970)

where $a(t)$ is acceleration time history; and $\mathrm{t_{dur}}$ is the total duration of the acceleration time history. The $D_{5\text{-}75}$ is the time between instances $AI_N$ reaches 5% and 75%.

### 4.1.2 Spectral Matching

To be used for analysis, selected time histories must be conditioned to match the target spectra. Spectral matching analyses are performed to generate spectral-compatible acceleration time histories using the spectral matching computer program, RspMatch09[35, 36, 37]. RspMatch09 uses a time domain spectral matching method, where adjustment of initial time series (seed motions) is made by adding wavelet functions to the initial acceleration time history in time domain. This adjustment is repeated until its spectrum becomes comparable to the target spectrum over the desired frequency range.

Spectral matching analyses are performed by running RspMatch09 multiple times, which is specified in the RspMatch09 input file. The output files from the last run are used to confirm that the adjusted time histories meet the criteria stated in Appendix F of R.G. 1.208[38] and Option 1 – Approach 2 for Design Time Histories in SRP 3.7.1[39]. Ground motions or sets of ground motions that are generated to "match" or "envelop" given design response spectral shapes should comply with the following six steps:

1. The time history should have a sufficiently small time increment and sufficiently long durations. Time histories should have a Nyquist frequency of at least 50 Hz (e.g., a time increment of at most 0.010 seconds) and a total duration of 20 seconds. If frequencies higher than 50 Hz are of interest, the time increment of the record must be suitably reduced to provide a Nyquist frequency (Nyquist frequency, $N_f = 1/(2\Delta t)$, where $\Delta t$ = time increment) above the maximum frequency of interest. The total duration of the record can be increased by zero padding to satisfy these frequency criteria.

2. Spectral accelerations at 5 percent damping are computed at a minimum of 100 points per frequency span, uniformly spaced over the log frequency scale from 0.1 Hz to 50 Hz or the Nyquist frequency. If the target response spectrum is defined in the frequency range from 0.2 Hz to 25 Hz, the comparison of the modified response spectrum with the target spectrum is made at each frequency computed in this frequency range.

3. The computed 5 percent damped response spectrum of the average of all accelerograms should not fall more than 10 percent below the target spectrum at any one frequency (see Figure 4.4). To prevent spectra in large frequency windows from falling below the target spectrum, the spectra within a frequency window of no larger than ± 10 percent centered on the frequency should be allowed to fall below the target spectrum. This corresponds to spectra

---

[35] Paul C. Rizzo Associates, "Spectral Matching Computer Program: RspMatch09, Version 1.1, User Manual," Rev. 0, (April 2011)

[36] Paul C. Rizzo Associates, "V&V for Spectral Matching Computer Program RspMatch09," Rev. 1, (March 2012)

[37] L. Al Atik, and N. Abrahamson, "An Improved Method for Nonstationary Spectral Matching.," *Earthquake Spectra*, Vol. 26, No. 3, pp. 601-617. (August 2010)

[38] US Nuclear Regulatory Commission, "Standard Review Plan 3.7.1, Seismic Design Parameters," NUREG-8000, Revision 3, Washington, D.C. (March 2007)

[39] US Nuclear Regulatory Commission, "Standard Review Plan 3.7.1, Seismic Design Parameters," NUREG-8000, Chapter 3, Revision 4, Washington, D.C. (December 2014)

at no more than nine adjacent frequency points defined in Step 2 above from falling below the target spectrum.

4. R.G. 1.208[40] specifies that:
   "*The mean of the 5 percent damped response spectra should not exceed the target spectrum at any frequency by more than 30 percent (a factor of 1.3) in the frequency range between 0.2 Hz and 25 Hz. If the spectrum for the accelerogram exceeds the target spectrum by more than 30 percent at any frequency in this frequency range, the power spectral density of the accelerogram needs to be computed and shown to not have significant gaps in energy at any frequency over the frequency range. An additional check over the 0.2 to 25 Hz frequency range is that the mean ratio (ratio of the average record value to the target value) be greater than 1.0.*"

   Also, SRP 3.7.1 (Revision 4) states that:
   *"The computed 5 percent damped response spectrum of the artificial ground motion time history shall not exceed the target response spectrum at any frequency by more than 30 percent (a factor of 1.3) in the frequency range of interest. In addition, the power spectrum density of the accelerogram needs to be computed and shown to not have significant gaps in energy at any frequency over this frequency range."*

   In this project, both conditions are satisfied. Therefore, the power spectrum density (PSD) of the matched accelerograms is checked for energy gaps in frequency.

5. Modified motions should have typical strong motion durations (defined by 5-75% Arias intensity), peak ground acceleration (PGA), peak ground velocity (PGV), and peak ground displacement (PGD), and ratios of PGV/PGA (V/A) and PGA·PGD/PGV$^2$ (AD/V$^2$), which are generally consistent with characteristics for the magnitude-distance pairs for controlling events considered.

6. To be considered statistically independent, the directional correlation coefficients between pairs of time histories should not exceed a value of 0.16. The directional correlation coefficient is a measure of the degree of linear relationship between two earthquake accelerograms. For accelerograms *X* and *Y*, the directional correlation coefficient is given by Equation 4.5.

$$\rho_{xy} = \{ (1 / n) ( \sum_{i=1}^{n} [ (X_i - x)(Y_i - y) ] ) \} \div \{ \sigma_x \sigma_y \} \tag{4.5}$$

   where $n$ is the number of discrete acceleration-time data points, $x$ and $y$ are the mean values, and $\sigma_x$ and $\sigma_y$ are the standard deviations of $X$ and $Y$, respectively.

Note that Step 6 is checked only for the final set of adjusted design time histories. Step 5 is not considered since the selection of seed motions is not based on the magnitude-distance pairs, but those ground motion characteristic parameters are provided for the final set. Also note that $D_{5\text{-}75}$

---

[40] US Nuclear Regulatory Commission, Regulatory Guide 1.208, "A Performance-Based Approach to Define the Site-Specific Earthquake Ground Motion," (March 2007)

for the final adjusted time histories should be greater than 6 seconds (SRP 3.7.1, Rev. 4). The Arias intensity $D_{5\text{-}75}$ criteria are considered in the selection of seed motions. The $D_{5\text{-}75}$ of the adjusted motion may be altered and may be slightly less than six seconds. Those motions are still accepted in this project.

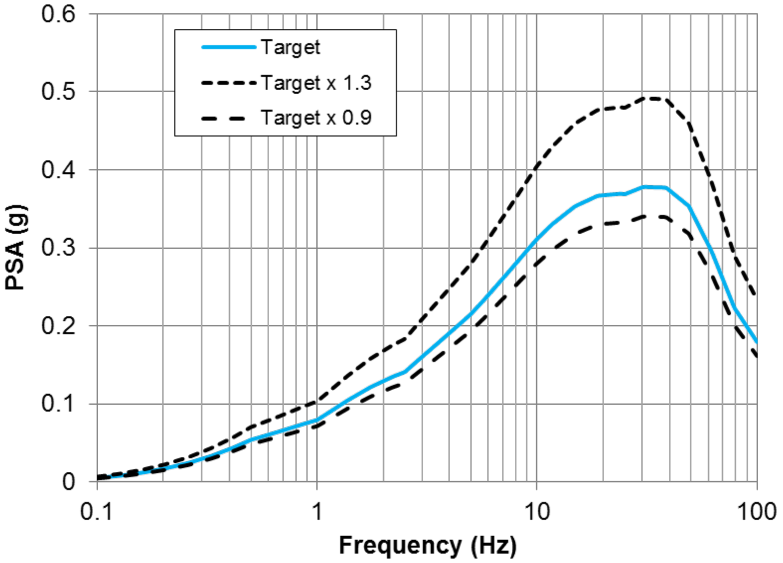

Figure 4.4. Horizontal target response spectra with its upper and lower bounds

### 4.1.3 Power Spectral Density Check

Smoothed Power Spectral Density (PSD) function of the matched time histories are computed in order to check and confirm that there is no significant gaps in the energy contents of the matched time histories. PSD of the time histories are obtained based on Appendix A of SRP 3.7.1 as follows:

$$S_0 = \frac{2|F(f)^2|}{2\pi T_D} \tag{4.6}$$

where $T_D$ is the strong motion duration over which $F(f)$ is evaluated. Duration $T_D$ represents the duration of near maximum and nearly stationary power of an acceleration time history record. Computed PSD is smoothed based on SRP 3.7.1 that is average PSD over a frequency band width of ±20 percent, centered on the frequency ($f$).

The target PSDs in SRP 3.7.1 are earthquake magnitude and source-site displacement dependent. The magnitude and distance of the 1E-4 low frequency controlling earthquake and 1E-4 high frequency controlling earthquake for the Central Illinois site are used in selecting the appropriate magnitude and distance bin.

When a single set of time histories are used in the analyses, meeting the PSD criterion usually an iterative process. In most cases, there would be certain energy gaps for the time histories obtained from the initial iteration. Those gaps may be eliminated by adding more frequency passing steps for the frequency range where the energy gaps are observed. Several try-and-error iterations are usually needed for this fine-tune process. The seed motion needs to be changed if the energy gaps cannot be eliminated after several iterations.

## 4.2 Assumptions and Justification

The assumptions used in this research are described in the context in this section.

## 4.3 Properties of Target Spectra

The horizontal target spectra (1E-4 UHRS) for Central Illinois site was developed by RIZZO[41]. According to Step 2 in Section 4.1.2 spectral accelerations at 5 percent damping should be computed at a minimum of 100 points per frequency decade, uniformly spaced over the log frequency scale from 0.1 Hz to 50 Hz or the Nyquist frequency. Therefore, the GMRS is interpolated at 301 frequencies uniformly spaced over the log frequency scale from 0.1 Hz to 100 Hz with 100 points per frequency decade.

The vertical target spectra are derived using the Vertical-to-Horizontal (V/H) spectral ratio. The V/H ratios for rock sites in central and Eastern United States (CEUS) in NUREG/CR-6728. Since the horizontal target spectra are developed for CEUS hard rock condition, the recommended V/H ratios from NUREG/CR-6728 can readily be used without any site-specific adjustment. The rock site V/H ratios in NUREG/CR-6728 are dependent on peak ground acceleration (PGA). The CEUS and rock V/H ratios are shown in Table 4.1.

Table 4.1. Recommended V/H ratios for CEUS rock sites conditions in NUREG/CR-6728

| **Frequency (Hz)** | **≤0.2g*** | **0.2g-0.5g*** | **>0.5g*** |
|---|---|---|---|
| 0.1 | 0.67 | 0.75 | 0.9 |
| 10 | 0.67 | 0.75 | 0.9 |
| 18.75 | 0.70 | 0.81 | 1.01 |
| 22.06 | 0.73 | 0.85 | 1.08 |
| 25 | 0.75 | 0.88 | 1.12 |
| 31.25 | 0.77 | 0.95 | 1.25 |
| 37.5 | 0.81 | 1.00 | 1.37 |
| 41.67 | 0.84 | 1.07 | 1.44 |
| 46.88 | 0.85 | 1.12 | 1.50 |
| 62.5 | 0.90 | 1.14 | 1.52 |
| 75 | 0.89 | 1.12 | 1.48 |
| 93.75 | 0.81 | 1.02 | 1.33 |
| 100 | 0.78 | 1.00 | 1.30 |

*Range in rock outcrop horizontal component peak acceleration

V/H ratios of Table 6.1 are interpolated at 301 frequencies and are used in interpolation of the horizontal GMRS. The vertical target spectra ordinates at 301 frequencies are therefore calculated from the interpolated V/H ratios and horizontal target spectra values. The spectral ordinate of

---

[41] RIZZO Associates, “Verification of Probabilistic Seismic Hazard Analysis Results for Central and Eastern United States Test Sites (DRAFT),” (June 2014)

horizontal target at 100 Hz is used as the PGA to determine the V/H ratios of Table 4.1. Since the spectral acceleration of horizontal target at 100 Hz is 0.18 g, the V/H ratios are taken as average of the values for the PGA range of ≤0.2g in Table 4.1. The interpolated horizontal and vertical GMRS are shown in Figure 4.5.

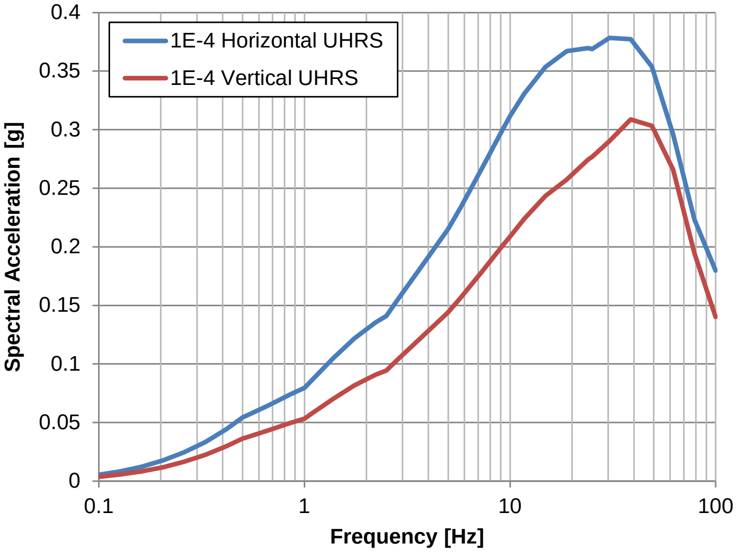

Figure 4.5. Horizontal and vertical ground motion target spectra

The 1E-4 lower frequency (LF) and high frequency (HF) controlling earthquakes for the Central Illinois site are also needed for the purpose of PSD check because the PSD targets defined in the SRP 3.7.1 are magnitude-distance bin dependent. The magnitude and distance for the 1E-4 LF and HF controlling earthquakes are shown in Table 4.2.

Table 4.2 1E-4 LF and HF controlling earthquakes for Central Illinois site

| Mean Annual Frequency of Exceedance | Frequency | Magnitude | Distance (km) |
|---|---|---|---|
| 1E-4 | LF (1.75 Hz) | 7.2 | 234 |
| | HF (7.5 Hz) | 4.0 | 38 |

## 4.4 Results

### 4.4.1 Seed Motion Information

The seed motion selection is performed following the steps below.

- The original horizontal target spectra developed by RIZZO (Figure 4.5) is defined at 36 frequency points and is introduced to the PEER web application ( http://ngawest2.berkeley.edu/spectras/12718/edit ) using the “User Defined Spectrum” as shown in Figure 4.6.
- The option of “Scaling Method” is checked as “Minimize MSE” as shown Figure 6.7.

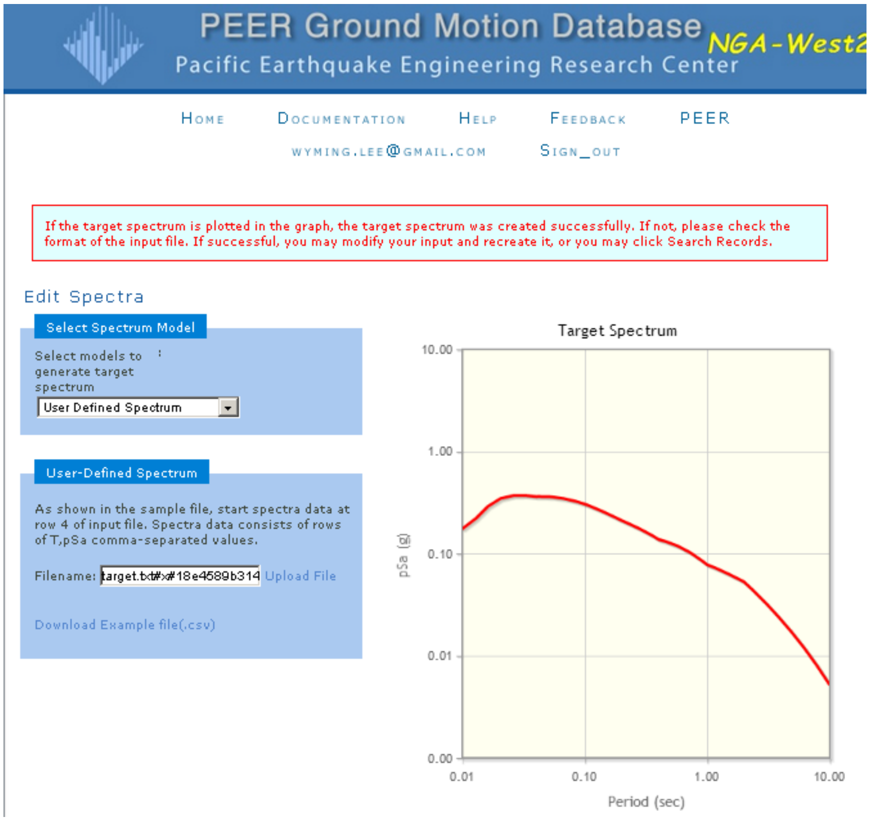

If the target spectrum is plotted in the graph, the target spectrum was created successfully. If not, please check the format of the input file. If successful, you may modify your input and recreate it, or you may click Search Records.

Select models to generate target spectrum : User Defined Spectrum

As shown in the sample file, start spectra data at row 4 of input file. Spectra data consists of rows of T,pSa comma-separated values.

Filename: target.txt#x#18e4589b314

Figure 4.6. Uploading the user-defined target spectrum using PEER database tool

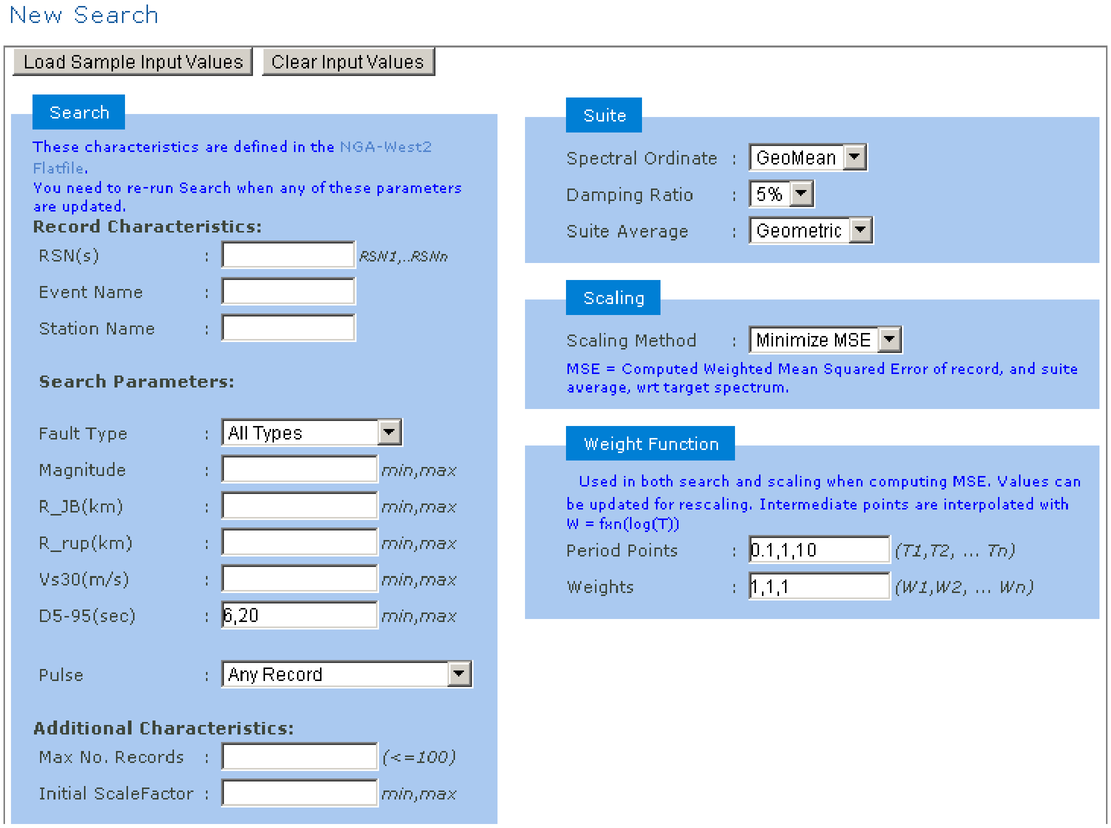

These characteristics are defined in the NGA-West2 Flatfile.
You need to re-run Search when any of these parameters are updated.

**Record Characteristics:**

RSN(s) : RSN1,..RSNn
Event Name :
Station Name :

**Search Parameters:**

Fault Type : All Types
Magnitude : min,max
R_JB(km) : min,max
R_rup(km) : min,max
Vs30(m/s) : min,max
D5-95(sec) : 6,20 min,max

Pulse : Any Record

**Additional Characteristics:**

Max No. Records : (<=100)
Initial ScaleFactor : min,max

Spectral Ordinate : GeoMean
Damping Ratio : 5%
Suite Average : Geometric

Scaling Method : Minimize MSE
MSE = Computed Weighted Mean Squared Error of record, and suite average, wrt target spectrum.

Used in both search and scaling when computing MSE. Values can be updated for rescaling. Intermediate points are interpolated with W = fxn(log(T))

Period Points : 0.1,1,10 (T1,T2, ... Tn)
Weights : 1,1,1 (W1,W2, ... Wn)

Figure 4.7. Search criteria for the seed motions

- The “Weight Function” for period range of 0.01 sec to 10 sec is defined as 1 (Figure 4.7).
- The range of Arias Intensity ($D_{5\text{-}95}$) is chosen to be between 6 to 20 seconds (Figure 4.7).
- Hitting on “Search” button show the accelerograms found which are ranked by the MSE calculated using Equations 4.1 through 4.3 for the geometrical mean.

Among all the records found by the PEER NGA-West2 web application, 13 records are selected to match the target spectra. The criteria to select those sequences are: 1) accelerograms are recorded with time increment of 0.005 sec, 2) the $D_{5\text{-}75}$ duration is greater than or close to 6 sec, and 3) the total duration of the time history is long enough to accommodate low-frequency wavelet needed to match below 0.2 Hz without significant distortion of the displacement. The un-scaled horizontal accelerograms along with the un-scaled vertical acceleration are used for spectral matching in this calculation.

Five more records from NUREG/CR-6728 database are selected based on the same considerations. Thus, so far in this project, 18 records (13 from PEER web application and five from NUREG database) have been selected and processed to match the target spectrum. Tables 4.2 and 4.3 show the seed motion information, for the PEER NGA-West2 Ground Motion Database and NUREG/CR-6728 database, respectively.

Lowest usable frequency provided in the last column of Table 4.2 is the recommended lowest usable frequency for the record. The recommended lowest usable frequency is related to filtering of a record by the record processing organization to remove low-frequency (long-period) noise. Filtering results in suppression of ground motion amplitudes and energy at frequencies lower than the lowest usable frequency such that the motion is not representative of the real ground motion at those frequencies. It is a user’s choice on whether to select or reject a record on the basis of the lowest usable frequency. Because of the suppression of ground motion at frequencies lower than the lowest usable frequency, it is recommended that selected records have lowest usable frequencies equal to or lower than the lowest frequency of interest.

The unscaled accelerogram file names along with the calculated PGA, PGD, PGV, V/A, $AD/V^2$ and $D_{5\text{-}95}$ are shown in Table 4.4.

Table 4.2 Seed records used for the time history matching from NGA-West2 database

| Spectral Ordinate | RSN | MSE | SF | $D_{5\text{-}75}$ | dt (sec) | Event | Year | Station | Mag. | Mechanism | Rjb (km) | Rrup (km) | Vs30 (m/s) | Lowest Useable Freq. (Hz) |
|---|---|---|---|---|---|---|---|---|---|---|---|---|---|---|
| GM | 94 | 0.371 | 3.075 | 7.3 | 0.005 | "San Fernando" | 1971 | "Wrightwood - 6074 Park Dr" | 6.61 | Reverse | 61.64 | 62.23 | 486 | 0.25 |
| GM | 97 | 0.447 | 1.790 | 6.1 | 0.005 | "Point Mugu" | 1973 | "Port Hueneme" | 5.65 | Reverse | 15.48 | 17.71 | 249 | 0.25 |
| GM | 155 | 0.394 | 5.481 | 10.5 | 0.002 | "Norcia Italy" | 1979 | "Bevagna" | 5.9 | Normal | 31.43 | 31.45 | 401 | 0.625 |
| GM | 160 | 0.391 | 0.233 | 6.1 | 0.005 | "Imperial Valley-06" | 1979 | "Bonds Corner" | 6.53 | strike slip | 0.44 | 2.66 | 223 | 0.125 |
| GM | 162 | 0.300 | 0.561 | 7.2 | 0.005 | "Imperial Valley-06" | 1979 | "Calexico Fire Station" | 6.53 | strike slip | 10.45 | 10.45 | 231 | 0.05 |
| GM | 188 | 0.263 | 2.607 | 6.3 | 0.005 | "Imperial Valley-06" | 1979 | "Plaster City" | 6.53 | strike slip | 30.33 | 30.33 | 317 | 0.15 |
| GM | 190 | 0.258 | 1.431 | 6.2 | 0.005 | "Imperial Valley-06" | 1979 | "Superstition Mtn Camera" | 6.53 | strike slip | 24.61 | 24.61 | 362 | 0.125 |
| GM | 209 | 0.130 | 1.094 | 6.2 | 0.005 | "Imperial Valley-08" | 1979 | "Westmorland Fire Sta" | 5.62 | strike slip | 9.39 | 9.76 | 194 | 0.0875 |
| GM | 213 | 0.558 | 3.326 | 6.7 | 0.005 | "Livermore-01" | 1980 | "Fremont - Mission San Jose" | 5.8 | strike slip | 34.66 | 35.68 | 368 | 0.25 |
| GM | 214 | 0.501 | 1.387 | 7.8 | 0.005 | "Livermore-01" | 1980 | "San Ramon - Eastman Kodak" | 5.8 | strike slip | 15.19 | 17.24 | 378 | 0.15 |
| GM | 230 | 0.491 | 0.446 | 7.1 | 0.005 | "Mammoth Lakes-01" | 1980 | "Convict Creek" | 6.06 | Normal Oblique | 1.1 | 6.63 | 382 | 0.25 |
| GM | 231 | 0.359 | 0.605 | 7.5 | 0.005 | "Mammoth Lakes-01" | 1980 | "Long Valley Dam (Upr L Abut)" | 6.06 | Normal Oblique | 12.56 | 15.46 | 537 | 0.1375 |
| GM | 497 | 0.115 | 1.376 | - | 0.005 | "Nahanni- Canada" | 1985 | "site 3" | 6.76 | Reverse | 4.9 | 5.3 | 660 | 0.12 |

*Definitions and Notes*:

**Spectral Ordinate**: GM denotes geometric mean of the two horizontal components

**RSN**: Record sequence number. A unique number assigned to each NGA-West2 record for identification purposes

**MSE**: Mean square error

**SF**: Scaling factor

**$D_{5\text{-}75}$ (sec)**: Significant duration, the time needed to build up between 5 and 75 percent of the total Arias intensity. If the search is for two components in pair, durations for both components are given.

**Event**: Name of the earthquake event

**Year**: Year of earthquake

**Station**: Unique name of strong-motion station

**Mag.** Moment magnitude of earthquake

**Mechanism** Type of Fault Mechanism. Available mechanisms are: Strike-Slip, Normal, Normal-Oblique, Reverse, Reverse-Oblique.

**Rjb (km)**: Joyner-Boore distance to rupture plane

**Rrup (km)**: Closest distance to rupture plane

**VS30 (m/s)**: Average shear velocity of top 30 m

Table 4.3 Seed records used for the time history matching from NUREG/CR-6728 database

| **Record Name** | **5-75% Duration (sec)** | **Earthquake Name** | **Year** | **Station** | **Magnitude** |
|---|---|---|---|---|---|
| SON | 9.7 | San Fernando | 1971 | San Onofre - So Cal Edison | 6.6 |
| CSM | 6.7 | San Fernando | 1971 | Cedar Springs, Allen Ranch | 6.6 |
| LVL | 6.3 | Mammoth Lakes | 1980 | Long Valley Dam (L Abut) | 6.0 |
| L04 | 6.1 | San Fernando | 1971 | Lake Hughes #4 | 6.6 |
| PUL | - | Northridge | 1994 | Pacoima Dam (upperleft) # | 6.7 |

*Note*: Record name corresponds to the file name of the seed motions

Table 4.4 Ground motion parameters for the selected seed motions

| **ID** | **Component** | **PGA (g)** | **PGV** | **PGD** | **V/A** | **AD/V$^2$** | $D_{5\text{-}75}$ |
|---|---|---|---|---|---|---|---|
| NGA-497 | S3-FN (X) | 0.168 | 5.7 | 2.8 | 33.7 | 14.3 | 7.0 |
| | S3-FP (Y) | 0.148 | 4.9 | 1.6 | 32.9 | 9.5 | 7.1 |
| | S3-UP (Z) | 0.140 | 6.7 | 3.0 | 48.1 | 9.1 | 6.8 |
| NRG-CSM | CSM095 (X) | 0.050 | 1.9 | 0.4 | 37.5 | 5.4 | 6.0 |
| | CSM185 (Y) | 0.035 | 1.2 | 0.5 | 35.4 | 11.4 | 6.7 |
| | CSMDWN (Z) | 0.026 | 1.8 | 0.6 | 67.8 | 5.0 | 6.5 |
| NRG-L04 | L04111 (X) | 0.488 | 8.3 | 1.2 | 17.0 | 8.1 | 6.1 |
| | L04201 (Y) | 0.418 | 12.4 | 1.4 | 29.7 | 3.7 | 6.3 |
| | L04DWN (Z) | 0.386 | 9.6 | 1.8 | 24.8 | 7.4 | 5.0 |
| NRG-LVL | LVL000 (X) | 0.230 | 8.1 | 0.9 | 35.1 | 3.2 | 6.7 |
| | LVL090 (Y) | 0.129 | 5.8 | 2.2 | 45.1 | 8.2 | 6.5 |
| | LVL-UP (Z) | 0.178 | 6.6 | 0.8 | 37.2 | 3.1 | 5.3 |
| NRG-PUL | PUL104 (X) | 3.942 | 65.0 | 6.1 | 16.5 | 5.6 | 1.7 |
| | PUL194 (Y) | 3.592 | 87.1 | 15.3 | 24.2 | 7.1 | 1.8 |
| | PUL-UP (Z) | 4.253 | 103.2 | 13.3 | 24.3 | 5.2 | 1.2 |
| NRG-SON | SON033 (X) | 0.039 | 1.6 | 0.8 | 42.5 | 11.0 | 9.7 |
| | SON303 (Y) | 0.039 | 1.9 | 0.7 | 47.8 | 7.2 | 10.0 |
| | SONDWN (Z) | 0.046 | 1.8 | 0.8 | 38.4 | 11.1 | 9.2 |
| RSN-094 | WTW025 (X) | 0.055 | 3.3 | 1.6 | 59.6 | 7.9 | 7.0 |
| | WTW295 (Y) | 0.046 | 5.1 | 3.0 | 111.9 | 5.2 | 7.3 |
| | WTW-UP (Z) | 0.029 | 3.1 | 2.5 | 104.3 | 7.6 | 9.5 |
| RSN-097 | PHN180 (X) | 0.128 | 14.3 | 4.1 | 112.1 | 2.5 | 3.6 |
| | PHN270 (Y) | 0.075 | 4.9 | 1.0 | 64.9 | 3.0 | 6.1 |
| | PHN-UP (Z) | 0.044 | 2.0 | 0.5 | 45.5 | 5.3 | 3.7 |
| RSN-155 | BEV-EW (X) | 0.023 | 2.1 | 0.7 | 90.6 | 3.7 | 9.2 |
| | BEV-NS (Y) | 0.036 | 2.7 | 0.4 | 74.0 | 2.2 | 10.5 |
| | BEV-UP | 0.023 | 1.0 | 0.2 | 42.7 | 4.1 | 10.9 |
| RSN-160 | BCR140 (X) | 0.599 | 46.8 | 20.2 | 78.1 | 5.4 | 6.1 |
| | BCR230 (Y) | 0.777 | 44.9 | 15.1 | 57.8 | 5.7 | 4.7 |
| | BCR-UP (Z) | 0.532 | 12.2 | 3.3 | 22.9 | 11.5 | 4.5 |
| RSN-162 | CXO225 (X) | 0.277 | 22.5 | 9.9 | 81.1 | 5.4 | 5.8 |
| | CXO315 (Y) | 0.203 | 18.7 | 15.9 | 91.7 | 9.1 | 7.1 |
| | CXO-UP (Z) | 0.194 | 7.0 | 2.7 | 36.2 | 10.5 | 6.5 |
| RSN-188 | PLS045 (X) | 0.043 | 3.2 | 1.2 | 73.9 | 5.1 | 6.3 |
| | PLS135 (Y) | 0.058 | 5.9 | 2.5 | 101.4 | 4.1 | 5.8 |
| | PLS-UP (Z) | 0.026 | 2.5 | 1.1 | 93.2 | 4.8 | 9.0 |
| RSN-190 | SUP045 (X) | 0.111 | 5.1 | 2.1 | 45.6 | 9.1 | 6.2 |
| | SUP135 (Y) | 0.202 | 8.9 | 2.8 | 44.2 | 6.9 | 2.2 |
| | SUP-UP (Z) | 0.080 | 2.1 | 0.9 | 26.1 | 16.1 | 5.8 |
| RSN-209 | WSM090 (X) | 0.113 | 12.0 | 10.1 | 106.3 | 7.8 | 6.2 |
| | WSM180 (Y) | 0.151 | 10.0 | 3.4 | 66.4 | 5.0 | 3.7 |
| | WSM-UP (Z) | 0.118 | 3.0 | 1.7 | 25.6 | 22.1 | 3.3 |
| RSN-213 | FRE075 (X) | 0.045 | 4.3 | 1.0 | 96.6 | 2.3 | 5.6 |
| | FRE345 (Y) | 0.051 | 4.2 | 1.1 | 82.4 | 3.3 | 6.7 |
| | FRE-UP (Z) | 0.027 | 2.2 | 0.6 | 83.4 | 3.4 | 9.5 |

| | | | | | | | |
|---|---|---|---|---|---|---|---|
| RSN-214 | KOD180 (X) | 0.150 | 20.8 | 5.9 | 138.8 | 2.0 | 4.6 |
| | KOD270 (Y) | 0.064 | 8.3 | 1.6 | 130.4 | 1.5 | 7.9 |
| | KOD-UP (Z) | 0.037 | 3.0 | 0.6 | 81.1 | 2.4 | 7.7 |
| RSN-230 | CVK090 (X) | 0.419 | 23.8 | 4.1 | 56.6 | 3.0 | 6.6 |
| | CVK180 (Y) | 0.442 | 23.5 | 5.4 | 53.2 | 4.3 | 7.1 |
| | CVK-UP (Z) | 0.387 | 21.1 | 6.1 | 54.6 | 5.2 | 5.7 |
| RSN-231 | LUL000 (X) | 0.430 | 23.7 | 7.6 | 55.2 | 5.7 | 6.9 |
| | LUL090 (Y) | 0.271 | 13.9 | 3.2 | 51.2 | 4.5 | 7.5 |
| | LUL-UP (Z) | 0.123 | 8.4 | 1.7 | 68.4 | 3.0 | 7.2 |

*Notes*:

1) Motions with ID named “NRG” are from NUREG/CR-6728 database. Others are from the PEER NGA-West2 database.
2) First column (Name) corresponds to the file name of the motions
3) PGA denotes peak ground acceleration
4) PGV denotes peak ground velocity
5) PGD denotes peak ground displacement
6) The “ID” are used for the identity of set of motions
7) The seed motion file name is used to differentiate the three components. The two horizontal components are abbreviated as “X” and “Y” and the vertical component is “Z”.

As described in Section 4.2, seed motions from other regions different from CEUS rock conditions can be used in this project based on a previous study[42], which manipulates ground motions originating in the Western United States to resemble those that might occur in the eastern United States. This study reported unbiased estimates of the structural response after comparing transformed ground motions to a control of group of records from the target scenario.

### 4.4.2 Characteristics of Matched Ground Motions

In this section, the matched (adjusted) ground motion time histories are checked against the criteria established in SRP 3.7.1 and RG 1.208, which were described in Section 4.1.

#### 4.4.2.1 Spectra Matching

The spectral matching is performed using software RspMatch09 (Section 4.1.2). RspMatch09 uses wavelet functions to modify the initial time series such that its response spectrum is compatible with the design spectrum. A fundamental assumption of this methodology is that the time of the peak response does not change as a result of the wavelet adjustment[43]. The goal is to modify the time history such that its computed response spectrum matches the target spectrum across the whole frequency range while maintaining realistic velocity and displacement time series. The spectral matching is performed in multiple passes as needed. In each pass a determined period range of the response spectrum is matched. The output of each pass (adjusted time history) is the input for the consecutive pass. In the first pass the matching is performed only for a short period

---

[42] J.E. Carballo, and C.A. Cornell, “Probabilistic Seismic Demand Analysis: Spectrum Matching and Design,” Report No. RMS-41, Reliability of Marine Structures Program, Stanford University, Palo Alto, California, (July 2000)

[43] L. Al Atik, and N. Abrahamson, “An Improved Method for Nonstationary Spectral Matching.,” *Earthquake Spectra*, Vol. 26, No. 3, pp. 601-617. (August 2010)

range. Longer period range of response spectrum is matched in the consecutive passes. The last pass covers the whole period range of interest (0.01 sec to 10 sec here).

As an example, the horizontal target spectrum and vertical target spectrum are shown in Figure 4.8, along with the response spectra of one set of matched time histories. Target spectra times 1.3 (i.e., 30 % above) and 0.9 (i.e., 10 % below) are also plotted. The matched spectra are within this range. There are no more than 9 consecutive spectral points falling below the target spectrum; and in the mean ratio of the average record value to the target value over the 0.2 to 25 Hz frequency is greater than 1.0. All the associated numerical values and criteria checks are performed using Excel spreadsheets named as the record names in corresponding folders.

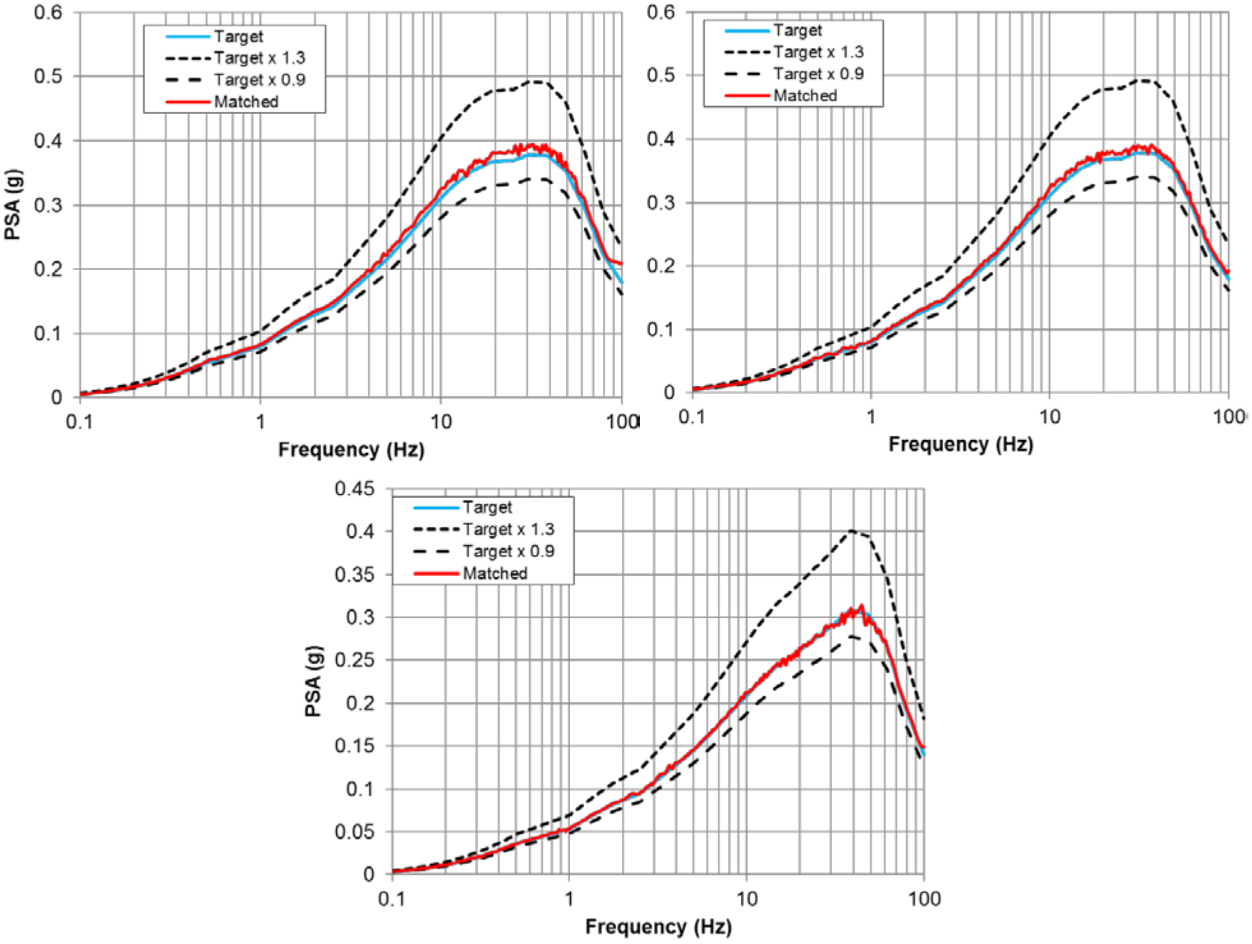

Figure 4.8. An example of PSA matching for Motion rsn-097 in horizontal X-direction (top left plot), Y-direction (top right), and vertical Z-direction (bottom plot)

### 4.4.2.2 Ground Motion Parameters

The ground motion parameters for the matched time histories (Table 4.4) are in general consistent with the typical values for magnitude and distance range for the controlling earthquake (RIZZO, 2014) as listed in the Table 3-6 in NUREG/CR-6728.

The ground motion durations ($D_{5-75}$) of all the matched time histories are close to or greater than or close 6.0 seconds, except “NRG-PUL”. The correlation coefficients between the two horizontal components are less than 0.16 for all the matched motions.

The time histories and the normalized Arias intensity plot of all the motions, including seed motions and the matched motions, are presented in Appendix B. For each set of the matched motions, the three components are aligned based on the arrival time of 5% normalized Arias intensity.

Table 4.5 Matched ground motion parameters

| ID | Component | PGA (g) | PGV (cm/s) | PGD (cm) | V/A (cm/sec/g) | AD/V$^2$ | $D_{5-75}$ (sec) | Correlation Coef. (X, Y) |
|---|---|---|---|---|---|---|---|---|
| NGA -497 | S3-FN (X) | 0.196 | 9.7 | 9.7 | 49.7 | 19.7 | 7.1 | 0.031 |
| | S3-FP (Y) | 0.141 | 10.5 | 5.4 | 74.4 | 6.7 | 7.7 | |
| | S3-UP (Z) | 0.129 | 6.7 | 4.5 | 51.7 | 12.7 | 7.6 | --- |
| NRG-CSM | CSM095 (X) | 0.176 | 11.6 | 8.9 | 66.0 | 11.4 | 5.7 | 0.055 |
| | CSM185 (Y) | 0.164 | 12.8 | 7.1 | 77.8 | 7.1 | 6.5 | |
| | CSMDWN (Z) | 0.142 | 5.6 | 4.5 | 39.5 | 19.8 | 7.1 | --- |
| NRG-L04 | L04111 (X) | 0.183 | 6.7 | 6.5 | 36.8 | 25.7 | 5.4 | 0.020 |
| | L04201 (Y) | 0.156 | 8.5 | 7.9 | 54.5 | 16.8 | 5.6 | |
| | L04DWN (Z) | 0.122 | 5.1 | 5.4 | 41.8 | 25.1 | 6.3 | --- |
| NRG-LVL | LVL000 (X) | 0.185 | 7.5 | 8.7 | 40.8 | 27.8 | 6.5 | 0.047 |
| | LVL090 (Y) | 0.162 | 10.6 | 6.4 | 65.4 | 9.1 | 6.6 | |
| | LVL-UP (Z) | 0.117 | 5.1 | 4.2 | 43.8 | 18.4 | 6.1 | --- |
| NRG-PUL | PUL104 (X) | 0.159 | 10.9 | 7.8 | 68.3 | 10.3 | 2.5 | 0.020 |
| | PUL194 (Y) | 0.193 | 10.7 | 8.7 | 55.5 | 14.3 | 1.6 | |
| | PUL-UP (Z) | 0.139 | 7.3 | 5.1 | 53.0 | 12.9 | 2.1 | --- |
| NRG-SON | SON033 (X) | 0.165 | 8.1 | 5.7 | 49.1 | 14.1 | 8.7 | 0.065 |
| | SON303 (Y) | 0.157 | 9.9 | 6.0 | 62.6 | 9.5 | 10.3 | |
| | SONDWN (Z) | 0.124 | 8.9 | 4.5 | 71.6 | 6.9 | 8.1 | --- |
| RSN-094 | WTW025 (X) | 0.164 | 8.6 | 11.0 | 52.5 | 24.0 | 8.9 | 0.033 |
| | WTW295 (Y) | 0.136 | 12.5 | 13.2 | 91.5 | 11.4 | 10.6 | |
| | WTW-UP (Z) | 0.145 | 4.9 | 5.5 | 33.8 | 32.4 | 10.6 | --- |
| RSN-097 | PHN180 (X) | 0.209 | 17.7 | 21.8 | 84.5 | 14.3 | 5.7 | 0.131 |
| | PHN270 (Y) | 0.167 | 10.3 | 11.4 | 61.6 | 17.7 | 7.1 | |
| | PHN-UP (Z) | 0.148 | 5.5 | 3.2 | 37.0 | 15.6 | 5.5 | --- |
| RSN-155 | BEV-EW (X) | 0.156 | 9.4 | 7.5 | 60.4 | 13.0 | 7.8 | 0.071 |
| | BEV-NS (Y) | 0.204 | 11.5 | 17.2 | 56.2 | 26.2 | 10.2 | |
| | BEV-UP | 0.143 | 7.0 | 8.5 | 49.3 | 24.2 | 11.5 | --- |
| RSN-160 | BCR140 (X) | 0.157 | 11.2 | 8.7 | 71.5 | 10.6 | 7.2 | 0.057 |
| | BCR230 (Y) | 0.166 | 11.2 | 7.3 | 67.5 | 9.5 | 6.1 | |

| | | | | | | | | |
|---|---|---|---|---|---|---|---|---|
| | BCR-UP (Z) | 0.126 | 5.9 | 4.9 | 46.9 | 17.5 | 5.0 | --- |
| RSN-162 | CXO225 (X) | 0.175 | 10.9 | 8.0 | 62.3 | 11.5 | 8.1 | 0.081 |
| | CXO315 (Y) | 0.161 | 11.1 | 7.9 | 68.9 | 10.2 | 10.0 | |
| | CXO-UP (Z) | 0.126 | 5.3 | 4.0 | 42.2 | 17.3 | 8.1 | --- |
| RSN-188 | PLS045 (X) | 0.172 | 12.2 | 11.6 | 70.5 | 13.3 | 7.3 | 0.019 |
| | PLS135 (Y) | 0.169 | 9.4 | 7.7 | 55.9 | 14.2 | 7.2 | |
| | PLS-UP (Z) | 0.139 | 5.5 | 5.5 | 39.9 | 24.6 | 8.7 | --- |
| RSN-190 | SUP045 (X) | 0.170 | 13.6 | 6.1 | 79.9 | 5.5 | 6.9 | 0.005 |
| | SUP135 (Y) | 0.164 | 11.9 | 6.8 | 72.5 | 7.8 | 4.8 | |
| | SUP-UP (Z) | 0.151 | 6.2 | 4.0 | 40.7 | 15.7 | 6.8 | --- |
| RSN-209 | WSM090 (X) | 0.184 | 11.0 | 8.4 | 59.7 | 12.7 | 7.3 | 0.017 |
| | WSM180 (Y) | 0.169 | 15.2 | 7.3 | 89.8 | 5.3 | 5.3 | |
| | WSM-UP (Z) | 0.151 | 8.5 | 3.6 | 55.9 | 7.4 | 4.3 | --- |
| RSN-213 | FRE075 (X) | 0.187 | 11.0 | 10.0 | 58.8 | 15.2 | 6.2 | 0.076 |
| | FRE345 (Y) | 0.176 | 12.1 | 7.2 | 68.7 | 8.6 | 4.7 | |
| | FRE-UP (Z) | 0.107 | 8.7 | 11.0 | 81.1 | 15.3 | 6.8 | --- |
| RSN-214 | KOD180 (X) | 0.175 | 13.6 | 8.7 | 77.9 | 8.0 | 5.9 | 0.014 |
| | KOD270 (Y) | 0.168 | 11.9 | 6.7 | 71.1 | 7.7 | 5.5 | |
| | KOD-UP (Z) | 0.116 | 6.7 | 6.6 | 57.8 | 16.7 | 7.2 | --- |
| RSN-230 | CVK090 (X) | 0.150 | 11.3 | 16.9 | 75.4 | 19.4 | 7.5 | 0.020 |
| | CVK180 (Y) | 0.191 | 12.6 | 7.5 | 66.1 | 8.8 | 6.7 | |
| | CVK-UP (Z) | 0.124 | 7.8 | 9.2 | 62.8 | 18.4 | 5.2 | --- |
| RSN-231 | LUL000 (X) | 0.201 | 12.2 | 6.6 | 60.8 | 8.7 | 7.8 | 0.080 |
| | LUL090 (Y) | 0.196 | 10.1 | 7.8 | 51.6 | 14.8 | 7.3 | |
| | LUL-UP (Z) | 0.114 | 6.0 | 4.8 | 52.8 | 14.9 | 8.4 | --- |

#### 4.4.2.3 Power Spectral Density Checking

According to SRP 3.7.1, both Revisions 3 and 4[44], the energy gap check can be performed utilizing the results for the average of the suite of multiple time histories. The smooth PSD of all the matched time histories, along with the median PSD, are compared against the PSD target from SRP 3.7.1 in Figure 4.9. Although all the matched time histories are matched to the same target response spectra and perform very well in terms of response spectrum matching, i.e. all the criteria are satisfied for individual time histories, the corresponding PSDs show relatively large variability. The median PSD from all the time histories are compared with PSD target defined in SRP 3.7.1. No significant energy gap is observed when the Revision 3 PSD target is considered. However, significant energy gap is observed in the frequency range higher than 10 to 20 Hz, when the Revision 4 PSD target is considered.

---

[44] US Nuclear Regulatory Commission, “Standard Review Plan 3.7.1, Seismic Design Parameters,” Revisions 3 and 4, Washington, D.C. (March 2007, and December 2014)

Note that the Revision 4 of SRP 3.7.1 was published recently in December, 2014 and the industry has started testing the PSD target defined in this revision. Therefore, the difference between target PSD in Revisions 3 and 4 of SRP 3.7.1 and the issue of energy gap between PSD of matched time histories and PSD target in Revision 4 are still an open questions in the industry.

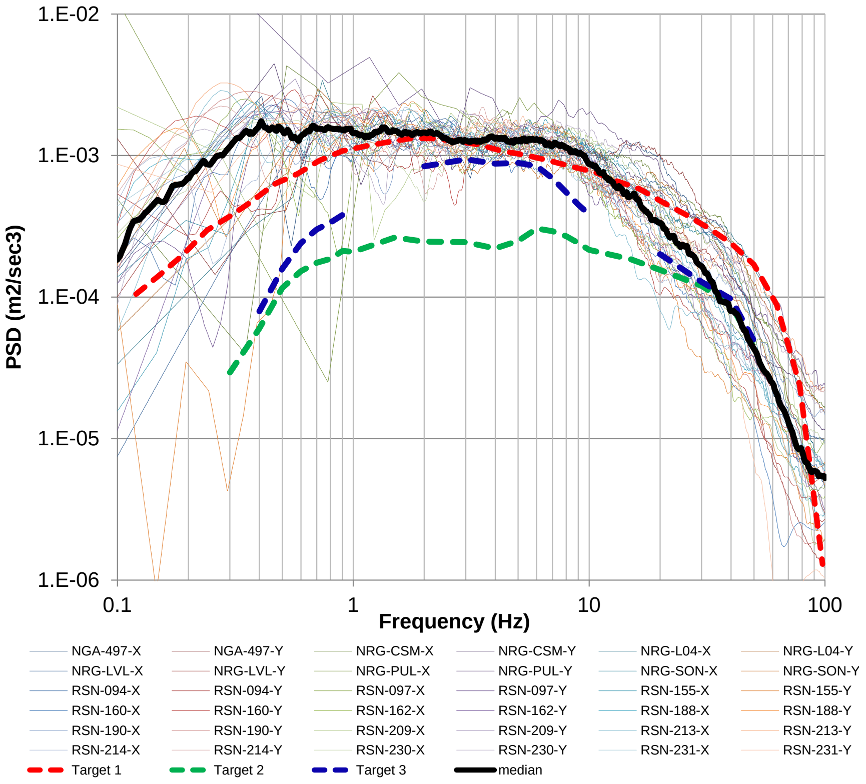

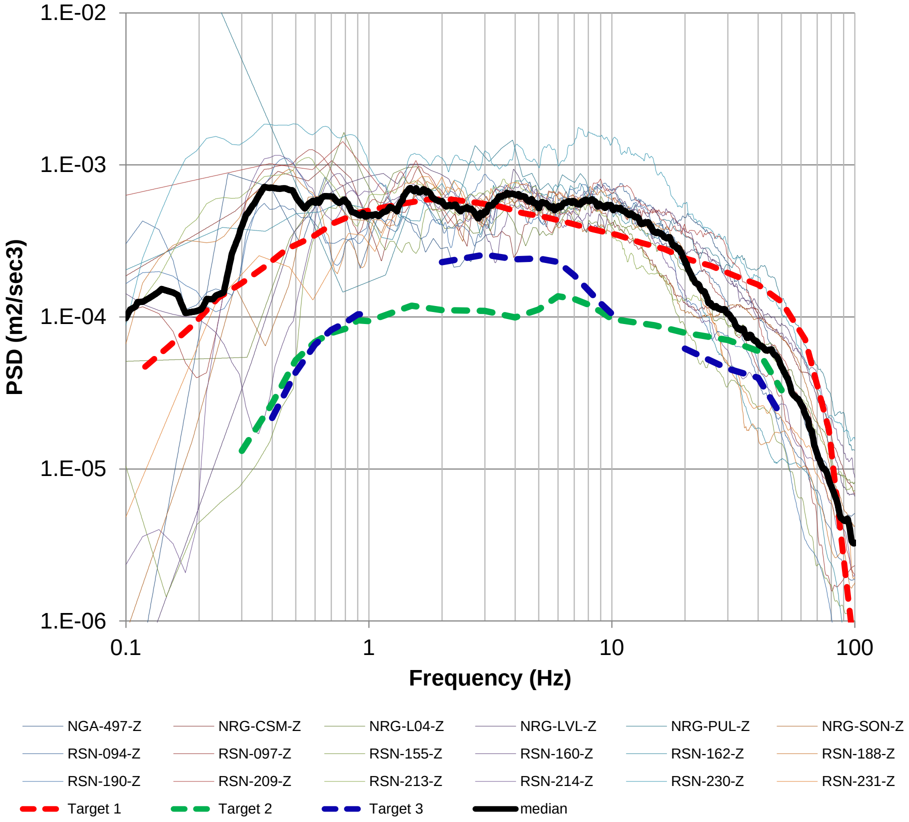

Figure 4.9. Power spectral density of matched time histories in horizontal (top) and vertical (bottom) directions

In Figure 4.9, Target 1 spectrum (red dashed line) is the 70% of the CEUS rock PSD in Revision 4 of SRP 3.7.1 as average of LF & HF controlling earthquake (*M*=6.0 and *R*=38 km). Target 3 spectrum is the 80% of the CEUS rock PSD in Revision 3 of SRP 3.7.1 per HF controlling earthquake (*M*=6.0 and *R*=38 km). Target 4 is the 80% of the CEUS rock PSD in Revision 3 of SRP 3.7.1 per LF controlling earthquake (*M*=7.2 and *R*=234 km).

Out of the 18 sets of matched time histories, three sets have the potential to be further fine-tuned to meet the criteria given in both Revisions 3 and 4 of SRP 3.7.1. In other words, those sets of motions may be fine-tuned so that the PSD of the matched motions can envelope both Revisions 3 and 4 PSD target. The motion fine-tune is a trial-and-error process by adding more passing frequencies in the RspMatch09 input files in the frequency range where minor energy gaps are observed. Those fine-tunes are needed if a single set of time histories are used in the analyses. The smoothed PSD of the three sets of motions are presented in Figures 4.10 through 4.12, along with the PSD targets from both Revisions 3 and 4 of SRP 3.7.1.

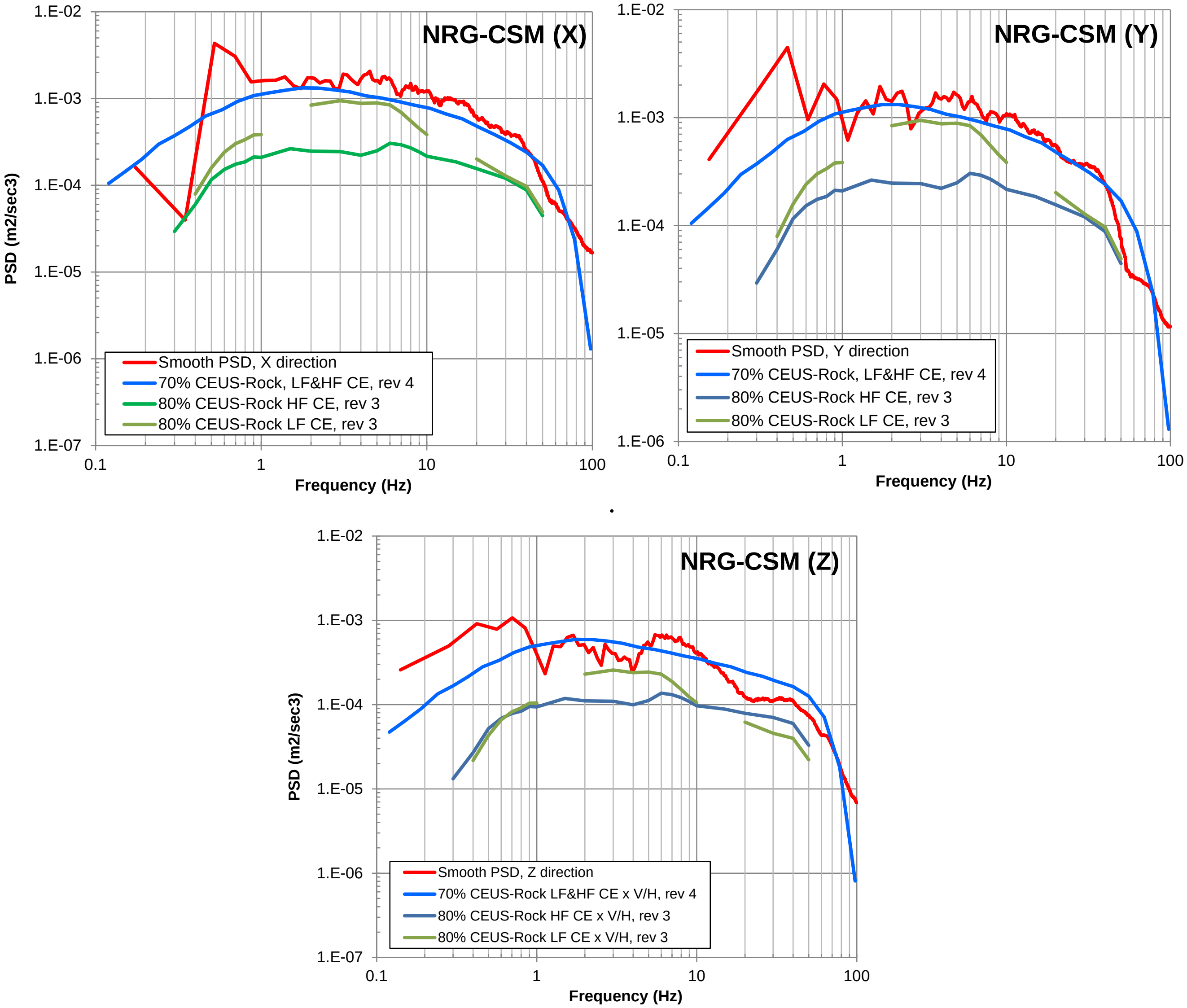

Figure 4.10. Smooth PSD of matched motion NRG-CSM in X, Y, and Z directions

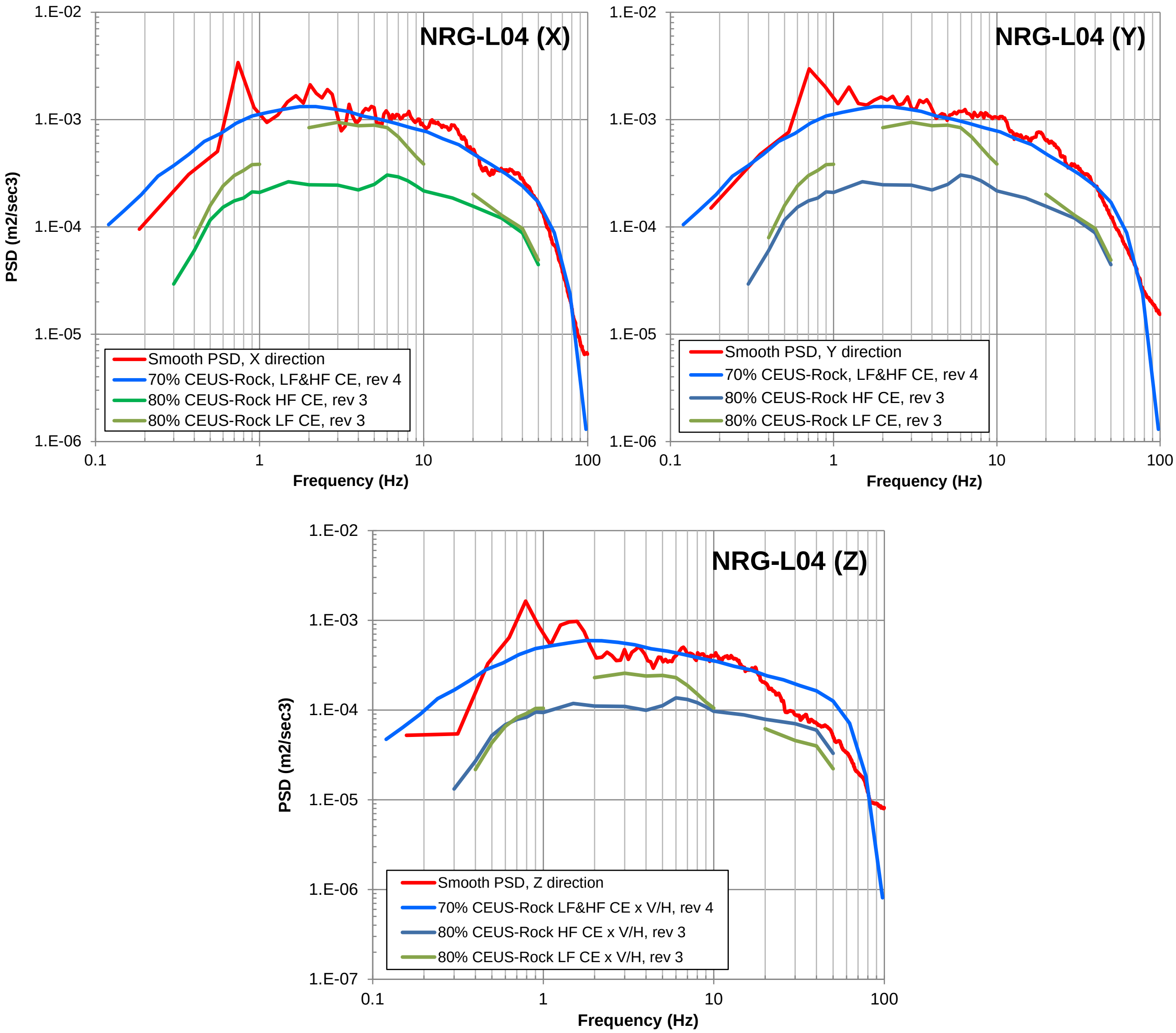

Figure 4.11. Smooth PSD of matched motion NRG-L04 in X, Y, and Z directions

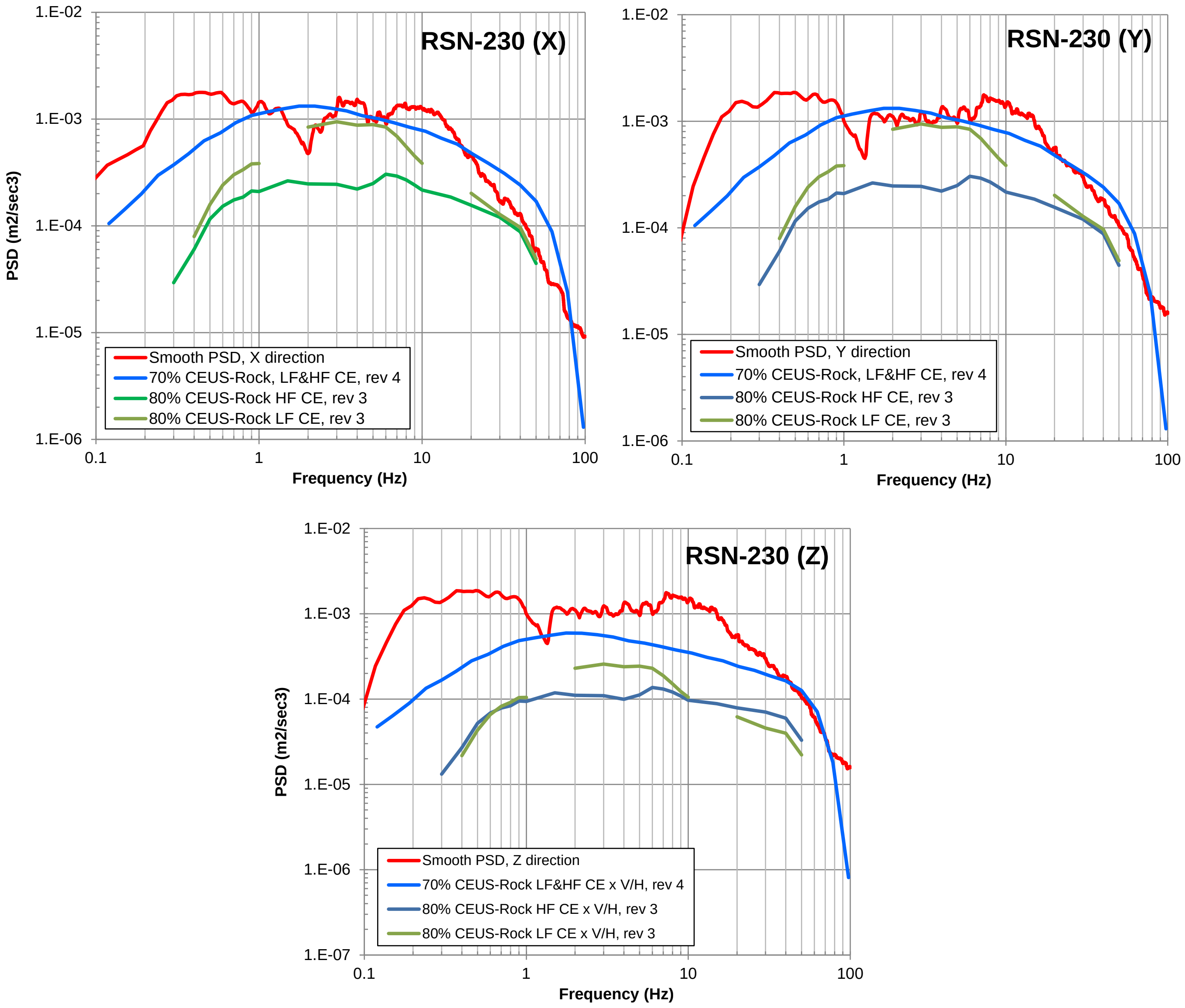

Figure 4.12. Smooth PSD of matched motion RSN-230 in X, Y, and Z directions

### 4.4.2.4 Time Histories

Although it is not required in SRP 3.7.1, the time histories of the matched motions and the scaled seed motions are often compared in practice. In certain low-frequency sensitive analyses, such as those for pipelines or spent fuel pool, the distortion in displacement time history is of particular interest. Two extreme cases in the displacement time history comparisons are shown in Figures 4.13 and 4.14. In Figure 4.13, the matched motion has minimum distortion in displacement time history because the response spectrum of the seed motion is similar to the target spectrum in the low frequency range (as shown in Figure 4.15). In Figure 4.14, the distortion in the matched displacement time history is very prominent, since the seed motion is lack of low frequency content, as shown in the comparison in Figure 4.16. Above mentioned observations have a theoretical basis, since the displacement history of a ground motion is largely controlled by its low frequency content.

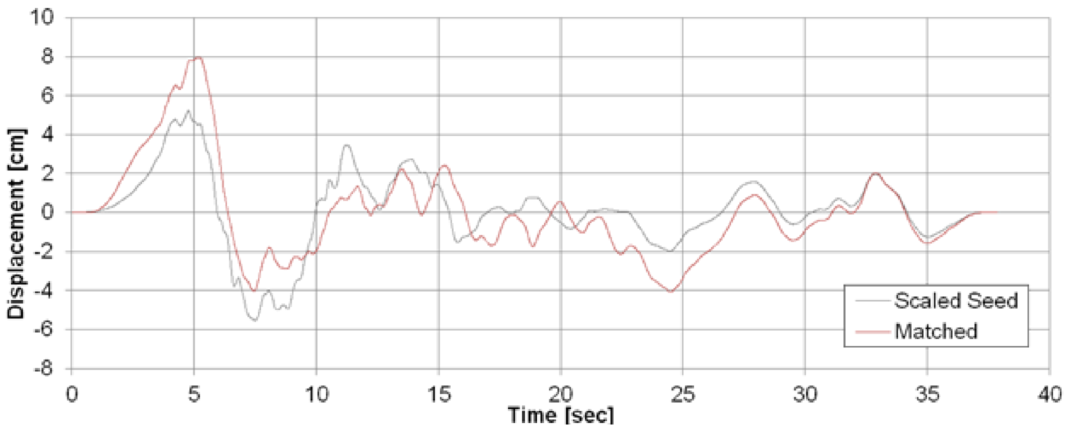

Figure 4.14. Comparison of displacement time histories of scaled seed motion and matched motion (X component, RSN-162)

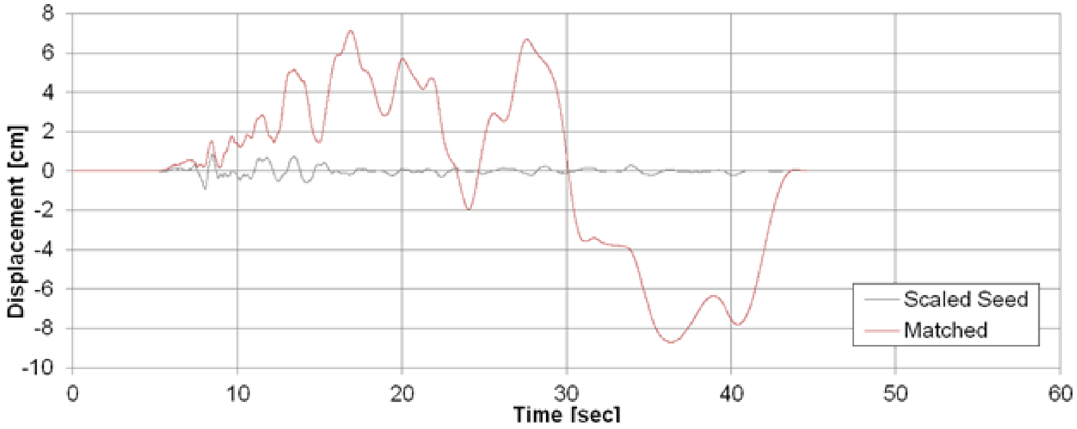

Figure 4.14. Comparison of displacement time histories of scaled seed motion and matched motion (X Component, NRG-LVL)

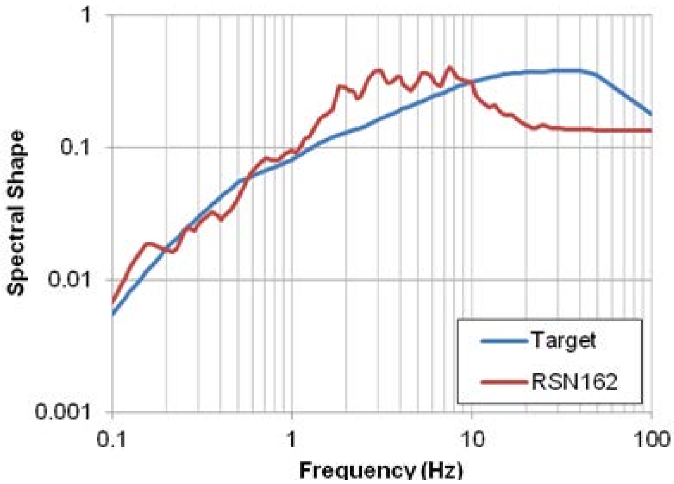

Figure 4.1.Comparison of target spectrum and response spectrum of seed motion (RSN-162)

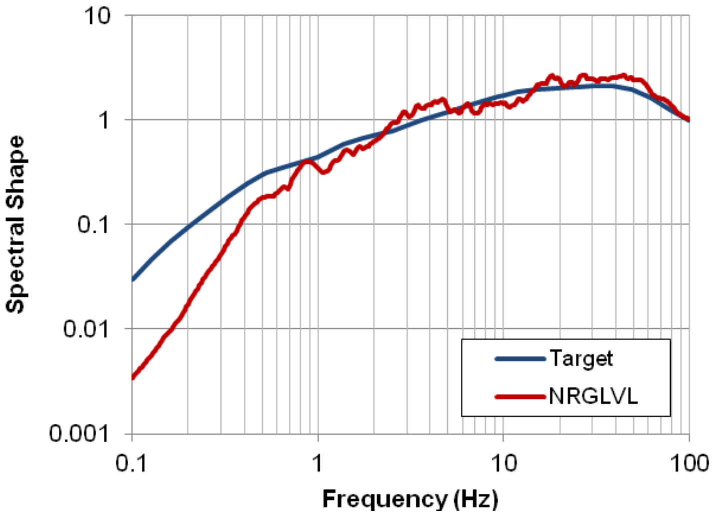

Figure 4.2. Comparison of target Spectrum and response spectrum of seed motion (NRG-LVL)

As indicated in Section 5.3.3 of NIST[45], the UHRS is a conservative target spectrum for seismic analysis of structures, especially for very rare levels (i.e., very low mean annual frequency of exceedance) of ground motion, where it is most unlikely that high amplitude spectral values are observed at all periods in a single ground motion sets. The displacement distortion observed for some of the matched motion is one of the consequences of using UHRS as the target spectrum. Although this may be avoided by carefully selecting the seed motion, the number of "good" seed motions is very limited in most applications. In this project, only three sets of matched motions have relatively small displacement distortion out of the 18 sets. Section 5.3.6 of NIST gives recommendations how to select an appropriate target spectrum, depending on the purpose of the Response-History Analyses.

## 4.5 Concluding Remarks

Two horizontal and one vertical time history components are developed for 18 different ground surface input motions for a CEUS rock site (Central Illinois site). Response spectra of the generated ground motions matched the selected target spectra (1E-4 rock UHRS) reasonable well. The matching criteria set by different guideline documents are met.

---

[45] National Institute of Standards and Technology, "Selecting and Scaling Earthquake Ground Motions for Performing Repsone-History Analyses," NIST GCR 1-917-15 (November 2011)

# 5. DEMONSTRATION EXAMPLES

## 5.1 Introduction

Three demonstration examples or case studies were developed to support the development and description of analysis tools. Several commercially available software packages have been used to model and analyze nuclear power plant (NPP) structures with varying degrees of complexity and accuracy. It was originally intended to use MOOSE to a greater extent in the performance of finite element structural analysis than was possible because of the state of development of MOOSE capabilities. Nevertheless, the case studies are directly relevant to the ultimate applications of MOOSE. Case studies or examples have been defined within the scope of this project as means to develop and demonstrate the dynamic seismic probabilistic risk assessment (SPRA) methodology. The case studies broadly address different elements of an SPRA for an NPP. Each case study has evolved during the course of the program.

Case Study 1 examines the probability of failure of non-structural components (NCs) in an auxiliary building. Most of the safety related components in the plant, such as the components of the emergency core cooling system are located in the auxiliary building, where they can be readily accessed while the plant is operating, rather than in the containment building. The characteristics of the auxiliary building determine the location dependence of accelerations experienced by the NSCs. This not only affects their marginal failure probabilities but also their joint failure probabilities (an important aspect of SPRA that is treated superficially in NPP SPRAs). Chapters 6 to 8 address the results of example calculations performed within the scope of Case Study 1. Chapter 7 describes the performance of an uncertainty analysis using a stick model to describe the behavior of the auxiliary building and its impact on the marginal and joint failure probabilities of essentially identical NSCs. In Chapter 7 2D and 3D structural modeling results are compared with respect to ability to describe structural response. In Chapter 7 this study is extended to include the response to auxiliary building with different characteristic shapes and flexible slabs.

Case Study 2 addresses dependent failures of NCs and the effectiveness of actions to recover equipment during the course of a seismic event. There are a number of potential water sources that can result in flooding of equipment in a seismic event. Case Study 2 examines the failure of condensate storage tanks (CSTs), the potential for flooding of safety-related NCs, and the potential for recovering safety related functions without resulting in core damage. The flooding scenarios are by their nature time-dependent. Within this case study, we also examine the effect of aftershocks and the availability of FLEX equipment on the timely recovery of safety functions using dynamic event tree analysis (DET). Chapters 4 to 6 describe different aspects of Case Study 2. Chapter 8 presents the results of the DET analysis, including a description of the aftershock model. Chapter 9 describes the development of a reduced order flooding model and the tuning of that model against a high fidelity transient hydraulic analysis. Chapter 10 describes the modeling of condensate storage tank response to seismic loads.

Case Study 3 examines the response of the containment building in a seismic event and the impact of that response on safety-related equipment. Most SPRAs today focus on events initiated while the plant is in full power operation. Case Study 3 examines an event in which the plant is in a refueling mode, in particular the potential for failure of the polar crane failing and dropping onto an exposed core. Chapter 11 describes the modeling of the containment building response and the failure of the polar crane.

## 5.2 Case Study 1

The objective of Case Study 1 is to examine an alternative to the standard Separation of Variables (SOV) approach to the combination of loads and system responses that is more typical of advanced methods of the treatment of uncertainty in safety analyses under development within the Light Water Reactor Safety Sustainability (LWRS) program. The study also explicitly examines common cause failure behavior of essentially identical equipment at the same physical location and at different floor levels of a building. By sampling over distributions of the uncertainty parameters that model structural response, the analysis captures the dependencies implicit in the transmission of loads through the structures. This specific case study involves the failure of components for which fragility curves are obtained from testing.

Much of SPRA involves the response of very sturdy structures within the linear regime on which safety-related components attached to the structure exceed their failure limit. In this case study, an auxiliary building is modeled for which essentially identical non-structural components (NSCs), e.g., electrical cabinets, are located on different floors of the building. In the initial studies, the building was modeled (Figure 1) with a simple surrogate model, a "stick" model, which is common practice in seismic analysis. Uncertainty distributions were assigned to the masses of the two floors in the building and to the stiffness for each floor as indicated in the figure. The fragility curve of the safety-related equipment is assumed to have the form of a log normal cumulative distribution function. The median failure acceleration for the equipment is assumed to have been determined by experiment. The log normal standard deviations are based on judgment (EPRI has provided guidelines for estimating the log normal standard deviations). Because of the complexity of determining the fragility associated with the functional failure of typical safety-related equipment, this project did not attempt to model the fragility of this type of equipment from a first principles approach. The structural response of the building is obtained by simulation while sampling from distributions of model uncertainties for a set of input accelerations. By sampling over distributions of the uncertain parameters that model structural response, the analysis captures the correlations implicit in the transmission of loads through the structures. The marginal failure probability for a non-structural component is obtained from Equation 5.1.

$$P_f = \int F(a) g(a) da \tag{5.1}$$

where $F(a)$ is the fragility curve for the component (cumulative distribution function) and $g(a)$ is the density function for the acceleration imposed on the component obtained from the stick model results for the population of samples. A similar expression is used to determine the joint failure probability of NSC 1 and NSC 2 in Figure 5.1 but with the additional constraint that for a given sample, the accelerations at both locations exceed the capacity of the component.

Section 5.2.1 describes the analyses performed for Case Study 1, presents results of the case study, and in the final section discusses those aspects of the analysis tools being developed that require further development.

### 5.2.1 Description of Case Study 1: Auxiliary Building with Non-Structural Components

For Case 1, an uncertainty analysis is performed of the structural response of a building to seismic loads and the associated failure of safety-related equipment in different locations within the building. The fragility of the safety-related equipment is based on experiment and has the form of a log normal distribution, which is the approach currently taken by industry. The structural response of the building is obtained by simulation while sampling from distributions of uncertainties in a manner similar to the techniques being used by INL with the RAVEN code[46]. The resulting distributions describing the structural response of the building are not constrained to be log normal distributions, which is a limitation of the industry's SOV approach. A stick model is used to analyze the seismic response of the building. The magnitude of the error associated with stick models depends on the design of the structure. Two essentially identical non-structural components, NSC1 and NSC2, are considered at two different levels of the building. The failure probability of Components NSC1 and NSC2 are assessed independently. The joint failure probability of Component NSC1 and Component NSC2 is also assessed.

### 5.2.2 Models of Case 1

Figure 5.1 illustrates: (a) the simplified model of the auxiliary building, (b) a stick model used for the characterization of the building with components NSC1 and NSC2 affixed to the first and second floors of the building (the building also has a basement level), and (c) the nonstructural components restrained on floors. In this study, the fundamental frequency of the auxiliary building is assumed as 7.5 Hz, based on analyses performed by Kitada[47] for the fundamental frequencies of a model auxiliary building. Kitada's assessment indicated that in the two horizontal directions the fundamental frequencies were approximately 6-8 Hz. The structure of the auxiliary building appears to be comparatively rigid.

Nonstructural components NSC1 and NSC2 represent electrical equipment. According to the literature review on the fragility functions of electrical equipment based on the shaking table test,

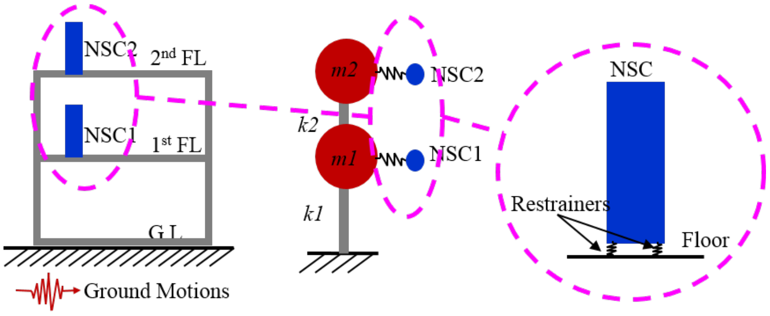

(a) (b) (c)

Figure 5.1. Case 1 Simplified Stick Model.

---

[46] C. Rabiti, A. Alfonsi, D. Mandelli, J. Cogliati, R. Martinueau, C. Smith, "Deployment and Overview of RAVEN Capabilities for a Probabilistic Risk Assessment Demo for a PWR Station Blackout," Idaho National Laboratory report: INL/EXT-13-29510 (2013).

[47] Y. Kitada, T. Hirotani and M. Iguchi, "Models Test on Dynamic Structure-Structure Interaction of Nuclear Power Plant Buildings," Nuclear Engineering and Design, 192, 205-236 (1999)

the capacity function of a specific type of battery racks was derived as a lognormal distribution with 1.01 g of median ($m_R$) peak floor acceleration (PFA), with $\beta_R$ = 0.28, and $\beta_U$ = 0.63. Figure Nonstructural components NSC1 and NSC2 represent electrical equipment. According to the literature review on the fragility functions of electrical equipment based on the shaking table test, the capacity function of a specific type of battery racks was derived as a lognormal distribution with 1.01 g of median ($m_R$) peak floor acceleration (PFA), with $\beta_R$ = 0.28, and $\beta_U$ = 0.63. Figure 5.2 shows: (a) one example of battery racks, and (b) parameters for the fragility curves of various electrical equipment based on shaking table tests and expert judgement, (c) the logarithmic standard deviation of capacities of the battery rack, and (d) the probability density function of battery rack's capacity. These parameters apply to the electrical equipment as a whole, while different levels of capacity parameters can be defined for one type of electrical equipment if more limit states are determined. Electrical equipment can have various limit states including different reasons for operational failure and types of physical damage. It is common that electrical equipment reaches the operational failure earlier than physical (structural) failure such as falling apart or tip-over[48].

### 5.2.3 Sampling of Models

Dynamic characteristics of the auxiliary building depend on the mass of the first and second stories ($m_1$ and $m_2$) and stiffness of the first and second stories ($k_1$ and $k_2$) of the structure. In this study, the fundamental frequency of the building is assumed 7.5 Hz, and the mean values for the mass and stiffness of structure are estimated based on this fundamental frequency. Due to potential construction errors or variation in the dimensions of structural components and uncertainty in material properties, it is assumed that the variation of mass and stiffness is represented by normal distributions with 5% coefficient of variation for each variable. The damping effect of the building structure is also considered with damping ratio ($\zeta_B$). It is assumed that the value of $\zeta_B$ is uniformly distributed between 2% and 5%. These values are typical damping ratios for reinforced concrete and steel structures in practice[49].

The dynamic response of a nonstructural component, especially the battery rack, depends on the location of these components in a building and types of restrainers. Here, it is assumed that the battery racks are rugged on each floor with restrainers. The seismic response of these components is computed based on the seismic response of the corresponding floor of the building and the fundamental frequency ($T_n$) of the battery rack when treated as a single degree of freedom (SDOF) system. Most types of electrical equipment in nuclear power plants are required to pass a certain level of shaking table tests for their seismic quality assessment. One type of such tests is the resonance test which showed that the fundamental frequency of most electrical equipment is in the range of 4-16 Hz[50, 51]. Therefore, in this study it is assumed that the fundamental frequencies of

---

[48] Hur J. "Seismic performance evaluation of switchboard cabinets using nonlinear numerical models." Georgia Institute of Technology, Atlanta, GA (2012)

[49] IBC, ICC. "International building code." *International Code Council, Inc.(formerly BOCA, ICBO and SBCCI)* 4051 60478-5795 (2006)

[50] NUREG - U.S. Nuclear Regulatory Commission "Seismic Fragility of Nuclear Power Plant Components [PHASE II]," NUREG/CR-4659, BNL-NUREG-52007, Vol. 2-4, Department of Nuclear Energy, Brookhaven National Laboratory, Long Island, NY (1987)

[51] Kim M. K., Choi I-K., and Seo J-M.. "A shaking table test for an evaluation of seismic behavior of 480V MCC." Nuclear Engineering and Design243: 341-355 (2012)

the battery racks follow the uniform distribution from 4 to 16 Hz. These frequencies can be reduced, if battery racks are not fully restrained.

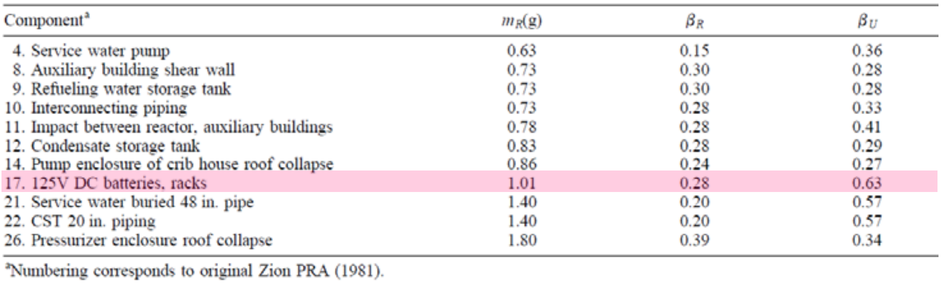

| Component$^{a}$ | $m_R$(g) | $\beta_R$ | $\beta_U$ |
|---|---|---|---|
| 4. Service water pump | 0.63 | 0.15 | 0.36 |
| 8. Auxiliary building shear wall | 0.73 | 0.30 | 0.28 |
| 9. Refueling water storage tank | 0.73 | 0.30 | 0.28 |
| 10. Interconnecting piping | 0.73 | 0.28 | 0.33 |
| 11. Impact between reactor, auxiliary buildings | 0.78 | 0.28 | 0.41 |
| 12. Condensate storage tank | 0.83 | 0.28 | 0.29 |
| 14. Pump enclosure of crib house roof collapse | 0.86 | 0.24 | 0.27 |
| 17. 125V DC batteries, racks | 1.01 | 0.28 | 0.63 |
| 21. Service water buried 48 in. pipe | 1.40 | 0.20 | 0.57 |
| 22. CST 20 in. piping | 1.40 | 0.20 | 0.57 |
| 26. Pressurizer enclosure roof collapse | 1.80 | 0.39 | 0.34 |

$^{a}$Numbering corresponds to original Zion PRA (1981).

(a) DC Battery Racks (b) Fragility curves of key components at Zion Nuclear Power Plant[52]

$$m_R = 1.01\text{g}$$
$$\beta_R = 0.28\text{ g}$$
$$\beta_U = 0.63\text{ g}$$
$$\beta = \sqrt{{\beta_R}^2 + {\beta_U}^2} = 0.69\text{g}$$

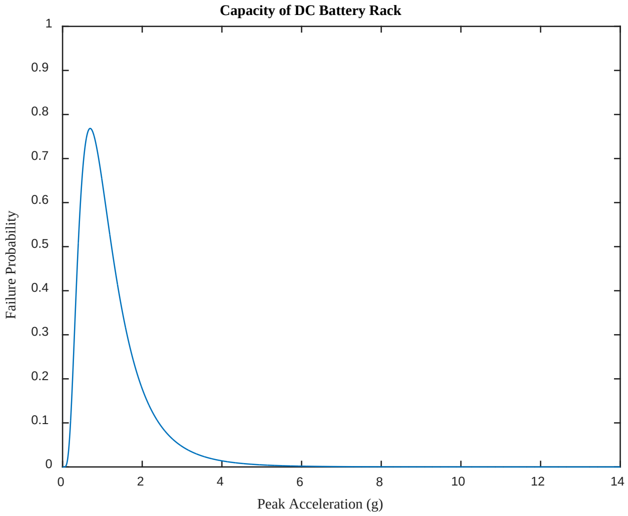

(c) Logarithmic Standard Deviations for the Cap the Battery Racks

(d) Performance Capacity of the Battery Rack

Figure 5.2. Nonstructural Component, Battery Rack

Several properties of the structural system are considered as stochastic variables to account for uncertainties in the simulations. The stochastic variables include the masses of each story the two-story building $m_1$ and $m_2$, stiffness of each story of the structure $k_1$ and $k_2$, damping of the building $\zeta_B$, and fundamental frequencies of nonstructural components ($T_n$). In order to observe effects of different degrees of correlation in the sampling approach, three subcases of samples were generated. Each subcase has 10,000 sample sets for $m_1$, $m_2$, $k_1$, $k_2$, $\zeta_B$ and $T_n$.

In each sample set of Subcase 1, $m_1$ and $m_2$ has the same value from the same distribution, and $k_1$ and $k_2$ are also the same from the same distribution. For Subcase 2, each sample set has different values of $m_1$ and $m_2$. They are independently drawn from the same distribution. The $k_1$ and $k_2$ of

---

[52] Ellingwood, B. R. "Issues related to structural aging in probabilistic risk assessment of nuclear power plants." Reliability Engineering & System Safety 62.3: 171-183 (1998)

each sample set are different as well but they are generated from the same distribution. As shown in Figure 5.3, $m_1$ and $m_2$ and $k_1$ and $k_2$ in Subcase 1 are perfectly correlated, while $m_1$ and $m_2$ and $k_1$ and $k_2$ in Subcase 2 are independent even though $m_1$ and $m_2$ are generated from the same distribution. In Subcase 3, it is assumed that all heavy nonstructural components in an auxiliary building are installed on the first floor. Therefore, the mass of the first floor (FL1) is considerably larger than that of the second floor (FL2). In addition, the structural stiffness ($k_1$) of the FL1 is also larger than that of FL2. Therefore, the mean values of $m_1$ and $m_2$ are different, the mean value of $m_1$ is twice larger than $m_2$, and they are independently generated from different distributions as shown in Figure 5.3(d). Samples of $k_1$ and $k_2$ are also generated from different distributions as shown in Figure 5.3(e). The mean of $k_1$ is two times larger than $k_2$.

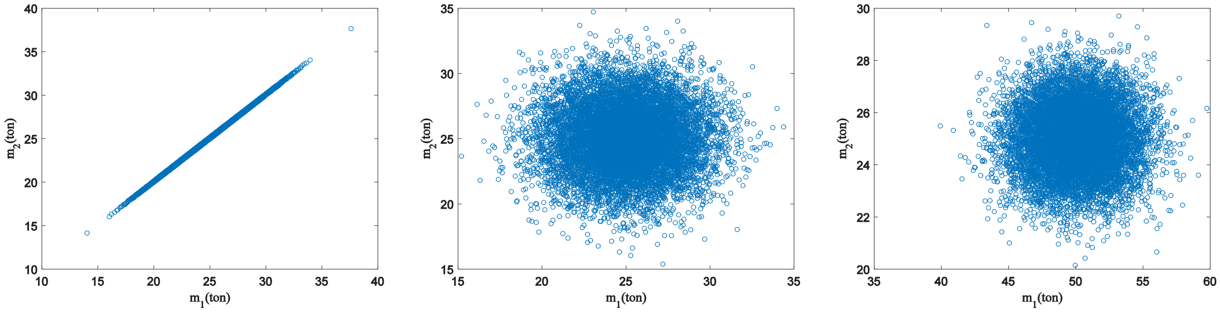

(a) Masses of Subcase 1 (b) Masses of Subcase 2 (c) Masses of Subcase 3

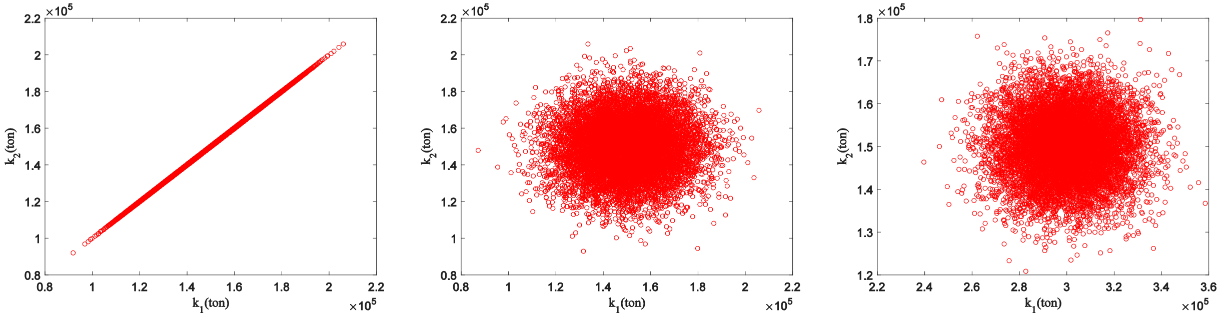

(d) Stiffness of Subcase 1 (e) Stiffness of Subcase 2 (f) Stiffness of Subcase 3

Figure 5.3. Effects of uncertainties in $m_1$ & $m_2$ and $k_1$ and $k_2$ of Subcases

Subcase 1: $m_1 = m_2$, $k_1 = k_2$

- $T_B$: Fundamental frequency of the building ~ Normal distribution (μ= 7.5 Hz and the distribution is determined by the sets of mass and stiffness)
- $m_1$ and $m_2$ ~ Normal distribution (μ= 25 ton, the coefficient of variation (c.o.v) = 0.05, $\sigma$ = c.o.v × μ)
- $k_1$ and $k_2$~ Normal distribution (μ= 1.6E+5kN/m, c.o.v = 0.05, $\sigma$ = c.o.v × μ)
- $\zeta_B$: Damping ratio of auxiliary building ~ uniform distribution (2-5%)
- $T_n$: Fundamental frequency of electrical equipment ~ uniform distribution (4-16 Hz)

Subcase 2: Independent $m_1$ and $m_2$ from the same distribution. Independent $k_1$ and $k_2$ from the same distribution

- $T_B$: Fundamental frequency of the building ~ Normal distribution (μ= 7.5 Hz and distribution is determined by the sets of mass and stiffness)
- $m_1$ and $m_2$ ~ Normal distribution (μ= 25 ton, c.o.v= 0.05, σ = c.o.v × μ)
- $k_1$ and $k_2$~ Normal distribution (μ= 1.6E+5kN/m, c.o.v = 0.05, σ = c.o.v × μ)
- $\zeta_B$: Damping ratio of auxiliary building ~ uniform distribution (2-5%)
- $T_n$: Fundamental frequency of electrical equipment ~ uniform distribution (4-16Hz)

Subcase 3: Independent $m_1$ and $m_2$ from the different distributions. Independent $k_1$ and $k_2$ from the different distributions.

- $T_B$: The first fundamental frequency of the building is μ= 8.7 Hz, and the second frequency is 17.4 Hz)
- $m_1$ ~ Normal distribution (μ= 50 ton, c.o.v = 0.05, σ = c.o.v × μ)
- $m_2$ ~ Normal distribution (μ= 25 ton, c.o.v = 0.05, σ = c.o.v × μ)
- $k_1$ ~ Normal distribution (μ= 3.0E+5kN/m, c.o.v = 0.05, σ = c.o.v × μ)
- $k_2$ ~ Normal distribution (μ= 1.5E+5kN/m, c.o.v = 0.05, σ = c.o.v × μ)
- $\zeta_B$: Damping ratio of the auxiliary building ~ uniform distribution (2-5%)
- $T_n$: The fundamental frequency of electrical equipment ~ uniform distribution (4-16 Hz)

### 5.2.4 Dynamic Analysis

Three subcases of analyses were performed as discussed above. For each subcase, 10,000 samples of input variables and ground motion histories were made. For each sample set, a dynamic analysis was performed in order to obtain the dynamic response of two floors at the locations of the equipment and the absolute accelerations of the equipment by solving Equation 5.2.

$$\boldsymbol{M}\begin{Bmatrix}\ddot{u_1}\\ \ddot{u_2}\end{Bmatrix}+\boldsymbol{C}\begin{Bmatrix}\dot{u_1}\\ \dot{u_2}\end{Bmatrix}+\boldsymbol{K}\begin{Bmatrix}u_1\\ u_2\end{Bmatrix}=-\boldsymbol{M}l\ddot{u}_g \tag{5.2}$$

where $\boldsymbol{M}=\begin{bmatrix}m1 & 0\\ 0 & m2\end{bmatrix}$ is the mass matrix, $\boldsymbol{K}=\begin{bmatrix}k1+k2 & -k2\\ -k2 & k2\end{bmatrix}$ is the stiffness matrix, $\boldsymbol{C}=a_0M+a_1K$ is the mass and stiffness proportional damping matrix with $a_0=\frac{2\zeta\omega_1\omega_2}{\omega_1+\omega_2}$ and $a_1=\frac{2\zeta}{\omega_1+\omega_2}$, $\zeta$ is the damping ratio (5% here) and $\omega_1$ and $\omega_2$ are first and second modal frequencies of the structure, respectively.

Equation 5.2 was solved using the Bogachi-Shampine method[53], which is implemented in the built-in function, *ode 23,* in MATLAB[54]. It is a Runge–Kutta method of order three with four stages with the First Same As Last (FSAL) property, so that it uses approximately three function evaluations per time step. The solution of Equation 5.2 provides: (1) the absolute floor

---

[53] Shampine, L.F., Reichelt, M. W. "The Matlab ODE Suite", SIAM Journal on Scientific Computing 18(1): 1–22 (1997)

[54] MathWorks. Bioinformatics Toolbox: User's Guide (R2012a) (2012)

accelerations FA1 ($\ddot{u}_1$) and FA2 ($\ddot{u}_2$), and (2) floor displacements FD1 ($u_1$) and FD2 ($u_2$). Using these histories of FA1 and FA2, fundamental frequencies of NSCs, $T_n$ and constant damping ratio for the NSC, 5%, absolute acceleration histories of NSCs are computed.

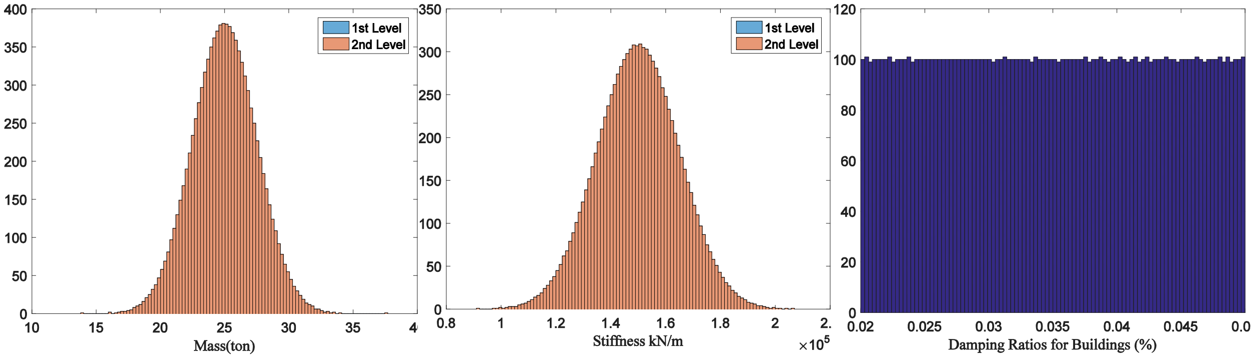

(a) Mass Distribution of Subcase 1 and 2 (b) Stiffness Distribution of Subcase 1 and 2 (c) Damping Ratio of Building of Subcases 1,2, and 3

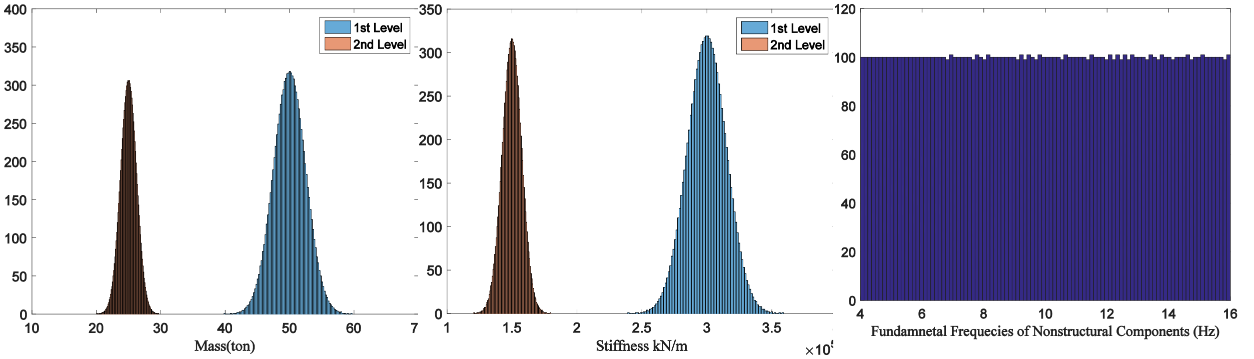

(d) Mass Distribution of Subcase 3 (e) Stiffness Distribution of Subcase 3 (f) Fundamental frequencies of nonstructural components of Subcases 1,2, and 3

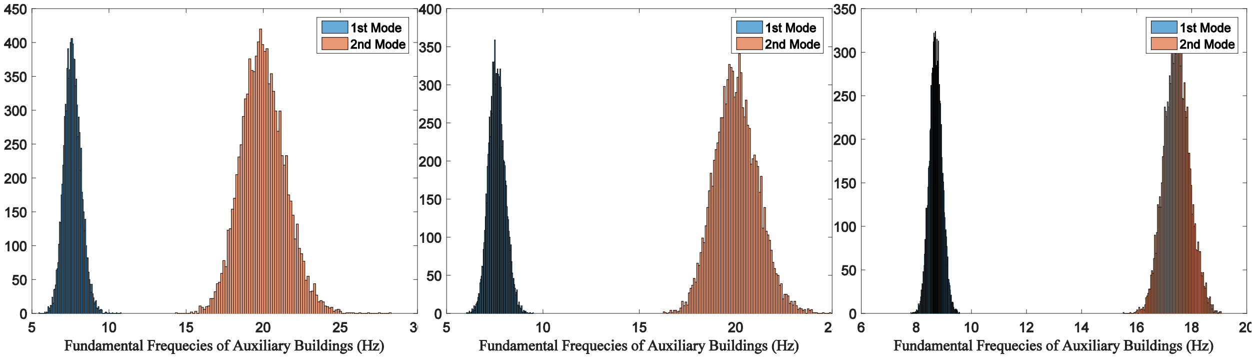

(g) Fundamental Frequencies of Building Subcase 1 (h) Fundamental Frequencies of Building Subcase 2 (i) Fundamental Frequencies of Building Subcase 3

Figure 5.4 Distribution of Sample Variables

### 5.2.4 Ground Motion (GM) Histories

For the evaluation of the seismic performance of nonstructural components, a suite of ground motions is applied to the simulations. These ground motions are based on historical records in Los Angeles, California and were developed as a part of the SAC Phase 2 Steel Project[55]. The acceleration time histories were selected based on the joint magnitude-distance probabilistic models. The suite consists of 60 pairs of time histories at three intensity levels; 2%, 10% and 50% probabilities of exceedance in 50 years. They were derived from historical records or from physical simulations and have been altered so that their mean response spectrum matches the 1997 National Earthquake Hazards Reduction Program (NEHRP) design spectrum[56]. In addition, their associated soil type was SB-SC to soil type SD, and their hazard levels were specified by the 1997 U.S. Geological Survey (USGS) maps. A summary of the characteristics of these selected ground motions is shown in Table 5.1 and Figure 5.5, including peak ground acceleration, PGA.

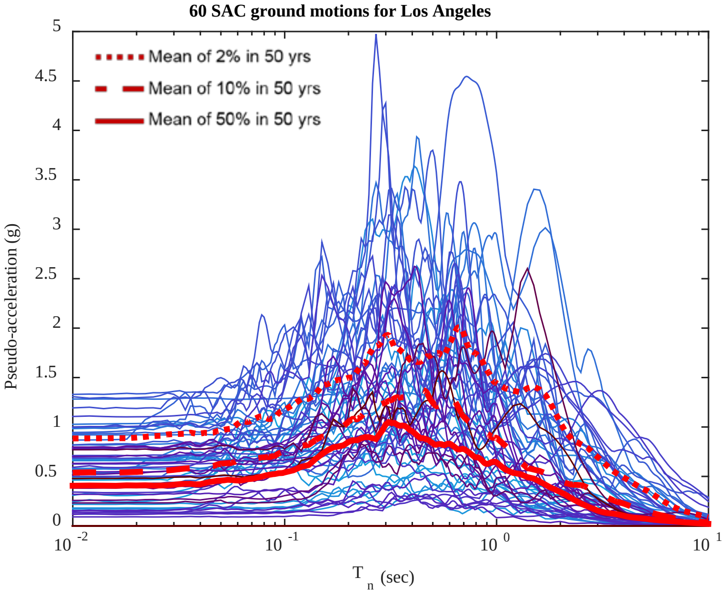

Figure 5.5 Response Spectra of Ground Motions Histories

Table 5.1 Characteristics of selected acceleration time histories

| Ground Motion characteristics | 2 % \| 50 years (min - max) | 10 % \| 50 years (min - max) | 50 % \| 50 years (min - max) |
|---|---|---|---|
| Earthquake Magnitude (M) | 6.7 - 7.4 | 6 - 7.3 | 5.7 - 7.7 |
| Distance from Fault (km) | 1.2 - 17.5 | 1.2 - 36 | 1 - 107 |
| Duration (sec) | 14.9 - 59.98 | 14.9 - 79.98 | 26.14 - 79.98 |
| PGA (g) | 0.42 - 1.33 | 0.23 - 1.02 | 0.11 - 0.79 |

---

[55] SAC Joint Venture Steel Project Phase 2, “Project Title: Develop Suites of Time Histories”, Pasadena, CA (1997)

[56] Building Seismic Safety Council. "NEHRP recommended provisions for seismic regulations for new buildings [1997 ed.]." *Federal Emergency Management Agency, FEMA* 302: 337 (1998)

## 5.3 Analysis

### 5.3.1 Seismic Analysis Results

This section presents the time history analysis results of two sample sets from Subcase 1 based on the Equation 5.2. Both sample sets have the same values of variables except the ground motion histories. One set is subjected to Ground Motion (GM)#21 among 60 GM histories, and the other set is subjected to GM #1. For the variables, $m_1$ is the same as $m_2$; $k_1$ is also the same as $k_2$; the fundamental frequency of the building structure is 7.6 Hz; and the second fundamental frequency is 19.9 Hz. The damping ratio for the building is 5%.

#### 5.3.1.1 GM#21

From the 60 GM histories, #21 has one of the highest PGAs. Figure 5.6(a) presents the history of GM#21. The PGA is 1.28g at 17.5 sec. Figures 5.6(b) through 5.6(e) show the results of time history analyses. FL1 and FL2 displacement histories are presented in Figure 5.7(b). As expected, the maximum displacement of FL2 is larger than that of FL2. Figure 5.7(c) shows the absolute acceleration histories of FL1 and FL2, which are very close to each other. As shown in Figure 5.7(d), in comparison with the GM acceleration, the values of relative acceleration ($\ddot{u_1} - \ddot{u_g}$ and $\ddot{u_2} - \ddot{u_g}$) are relatively small. In addition, GM#21 is a recorded data from the Kobe 1995, and its dominant frequency range is relatively low, i.e., Kobe 1995 contains relative long periods. On the other hand, the auxiliary buildings and nonstructural components have relatively high fundamental frequencies. Therefore, their dynamic behavior, e.g., relative acceleration, is less sensitive to the GM#25. Accordingly, the total acceleration histories of FL1 ($\ddot{u_1}$) and FL2 ($\ddot{u_2}$) as well as the total acceleration histories of NSC1 and NSC2 are close to each other when subjected to the GM#21.

#### 5.3.1.2 GM#1

Figures 5.7(a) through 5.7(e) show the results of time history analyses of the same sample sets (i.e., among 10,000 samples from Subcase 1) as the previous analyses except in this case for GM#1 rather than GM#21. In comparison to GM#21, GM #1 has a relatively low PGA of 0.46g as shown in Figure 5.7(a). Therefore, the peak floor displacements of FL1 and FL2 are also small and equal to 2.3 mm and 3.5 mm, respectively. The peak floor accelerations of FL1 and FL2 are 0.38g and 0.62g, respectively. The peak acceleration of NSC1 and NSC2 are also relatively low, 0.78g and 1.2g, respectively. Comparison of the results for GM#21 and GM#1 show greater difference between the floor acceleration time histories of FL1 and FL2. GM#1 is a recorded history from the 1940 El Centro earthquake, and its dominant frequency range is relatively high compared to GM#21 (i.e., El Centro 1940 contains relative low periods). Therefore, the response acceleration history of rigid structures such as auxiliary buildings or nonstructural components are more sensitive to the GM#1 than GM#21. The acceleration histories of NSC1 and NSC2 show greater difference than those of GM#21 as shown in Figure 5.7(e).

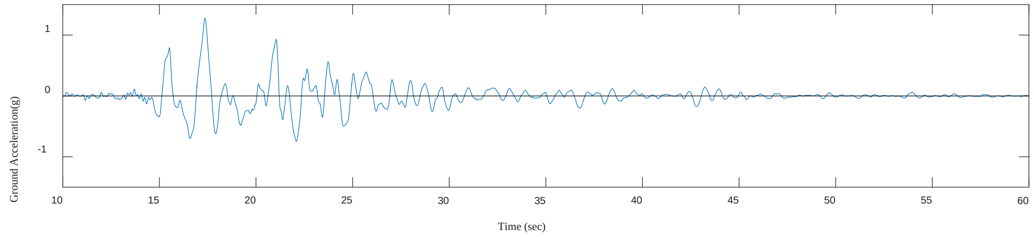

(a) GM#21Time History

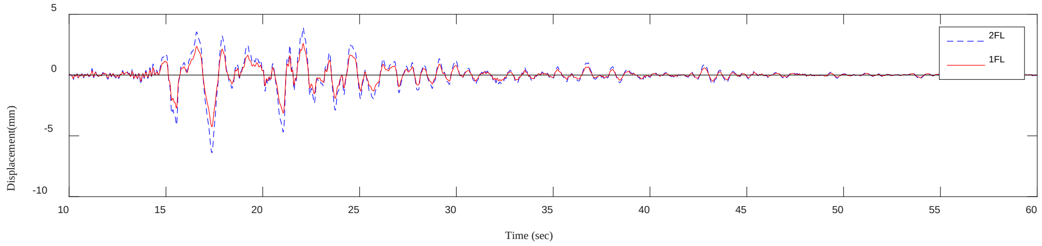

(b) Floor Displacement Time History

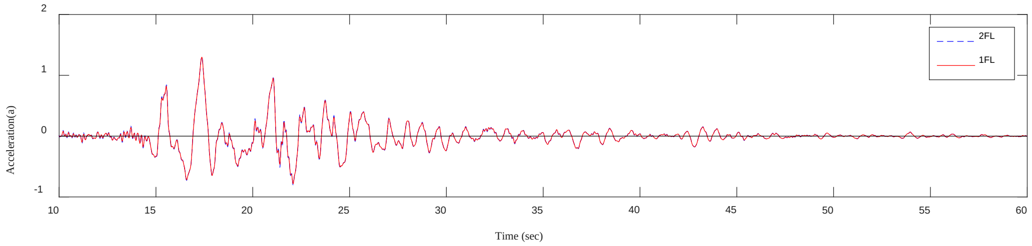

(c) Floor Acceleration Time History

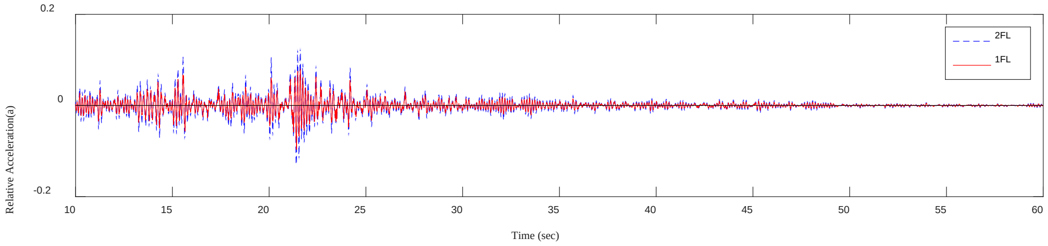

(d) Relative Floor Acceleration Time History

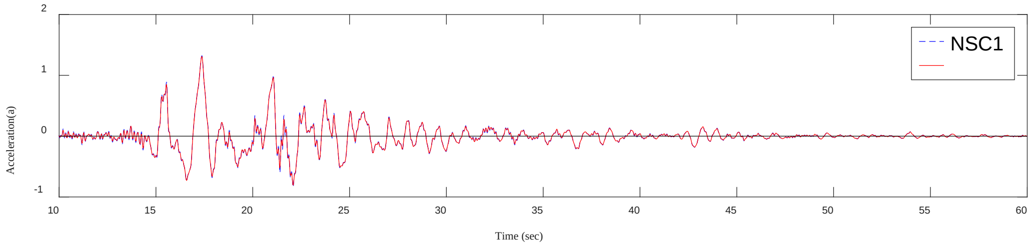

(e) NSC Acceleration Time History

Figure 5.6 Time History Analysis with GM#21

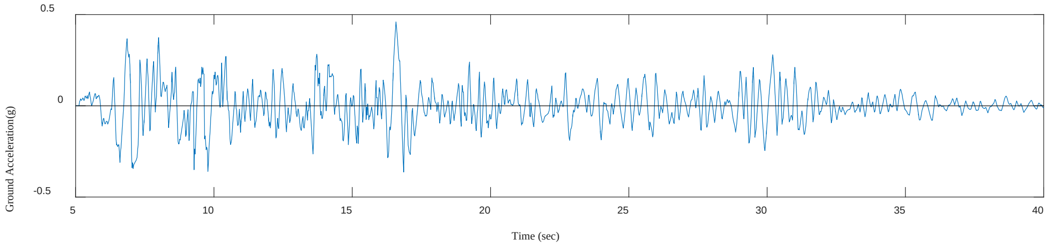

(a) GM Time History #1

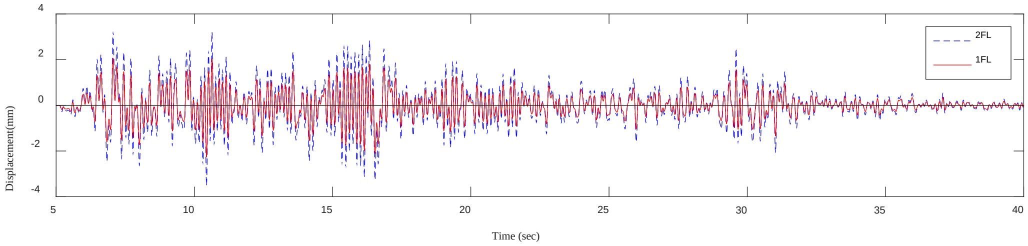

(b) Floor Displacement Time History

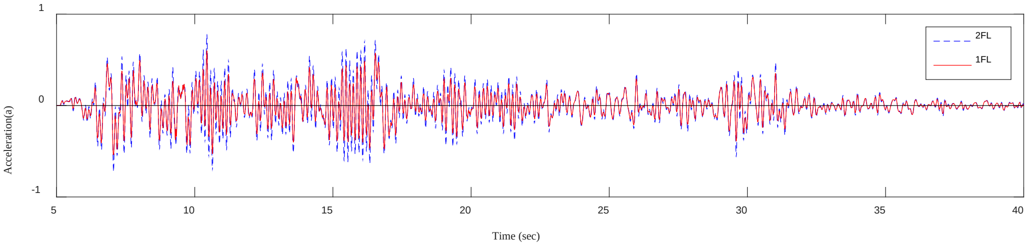

(c) Floor Acceleration Time History

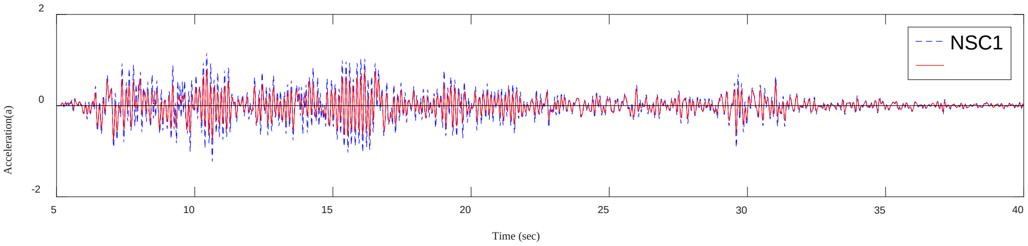

(d) NSC Acceleration Time History

Figure 5.7 Time History Analysis with GM#1

### 5.3.2 Peak Acceleration of NSCs

Past studies have shown that the seismic performance of electrical components in nuclear power plants is affected by the frequency content of earthquake ground motions (i.e., NSCs are frequency-sensitive), and that the acceleration response is a critical engineering demand parameter to evaluate their failure modes [57]. In order to evaluate the failure probabilities of two NSCs located in different levels of a building, their peak accelerations were determined for each simulation. As explained in Section 5.2.2, 60 ground motion histories were randomly assigned to 10,000 sample

---

[57] NUREG - U.S. Nuclear Regulatory Commission, “Seismic Fragility of Nuclear Power Plant Components [PHASE II],” NUREG/CR-4659, BNL-NUREG-52007, Vol. 2-4, Department of Nuclear Energy, Brookhaven National Laboratory, Long Island, NY (1987)

sets in each subcase, and all sample sets were analyzed as elaborated in the same section. Figure 5.8 shows simulation results of three subcases. Figures 5.8(a1) and (a2) present the result of Subcase 1, Figures 5.8(b1) and (b2) present the result of Subcase 2, and Figures 5.8(c1) and (c2) present the result of Subcase 3. Figures 5.8(a2), (b2), and (c2) are zoomed in Figures 5.8(a1), (b1), and (c1) to display the very few cases where the response of NSC1 is larger than that of NSC2. The red line in these figures represents the case of NSC1 equal to NSC2. This pattern in the response of NSCs is attributed to the dynamic characteristics of the auxiliary buildings. Considering mode shapes of the building structures and their corresponding frequencies, it is expected that displacement and acceleration responses of FL2 are larger than those of FL1 for most cases. However, in few cases, the response of NSC1 is larger than that of NSC2 as shown in three Subcases (blue circles below the red lines). These particular cases are observed more in Subcase 3 than two other Subcases.

As expected, Subcase 3 shows the highest dispersion among all cases. In addition, Subcase 2 has higher dispersion than Subcase 1, since $m_1$ and $m_2$, and $k_1$ and $k_2$ in Subcase 2 are independent.

### 5.3.3 Estimation of Failure Probability

The conditional failure probability of a NCS ($\boldsymbol{P_f}$) is computed using the probabilistic capacities, based on, experiment and the simulation results for the distribution of accelerations of the two NSCs for the given ground motion sets. The resistance (capacity) model ($\boldsymbol{R}$) is developed with the probabilitic capacity of the nonstructural components previously mentioned in Figure 5.2, and the Strength (demand/response) model ($\boldsymbol{S}$) is determined by the simulation result of 10,000 samples for each subcase. $S_1$ and $S_2$ present the peak acceleration response of NSC1 and NSC2, respectively.

The joint probability of failure of two components with the same resistance model can be found as below, where $\boldsymbol{f}()$ is a probability density function, and $\boldsymbol{F}()$ is a cumulative distribution function.

$$\boldsymbol{P_f = P[(R - S_1 < 0) \cap (R - S_2 < 0)] = \iiint_{Domain} f_{R,S_1,S_2}(r, s_1, s_2) dr ds_1 ds_2} \tag{5.3}$$

$$\boldsymbol{= \int_{-\infty}^{\infty} \int_{r}^{\infty} \int_{r}^{\infty} f_{S_1,S_2}(s_1, s_2) f_R(r) ds_1 ds_2 dr} \tag{5.4}$$

$$\boldsymbol{= \int_{-\infty}^{\infty} [1 - F_{S_1}(r) - F_{S_2}(r) + F_{S_1,S_2}(r, r)] f_R(r) dr} \tag{5.5}$$

The joint probability of failure of two components with correlated resistance models ($\boldsymbol{R}$) and correlated strength/demand ($\boldsymbol{S}$) models can be found as

$$\boldsymbol{P_f = P[(R_1 - S_1 < 0) \cap (R_2 - S_2 < 0)]} \tag{5.6}$$

$$\boldsymbol{= \int_{-\infty}^{\infty} \int_{-\infty}^{\infty} \int_{r_2}^{\infty} \int_{r_1}^{\infty} f_{R_1,R_2,S_1,S_2}(r_1, r_2, s_1, s_2) ds_1 ds_2 dr_1 dr_2} \tag{5.7}$$

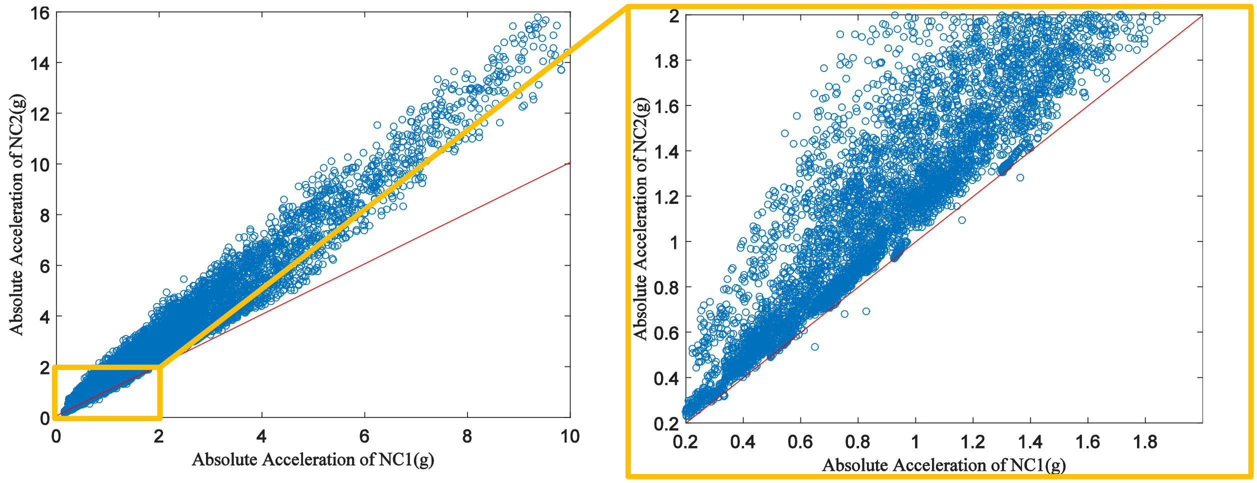

(a1) Subcase 1: Peak Acceleration of NSCs (a2) Subcase 1: Peak Acceleration of NSCs (Zoomed)

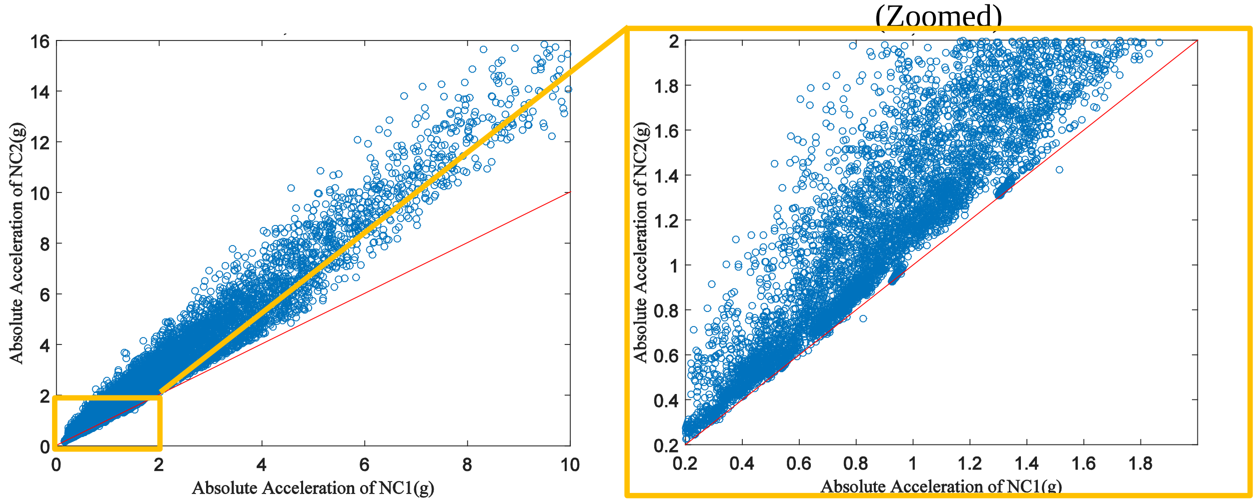

(a1) Subcase 2: Peak Acceleration of NSCs (a2) Subcase 2: Peak Acceleration of NSCs (Zoomed)

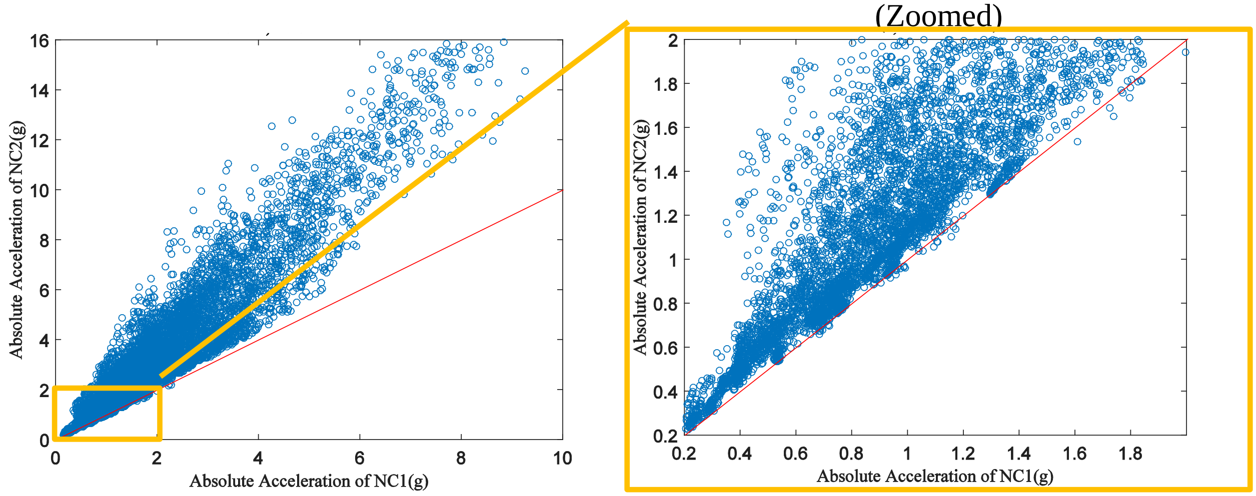

(a1) Subcase 3: Peak Acceleration of NSCs (a2) Subcase 3: Peak Acceleration of NSCs (Zoomed)

Figure 5.8 Peak Acceleration of NCSs

Assuming that resistance and demand models are statistically independent,

$$\boldsymbol{P_f} = \int_{-\infty}^{\infty}\int_{-\infty}^{\infty}\int_{r_2}^{\infty}\int_{r_1}^{\infty} \boldsymbol{f_{S_1,S_2}(s_1,s_2) f_{R_1,R_2}(r_1,r_2) ds_1 ds_2 dr_1 dr_2} \tag{5.8}$$

$$= \int_{-\infty}^{\infty}\int_{-\infty}^{\infty}\left[1 + \boldsymbol{F_{S_1,S_2}(r_1,r_2)} - \boldsymbol{F_{S_1}(r_1)} - \boldsymbol{F_{S_2}(r_2)}\right]\boldsymbol{f_{R_1,R_2}(r_1,r_2) dr_1 dr_2} \tag{5.9}$$

$$= \int_{-\infty}^{\infty}\int_{-\infty}^{\infty}\left[\boldsymbol{G_{S_1}(r_1)} + \boldsymbol{G_{S_2}(r_2)} - \boldsymbol{G_{S_1,S_2}(r_1,r_2)}\right]\boldsymbol{f_{R_1,R_2}(r_1,r_2) dr_1 dr_2} \tag{5.10}$$

where $\boldsymbol{G_X}$ represents the complementary cumulative distribution function of $\boldsymbol{X}$.

Based on these equations, the conditional failure probabilities of two NSCs are estimated given the ground motions for each case, and the results are summarized in Table 5.2. These results are based on the assumption that the probilistic capacities (fragilities) of NSC1 and NSC2 are the same and that they are fully correlated. For the joint failure probability of NSC1 and NSC2, the cumulative distribution function, $\boldsymbol{F_{S_1,S_2}(r_1,r_2)}$ and complementary cumulative distribution function, $\boldsymbol{G_{S_1,S_2}(r_1,r_2)}$ are generated as shown in Figure 7.12. Note that at the fifth significant figure in Table 7.3, the joint failure probability differs (is slightly smaller than) the probability of failure of NSC1. This is not a numerical round off error but represents a small set of events from the 10,000 samples for which the acceleration at Level 1 is actually greater than the acceleration at Level 2. For cases in which both the loads on the equipment and the fragilityof the equipment are fully correlated, the joint failure probability would be identical to the smaller of the marginal failure probabilities. Thus, although the correlation associated with the load is not 100%, it is very close.

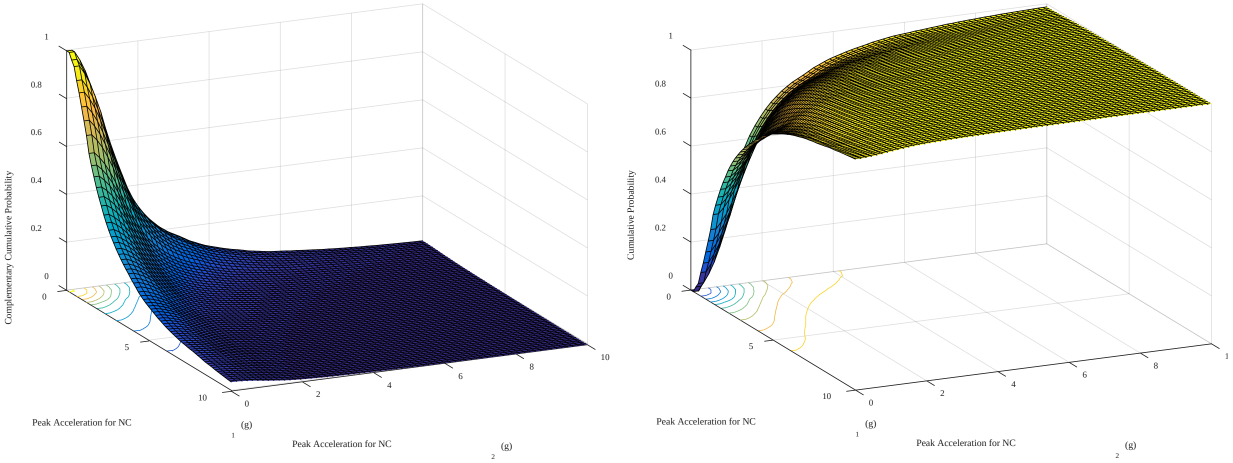

(a) Joint Complementary Cumulative Distribution Functionof NC1 and NC2 $\boldsymbol{G_{S_1,S_2}(r_1,r_2)}$ in Equation 7.12

(b) Joint Cumulative Distribution Function of NC1 and NC2 $\boldsymbol{F_{S_1,S_2}(r_1,r_2)}$ in Equation 7.11

Figure 5.9 Joint Cumulative Distribution Function for the Failure Probability of NC1 and NC2 in Subcase 1

Table 5.2 Conditional Failure Probabilities of Nonstructural Components given GM sets

| Subcases | $P_f$(NC1\|GMs) | $P_f$(NC2\|GMs) | $P_f$(NC1 ∩ NC2\|GMs) |
|---|---|---|---|
| Subcase1: $m_1=m_2$, $k_1=k_2$ | 0.61206 | 0.70915 | 0.61202 |
| Subcase2: Independent $m_1$&$m_2$ and $k_1$&$k_2$ from same distributions | 0.61252 | 0.70818 | 0.61251 |
| Subcase3: Independent $m_1$&$m_2$ and $k_1$&$k_2$ from different distributions | 0.61284 | 0.72404 | 0.61282 |

### 5.3.4 Effect on Joint Failure Probability of Capacity Correlation

In the previous section, it was not only assumed that the capacity functions for the components at the two different levels of the auxiliary building were identical in form but that they were 100% correlated. In this section, we examine the impact on the joint failure probability of different levels of correlation of capacities.

The strength of correlation between two stochastic variables $Y_i$ and $Y_j$ is defined by Equation 5.11.

$$\rho = \frac{Cov(Y_i,Y_j)}{\sqrt{Var(Y_i)Var(Y_j)}} \tag{5.11}$$

In the seismic safety margins program undertaken at Lawrence Livermore National Laboratory, the treatment of the correlation of loads and component fragility were based on the decomposition of correlation into two elements as indicated in Equation 5.12.[58]

$$\rho_C = \frac{\beta_{S1}\beta_{S2}}{\sqrt{\beta_{S1}^2+\beta_{R1}^2}\sqrt{\beta_{S2}^2+\beta_{R2}^2}}\rho_{R1\mathrm{R2}} + \frac{\beta_{R1}\beta_{R2}}{\sqrt{\beta_{S1}^2+\beta_{R1}^2}\sqrt{\beta_{S2}^2+\beta_{R2}^2}}\rho_{R1\mathrm{R2}} \tag{5.12}$$

where $\rho_C$ is the correlation coefficient between failures of the NSC1 and NCS2, $\beta_{S1}$ and $\beta_{S2}$ are, respectively, the logarithmic standard deviations of the structural responses (loads) for NCS1 and NSC2, $\beta_{R1}$ and $\beta_{R2}$ are, respectively, the logarithmic standard deviations of the capacities for NCS 1and NCS2, $\rho_{S1S2}$ is the correlation coefficient between the structural response at the locations of NCS1 and NCS2, and $\rho_{R1R2}$ is the correlation coefficient for the capacity of the two components.

For Case 1 with essentially identical components with median failure acceleration of 1.01g and a logarithmic standard deviation of 0.6894, an assessment was made of the probability of failure of both NCS1 and NCS2 for different degrees of correlation between the fragilities. The analysis was performed using bivariate sampling from the log normal distributions for the components. Monte Carlo sampling was performed using one million correlated draws from the fragility curve, which is effectively 100 correlated draws from the fragility curves for each of the 10,000 random samples characterizing the loads at FL1 and FL2 of the auxiliary building obtained by exercising the structural model. For each draw, the value of the peak accelerations at Levels 1 and 2 were compared with the capacity of the component. If NSC1 failed, a tally would be given to failure of

---

[58] M. Bohn et al. “Application of the SSMR Methodology to the Risk a Zion Nuclear Power Plant,” NUREG/CR-3428 (1983)

that component, if NCS2 failed, a tally would be given to that component and if they both failed a tally would be registered for joint failure. The total of the tallies was then divided by the total number of iterations (one million).

Three levels of component correlation were studied: $\rho_{R1R2}$ = 0, 0.5 and 1. As indicated in Section 5.3.3, even though NSC1 and NSC2 are on different levels of the auxiliary building, the correlation of the loads $\rho_{R1R2}$ is essentially unity for this case. As expected, the marginal failure probabilities of NCS1 and NCS2, which are unaffected by the correlation of the component fragilities, were determined to be 0.61 and 0.71, the same as the values reported in the previous section for this case. However, for component correlations $\rho_{R1R2}$ = 0, 0.5 and 1, the joint failure probabilities are 0.52, 0.57 and 0.61 respectively. For full correlation of both the load (demand) on the component and the fragility of the component, the joint probability should be identical to the lower probability of failure of the two components. Whenever the load on the component at FL1 exceeds the acceleration at which the component would fail, for fully correlated load the load on the component at FL2 will be higher than at FL1 and since the components are identical the component at FL2 will also fail. Thus, the failure probability of the component at FL1 determines the joint failure probability as well. For Case 1 the probability of failure of NSC1 is 0.61, which is less than the probability of failure of NSC2. Thus, the joint failure probability of 0.61 is consistent with expectations. Note that for fully independent component failure probabilities (both the loads at the two levels and fragilities of the components uncorrelated) the joint failure probability would be 0.43, the product of the two probabilities. However, because of the high degree of correlation of the loads, the observed joint failure probability is 0.52. This difference affects not only the behavior of essentially identical equipment but also potentially the joint failure probability of different types of equipment at different locations within the plant, particularly if they have similar natural frequencies.

Depending on the type of component, the amount of correlation, $\rho_{F1F2}$, for essentially identical equipment differs. Expert judgment is used to assess the degree of correlation. Factory manufactured equipment typically would be assigned a correlation close to unity. Field fabricated components should have lower assigned correlations. At high failure probabilities, on the order of 0.5 or greater, degree of correlation does not particularly affect the joint failure probability within the associated uncertainties. However, at lower failure probabilities, typical of the failure probabilities observed in SPRAs, the effect can be an order of magnitude or greater on the probability of a cutset[59]. Although the potential for dissimilar equipment to have correlated loadings, potentially leading to significant common cause relationships, has been recognized for many years, in practice in SPRAs for commercial reactors, dissimilar equipment at different locations within a building is not analyzed to determine the potential for common cause failure.

---

[59] Private communication with Robert Budnitz based on Seismic Workshops held in Newport Beach, California (2011 and 2012)

# 6. CASE STUDY 1: AUXILIARY BUILDING MODELING

An essential structure for seismic probabilistic risk assessment (SPRA) at nuclear power plants (NPPs) is the auxiliary building. The auxiliary building is typically connected to the containment structure and houses crucial auxiliary and safety systems related to the reactor, which is located in the containment structure. These systems include radioactive waste, chemical and volume control, and emergency cooling systems (NRC 2016). Due to the high rigidity of these buildings, seismic events are unlikely to lead to structural failure of the structure. However, they could lead to failure of key safety systems, which could subsequently lead to radioactive release from the NPP.

To appropriately predict the dynamic response of these safety systems, also referred to as nonstructural components (NCs), the dynamic response of the auxiliary building must first be predicted. Therefore, both two-dimensional (2D) and three-dimensional (3D) structural models were created for an auxiliary building. 2D models were created in the form of lumped-mass stick models, and 3D models were created using finite elements (FE) in SAP2000[60]. Models were based off a realistic auxiliary building found in literature (HAER 1968). Several cases were created to illustrate important building and model characteristics, such as torsion and slab flexibility. As SPRA demands a large number of analyses, 2D stick models were studied to evaluate their capability of capturing 3D building response. Specifically, the capability of 2D stick models to incorporate slab flexibility was a focus of this study.

## 6.1 Auxiliary Building Structure Models

The realistic auxiliary building developed in this studied was based off the primary auxiliary building from the Connecticut Yankee NPP. This building was a two story reinforced concrete building with a partial basement. Due to the unavailability of structural plans for this, or any, auxiliary building, structural plans were recreated using basic structural engineering principles and drawings of the Connecticut Yankee auxiliary building. Not all aspects of the realistic auxiliary building created are entirely accurate; however, it is believed that sufficient details were created to represent a typical NPP auxiliary building.

As part of this study, a total of six auxiliary building cases were investigated to illustrate a few key aspects of dynamic behavior of NPP auxiliary buildings. Throughout this chapter, the six cases (actually subcases of Case Study 1) will be referred to as: Case 0, Case 1, Case 2, Case 3, Case 4, and Case 5. As mentioned, the realistic building, Case 1, was recreated to match the Connecticut Yankee auxiliary building. This case was a three story reinforced concrete building with minor irregularities in plan and significant irregularities in stiffness and mass. The remaining cases were created from this realistic building. A symmetrical building, Case 0, was created by transforming case 1 into a perfectly symmetrical building in terms of mass, stiffness, and geometry. Cases 2 through 5 were also created by transforming Case 1. However, these cases were created to strategically increase the distance between the center of mass (CM) and center of rigidity (CR). Cases 2 through 5 were created so that geometric irregularities also increased concurrently with increased distance between the CM and CR. Most importantly, all cases were created so that each

---

[60] SAP2000, Version 18. Computers and Structures, Inc., Berkeley, CA. www.csiberkeley.com (2016).

case had approximately the same mass and stiffness at each story and consequently, for the entire structure.

To illustrate each case, basic structural plan sets were created for each case. Along with the plan sets, loading diagrams were created to illustrate locations of live loads, which represented heavy equipment loads in a typical auxiliary building. Based off equipment placement obtained in the arrangement plans, these loads are particularly important because they illustrate how irregular the mass of a typical NPP auxiliary building can be even if no geometric and stiffness irregularities exist. The structural plans and loading diagrams for Cases 0, 1, and 5 can be seen in Figures 6.1 through 6.6. Tables 6.1 and 6.2 provide supplementary information for the structural plans included in Figures 6.1 through 6.6. Only Cases 0, 1, and 5 were shown in this chapter to illustrate extreme cases for the study. The remaining structural plan sets and loading diagrams can be found in Appendix C.

Table 6.1 Structural components' dimensions for Cases 1, 2, 3, 4, and 5

| Beams and girders | | Columns | | Walls | |
|---|---|---|---|---|---|
| Girder name | Dimension (in. x in.) | Column name | Dimension (in. x in.) | Wall name | Thickness (in.) |
| G1, G2, B1, B2 | 15 x 20 | C1 | 12 x 12 | W0 | 10 |
| G3 | 20 x 20 | C2 | 24 x 24 | W1 | 12 |
| G4, G5, G10, B3, B4 | 24 x 36 | C3 | 24 x 36 | W2 | 18 |
| G6, G7, G11, B5 | 36 x 48 | C4 | 36 x 36 | W3 | 24 |
| G8, G9, G12 | 36 x 60 | | | | |

Table 6.2 Structural components' dimensions for the Case 0

| Beams and girders | | Columns | | Walls | |
|---|---|---|---|---|---|
| Girder name | Dimension (in. x in.) | Column name | Dimension (in. x in.) | Wall name | Thickness (in.) |
| G1 | 15 x 20 | C1 | 18 x 18 | W0 | 8 |
| G2 | 20 x 20 | C2 | 36 x 36 | W1 | 10 |
| G3 | 30 x 36 | | | W2 | 12 |
| G4 | 36 x 48 | | | W3 | 18 |
| | | | | W4 | 24 |

The loading diagrams contain highlights that illustrate several areas on each floor slab that have different equipment live loads. The loadings associated with those highlights are shown in Table 6.3. Along with the equipment live loads, Table 6.4 contains each floor's dead load information, which accounts for self-weight of slab, slab toppings, and other nonmoving loads. For each case, the loads in Table 6.4 are uniformly distributed over the entire area of each floor slab.

Each case contains three stories, with floor to floor heights of 13, 18, and 18 ft. Two elevations of the Case 1 building are shown in Figure 6.7. Due to similarities in elevation, only section cuts for Case 1 were shown.

Table 6.3 Live load information for auxiliary building cases

| | Equipment live loads (psf) | | | | | |
|---|---|---|---|---|---|---|
| Section name | Case 0 | Case 1 | Case 2 | Case 3 | Case 4 | Case 5 |
| A | 40 | 15 | 15 | 15 | 15 | 15 |
| B | N/A | 20 | 20 | 20 | 20 | 20 |
| C | N/A | 55 | 55 | 55 | 55 | N/A |
| D | N/A | 150 | 150 | 150 | N/A | N/A |
| E | N/A | 360 | 360 | 360 | N/A | N/A |

Table 6.4 Dead load information for auxiliary building cases

| | Dead loads (psf) | | | | | |
|---|---|---|---|---|---|---|
| | Case 0 | Case 1 | Case 2 | Case 3 | Case 4 | Case 5 |
| 1st floor | 188 | 188 | 208 | 263 | 458 | 608 |
| 2nd floor | 188 | 188 | 198 | 243 | 423 | 558 |
| 3rd floor/roof | 112 | 112 | 122 | 147 | 207 | 267 |

As mentioned, an important characteristic of each case is the difference in distance between the CM and CR for each model. Table 6.5 summarizes the locations of CM and CR for each case with respect to gridline A.

Table 6.5 Summary of CM and CR locations for auxiliary building cases

| | Distance from gridline A (ft) | | | | | |
|---|---|---|---|---|---|---|
| | Case 0 | Case 1 | Case 2 | Case 3 | Case 4 | Case 5 |
| CM | 74.0 | 71.6 | 69.2 | 64.2 | 55.5 | 57.1 |
| CR | 74.0 | 72.4 | 70.8 | 67.9 | 50.8 | 49.8 |
| Distance from CM to CR | 0.0 | 0.8 | 1.6 | 3.7 | 4.7 | 7.3 |

## 6.2 Description of Structural Models

Two types of structural models were investigated for the auxiliary building. The first type was a typical 3D structural model. The second type was a 2D stick model. Due to their simplicity, 2D stick models may not accurately capture the behavior of structures when representing structures with significant irregularities in mass, geometry, and stiffness.

In development of 2D stick models, rigid diaphragm behavior is generally assumed. Rigid slab behavior is commonly accepted in structural engineering as an acceptable but approximate assumption for certain applications. However, recent events[61] for example, have emphasized the limited capability of structural models with rigid slab behavior, and therefore 2D stick models, to accurately predict the dynamic response of NPP structures. Models developed for each case in this research include two 3D structural models and two 2D stick models. Included in the two 2D and 3D models for each case is a model with rigid slab behavior and a model with semi-rigid slab behavior. Due to the 2D nature of the stick models, stick models can be developed to only represent one major axis of the structure. For this study, only stick models based on transverse direction structural components were developed for each case. All modeling in this study was completed in SAP2000[62]. Modeling technique and instructions for development of both 2D and 3D models can be found in Appendix B.

### 6.2.1 Simplified 2D Models

The most common type of 2D stick model, known as a lumped-mass stick model, was chosen to be used for the auxiliary building. In a typical lumped-mass stick model, several vertical beam elements are connected at nodes, which have an assigned mass. For a building structure, a vertical beam element and lumped-mass are used for each story. For beam elements, structural properties are often simply characterized with a story stiffness value equivalent to the sum of the story's lateral load-resisting elements in one direction for each respective beam. Lumped-mass values are assigned to nodes equivalent to the mass of beams and slabs of that floor level plus half the mass of columns and walls in stories directly above and below that floor. An illustration of the lumped-mass stick model used in this study along with its corresponding SAP2000 model is shown in Figure 2.8.

While several techniques are available to create lumped-mass sticks models, the technique chosen in this research was to develop the moment of inertia, $I_i$, of each vertical beam element from the stiffness matrix of the entire structure by way of a flexibility analysis of the 3D structural model. This process included applying three separate line loads of 1,000 kips per foot along the length of the building at each floor level; forming a flexibility matrix, $F$, based off the average floor response from this loading; then converting the flexibility matrix into a stiffness matrix, $K$; and finally converting the stiffness of each beam, $k_i$, obtained from the flexibility matrix into a moment of

---

[61] Nie, J.R., Hofmayer, C.H., Braverman, J.I., and Stovall, S.P. "A Study of the Effect of Floor Flexibility on Building Response Using KK NPP Experience," Paper presented at the 22nd International Conference on Structural Mechanics in Reactor Technology, San Francisco, CA (2013).

[62] SAP2000, Version 18. Computers and Structures, Inc., Berkeley, CA. www.csiberkeley.com (2016).

inertia, $I_i$. A moment of inertia value, $I_i$, was chosen instead of stiffness for each vertical beam for modeling purposes in SAP2000. Equations 6.1 and 6.2 are used in this conversion process.

$$K = F^{-1} \tag{6.1}$$

where $F = \begin{bmatrix} f_{11} & f_{21} & f_{31} \\ f_{12} & f_{22} & f_{32} \\ f_{13} & f_{23} & f_{33} \end{bmatrix}$, $K = \begin{bmatrix} k_1 + k_2 & -k_2 & 0 \\ -k_2 & k_2 + k_3 & -k_3 \\ 0 & -k_3 & k_3 \end{bmatrix}$, $f_{ij}$ is the displacement at story $i$ due to the unit loading at story $j$, and $k_i$ is the equivalent stiffness of story $i$.

$$I_i = \frac{k_i {H_i}^3}{12E_c} \tag{6.2}$$

where $I_i$ is the equivalent moment of inertia of story $i$, $H_i$ is the height of story $i$, and $E_c$ is the elastic modulus of concrete. $I_i$ is determined from Equation 6.2 using equivalent story stiffness, $k_i$, calculated from Equation 6.1. The equivalent stiffness, $I_i$, for each of the three stories are then used in SAP2000 to develop 2D stick models.

Each 2D stick model was developed based on a flexibility analysis of its corresponding 3D model. This included a stick model to represent both a rigid and semi-rigid slab for each case. In total, twelve stick models were created using this process. Tables 6.6 through 6.10 summarize the mass, stiffness, and moment of inertia values for each vertical beam and lumped-mass for 2D stick models of each case.

Table 6.6 Lumped-mass values for rigid and semi-rigid 2D stick models for each case

| | Mass (kip-s$^2$/ft) | | | | | |
|---|---|---|---|---|---|---|
| | Case 0 | Case 1 | Case 2 | Case 3 | Case 4 | Case 5 |
| $m_1$ | 162.55 | 165.1 | 165.22 | 165.53 | 165.54 | 164.51 |
| $m_2$ | 155.98 | 151.15 | 150.08 | 152.03 | 150.44 | 150.53 |
| $m_3$ | 70.28 | 69.85 | 70.44 | 71.20 | 69.29 | 69.92 |

Table 6.7 Story stiffness, $k_i$, of vertical beam elements in 2D rigid stick models

| | Stiffness (kip/ft x10$^5$) | | | | | |
|---|---|---|---|---|---|---|
| | Case 0 | Case 1 | Case 2 | Case 3 | Case 4 | Case 5 |
| $k_1$ | 7.41 | 8.35 | 8.23 | 7.59 | 6.85 | 6.52 |
| $k_2$ | 3.18 | 2.87 | 2.86 | 2.98 | 2.76 | 2.80 |
| $k_3$ | 3.18 | 2.91 | 2.90 | 3.04 | 2.78 | 2.85 |

Table 6.8 Story moment of inertia, $I_i$, of vertical beam elements in 2D rigid stick models

| | Moment of inertia (in.$^4$ x10$^7$) | | | | | |
|---|---|---|---|---|---|---|
| | Case 0 | Case 1 | Case 2 | Case 3 | Case 4 | Case 5 |
| $I_1$ | 6.50 | 7.33 | 7.22 | 6.67 | 6.02 | 5.72 |
| $I_2$ | 7.41 | 6.68 | 6.66 | 6.95 | 6.42 | 6.53 |
| $I_3$ | 7.41 | 6.78 | 6.77 | 7.07 | 6.48 | 6.63 |

Table 6.9 Story stiffness, $k_i$, of vertical beam elements in 2D semi-rigid stick models

| | Stiffness (kip/ft x10$^5$) | | | | | |
|---|---|---|---|---|---|---|
| | Case 0 | Case 1 | Case 2 | Case 3 | Case 4 | Case 5 |
| $k_1$ | 6.51 | 4.73 | 5.09 | 4.73 | 4.79 | 5.00 |
| $k_2$ | 2.96 | 1.37 | 1.39 | 1.60 | 1.96 | 1.73 |
| $k_3$ | 2.82 | 1.38 | 1.40 | 1.65 | 1.92 | 1.75 |

Table 6.10 Story moment of inertia, $I_i$, of vertical beam elements in 2D semi-rigid stick models

| | Moment of inertia (in.$^4$ x10$^7$) | | | | | |
|---|---|---|---|---|---|---|
| | Case 0 | Case 1 | Case 2 | Case 3 | Case 4 | Case 5 |
| $I_1$ | 6.09 | 5.75 | 5.63 | 5.41 | 4.85 | 5.33 |
| $I_2$ | 6.86 | 5.19 | 5.68 | 4.76 | 4.96 | 4.57 |
| $I_3$ | 6.55 | 1.38 | 5.08 | 4.69 | 4.78 | 4.42 |

### 6.2.2 Detailed 3D Models

The most appropriate method to capture dynamic behavior of a building structure is a 3D structural model. Typical structural models use a combination of beam-column frame and shell elements to represent beams, column, walls, floor slabs, and other structural members in a building. To create 3D structural models in this study, beam and thick shell elements were used to model the structural members of each case. For each case, a model with rigid and semi-rigid slab behavior was separately created. The modeling technique to accomplish rigid slab behavior in this study involved modifying the elastic modulus of each floor slabs' thick shell elements. For rigid slab behavior, an infinitely large number was used for the elastic modulus of concrete in floor slabs. For semi-rigid slab behavior, a value of 3,605 ksi was used for the elastic modulus of concrete in floor slabs.

### 6.3 Modal Analysis of Simplified 2D Models

Modal analysis of 2D stick and 3D structural models was used to capture the general dynamic properties of each model. However, due to the simplified nature of 2D stick models, general dynamic properties were obtained for only one axis of the original structure. The transverse direction of each case was chosen to be modeled by the stick models, and therefore, only dynamic properties of the transverse direction are represented in modal analysis. Modal information in the vertical direction was neglected and only results from significant modes in the transverse direction were shown. Tables 6.11 and 6.12 summarize the modal analysis results for 2D stick models of Cases 0, 1, and 5 in terms of natural frequency, mass participation ratio, and cumulative mass participation ratio. Figure 6.8 shows the three significant mode shapes shared by all cases of 2D stick models. Modal information for the remaining 2D stick models is shown in Appendix C.

Table 6.11 2D rigid slab stick models' modal information for Cases 0, 1, and 5

| Mode number | Natural frequency (Hz) | Mass participation ratio | Cumulative mass participation ratio |
|---|---|---|---|
| Case 0 | | | |
| 1 | 16.14 | 81.4% | 81.4% |
| 2 | 41.96 | 13.8% | 95.2% |
| 3 | 50.71 | 4.8% | 100% |
| Case 1 | | | |
| 1 | 16.07 | 77.5% | 77.5% |
| 2 | 41.79 | 13.8% | 91.3% |
| 3 | 49.87 | 8.7% | 100% |
| Case 5 | | | |
| 1 | 15.31 | 81.1% | 81.1% |
| 2 | 39.46 | 14.9% | 96.0% |
| 3 | 48.00 | 4.0% | 100% |

Table 6.12 2D semi-rigid slab strick models' modal information for cases 0, 1, and 5

| Mode number | Natural frequency (Hz) | Mass participation ratio | Cumulative mass participation ratio |
|---|---|---|---|
| Case 0 | | | |
| 1 | 15.54 | 81.0% | 81.0% |
| 2 | 39.97 | 13.1% | 94.2% |
| 3 | 48.43 | 5.8% | 100% |
| Case 1 | | | |
| 1 | 14.11 | 76.9% | 76.9% |
| 2 | 35.62 | 11.9% | 88.8% |
| 3 | 43.45 | 11.2% | 100% |

|  |  |  |  |
|---|---|---|---|
| Case 5 |  |  |  |
| 1 | 13.40 | 76.4% | 76.4% |
| 2 | 34.40 | 12.1% | 88.5% |
| 3 | 41.53 | 11.5% | 100% |

An important characteristic of the models is the similarity in natural frequency of each significant mode. This was intentionally done, by creating each case with approximately the same mass and stiffness, so that an appropriate comparison between models could be completed. From Table 6.11, the natural frequencies of the first mode for Cases 0, 1, and 5 were 16.14 Hz, 16.07 Hz, and 15.31 Hz, respectively. Similarly, the mass participation ratios of the first mode in each case, shown in Tables 6.11 and 6.12, were between 76% and 81%. This corresponds to the mode that dominates the total dynamic response of the structure. Table 6.13 summarizes the natural frequency values for each of the three significant modes for all cases of 2D stick models.

Table 6.13 Natural frequencies of 2D stick models for rigid and semi-rigid slab behavior

| Mode number | Natural frequency (Hz) |  |  |  |  |  |
|---|---|---|---|---|---|---|
|  | Case 0 | Case 1 | Case 2 | Case 3 | Case 4 | Case 5 |
| Rigid slab models |  |  |  |  |  |  |
| 1 | 16.14 | 16.07 | 16.02 | 15.95 | 15.39 | 15.31 |
| 2 | 41.96 | 41.79 | 41.58 | 41.32 | 39.67 | 39.46 |
| 3 | 50.71 | 49.87 | 49.71 | 49.77 | 47.86 | 48.00 |
| Semi-rigid slab models |  |  |  |  |  |  |
| 1 | 15.54 | 14.11 | 14.50 | 13.54 | 13.60 | 13.40 |
| 2 | 39.97 | 35.62 | 36.32 | 34.96 | 34.74 | 34.40 |
| 3 | 48.43 | 43.45 | 44.44 | 42.07 | 41.91 | 41.53 |

An important point to notice in Table 6.13 is the difference in natural frequencies between 2D stick models that represent rigid slab behavior versus semi-rigid slab behavior. All models with semi-rigid slab elements have smaller natural frequencies for every mode, indicating decreased stiffness compared to rigid slab models. Also, in general, natural frequencies decrease as models become more irregular with rigid slab behavior. However, natural frequencies of models with semi-rigid slab behavior do not necessarily decrease as the building models become more irregular.

### 6.4 Modal Analysis of Detailed 3D Models

While 2D stick models can represent dynamic properties along only one major axis of a structure, 3D structural models can capture dynamic properties of each major axis. For comparison purposes, dynamic properties of the 3D models about the transverse direction were shown in this section. Tables 6.14 and 6.15 summarize the transverse direction modal information of each 3D structural model. Figures 6.9 through 6.12 illustrate the significant mode shapes for the transverse direction modes for cases 1 and 5. In each figure, blue and purple colors signify either maximum or minimum displacements.

Table 6.14 3D rigid slab structural models' modal information for cases 0, 1, and 5

| Mode number | Natural frequency (Hz) | Mass participation ratio | Cumulative mass participation ratio |
|---|---|---|---|
| Case 0 | | | |
| 1 | 16.14 | 81.4% | 81.4% |
| 5 | 41.96 | 13.8% | 95.2% |
| 8 | 50.71 | 4.8% | 100% |
| Case 1 | | | |
| 1 | 16.04 | 77.4% | 77.4% |
| 5 | 41.77 | 13.9% | 91.5% |
| 7 | 49.69 | 7.3% | 98.9% |
| Case 5 | | | |
| 1 | 15.11 | 34.2% | 34.2% |
| 2 | 16.09 | 33.5% | 67.6% |
| 3 | 17.47 | 14.3% | 81.9% |
| 5 | 39.03 | 6.3% | 88.2% |
| 6 | 41.63 | 5.7% | 93.9% |
| 7 | 44.95 | 3.5% | 97.4% |
| 9 | 50.47 | 1.4% | 99.4% |

Unlike the 2D stick models, which captured three distinct modes for all cases due to the simplified system having three degrees-of-freedom, 3D structural models can capture many more significant modes. For Cases 0 and 1, the number of significant modes remained as three in Table 6.14 due to the lack of significant stiffness or plan irregularities. However, for Case 5, which had significant stiffness and plan irregularities, the number of significant modes was seven. Each of these modes for Case 5 had smaller mass participation in the transverse direction compared to Cases 0 and 1 due to torsional effects. For example, the first three modes of Case 5 contributed 82% of the total dynamic response whereas the first mode contributed approximately 80% of the total dynamic response for Cases 0 and 1.

Table 6.15 3D semi-rigid slab structural models' modal information for Cases 0, 1, and 5

| Mode number | Natural frequency (Hz) | Mass participation ratio | Cumulative mass participation ratio |
|---|---|---|---|
| Case 0 | | | |
| 1 | 15.22 | 79.9% | 79.9% |
| 9 | 39.30 | 10.5% | 91.3% |
| 15 | 47.07 | 6.1% | 98.0% |
| Case 1 | | | |
| 1 | 14.25 | 74.6% | 74.6% |
| 6 | 30.90 | 3.5% | 80.9% |

|  |  |  |  |
|---|---|---|---|
| 8 | 35.72 | 6.5% | 87.4% |
| 11 | 39.05 | 6.4% | 94.2% |
| Case 5 |  |  |  |
| 1 | 13.44 | 27.8% | 27.8% |
| 2 | 14.01 | 7.1% | 34.9% |
| 3 | 15.48 | 44.0% | 79.0% |
| 4 | 17.76 | 2.2% | 81.2% |
| 14 | 36.69 | 11.7% | 94.1% |

Due to the effect of slab flexibility in semi-rigid slab models, structures with limited stiffness or plan irregularity can have localized torsional effects. As shown for Case 1 in Table 6.15, four significant modes were captured in the transverse direction as opposed to three for the rigid slab model. Due to the perfectly symmetrical nature of Case 0, three significant modes were captured, which corresponded to the same number as the rigid slab model in Table 6.14. For Case 5 with slab flexibility, only five significant modes were captured (Table 6.15) as opposed to seven in Table 6.14. The natural frequencies of all modes were summarized in Table 6.16 to compare the number of significant modes needed to capture the total dynamic response of rigid slab and semi-rigid slab models. In Table 6.16, modes were grouped together based on cumulative mass participation ratios. For example, the first three significant modes of the Case 5 rigid slab model captured 82% of total mass participation. This corresponded to the first significant mode of the Case 0 rigid slab model, which captured 80% of the total mass participation. In Table 6.16, the first, second, and third modes correspond to 80%, 85%, and 95% of cumulative mass participation, respectively, for all models. In agreement with results from Tables 6.14 and 6.15, models with significant stiffness and plan irregularity required more modes to capture the total dynamic response of the structure. Also important to notice in Table 6.16, significant modes for all models with semi-rigid slab behavior had lower natural frequencies than corresponding modes for models with rigid slab behavior. This indicated lower total stiffness for models with semi-rigid slabs compared to models with rigid slabs.

Table 6.16 Comparison of natural frequencies of 3D structural models with rigid and semi-rigid slabs

| Mode number | Natural frequency (Hz) |  |  |  |  |  |
|---|---|---|---|---|---|---|
|  | Case 0 | Case 1 | Case 2 | Case 3 | Case 4 | Case 5 |
| Rigid slab models |  |  |  |  |  |  |
| 1 | 16.14 | 16.04 | 16.00 | 15.87 | 15.61 | 15.11 |
|  |  |  |  |  | 16.62 | 16.09 |
|  |  |  |  |  | 18.33 | 17.47 |
| 2 | 41.96 | 41.77 | 41.55 | 41.08 | 40.23 | 39.03 |
|  |  |  |  |  | 43.01 | 41.63 |
| 3 | 50.71 | 49.69 | 49.53 | 49.57 | 47.47 | 44.95 |
|  |  |  |  |  | 48.70 | 50.47 |

| Semi-rigid slab models | | | | | | |
|---|---|---|---|---|---|---|
| 1 | 15.22 | 14.25 | 14.32 | 14.37 | 14.14 | 13.44 |
| | | | | | | 14.01 |
| | | | | | 15.00 | 15.48 |
| | | | | | 15.61 | 17.76 |
| 2 | 39.30 | 30.90 | 25.59 | 31.91 | 31.89 | N/A |
| | | | 31.57 | | | |
| | | 35.72 | 35.64 | | 34.77 | |
| 3 | 47.07 | 39.05 | 39.05 | 36.59 | 40.16 | 36.69 |

## 6.5 Comparison of 2D and 3D Models

The modal analysis results for simplified 2D and detailed 3D models brought to view some fundamental limitations of simplified 2D models. For models with little structural irregularity and rigid slabs, 2D stick models were able to capture the fundamental frequencies of all significant transverse direction modes of 3D structural models. Comparing the fundamental frequencies of all significant modes for Cases 0 and 1 in Tables 6.13 through 6.15, natural frequencies of 2D models were all within 0.25 Hz of corresponding natural frequencies of 3D models.

As structural irregularity and slab flexibility increased in the developed cases, 2D models were less capable of capturing global and localized torsional effects. Due to torsional effects, the 3D rigid slab model for Case 5 captured seven significant transverse direction modes, whereas the corresponding 2D model was not able to capture the additional modes caused by torsion. However, the 2D models were able to approximately capture the natural frequencies of the several torsional modes with one mode. For example with Case 5, the first three modes of the 3D rigid slab model had natural frequencies of 15.11, 16.09, and 17.47 Hz in Table 6.14. The cumulative mass participation of these modes was 82%. Table 6.11 shows the corresponding 2D model for Case 5 was able to capture one mode with a mass participation of 81% and a natural frequency of 15.31 Hz. Similarly, due to localized torsion effects, the 3D semi-rigid slab model for Case 1 captured four significant transverse direction modes. Shown in Table 6.15, the second and third modes had natural frequencies of 30.9 Hz and 35.72 Hz. The total mass participation of these two modes was 10%. The corresponding 2D model for Case 1 was able to capture one mode for these two 3D modes with a total mass participation of 12% and a natural frequency of 35.62 Hz (Table 6.12).

## 6.6 Summary and Conclusions

A realistic auxiliary building was created based on plan sets retrieved for a primary auxiliary building at a decommissioned and now demolished NPP site. Five additional cases were created from the realistic auxiliary building, case 1, with approximately the same mass and stiffness. Case 0 was a perfectly symmetric building while cases 2 through 5 were created to increase the plan irregularity and the distance between the CM and CR with each subsequent case. As SPRA demands a large number of analyses, these cases were used to examine the effects of structural irregularity and slab flexibility on simplified models.

Detailed 3D structural models and simplified 2D stick models were created and modal analysis was used to compare general dynamic characteristics of detailed and simplified models. Due to the simplified nature of stick models, only three modes were captured for all stick models. However, 3D structural models were able to capture three or many more modes. For models with limited irregularity (Cases 0 and 1) and rigid slabs, 3D models captured the same number of modes as stick models. However, as slab flexibility and structural irregularity increased, the number of modes increased for 3D models. The most extreme case was shown in Table 6.14, where the 3D rigid slab model for Case 5 captured seven transverse direction modes. For cases with limited structural irregularity, natural frequencies of significant modes in stick models were within 5% of the corresponding natural frequencies of 3D models. However, as structural irregularity increased in cases, the difference between corresponding natural frequencies of stick and 3D models increased. Tables 6.13 and 6.16 show that for Case 5 with the most significant structural irregularity, natural frequencies of stick models were up to 30% different compared to the corresponding natural frequencies of 3D models. Overall, while stick models were only able to capture three modes, they were able to approximately capture the natural frequencies of all significant transverse direction modes in 3D models.

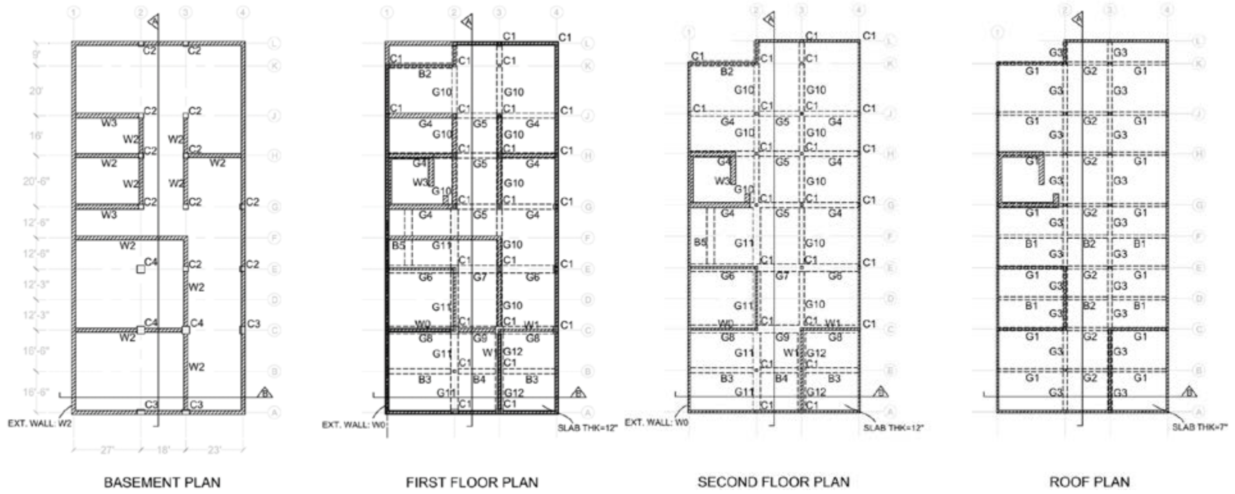

Figure 6.1 Structural plan for case 1 auxiliary building

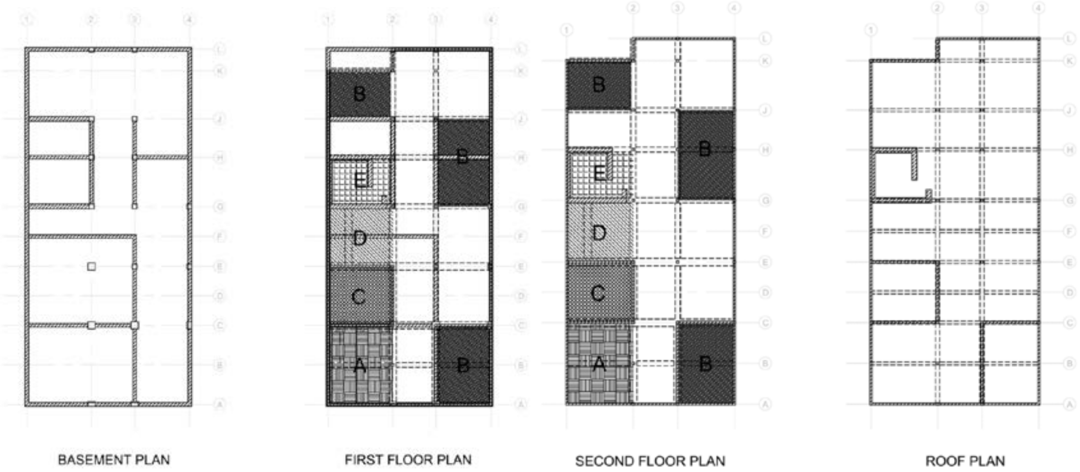

Figure 6.2 Loading diagram for Case 1 auxiliary building

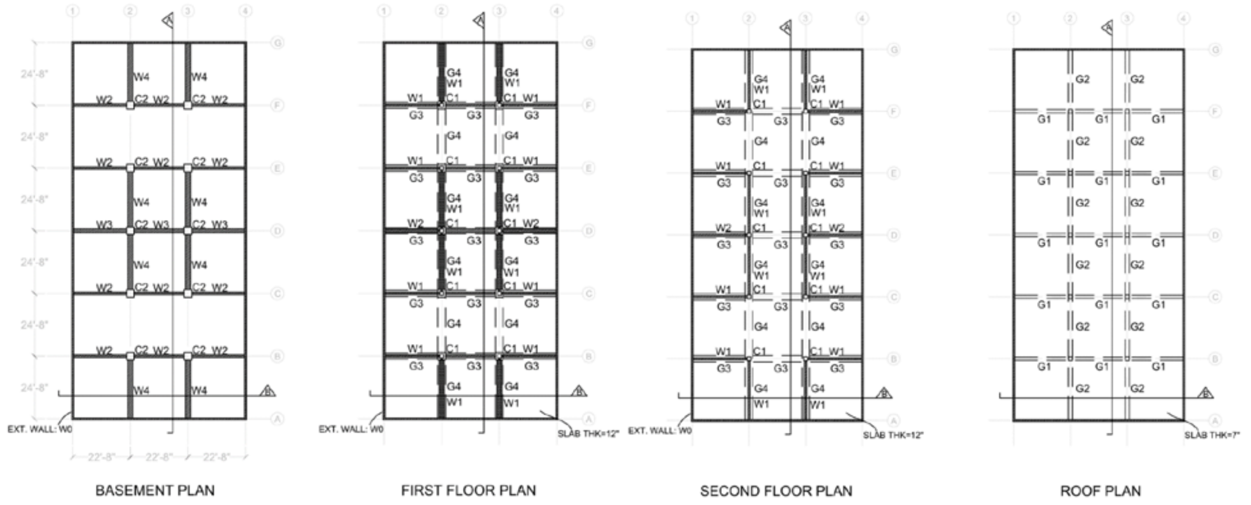

Figure 6.3 Structural plan for Case 0 auxiliary building

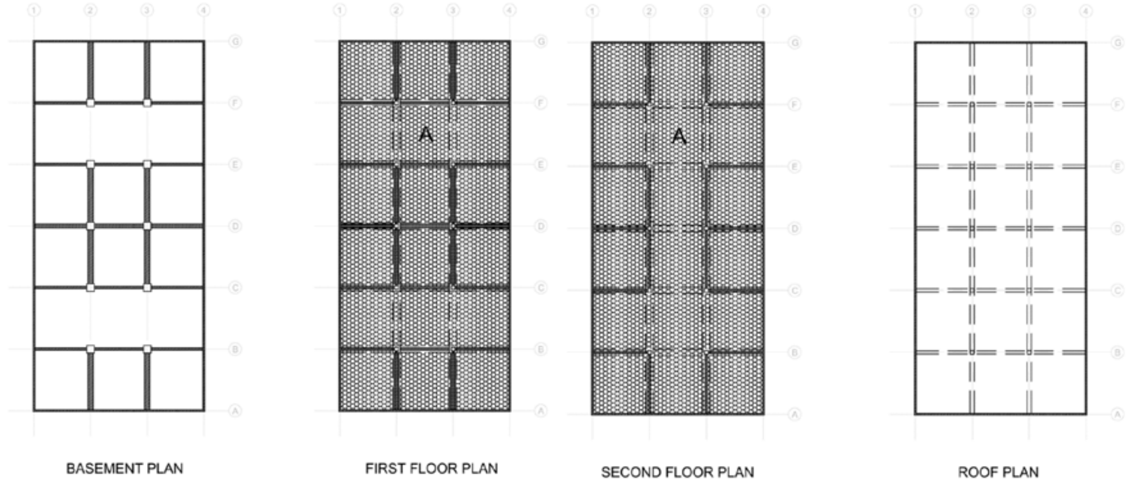

Figure 6.4 Loading diagram for Case 0 auxiliary building

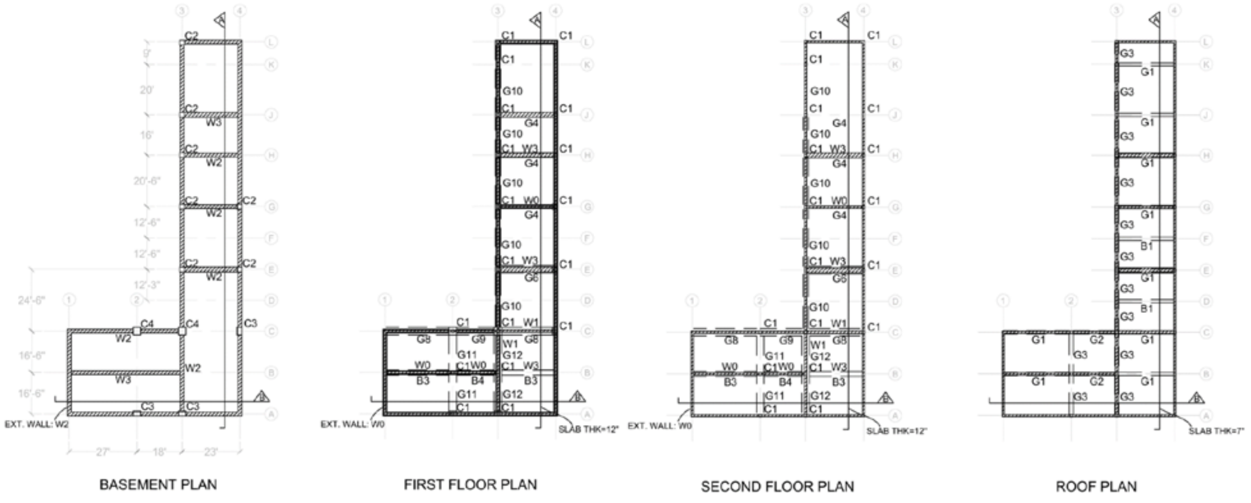

Figure 6.5 Structural plan for Case 5 auxiliary building

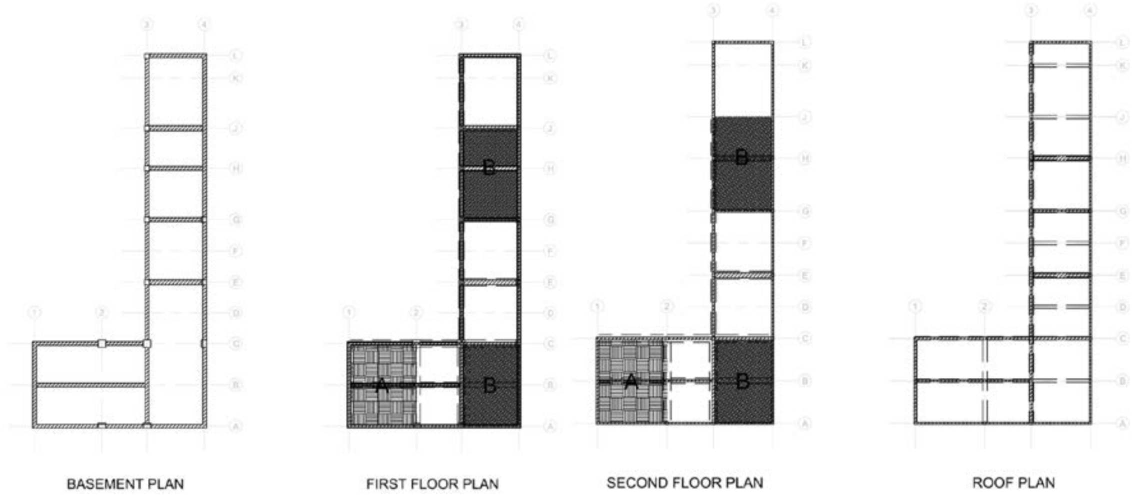

Figure 6.6 Loading diagram for Case 5 auxiliary building

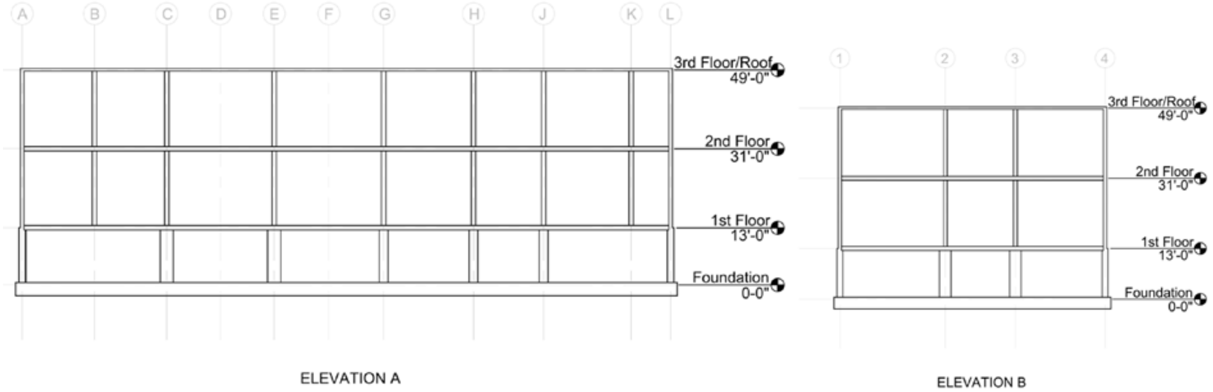

Figure 6.7 Elevations A and B for Case 1 auxiliary building

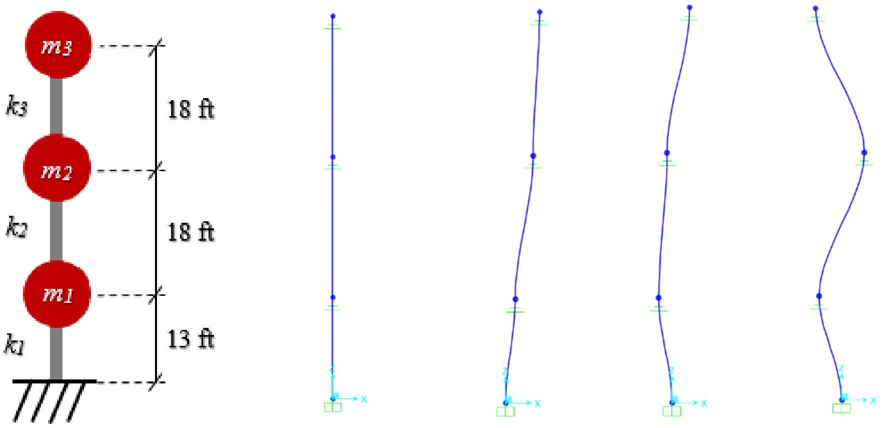

(a) (b) (c) (d) (e)

Figure 6.8 2D stick model and mode shapes: (a) illustration, (b) SAP2000 model, (c) mode 1, (d) mode 2, and (e) mode 3

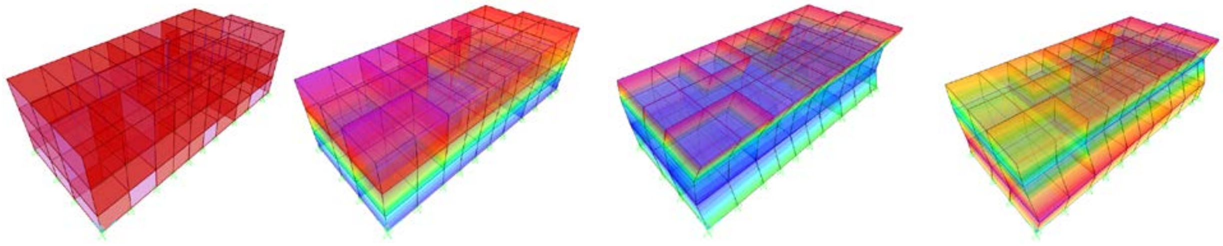

(a) (b) (c) (d)

Figure 6.9 Mode shapes for 3D case 1 rigid slab structural model: (a) undeformed shape, (b) mode 1, (c) mode 5, and (d) mode 7

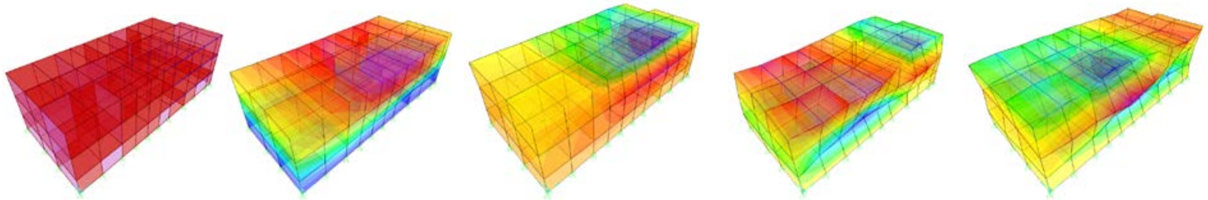

(a) (b) (c) (d) (e)

Figure 6.10 Mode shapes for 3D case 1 semi-rigid slab structural model: (a) undeformed shape, (b) mode 1, (c) mode 6, (d) mode 8, and (e) mode 11

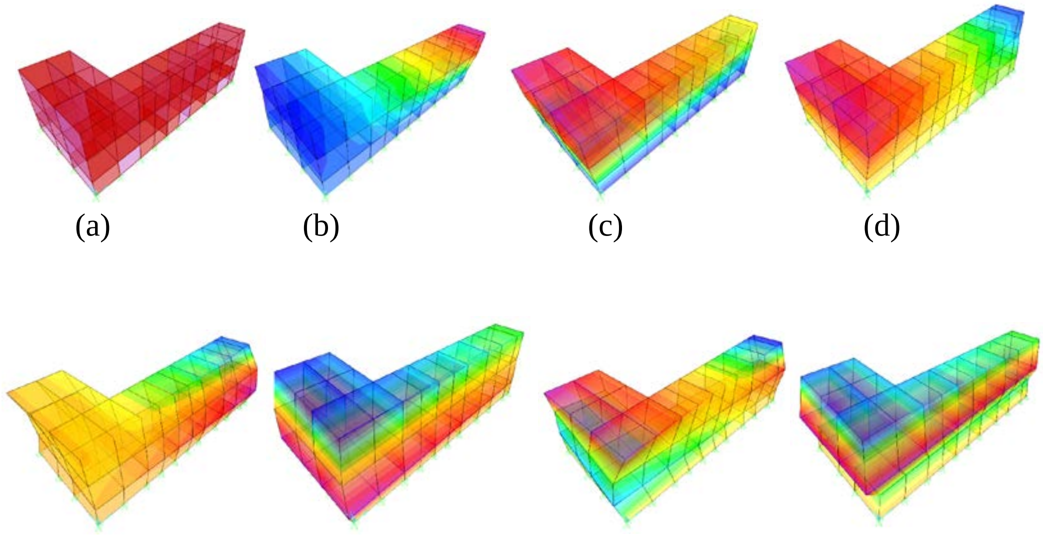

(a) (b) (c) (d)

(e) (f) (g) (h)

Figure 6.11 Mode shapes for 3D Case 5 rigid slab structural model: (a) undeformed shape, (b) Mode 1, (c) Mode 2, (d) Mode 3, (e) Mode 5, (f) Mode 6, (g) m\Mode 7, and (h) Mode 9

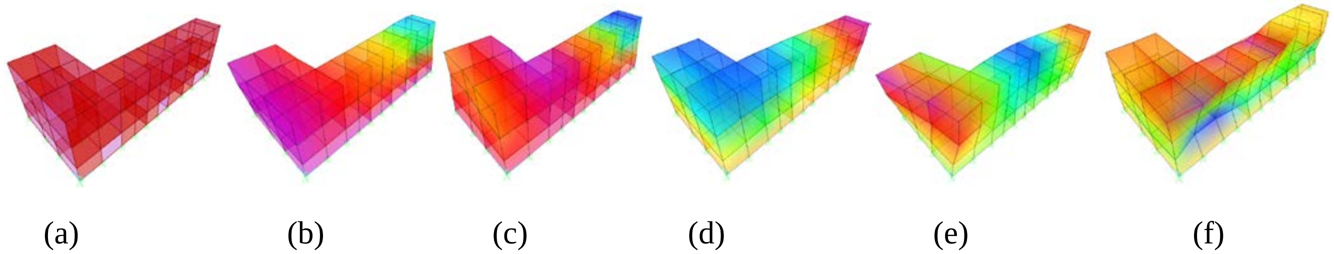

Figure 6.12 Mode shapes for 3D Case 5 semi-rigid slab structural model: (a) undeformed shape, (b) Mode 1, (c) Mode 2, (d) Mode 3, (e) Mode 4, and (f) Mode 14

## 7. CASE STUDY 1: DYNAMIC RESPONSE OF AUXILIARY BUILDING MODELS

Modal analysis was used to compare general dynamic behavior of the several auxiliary building cases in Section 6. However, SPRA uses time history analysis with input ground motions to develop failure probabilities for a structure and nonstructural components (NSCs). To evaluate the effects of structural irregularity and slab flexibility on dynamic structural response of the auxiliary building, time history analysis was completed for all models developed in Section 2. Similar to modal analysis, only one major direction, the transverse direction, of the structure was considered in time history analysis. El Centro ground motion was the ground motion chosen and was applied in the transverse direction for analysis. Key information obtained from time history analysis was displacement and acceleration values at each story. Maximum values from displacement and acceleration histories, which almost exclusively occur at the highest floor level from the ground, are often used for SPRA. For this reason, this chapter focuses on displacement and acceleration responses at the third floor level.

### 7.1 Time History Analysis of Simplified 2D Models

Due to the lumped and simplified nature of 2D stick models, displacement and acceleration of each floor were obtained at only one location at each floor level. Since during the derivation of 2D models the flexibility matrix was developed with the average response of all locations on one floor, the response histories obtained from time history analysis were equivalent to the average response of all locations at each respective floor from 3D structural models. Tables 7.1 and 7.2 summarize the maximum responses of 2D models at each floor level for displacement and acceleration, which were obtained from time history analysis. Figures 7.1 through 7.4 show al 2D models' response histories for displacement and acceleration, respectively, for the initial ten seconds at the third floor.

Table 7.1 Maximum response of 2D rigid slab stick models

| Floor | Case 0 | Case 1 | Case 2 | Case 3 | Case 4 | Case 5 |
|---|---|---|---|---|---|---|
| Maximum displacement (in.) | | | | | | |
| 1 | 0.0087 | 0.0075 | 0.0077 | 0.0086 | 0.0093 | 0.0098 |
| 2 | 0.0233 | 0.0234 | 0.0237 | 0.0243 | 0.0260 | 0.0261 |
| 3 | 0.0283 | 0.0290 | 0.0294 | 0.0298 | 0.0318 | 0.0317 |
| Maximum acceleration (ft/s$^2$) | | | | | | |
| 1 | 4.35 | 3.70 | 3.78 | 4.26 | 4.60 | 4.91 |
| 2 | 12.59 | 12.68 | 12.84 | 13.17 | 14.02 | 14.04 |
| 3 | 15.55 | 15.95 | 16.17 | 16.41 | 17.47 | 17.30 |

In agreement with the modal analysis results, Tables 7.1 and 7.2 show decreased stiffness for semi-rigid slab stick models compared to rigid slab stick models. This decrease in stiffness was reflected by larger maximum displacements, such as 0.0386 in. at the third floor of the Case 5 semi-rigid slab model compared to 0.0317 in. at the third floor of the Case 5 rigid slab stick model. This decrease in stiffness also led to smaller maximum accelerations. For example, the maximum acceleration for case 1 rigid slab model was 15.95 ft/s$^2$ at the third floor compared to 13.2 ft/s$^2$ at the third floor for the case 1 semi-rigid slab model.

Table 7.2 Maximum response of 2D semi-rigid slab stick models

| Floor | Case 0 | Case 1 | Case 2 | Case 3 | Case 4 | Case 5 |
|---|---|---|---|---|---|---|
| Maximum displacement (in.) | | | | | | |
| 1 | 0.0095 | 0.0075 | 0.0083 | 0.0094 | 0.0105 | 0.0095 |
| 2 | 0.0258 | 0.0232 | 0.0236 | 0.0299 | 0.0298 | 0.0308 |
| 3 | 0.0316 | 0.0292 | 0.0297 | 0.0373 | 0.0368 | 0.0386 |
| Maximum acceleration (ft/s$^2$) | | | | | | |
| 1 | 4.75 | 3.01 | 3.62 | 3.12 | 3.50 | 3.14 |
| 2 | 13.97 | 10.27 | 11.35 | 11.04 | 10.97 | 11.35 |
| 3 | 17.51 | 13.20 | 14.55 | 14.07 | 13.83 | 14.53 |

## 7.2 Time History Analysis of Detailed 3D Models

While 2D stick models capture only the overall response of each floor during time history analysis, 3D structural models capture each floor level's response at multiple locations. To investigate the effect of spatial response within a floor level, time history analysis results at five separate locations at each floor were collected and analyzed. These five locations are shown in Figure 7.5 at the third floor. The same locations were also used at the first and second floors. Tables 7.3 and 7.4 summarize the maximum responses at all five locations at the third floor for all cases. Figures 7.6 through 7.13 show the time history response for displacement and acceleration for Cases 1 and 5.

Table 7.3 Maximum response at five locations at third story level for 3D rigid slab structural models

| Case | Joint 1 | Joint 2 | Joint 3 | Joint 4 | Joint 5 |
|---|---|---|---|---|---|
| Maximum displacement (in.) | | | | | |
| 0 | 0.0283 | 0.0283 | 0.0283 | 0.0283 | 0.0283 |
| 1 | 0.0308 | 0.0291 | 0.0272 | 0.0297 | 0.0283 |
| 2 | 0.0313 | 0.0293 | 0.0272 | 0.0300 | 0.0284 |
| 3 | 0.0337 | 0.0294 | 0.0247 | 0.0309 | 0.0274 |
| 4 | 0.0217 | 0.0303 | 0.0398 | 0.0272 | N/A |
| 5 | 0.0212 | 0.0290 | 0.0376 | N/A | N/A |
| Maximum acceleration (ft/s$^2$) | | | | | |
| 0 | 15.55 | 15.55 | 15.55 | 15.55 | 15.55 |
| 1 | 17.12 | 16.01 | 14.78 | 16.41 | 15.49 |
| 2 | 17.35 | 16.14 | 14.79 | 16.57 | 15.57 |
| 3 | 18.83 | 16.10 | 13.23 | 17.01 | 14.88 |
| 4 | 10.99 | 16.40 | 24.27 | 14.38 | N/A |
| 5 | 10.67 | 14.94 | 23.79 | N/A | N/A |

Only the first ten seconds are shown due to the maximum responses happening within that time frame. All five locations for case 1 are shown in Figures 7.6 through 7.13, but due to plan irregularity removing two of the locations in Case 5, only three locations are shown for Case 5.

For the 3D rigid slab models in Table 7.3, the variance in spatial response within a floor level increased significantly as structural irregularity increased. For joints 1 and 3 in case 1, the maximum accelerations were 14.78 ft/s$^2$ and 17.12 ft/s$^2$, respectively. However, for joints 1 and 3 in case 5, the maximum accelerations were 10.67 ft/s$^2$ and 23.79 ft/s$^2$. The spatial response of the 3D rigid slab models was also significantly affected by the location of the CR. Since joint 1 is located on gridline A, Table 2.5 in Section 2 shows the distance from the CR decreased from 72.4 ft in case 1 to 49.8 ft in Case 5 for joint 1. From Table 7.3, the maximum displacements of joint 1 decreased from 0.0308 in. for Case 1 to 0.0212 in. for Case 5. Since joint 3 was located on gridline L, the distance from the CR increased from 75.6 ft to 98.2 ft (Table 7.5). This corresponded to an increased maximum displacement from 0.0283 in. in case 1 to 0.0376 in. in Case 5 according to Table 7.3.

Table 7.4 Maximum response at five locations at third story level for 3D semi-rigid slab structural models

| Case | Joint 1 | Joint 2 | Joint 3 | Joint 4 | Joint 5 |
|---|---|---|---|---|---|
| Maximum displacement (in.) | | | | | |
| 0 | 0.0268 | 0.0333 | 0.0268 | 0.0330 | 0.0330 |
| 1 | 0.0215 | 0.0341 | 0.0206 | 0.0306 | 0.0296 |
| 2 | 0.0227 | 0.0343 | 0.0197 | 0.0316 | 0.0278 |
| 3 | 0.0253 | 0.0327 | 0.0199 | 0.0328 | 0.0228 |
| 4 | 0.0233 | 0.0293 | 0.0246 | 0.0306 | N/A |
| 5 | 0.0260 | 0.0347 | 0.0395 | N/A | N/A |
| Maximum acceleration (ft/s$^2$) | | | | | |
| 0 | 14.66 | 18.30 | 14.66 | 18.14 | 18.14 |
| 1 | 9.57 | 15.83 | 9.14 | 13.85 | 13.68 |
| 2 | 10.17 | 16.14 | 8.80 | 14.75 | 12.65 |
| 3 | 12.67 | 15.18 | 9.64 | 15.88 | 10.20 |
| 4 | 10.82 | 15.18 | 12.47 | 15.94 | N/A |
| 5 | 14.80 | 17.63 | 16.14 | N/A | N/A |

For 3D models with semi-rigid slabs in Table 7.4, spatial response variance within a floor level was affected more prominently by distance to lateral load-resisting members. Locations near these elements experienced smaller responses compared to locations far from these elements. For example, the structural plans for Case 1 (Figure 7.5) show that at the third floor level, joint 1 is located at a shear wall and joint 2 is located 37 ft from the nearest shear wall. The corresponding maximum accelerations in Table 5.4 for joints 1 and 2 were 9.57 ft/s$^2$ and 15.83 ft/s$^2$, respectively.

Comparing spatial response of 3D models with rigid slab behavior and 3D models with semi-rigid behavior, selected locations generally experienced larger maximum displacements in models with semi-rigid slabs. From Table 7.3 and 7.4, maximum displacement at joint 4 increased for semi-rigid slab models compared to rigid slab models in all cases. For Cases 1 and 3, the maximum displacement at joint 4 for the rigid slab model was 0.0297 in. and 0.0309 in., respectively. For semi-rigid slab models, the maximum displacement at joint 4 for Cases 1 and 3 were 0.0306 and 0.0328 in., respectively. However, not all locations experienced increased maximum displacement in semi-rigid slab models compared to rigid slab models. Joint 2 in Case 4 had maximum displacements of 0.0303 in. and 0.0293 in., respectively, for the rigid slab and semi-rigid slab models.

Figures 7.6 through 7.13 show the first ten seconds of the response histories for 3D models with rigid and semi-rigid slab behavior for Cases 1 and 5. An important difference for spatial response of rigid slab and semi-rigid slab models was indicated in Figures 7.6 through 7.13. For rigid slab models, all locations follow basically the same response history with different peak responses. Figures 7.10 and 7.11 show this phenomenon for case 5. Not all locations in semi-rigid slab models, however, follow the same response history. Figures 5.12 and 5.13 show joints 1, 2, and 3 in case 5 share a similar response history, but peak responses at different time-steps occurred.

### 7.3 Comparison of 2D and 3D Models

To understand the limitations of simplified stick models compared to detailed 3D models, the two locations of maximum and minimum response from the five selected 3D model locations were compared to the singular response from stick models. For the 3D rigid slab models, the maximum and minimum response locations were joints 1 and 3. However, the location of the CM and CR (Table 7.5) dictated which location was the location of maximum and minimum response in each case. For Cases 1, 2, and 3, joint 1 was the location of maximum response since its location was the corner of the structure and was closer to the CM than the CR. For Cases 4 and 5, however, joint 1 was the location of minimum response since its location was the corner of the structure and

Table 7.5 Comparison of peak response at third story level for 2D stick and 3D structural rigid slab models

| Case | 2D | 3D | |
|---|---|---|---|
| | | Maximum | Minimum |
| Peak displacement (in.) | | | |
| 0 | 0.0283 | 0.0283 (all joints) | 0.0283 (all joints) |
| 1 | 0.0290 | 0.0308 (joint 1) | 0.0272 (joint 3) |
| 2 | 0.0294 | 0.0313 (joint 1) | 0.0272 (joint 3) |
| 3 | 0.0298 | 0.0337 (joint 1) | 0.0247 (joint 3) |
| 4 | 0.0318 | 0.0398 (joint 3) | 0.0217 (joint 1) |
| 5 | 0.0317 | 0.0376 (joint 3) | 0.0212 (joint 1) |
| Peak acceleration (ft/s$^2$) | | | |
| 0 | 15.55 | 15.55 (all joints) | 15.55 (all joints) |
| 1 | 15.95 | 17.12 (joint 1) | 14.78 (joint 3) |
| 2 | 16.17 | 17.35 (joint 1) | 14.79 (joint 3) |
| 3 | 16.41 | 18.83 (joint 1) | 13.23 (joint 3) |
| 4 | 17.47 | 24.27 (joint 3) | 10.99 (joint 1) |
| 5 | 17.30 | 23.79 (joint 3) | 10.67 (joint 1) |

was closer to the CR than the CM. The locations of maximum and minimum response in 3D semi-rigid slab models changed depending on the case. In 3D semi-rigid slab models, local lateral stiffness characteristics influenced the locations of maximum and minimum response. For example in Case 5, joint 1 is located at a shear wall and 16.5 ft from another shear wall whereas joint 2 is located directly in the middle of two shear walls spaced 25 ft apart. Consequently, the locations of maximum and minimum response were joints 2 and 1, respectively, for Case 5. Tables 7.5 and 7.6 summarize locations and values of maximum and minimum response for all cases. Figures 7.14 through 7.21 show the response histories of the 2D models and two extreme locations of 3D models.

Tables 7.5 and 7.6 summarize the two locations of maximum and minimum response at the third floor level for all cases. For Case 0 with rigid slab behavior and no irregularity, the 2D model was able to predict the peak response of all locations from the 3D model. This was due to the perfect symmetry of the case and rigid slab behavior, which allowed the lateral load-resisting elements to move perfectly together laterally. The peak displacement and acceleration of the Case 0 stick and 3D model at all locations were 0.0283 in. and 15.55 ft/s$^2$, respectively (Table 7.5). As structural irregularity increased for rigid slab models, the difference between the stick model's peak response and the 3D model's maximum and minimum response of the five selected locations increased. For Cases 1 and 5 in Table 7.5, the stick model's peak accelerations were 15.95 ft/s$^2$ and 17.3 ft/s$^2$, respectively. However, the maximum and minimum accelerations in 3D models were 17.12 ft/s$^2$ and 14.78 ft/s$^2$ for case 1 and 23.79 ft/s$^2$ and 10.67 ft/s$^2$ for Case 5.

Table 7.6 Comparison of peak response at third story level for 2D stick and 3D structural semi-rigid slab models

| Case | 2D | 3D | |
|---|---|---|---|
| | | Maximum | Minimum |
| Peak displacement (in.) | | | |
| 0 | 0.0316 | 0.0333 (joint 2) | 0.0268 (joints 1 and 3) |
| 1 | 0.0292 | 0.0341 (joint 2) | 0.0206 (joint 3) |
| 2 | 0.0297 | 0.0343 (joint 2) | 0.0197 (joint 3) |
| 3 | 0.0373 | 0.0328 (joint 4) | 0.0199 (joint 3) |
| 4 | 0.0368 | 0.0306 (joint 4) | 0.0233 (joint 1) |
| 5 | 0.0386 | 0.0395 (joint 3) | 0.0260 (joint 1) |
| Peak acceleration (ft/s$^2$) | | | |
| 0 | 17.51 | 18.30 (joint 2) | 14.66 (joints 1 and 3) |
| 1 | 13.20 | 15.83 (joint 2) | 9.14 (joint 3) |
| 2 | 14.55 | 16.14 (joint 2) | 8.80 (joint 3) |
| 3 | 14.07 | 15.88 (joint 4) | 9.64 (joint 3) |
| 4 | 13.83 | 15.94 (joint 4) | 10.82 (joint 1) |
| 5 | 14.53 | 17.63 (joint 2) | 14.80 (joint 1) |

Even though case 0 was perfectly symmetric, the flexibility of the floor slabs in the semi-rigid slab 3D model caused differences in peak spatial response. The peak displacement for the Case 0 stick model was 0.0316 in. according to Table 7.6. However, the maximum and minimum displacements for the 3D model were 0.0333 in. and 0.0268 in., respectively. Since the stick model is only able to predict one response per floor, it was not able to predict the responses of all locations even for the perfectly symmetric case. This was caused by the deformation of the slab in the 3D model.

Unlike the rigid slab models, the difference between maximum and minimum response did not always increase as structural irregularity increased. For example, the difference between maximum and minimum accelerations for Cases 1 and 5 were 6.69 ft/s$^2$ and 2.83 ft/s$^2$, respectively (Table 7.6). Therefore, when floor slab flexibility is considered, this research shows that stick models are not significantly less capable of predicting structural response of buildings with significant structural irregularity compared to buildings with limited structural irregularity.

## 7.4 Summary and Conclusions

Several cases of an NPP auxiliary building were created in section 2 to evaluate the limitations of simplified models for SPRA. Time history analysis was used to compare dynamic responses to seismic events using an input ground motion. Results indicated that both structural irregularity and slab flexibility have a significant effect on the dynamic behavior of a structure. Results also highlighted the limitations of simplified 2D models.

### 7.4.1 Effects of Irregularity on Structural Response

Three categories of building characteristics that cause torsional effects on buildings were studied in this thesis. These categories were plan, mass, and stiffness irregularity. When any of the three is present in a building, spatial response variability throughout each floor increases. Case 0 with perfectly rigid floor slabs highlights how a perfectly symmetric structure has the same spatial response at all locations within a floor level (Table 7.3 and 7.5). However, Tables 7.3 and 7.5 also highlight that highly irregular structures, such as Cases 4 and 5, can have significant differences in dynamic response between locations within a story. Figures 7.10 through 7.13 show the significant spatial response differences for Case 5 throughout the first ten seconds of the response histories.

### 7.4.2 Effects of Slab Flexibility on Structural Response

The two types of slab behavior investigated in this research were rigid and semi-rigid. Rigid and semi-rigid slab behavior was produced by assigning an infinitely large value and realistic value, respectively, to the floor slab’s elastic modulus. While rigid slab behavior is typically assumed when constructing 2D stick models for SPRA, the results of this research highlight how this assumption can misrepresent spatial response of 3D buildings. In general, rigid slab assumptions were shown to overestimate building stiffness and diminish the effects of localized structural characteristics. Tables 7.1 and 7.2 show that rigid slab models underestimated maximum displacements at several locations compared to semi-rigid slab models. Similarly, spatial responses for Case 0 with semi-rigid slabs highlights how the flexibility of floor slabs captures localized lateral stiffness characteristics (Tables 7.4 and 7.6). These localized lateral stiffness features are not captured in rigid slab models due to the rigid slab causing rigid body motion at each floor level. The maximum responses in Table 7.3 show the effect of rigid body motion for the selected locations. The response histories for Case 5 (Figures 7.10 through 7.13) also highlight how peak responses of different spatial locations can occur at different time-steps in semi-rigid slab models, whereas peak responses of different spatial locations in rigid slab models all occur at the same time-step.

### 7.4.3 Importance of 3D Models

The limited ability for 2D stick models to predict spatial response of 3D buildings has been shown for buildings with significant plan, mass, and stiffness irregularity, and with floor slabs that cannot be idealized as rigid. Cases 4 and 5 in Tables 7.3 and 7.5 highlight significant differences in peak responses at different locations within one floor level. Similarly, Tables 7.4 and 7.6 show that even for models with limited or no structural irregularity (Cases 0 and 1), significant differences in peak response at different locations within a floor level can occur when slab flexibility is considered. Unfortunately for simplified models, only select buildings can, according to modern standards (e.g., ASCE 7, 2010), idealize rigid slab behavior. It is also uncommon for NPP auxiliary buildings to not have plan, mass, or stiffness irregularity. Because of these details, the importance of 3D models to predict overall dynamic behavior of auxiliary buildings cannot be understated.

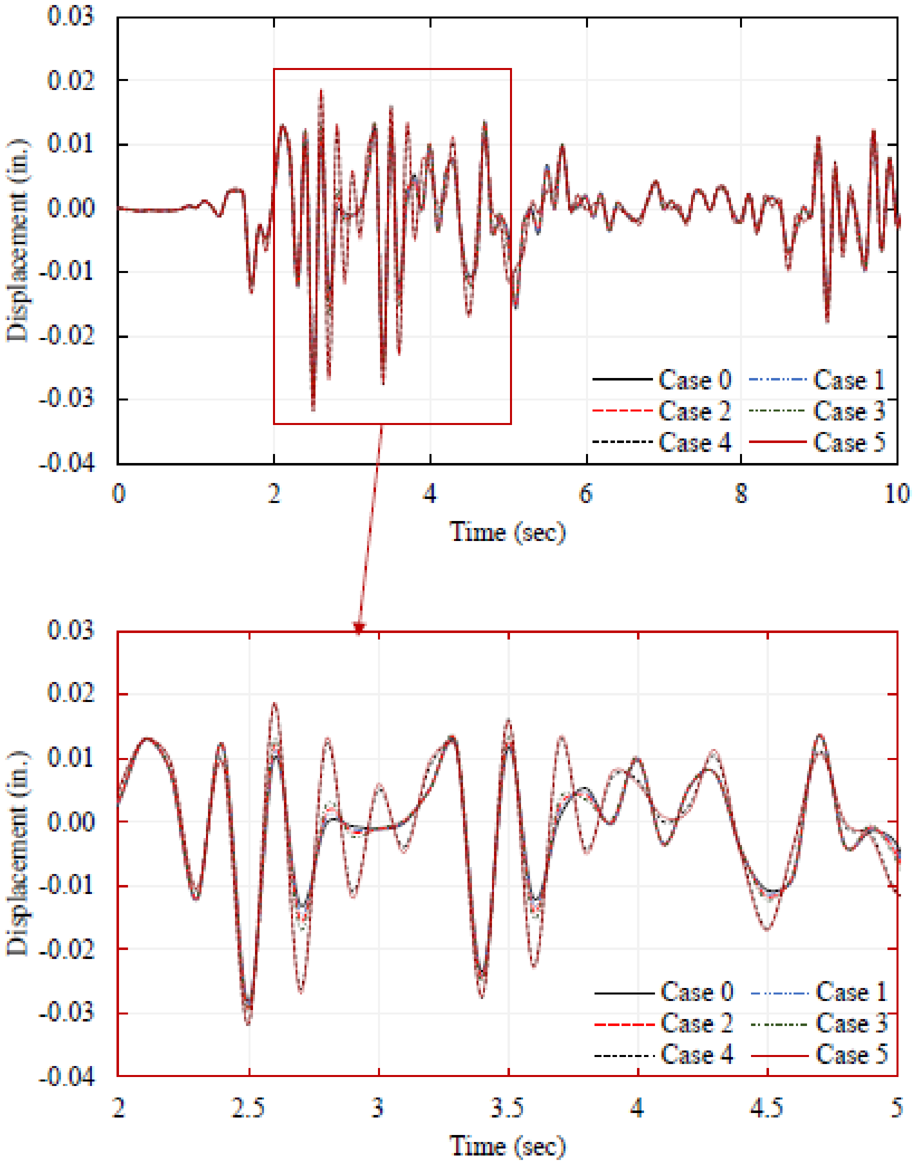

Figure 7.1 Displacement response history at third floor of 2D rigid slab stick models

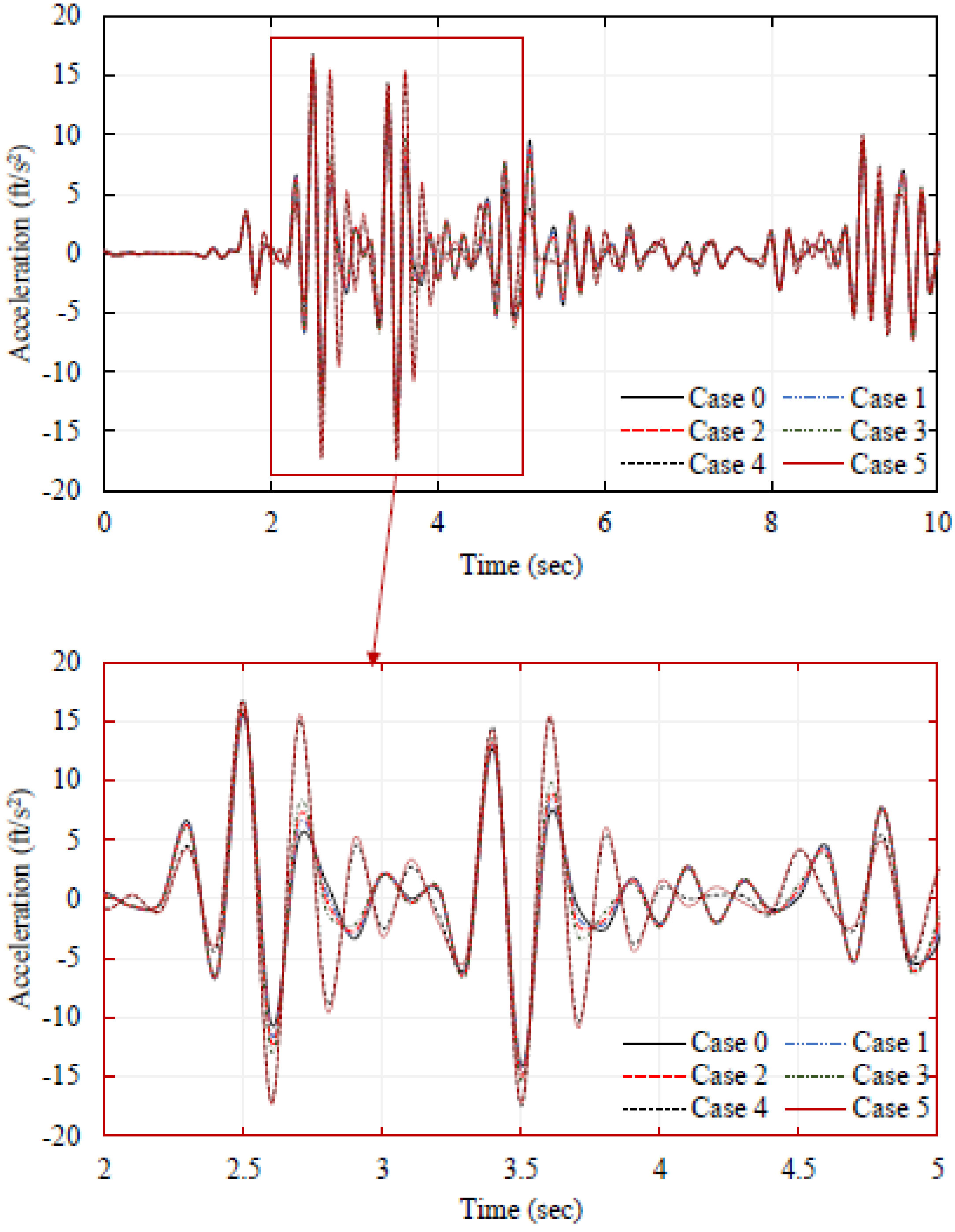

Figure 7.2 Acceleration response history at third floor of 2D rigid slab stick models

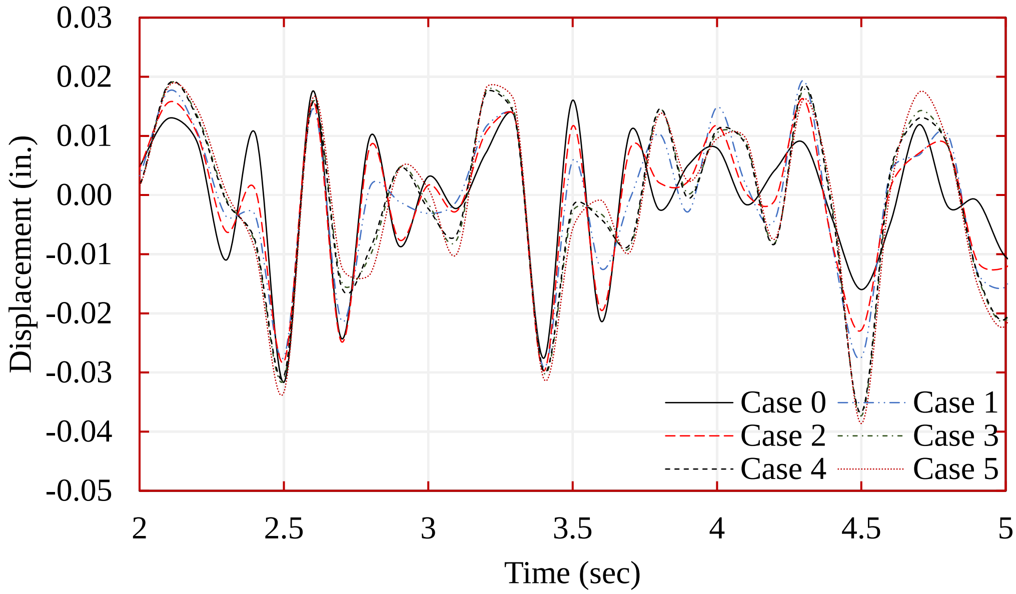

Figure 7.3 Displacement response history at third floor of 2D semi-rigid slab stick models

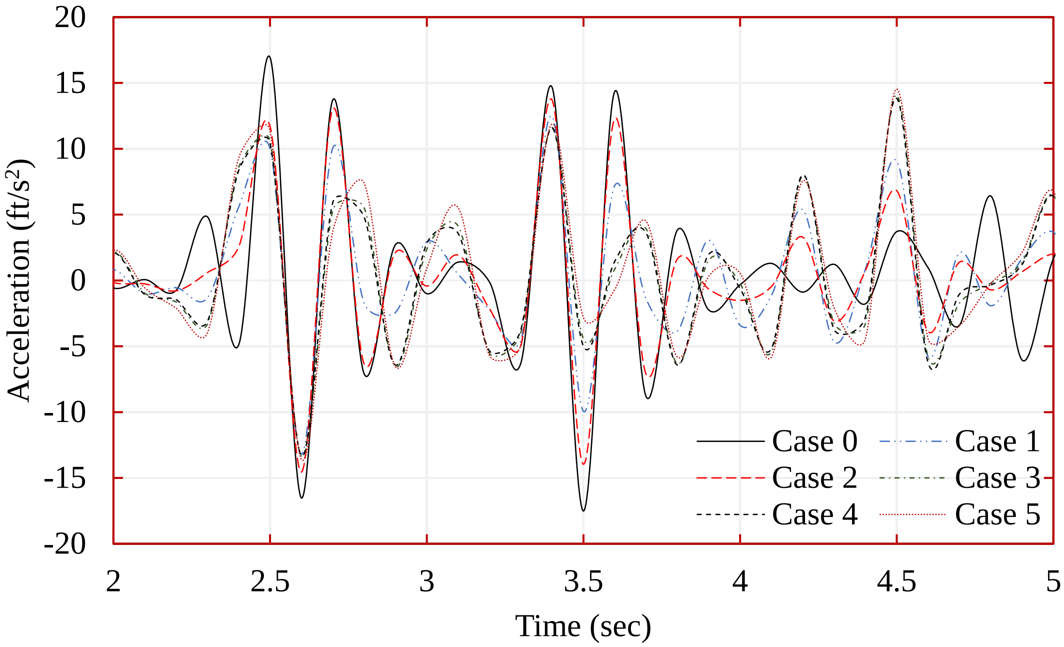

Figure 7.4 Acceleration response history at third floor of 2D semi-rigid slab stick models

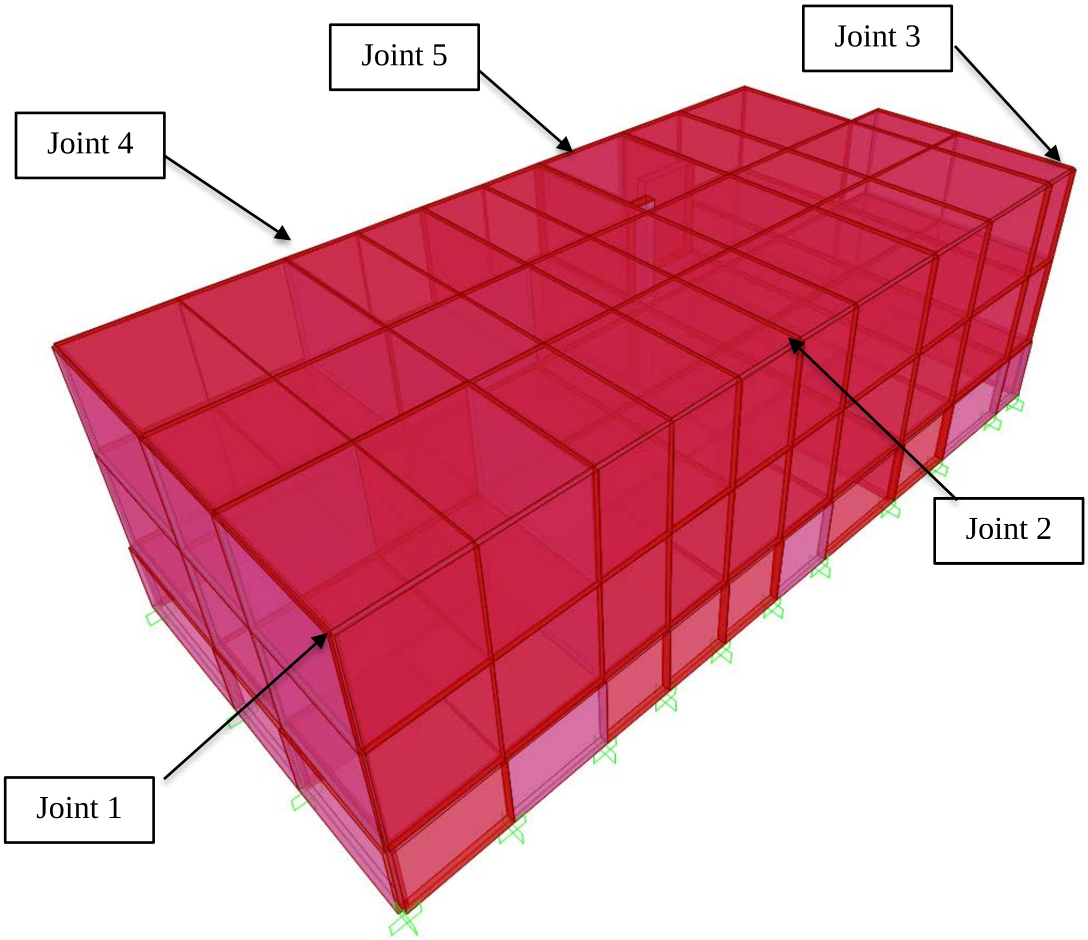

Figure 7.5 Five locations at 3rd floor level selected for time history analysis of 3D structural models

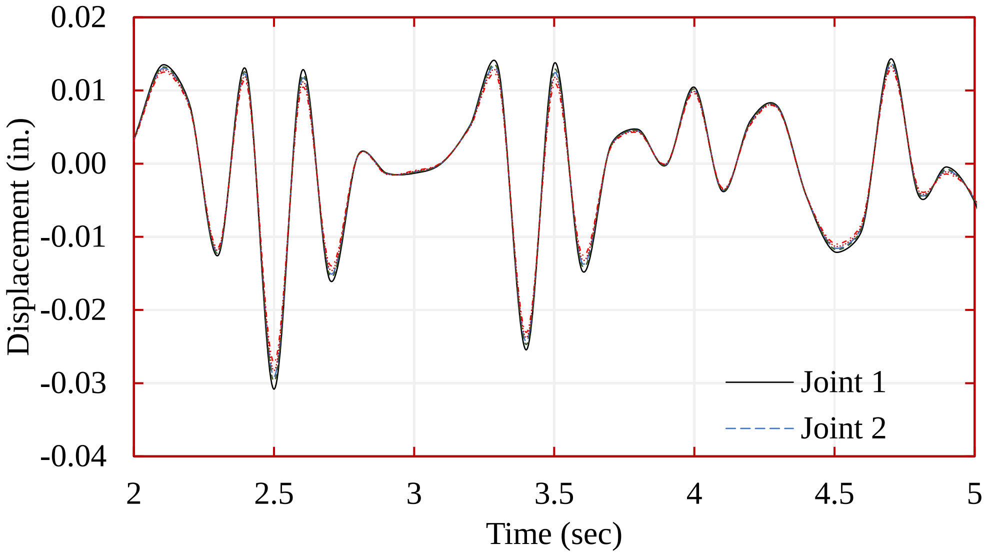

Figure 7.6 Displacement response history at third floor of 3D Case 1 rigid slab structural model at five separate locations

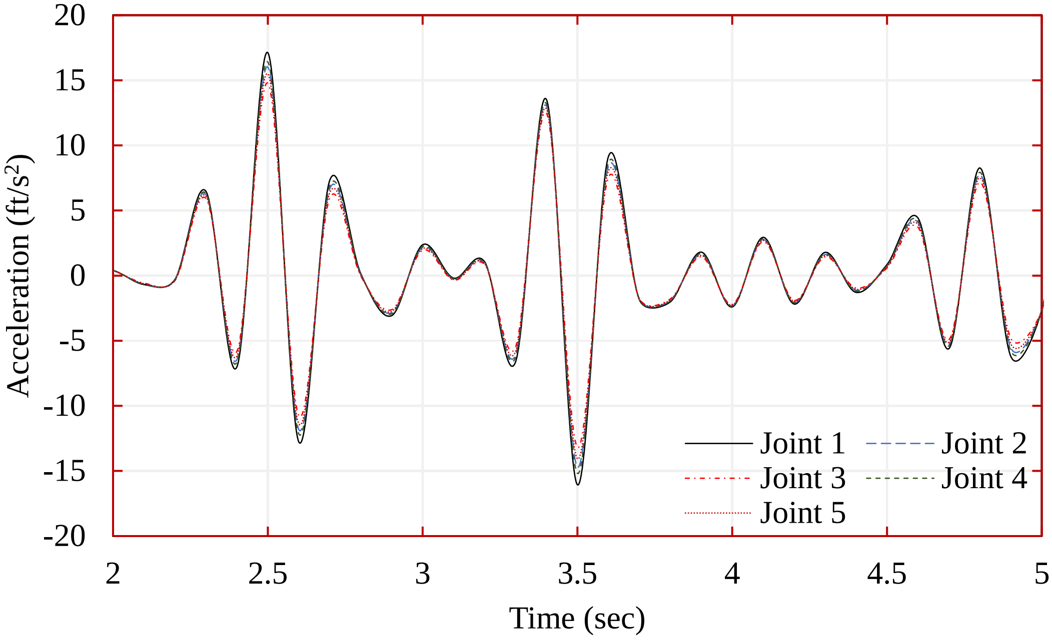

Figure 7.7 Acceleration response history at third floor of 3D Case 1 rigid slab structural model at five separate locations

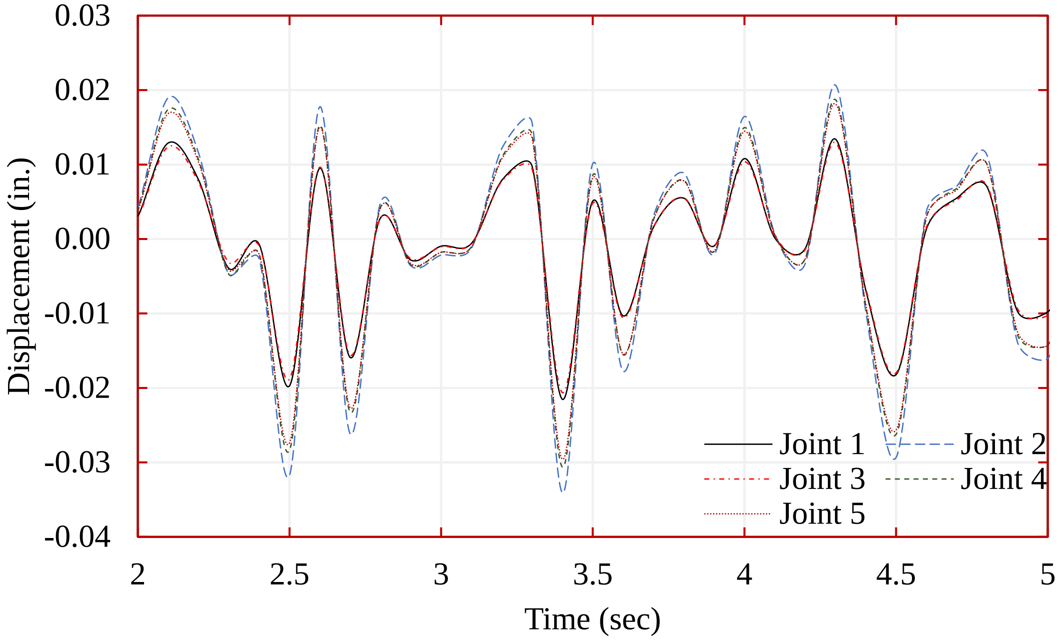

Figure 7.8 Displacement response history at third floor of 3D Case 1 semi-rigid slab structural model at five separate locations

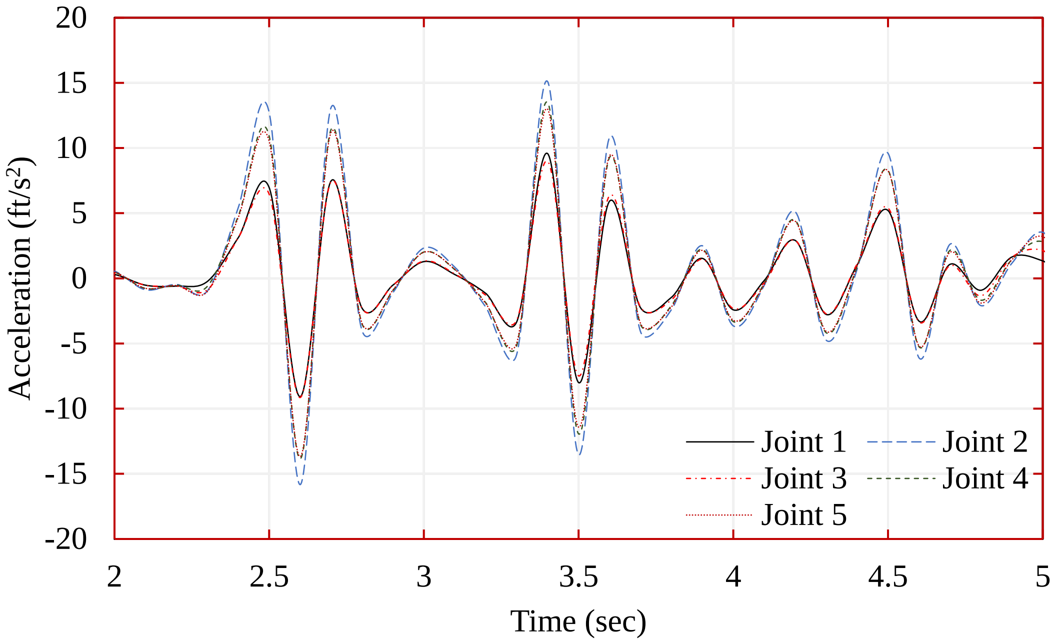

Figure 7.9 Acceleration response history at third floor of 3D Case 1 semi-rigid slab structural model at five separate locations

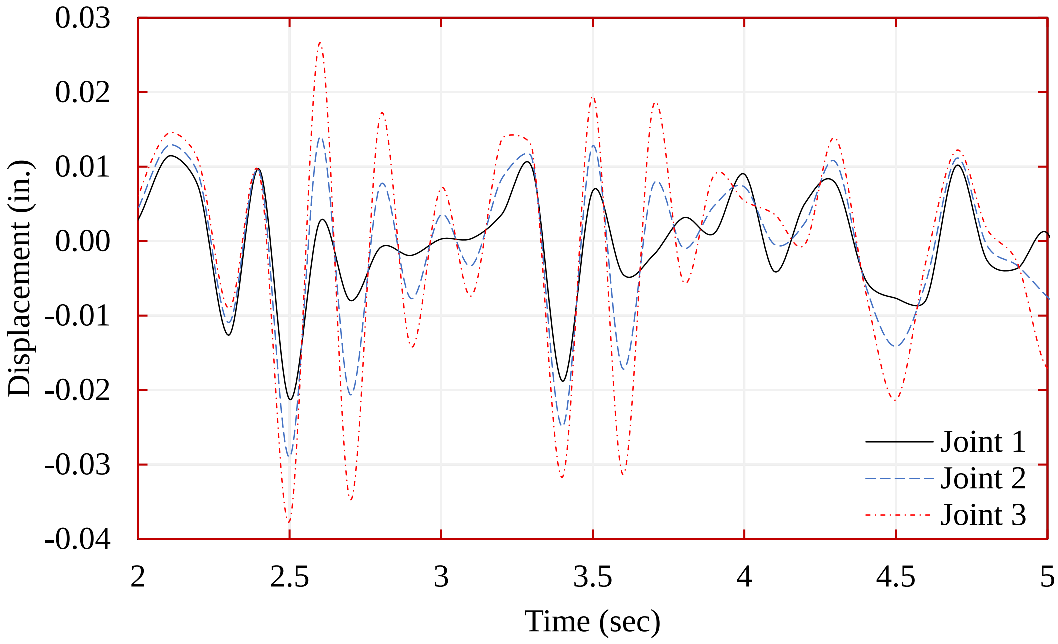

Figure 7.10 Displacement response history at third floor of 3D Case 5 rigid slab structural model at three separate locations

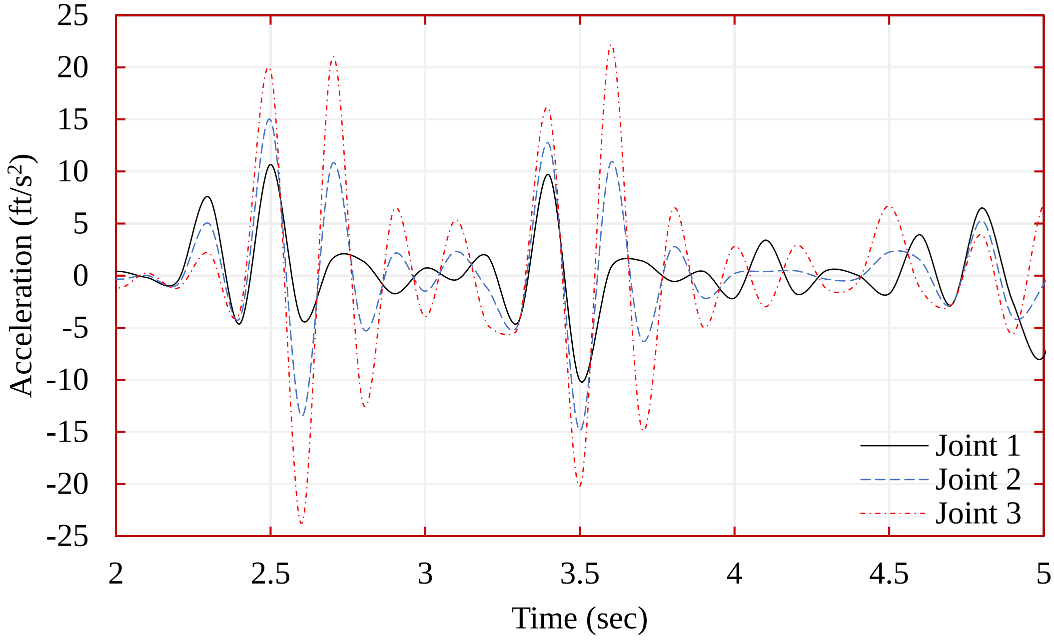

Figure 7.11 Acceleration response history at third floor of 3D Case 5 rigid slab structural model at three separate locations

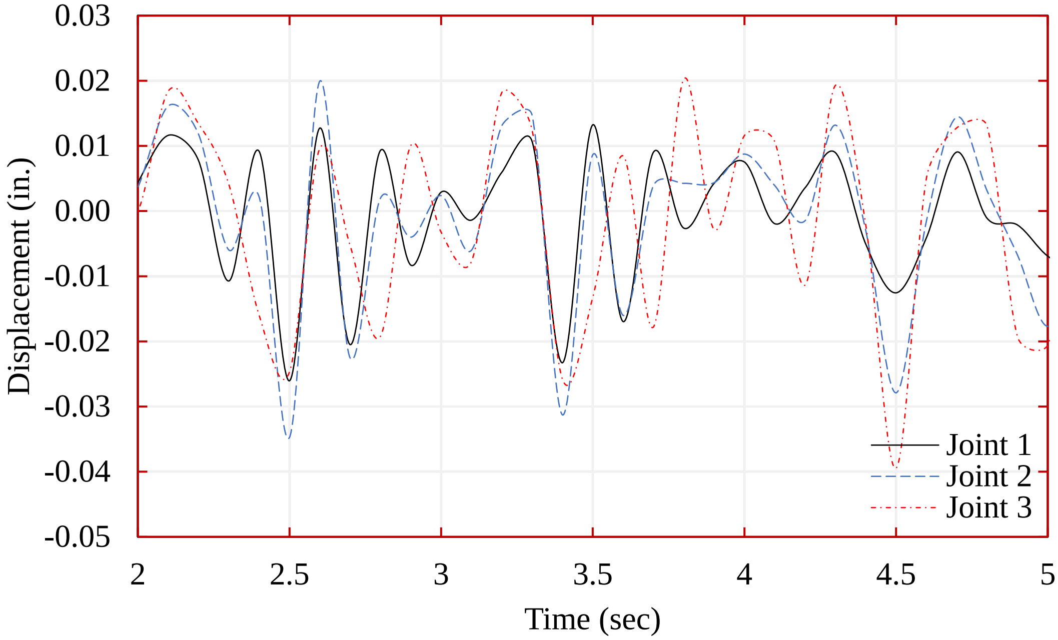

Figure 7.12 Displacement response history at third floor of 3D Case 5 semi-rigid slab structural model at three separate locations

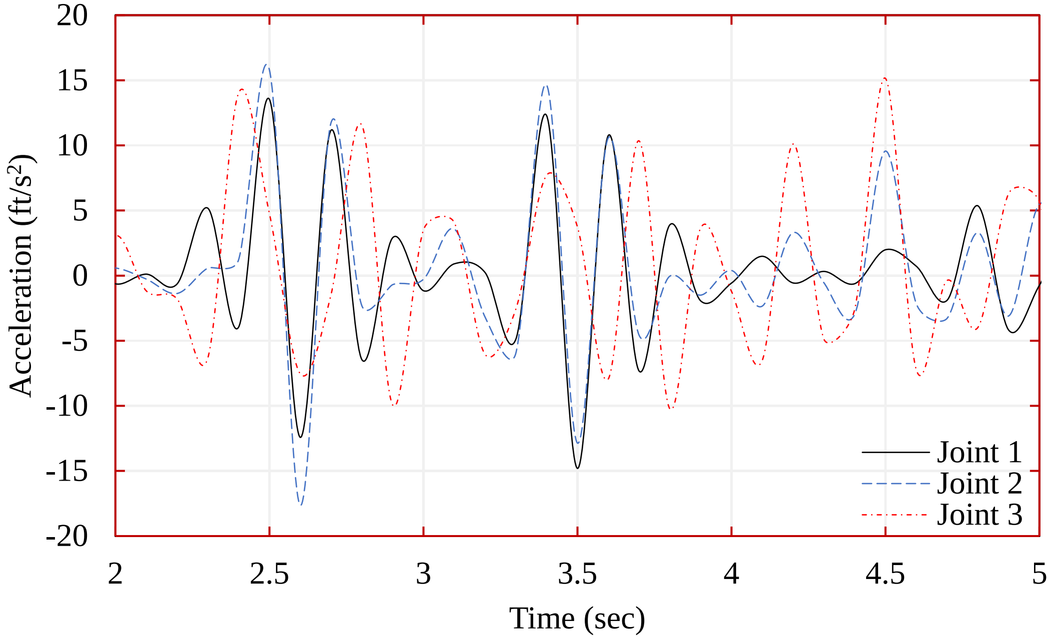

Figure 7.13 Acceleration response history at third floor of 3D Case 5 semi-rigid slab structural model at three separate locations

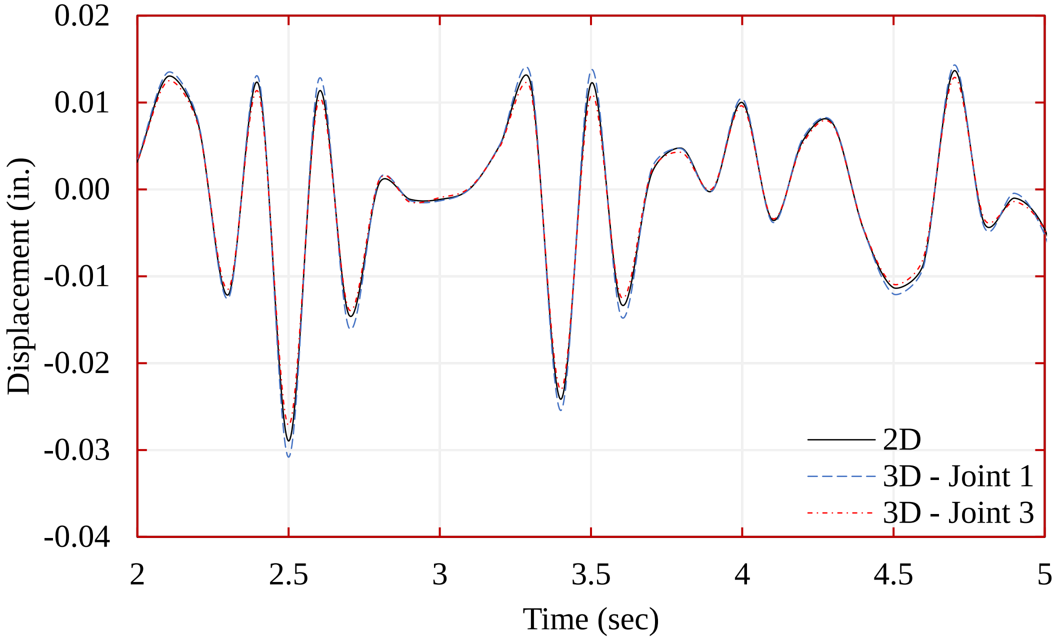

Figure 7.14 Displacement response history comparison of 2D and 3D rigid slab models at third floor for Case 1

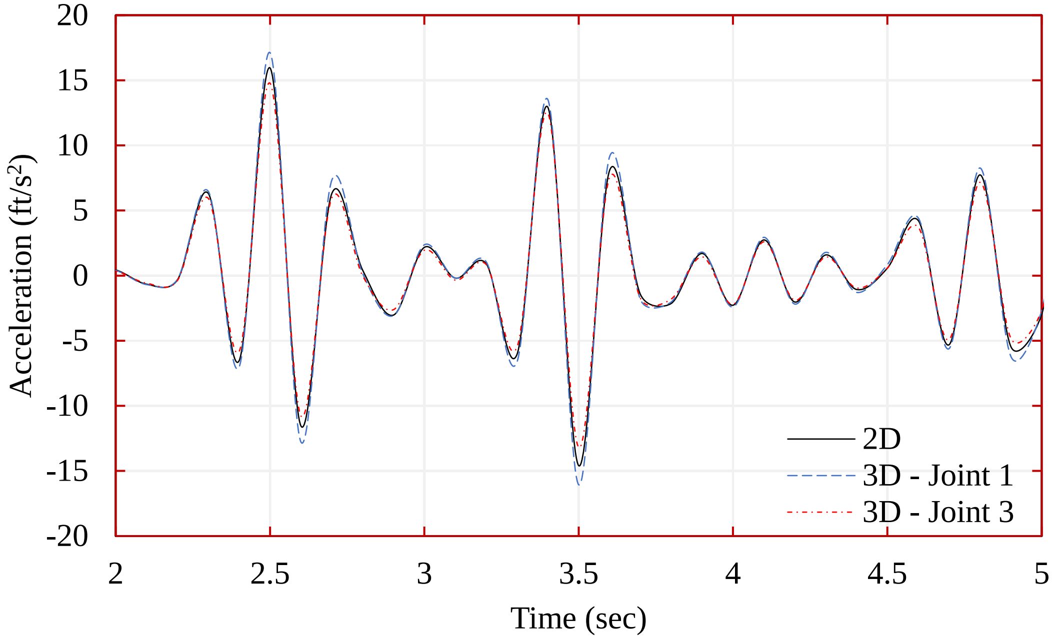

Figure 7.15 Acceleration response history comparison of 2D and 3D rigid slab models at third floor for Case 1

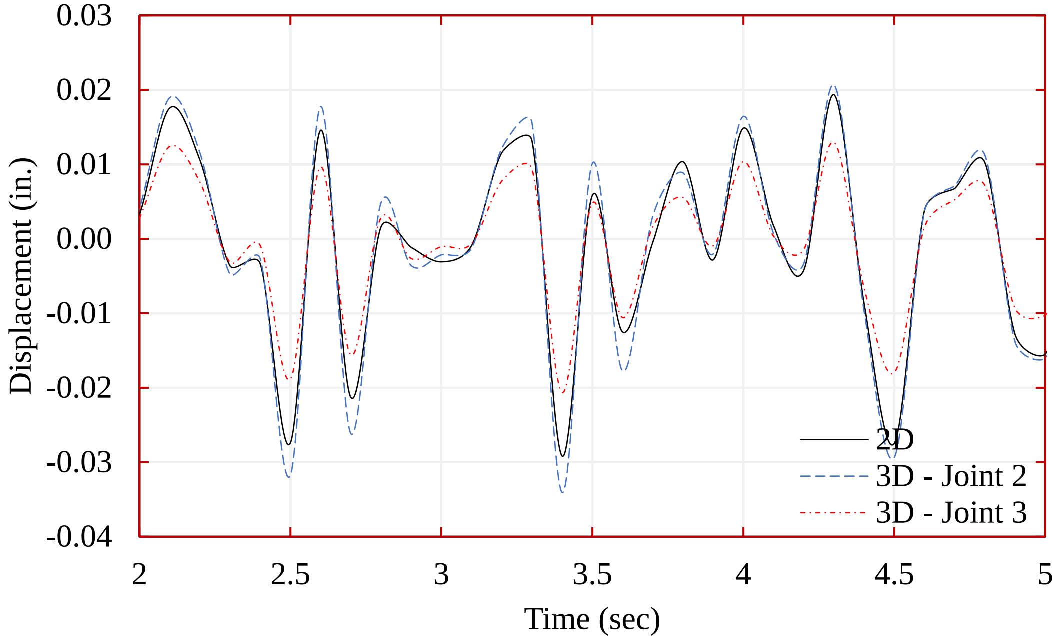

Figure 7.16 Displacement response history comparison of 2D and 3D semi-rigid slab models at third floor for Case 1

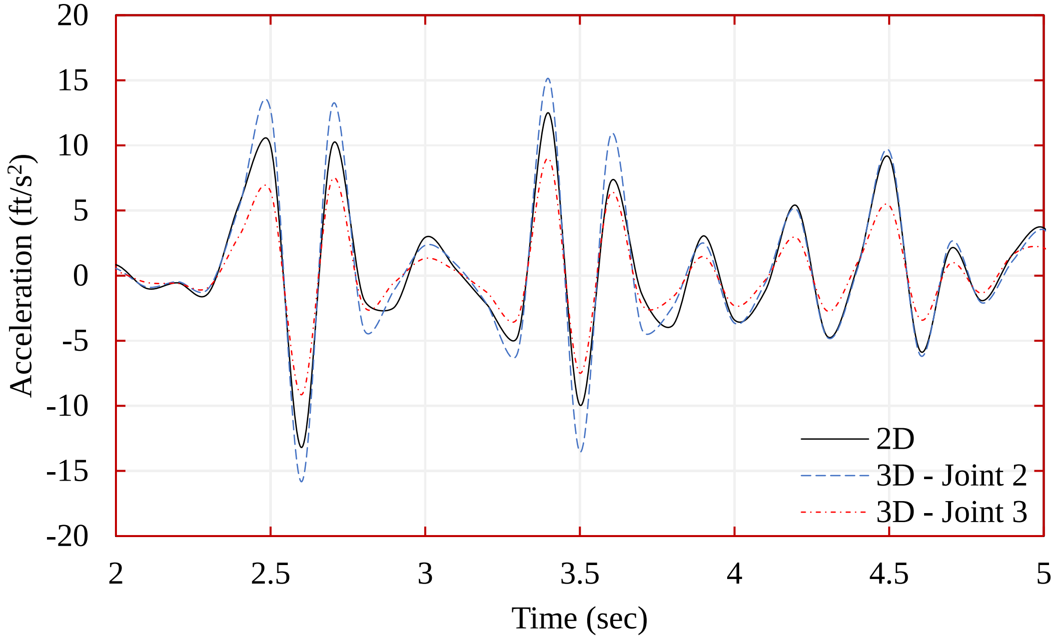

Figure 7.17 Acceleration response history comparison of 2D and 3D semi-rigid slab models at third floor for Case 1

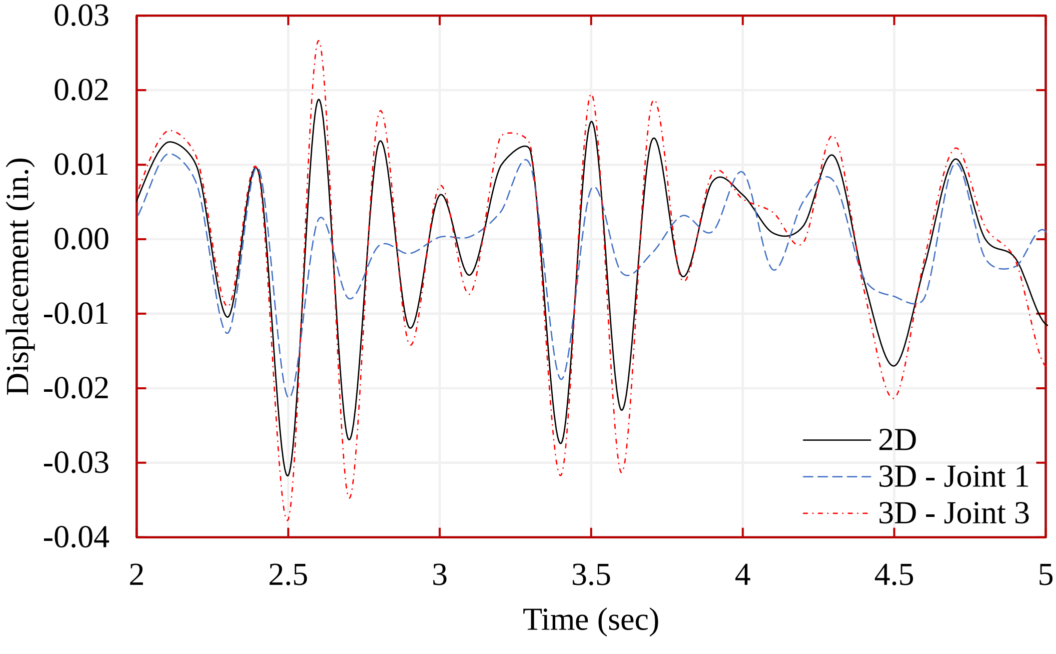

Figure 7.18 Displacement response history comparison of 2D and 3D rigid slab models at third floor for Case 5

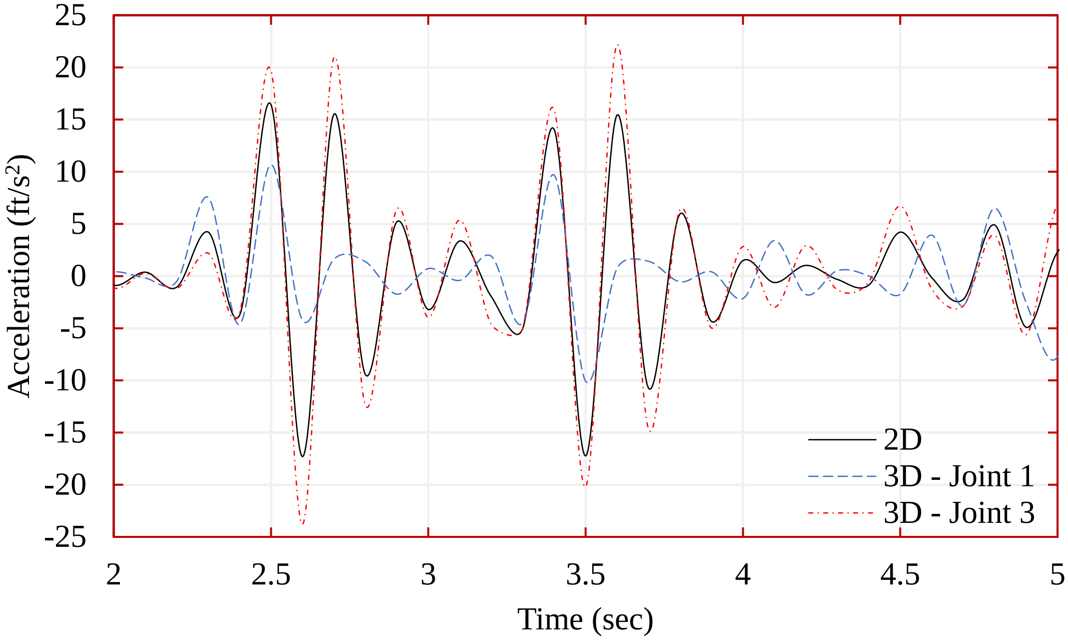

Figure 7.19 Acceleration response history comparison of 2D and 3D rigid slab models at third floor for Case 5

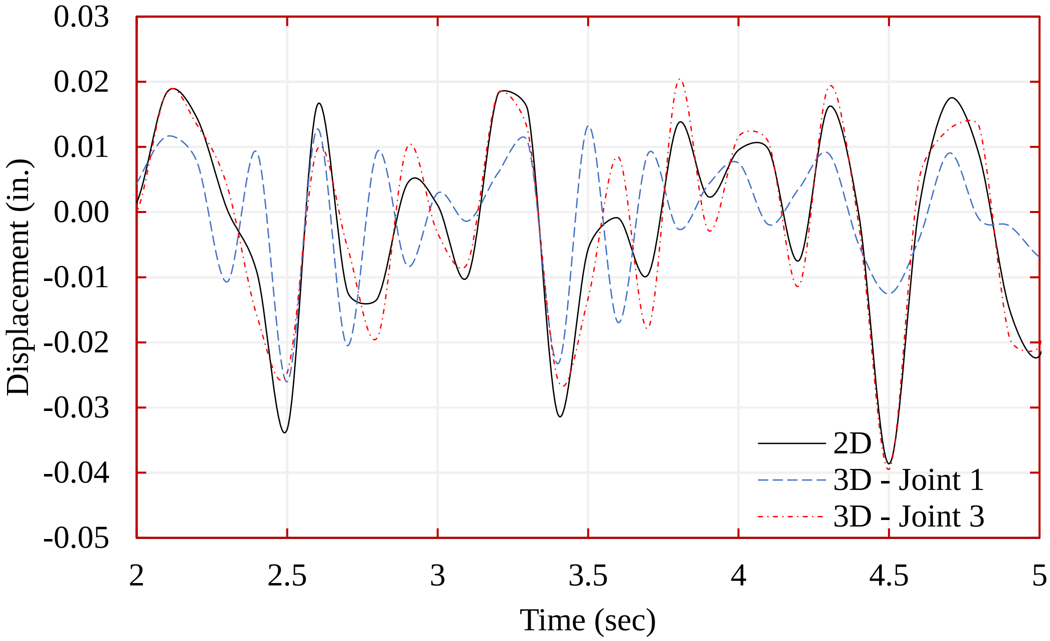

Figure 7.20 Displacement response history comparison of 2D and 3D semi-rigid slab models at third floor for Case 5

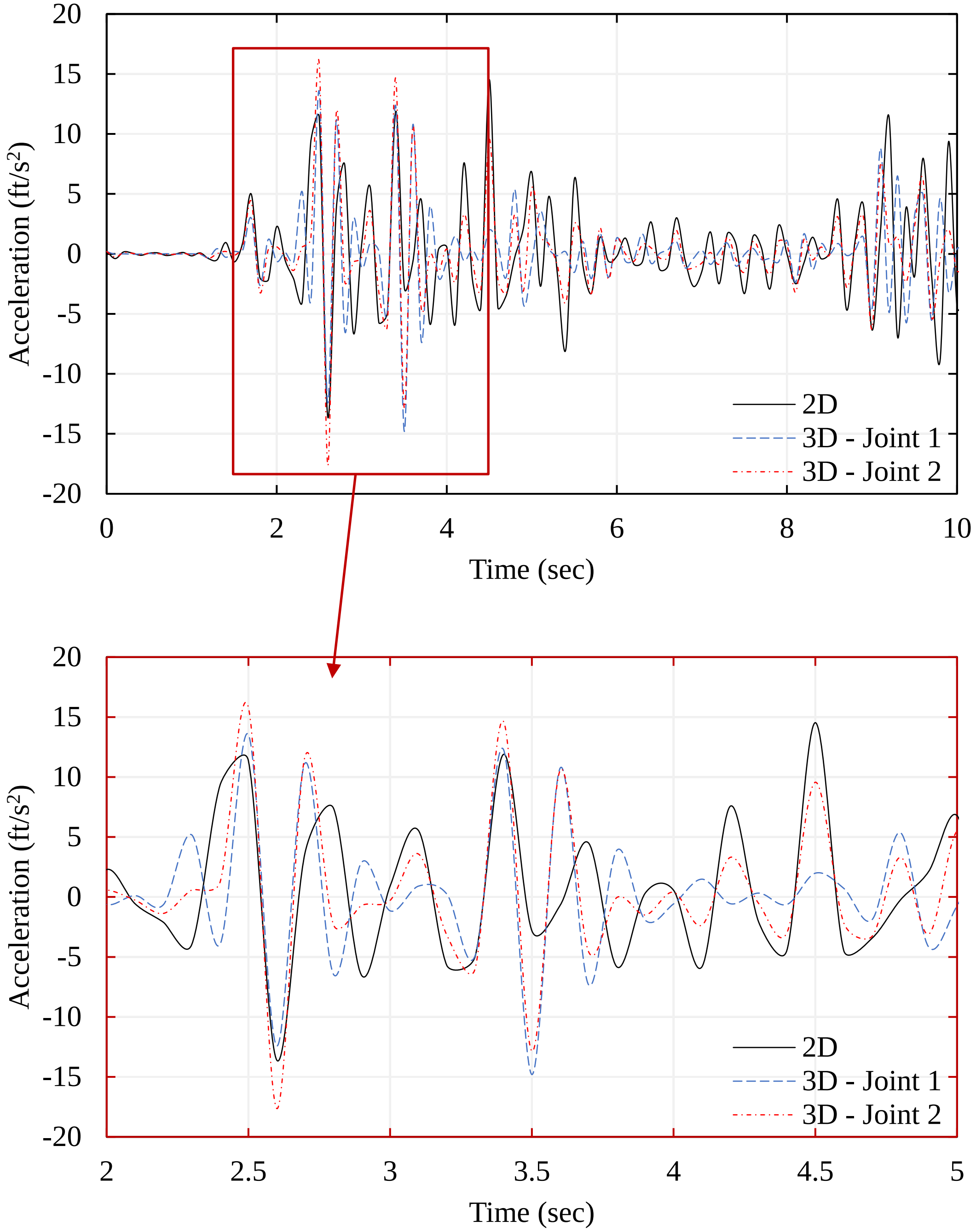

Figure 7.21 Acceleration response history comparison of 2D and 3D semi-rigid slab models at third floor for Case 5

# 8. CASE STUDY 2: SEISMICALLY INDUCED FLOODING AND INTEGRATED ANALYSIS

The Case 2 study examines a seismically-induced internal flood resulting in the flooding and failure of equipment providing critical safety functions, the need for human actions to restore those safety functions, modeling of common cause failures of critical components, and the impact of aftershocks on human performance within the framework of a dynamic event tree. Section 8.1 describes plant design features used in the study. Section 8.2 presents the general accident scenario being addressed involving seismically-induced flooding of safety equipment. Section 8.3 discusses the seismic hazard, the loads imposed and the fragility of the safety systems affected. Section 8.4 describes the recovery actions taken, which introduce the need for a dynamic approach to assessing the associated risk. Section 8.5 describes the aftershock model that has been developed and its impact in delaying recovery actions. A seismically-induced failure of condensate storage tanks (CSTs) leads to failure of a source of feed-water to the steam generators and to failure of high pressure injection (HPI) pumps, as described in Section 8.6. Sections 8.7 and 8.8, respectively, describe the dynamic model developed for the study and the results of analyses. Section 8.9 presents the conclusions.

## 8.1 Plant Design Features

For this study, the power plant under consideration is a large four-loop pressurized water reactor (PWR). The assumed plant design features do not represent a specific nuclear power plant or design characteristics of a specific reactor vendor. The example was developed to demonstrate some of the dynamic aspects of seismic events and is not intended to imply that a vulnerability exists in plants that have the characteristics of the scenario analyzed. The plant has two trains of diverse auxiliary feed-water (AFW) systems for which water is supplied from redundant CSTs. The CSTs are located in a building adjacent to the auxiliary building (see Figure 8.1). In the basement of the auxiliary building there are two rooms containing HPI pumps. A single charging pump is located in Room 1 and two safety injection pumps are located in Room 2. The rooms are separated by a fire door. Two primary system pilot operated relief valves (PORV) are actuated through equipment located in cabinets on the first floor of the building. In the event of loss of feed-water and charging capability, the operators must open the PORVs and implement feed and bleed

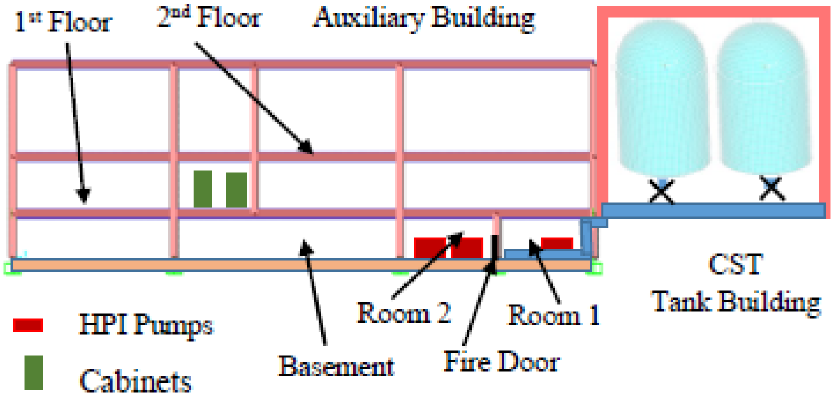

Figure 8.1 Seismically-induced Flooding Scenario of HPI Pump Rooms

operations with the HPI safety injection pumps. FLEX[63] equipment (backup equipment provided post-Fukushima) is located on site in a protected shed (not shown in Figure 1), which can provide an emergency source of AFW. It can be moved to the location of a pre-existing interface with the feed-water system and connected. The source of water available to the FLEX system is essentially infinite.

### 8.2 Accident Scenario

In the scenario examined, a seismic event leads to failure of one or both of the CSTs. Failure of both CSTs would result in the loss of the water source for AFW and ability to remove heat from the primary system of the PWR. A flow path exists from the CST building to the auxiliary building, as illustrated in Figure 8.1, such that the basement rooms of the building can be flooded. If the water level in a room exceeds two feet in height it is assumed that the pumps in that room will fail to operate. The door between basement Rooms 1 and 2 would fail when the water level in the first room reaches the 5-foot level. For this study, it is assumed that loss of the charging pump in Room 1 is unrecoverable. However, when Room 2 dries out, there is a possibility that the HPI function is recoverable. Table 8.1 identifies the performance characteristics of the safety related systems.

Table 8.1 Safety System Characteristics

| Components | Characteristics | Activation Set Point |
|---|---|---|
| PORV (2) | Open<br>Close | 16 MPa<br>15.5 MPa |
| HPI (2) | Shutoff Head<br>Maximum flow | 10 MPa<br>37.4 kg/s |
| AFW | Minimum flow | 450 kg/s |
| Low Pressure Injection | Maximum. pressure<br>Maximum flow | 2 MPa<br>382 kg/s |

Table 8.2 identifies the timing of events for a case based on MELCOR[64] analyses in which neither feed-water nor safety injection capability are recovered. Without cooling through the steam generators, the primary system pressure increases to the level of the relief valves (PORVs and safety relief valves) resulting in a rapid loss of primary system inventory with the cycling of relief valves. Gap release refers to failure of fuel pins resulting in a release of radionuclides from the cladding gap. Thus, the operating staff only have less than approximately 12,400 seconds to recover auxiliary feed-water flow by installing and operating the FLEX equipment to prevent core damage and provide additional time for the recovery of the HPI function.

During the period of cycling of the relief valves, the potential exists for a relief valve to stick open. Under these conditions a stuck-open relief valve is assumed to lead to fuel damage. If AFW is restored with FLEX equipment, the pressure in the primary system would decrease and this rapid loss of inventory would stop. However, there are other leakage paths from the primary system,

---

[63] Nuclear Energy Institute. Diverse and flexible coping strategies (FLEX), implementation guide. NEI 12-06, Washington, D.C. (2012)

[64] Sandia National Laboratories, NUREG/CR-6119, “MELCOR Computer Code Manuals, Vol. 2: Reference Manuals,” Version 1.8.6, Sandia National Laboratories (2006)

such as through reactor coolant pump seals, that would eventually lead to core uncovering if HPI is not re-established. Because the consequences of core damage accidents at high primary system pressure are potentially more severe than at low pressure, at some point in time the operator will depressurize the reactor coolant system with the PORVs, if they are operable. Although this would lead to core damage if the HPI system is unavailable, operation of the low pressure emergency core cooling system would be likely to arrest core damage prior to melt-through of the lower head of the vessel. We have assumed a mission time of 24 hr, beyond which core damage is assumed.

Table 8.2. Timing of Events without Recovery of HPI or AFW

| **Event** | **Time (seconds)** |
|---|---|
| Loss of feed-water flow | 60 |
| Pressurizer relief tank rupture (100 psig) | 6,900 |
| First gap release | 12,400 |

Aftershocks are very likely to occur following a main shock. Depending on the scenario and the magnitude of the aftershock, the aftershock can result in additional damage to a structure or the failure of safety-related equipment. For the purpose of this case study, we only examine the potential to delay recovery operations for aftershocks greater than 10% of the acceleration of the main shock.

## 8.3. Magnitude and Frequency of Seismic Loads

The seismic hazard for this study is based on an example provided by Ravindra.[65] The core damage frequency is evaluated at three seismic return frequencies: 3E-5 $yr^{-1}$, 1E-5 $yr^{-1}$ and 1E-6 $yr^{-1}$. Because the design basis earthquake is established at a return period of 1E-4 $yr^{-1}$and the design requirements assure a high confidence of a low probability of failure, the conditional probability of core damage at the design level is small. For each plant site, seismic hazard curves are developed that provide a family of curves (each curve representing a vibrational frequency) describing the relationship between peak acceleration and return period. The primary vibrational mode of the CSTs is assessed to be approximately 5 Hz. Figure 8.2 shows the 5 Hz seismic hazard curve describing the relationship between return period and the peak acceleration at a vibrational frequency of 5 Hz.

The failure mode of the CST is assumed to be the result of a failure of the bolts fastening the CST to the floor. There are two 8” diameter feed-water lines exiting the bottom of each CST. In Figure 8.1 one of each of the two pipes is indicated at the bottom of the CST with an X describing severance of the line. The load imposed on the piping associated with motion of the tank results in failure of one or more of the lines. Equal probability is assigned to the leak size associated with 0.5 $A_p$, 1 $A_p$, 1.5 $A_p$ and 2 $A_p$, where $A_p$ is the cross sectional area of a feed-water line. The median

---

[65] M. K. Ravindra, “Session III. SPRA Methodology Seismic Fragility Analysis,” *Proceeding of Post-Symposium Seminar: Seismic PRA: Post-Fukushima Implementation*, North Carolina (2014)

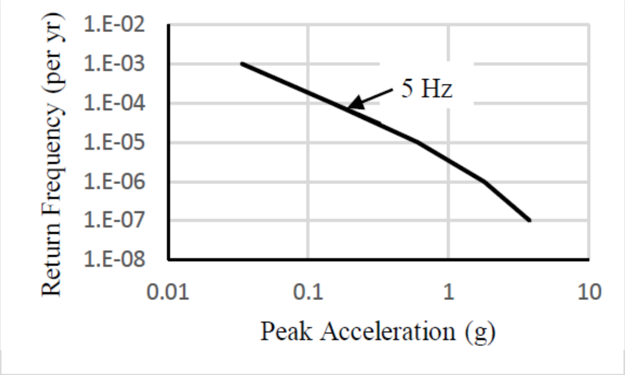

Figure 8.2. Peak Acceleration versus Return Frequency at Vibrational Frequency of 5 Hz[4]

acceleration of $A_m$=1.0g for failure of the CST, log normal standard deviation of β=0.4, and correlation coefficient ρ=0.5 between failure of the two tanks are characteristic values selected for the case study and are not based on analysis. Table 8.3 shows the 5 Hz accelerations associated with the design basis acceleration and the three return frequencies analyzed, the probability of failure of one of the tanks (Event A) and the probability of failure of both tanks (Event AB). The marginal probability of failure of a tank is obtained from the cumulative distribution function of the log normal distribution. The joint failure probability of two tanks was obtained by integrating the probability density function for a bivariate log normal distribution with correlation ρ. Within this project a finite element analysis of the buckling failure of the tank wall as the result of sloshing has been developed but is not considered in this paper.

Table 8.3. Spectral Accelerations and Failure Probabilities for CST Failure by Pipe Rupture ($A_m$=1, β=0.4, ρ=0.5)

| **Exceedance Frequency ($yr^{-1}$)** | **Spectral Acceleration (5 Hz)** | **$P_r$ (A)** | **$P_r$ (AB)** |
|---|---|---|---|
| 1E-4 | 0.17 | 4.7E-6 | Negligible |
| 3E-5 | 0.32 | 2.2E-3 | 1.6E-4 |
| 1E-5 | 0.6 | 0.10 | 3.3E-2 |
| 1E-6 | 1.8 | 0.93 | 0.88 |

Table 8.4 provides accelerations and failure probabilities for electrical cabinets containing control equipment for the remote operation of the PORVs. Inability to operate either PORV would defeat feed and bleed. A low value for $A_m$ and a high value for β, within the range of typical values[74] for equipment, were selected to represent potentially vulnerable equipment. A value of ρ=0.5 enables the effect of correlation to be demonstrated. In general practice, the value for $A_m$ is based on shaker table tests and the values for β and ρ are based on expert judgment. The acceleration for the electrical cabinets which are located on the first floor is multiplied by a factor of 1.5 to account for the higher acceleration experienced on the first floor relative to the ground acceleration, based on the results of a stick model of the auxiliary building. For full correlation between the response of the two cabinets, the joint failure probability would be equal to $P_r$(A). For fully uncorrelated response the joint failure probability would have been the product of the individual probabilities as shown in the last column of the table.

Table 8.4. Spectral Accelerations and Failure Probabilities PORV Control Cabinets ($A_m$=1, $\beta$=0.6894, $\rho$=0.5)

| Exceedance Frequency (yr$^{-1}$) | Spectral Acceleration (First Floor) | $P_r$(A) | $P_r$ (AB) | $P_r$ (A)x $P_r$ (B) |
|---|---|---|---|---|
| 1E-4 | 0.26 | .025 | 0.0047 | 6.3E-4 |
| 3E-5 | 0.48 | 0.14 | 0.055 | 0.0030 |
| 1E-5 | 0.9 | 0.44 | 0.28 | 0.078 |
| 1E-6 | 2.7 | 0.93 | 0.87 | 0.76 |

## 8.4 Recovery Actions

Three time critical recovery actions are considered in this study, recovery of operation of the PORVs, recovery of AFW flow by means of FLEX equipment, and recovery of HPI function after the room is dry. In order to support the modeling of these recovery actions, in practice it would be necessary to perform simulated recovery actions while attempting to include the additional stresses or barriers associated with an actual seismic event. For this case study, each recovery action was considered and an "expert" assessment was made of the probability of system recovery as a function of time. These estimates were then used as a basis for fitting a Weibull distribution to the probability of recovery as a function of time to obtain a scale factor $\lambda$ and shape factor $k$.

For the recovery of AFW by use of the FLEX equipment, it was assumed that at least 1 hour was required to move the equipment from its storage location and make the necessary connections. After 1 hour, recovery is represented by a Weibull distribution with parameters $\lambda = 1.28$ and $k = 1$. The recovery probability as a function of time is illustrated in Table 8.5. For the recovery of HPI, it was assumed that after the water level had completely receded through floor drains (See Section 8.6) that the HPI equipment could be restarted. A Weibull distribution was obtained with the values $\lambda = 1.5$ and $k = 0.85$. Recovery times are relative to the time $T_{dry}$, which is the time in the accident at which the HPI room becomes dry. For recovery of PORVs, it is assumed that the electrical cabinets containing the control logic to open the PORVs has failed but that a cabinet can be accessed by operating staff and that a signal can be imposed to operate the valves within 30

Table 8.5. Recovery Probabilities

| T-T0 (hr) | FLEX T0=0 | HPI T0=$T_{dry}$ | PORV T0=$T_{demand}$ |
|---|---|---|---|
| 0 | 0 | 0 | 0 |
| 1 | 0 | 0.51 | 0.19 |
| 2 | 0.54 | 0.72 | 0.75 |
| 3 | 0.79 | 0.84 | 0.97 |
| 4 | 0.90 | 0.90 | 1 |
| 5 | 0.96 | 0.94 | 1 |
| 6 | 0.98 | 0.96 | 1 |
| 7 | 0.99 | 0.99 | 1 |
| 8 | 0.99 | 0.98 | 1 |

minutes. Some time is then required to diagnose the problem and to obtain some means of imposing an appropriate signal to open the valves. This time period is represented by a Weibull distribution with λ =1.24 and *k*=1.73 following the first 30 minutes. However, the plant staff do not become aware that the PORVs are inoperable until the first attempt to open them remotely fails. $T_{demand}$ equals the time at which HPI is recovered, after which the operator would attempt to operate the PORVs.

During the time period prior to recovery of auxiliary feed-water by means of the FLEX equipment, the primary system PORVs will cycle to relieve pressure. Based on MELCOR analyses, during the first three hours the cycle rate is approximately 45 per hour and subsequently approximately 26 per hour. A stuck-oven relief valve failure is assessed to have the probability of 6E-3 per cycle.[66] A stuck-open relief valve prior to recovery of HPI was assumed to result in core damage based on MELCOR analyses.

### 8.5 Aftershock Analysis

A model similar to the model derived by Reasenberg[67] [68] to predict the probability of aftershocks as a function of time and the magnitude of the main shock has been developed in which the size of the earthquake is measured in peak ground acceleration. The model is based on two well-known earthquake "laws": the Omori Law,[69] describing the decrease in the rate of aftershocks as a function of time after the initial earthquake and the Gutenberg-Richter[76] distribution describing the frequency distribution of aftershocks as a function of earthquake magnitude.

The relationship between earthquake magnitude, Mercalli Magnitude Index (*M*), and the ground acceleration typically is described by the form of Equation 8.1 in which the values of the parameters are site dependent.[10]

$$M = \alpha \cdot \log(PGA) + \beta \tag{8.1}$$

Typical parameter values[70] for a plant in California are α = 2.3, β = 0.92. The mean number of shocks Λ in a given time interval is calculated from

$$\Lambda = \int_S^T \lambda(t)dt = \left(10^{a}(\frac{PGA_m}{PA})^{2.3b}\right)\left(\frac{1}{1-p}\right)\left[(T+c)^{1-p} - (S+c)^{1-p]}\right] \tag{8.2}$$

where λ(t) is the probability of one or more aftershocks per unit time. Λ is the mean number of aftershocks of magnitude PGA in the interval beginning with time S and ending with time T for a main shock acceleration of $PGA_m$. The parameters p and c in Equation 8.2 are empirically determined characteristics of a site.

---

[66] K. Metzroth, "A Comparison of Dynamic and Classical Event Tree Analysis for Nuclear Power Plant Probabilistic Safety/Risk Assessment," Dissertation, The Ohio State University (2011)

[67] P. A. Reasenberg and L. M. Jones, "Earthquake Hazard after a Mainshock in California," *Science*, 243, 1173-1176 (1989)

[68] P. A. Reasenberg and L. M. Jones, "Earthquake Aftershocks: Update," *Science*, Vol. 265, pp 1251-1252, 1994.

[69] T. Utsu, Y. Ogata and R. S. Matsura, "The Centenary of the Omori Formula for a Decay Law of Aftershock Activity," *J. Phys. Earth*, 43, 1-33 (1995)

[70] L. Linkimer, "Relationship between Peak Ground Acceleration and Modified Mercalli Intensity in Costa Rica," *Revista Geologica de America Central*, 38, 81-94, (2008)

There is some possibility that a shock occurring after the initial shock is larger than the initial shock. In this case the initial shock is referred to as a foreshock and the larger earthquake becomes the main shock. There is approximately a 5% probability of this occurring.[76] If structures respond to the main shock in an elastic manner, an aftershock is unlikely to result in additional structural damage. However, an aftershock similar in magnitude to the initial shock would be uncorrelated with the initial shock and could lead to additional probability of the failure of components. In this case study, consideration is only given to the human response aspects of an aftershock.

An aftershock greater than 10% of the main shock was assumed to result in a delay in completing recovery actions of 15 minutes as illustrated in Figure 8.3.

Figure 8.3. Delay Time Due to Aftershocks as a Function of Recovery Time Based on Equation (8.2)

### 8.6 Flooding Analysis

A Simplified Flooding Model (SFM) was developed in this project (see Section 11) to describe the flooding of compartments following a seismic event. The model is fast running to support the performance of dynamic uncertainty analyses. The model is in the process of being benchmarked against the FLUENT code.[71] In this case study the SFM is being used to examine flooding of the two HPI rooms in the basement of the auxiliary building (see Figure 8.1). The timing of failure associated with the flooding of HPI pumps and the subsequent dry out of the HPI rooms is determined in the analyses for different leak rates from failed piping from the CSTs. Tables 8.6 and 8.7 provide the volumes and flow paths in the flooding analysis. In Figure 8.1, the moat is a catch basin under the CSTs at the base of the CST building. The sump is located under the auxiliary building and receives water flowing through the floor drains in the auxiliary building. Table 8.8 provides the results of analyses performed for eight leak rates from the CSTs considered in the analyses.

Figure 8.4 illustrates the results for the case of a single tank failure (either tank) with a leak area associated with 2 $A_p$. In this analysis, the water level exceeds two feet at 385 seconds, which would result in failure of the charging pump. At 1,275 seconds the door between Rooms 5 and 6

---

[71] ANSYS, “ANSYS/FLUENT 12.0 User’s Guide,” www.ansys.com (April 2009)

fails and the high pressure safety injection pumps soon fail. At 4,840 seconds, the water level is effectively zero and actions could be taken to attempt to restart the safety injection pumps.

Table 8.6. Compartment Information

| Room | Name | Area ($m^2$) | Maximum Elevation (m) | Minimum Elevation (m) |
|---|---|---|---|---|
| 1 | Auxiliary CST | 45.6 | 6.23 | 0 |
| 2 | Main CST | 45.6 | 6.23 | 0 |
| 3 | CST Moat | 167.23 | 1.524 | 0 |
| 4 | Auxiliary Building | 278.71 | 4 | 0 |
| 5 | Auxiliary Basement Room 1 | 139.36 | 0 | -4 |
| 6 | Auxiliary Basement Room 2 | 139.36 | 0 | -4 |
| 7 | Auxiliary Sump | 278.71 | -4 | -10 |

Table 8.7. Flow Path Information

| Path | From/To | Area ($m^2$) | Diameter (m) | Length (m) | From/To Elevation (m) |
|---|---|---|---|---|---|
| 1 | 1/3 | 0.03 | 0.2 | 1 | 0/0 |
| 2 | 1/3 | 0.03 | 0.2 | 1 | 0/0 |
| 3 | 2/3 | 0.03 | 0.2 | 1 | 0/0 |
| 4 | 2/3 | 0.03 | 0.2 | 1 | 0/0 |
| 5 | 3/4 | 1 | 0.5 | 1.5 | 0/0 |
| 6 | 4/5 | 6 | 2.4 | 1 | 0/0 |
| 7 | 5/6 | 2.2 | 1.4 | 0.1 | -3.3/-3.3 |
| 8 | 5/7 | 0.005 | 0.08 | 1.5 | -4/-4 |
| 9 | 6/7 | 0.005 | 0.08 | 1.5 | -4/-4 |

Table 8.8. Results of Flow Analyses

| Flooding Scenario Number | CST Failure | Flow Area (Ap) | Time of HPI Failure | Time of Dryout |
|---|---|---|---|---|
| 1 | One | 0.5 | N/A | N/A |
| 2 | One | 1 | N/A | N/A |
| 3 | One | 1.5 | 2295 | 5285 |
| 4 | One | 2 | 1310 | 4840 |
| 5 | Two | 1 | 2335 | 9410 |
| 6 | Two | 2 | 985 | 8710 |

|  |  |  |  |  |
|---|---|---|---|---|
| 7 | Two | 3 | 640 | 8475 |
| 8 | Two | 4 | 470 | 8545 |

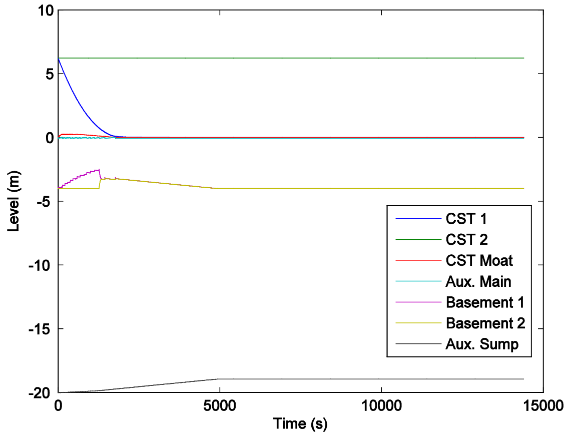

Figure 8.8. Water Levels in Flood Analysis

### 8.7 Event Tree Approach

Figure 8.5 illustrates a seismically-induced loss of offsite power event tree without recovery. As described in Section 8.4, probability distributions are developed that describe the probability of recovery of failed systems as a function of time. It is difficult to analyze recovery actions of this type within the framework of a fixed event tree. When the order of events on the tree can change

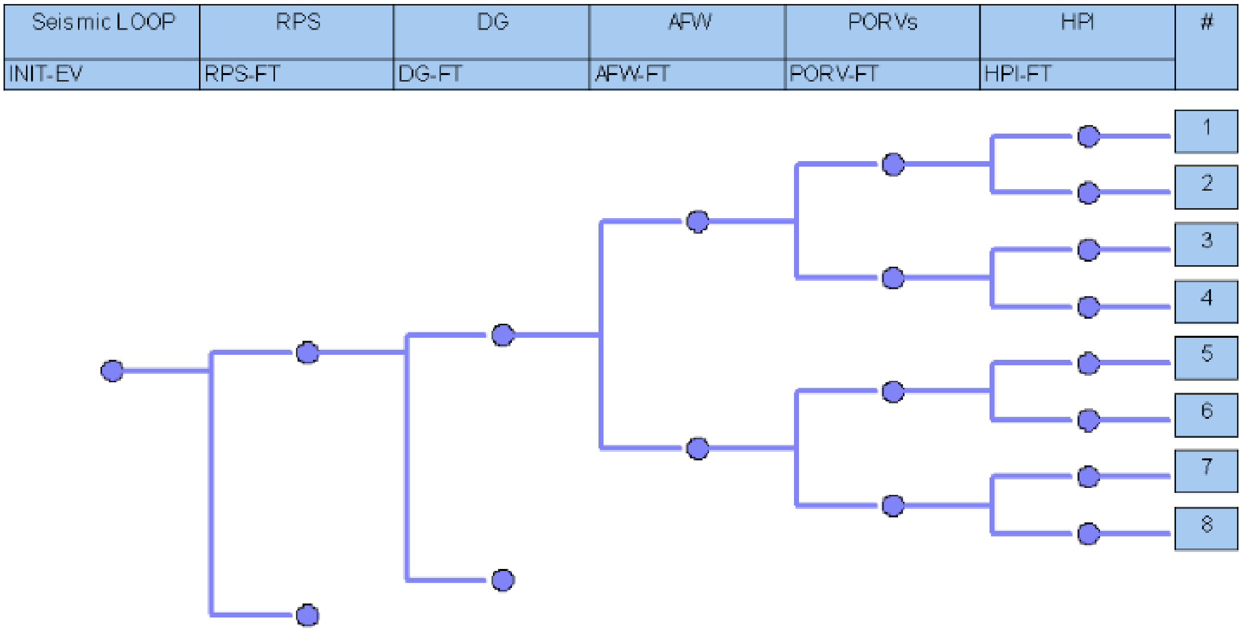

Figure 8.5. Seismic Event Tree

depending on the progression of the event, a dynamic event tree approach is more appropriate.[72] The alternative within a fixed event tree approach is to have multiple entries for events on a tree. For example, in NUREG-1150[73] the detailed Level 2 accident progression event trees addressed the potential for hydrogen combustion in the containment at multiple time periods in the accident scenario.

In this study, we have performed a limited dynamic event tree analysis. Calculations were performed with the MELCOR code[4] to establish criteria as to the conditions leading to core damage, depending on which systems had been failed and which systems had been recovered as a function of time.

System analysis fault trees from the internal events PRA provide the framework within which the seismic-induced failures are integrated. The existing front line and support system fault trees need to be modified to include seismic faults. The seismic-induced failures are included in the fault trees as basic events. These "fragility basic events" will then appear in the minimum cut-sets and thus indicate which combinations of seismic induced failures would lead to core damage. Passive components and structures which are not included in non-seismic PRA have been reviewed and additional basic events are added to the fault tree, such as door failure, which is not normally considered in an internal PRA but in this specific scenario can lead to flooding and failure of HPI Pumps 2 and 3 (the two HPI safety injection pumps in Room 2 of the auxiliary building) and can lead to core damage.

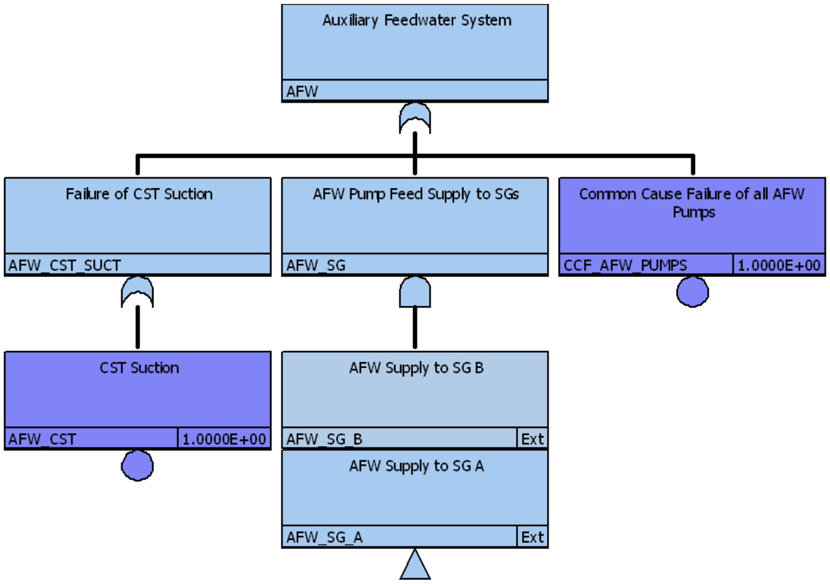

Figure 8.6. AFW Fault Tree without Seismic Events

---

[72] K. Metzroth, "A Comparison of Dynamic and Classical Event Tree Analysis for Nuclear Power Plant Probabilistic Safety/Risk Assessment," Dissertation, The Ohio State University (2011)

[73] US NRC, "Severe Accident Risks: An Assessment for Five U.S. Nuclear Power Plants," NUREG-1150, Washington, DC (December 1990)

The Level 1 fault tree of the AFW system in Figure 8.6 was created based on U.S. Nuclear Regulatory Commission's AFW system fault tree Design Class 2, which is the AFW system of Calvert Cliffs Unit 1.[74] This fault tree is modified to include the seismically-induced faults as shown in Figure 8.7. The AFW system fault tree top logic is revised to include seismic failure basic events. CST suction failure (basic event) is modified to become the union of random tank failure and seismic-induced CST suction failure.

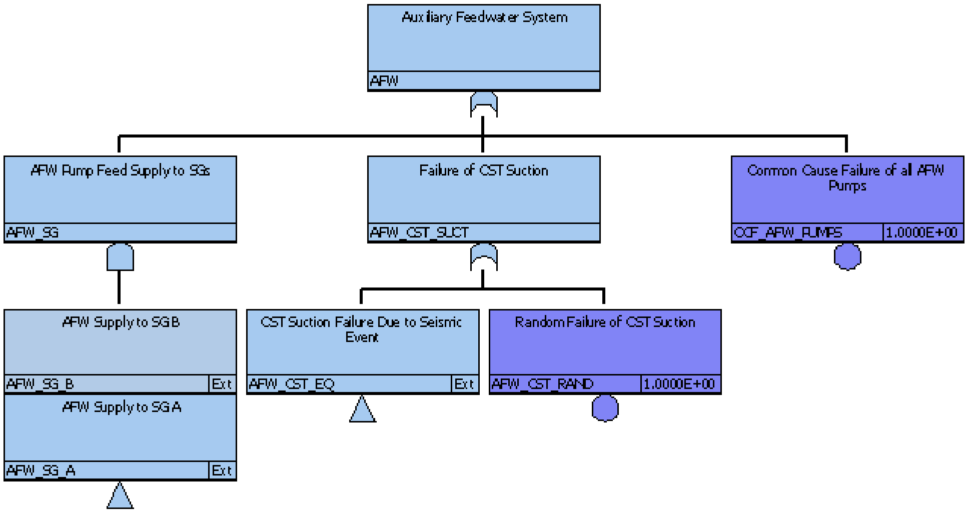

Figure 8.7. AFW Fault Tree Including Seismic Failure

The seismic subtree introduced into the AFW fault tree is shown in Figure 8.8. CST suction failure is the result of either outlet pipe failure or CST failure given the seismic event. Seismic event is represented as a house event in the model according to NRC's External Events Report[75] to denote a failure that is guaranteed to always occur for the given modeling conditions or is guaranteed to never occur for the given modeling conditions. The seismic subtrees are only activated when the seismic event is quantified and its flag is set to TRUE.

## 8.8 Dynamic Analysis of Core Damage Frequency

In this section, the dynamic SPRA analysis will be described including the common cause effects of flooding on system failure. Results will be presented for the quantification of core damage frequency. Typically, the SAPHIRE[14] code would be used to determine the associated severe fuel damage frequency. In this example, the only internal event included in the analysis was the random failure of one pathway for feed-water for scenarios in which only one of the CSTs is failed. Core damage frequencies for various branches on the event tree illustrated in Figure 8.5 were developed by determining conditional failure probabilities for combinations of component failure states from the dynamic analysis. The probability of core damage in these scenarios depends not only on the probability of failure of a component, such as HPI, but on the "timeliness" of the recovery action.

---

[74] US NRC "Risk Assessment of Operational Events-Handbook", Volume 2, External Events, Rev. 1.01 (2008)

[75] US NRC "Risk Assessment of Operational Events-Handbook", Volume 2- External Events, Rev. 1.01, (2008).

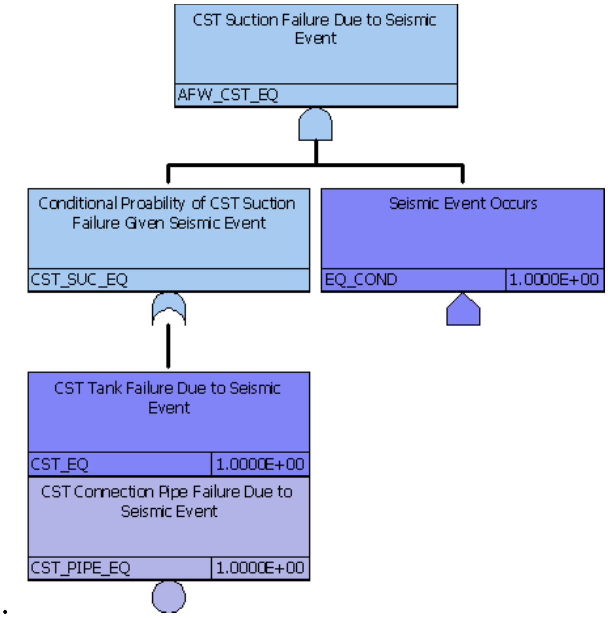

Figure 8.8. Subtree of CST Seismic-Induced Suction Failure

The dynamic analysis of the eight scenarios associated with different flooding rates (see Section 8.6) was performed with a MATLAB[76] model with Monte Carlo sampling from the recovery distributions (see Section 8.4 and Table 8.5) to determine conditional probabilities of core damage. Three return frequencies of seismic events were evaluated (3E-5 $yr^{-1}$, 1E-5 $yr^{-1}$ and 1E-6 $yr^{-1}$).

In the MATLAB analysis, random draws (100,000) were made from the recovery distributions for HPI, PORV operation, and feed-water (using FLEX equipment) to determine the relatives times of recovery for the different functions. Based on MELCOR analyses, rules were developed to determine whether a given state was associated with core damage or not:

1. If recovery of feed-water is delayed beyond 3.2 hr and HPI and PORV operability have not been previously restored, the scenario leads to core damage.
2. If recovery of feed-water is achieved prior to 3 hr or there has been no loss of feed-water, HPI and PORV operability can be delayed to up to 24 hr without core damage.
3. If HPI and PORV operability are not recovered by 24 hr, the scenario leads to core damage.

Although the probability of a stuck-open PORV was calculated during the time period prior to recovery of feed-water, that probability is not included in the following calculation of core damage frequency. Because of the simplified dynamic approach taken in this study, it was not possible to determine whether a core damage scenario associated with a stuck-open relief valve would have led to core damage without the relief valve being stuck-open, which could lead to double counting. A full dynamic event tree analysis would terminate a scenario if a PORV stuck open.

---

[76] http://www.mathworks.com/products/matlab/

The eight flooding scenarios (see Table 8.8) provide the dynamic analysis with the time at which flooding ends as it affects the potential for recovery of HPI. Loss of feed-water from a failed CST is assumed to occur at the time of the seismic event. Although the seismic failure probabilities increase with the level of the earthquake, the timing of the different scenarios is assumed not to be affected in the flooding model. Thus, it was possible to run the dynamic model once for all three seismic levels to obtain conditional probabilities of core damage.

For each flow scenario, there are multiple plant states that must be considered in combining conditional probabilities with state probabilities. For example, core damage can occur for a state associated with failure of AFW, PORVs not failed, and HPI failed. The conditional core damage probability depends on the success or failure of recovery actions, which is time dependent. The quantification of a specific scenario is illustrated as an example. For Flooding Scenario 3 in Table 8.8 with AFW failure but no failure of the PORVs, the conditional probability of failure was determined to be 0.165 in the Monte Carlo analysis. Referring back to Figure 8.5, this scenario corresponds to branch end-state 6. For a specific seismic level this conditional probability of core damage would be multiplied by the failure probability of AFW and the non-failure probability of PORV to obtain the failure probability for that state. Because Flooding Scenario 3 directly leads to HPI failure the associated conditional probability of HPI failure for that scenario is unity. Note that Flooding Scenarios 3 through 8 in Table 8.8 all make a contribution to this plant damage state. Flooding Scenarios 1 and 2 in Table 8.8 don't contribute to this state because they do not involve HPI failure.

Another state that contributes to core damage for Flooding Scenario 3 is one in which there is AFW success but PORV failure. In the fixed event tree (see Figure 8.5) this scenario corresponds to plant damage state 4. In this case the conditional probability would be multiplied by the non-failure probability for AFW and the PORV failure probability. Table 8.9 provides the overall conditional core damage probabilities and the overall frequencies for the three return frequencies.

Table 8.9. Results of Analysis

| **Return Frequency ($yr^{-1}$)** | **Conditional Core Damage Probability** | **Core Damage Frequency ($yr^{-1}$)** |
|---|---|---|
| 3E-5 | 0.0087 | 2.6E-7 |
| 1E-5 | 0.067 | 6.7E-7 |
| 1E-6 | 0.67 | 6.7E-7 |
| Total | | 1.6E-6 |

A sensitivity study was performed to assess the importance of delay associated with aftershocks in extending the time to perform recovery actions by setting the aftershock delay time to zero. At each return frequency, the effect of the delay associated with aftershocks was found to be a factor of two increase on core damage frequency.

## 8.10. Conclusions

A seismic event is by its very nature dynamic. The potential for aftershocks, the need for recovery actions, the need for operating staff to verify the status of the plant, the potential for seismically-induced flooding, and the potential for fires lead to conditions that would be very difficult to analyze realistically within the constraints of static event trees. To a degree, it is possible to adapt static event trees to account for dynamic events. To the extent that one of the objectives of SPRA is a quantitative assessment to demonstrate an acceptable level of plant risk, it is possible to make conservative assumptions rather that to undertake the additional potential expense of a dynamic analysis. However, the true benefit of PRA has been in providing insights into the nature of the risk and how to best protect against that risk, rather than a focus on the bottom line.

In the Fukushima accident, the tsunami had a much greater impact on the plant than the seismic loads. Nevertheless, the types of challenges faced by plant personnel were the same as what could be experienced in a very large seismic event. In order to evaluate the effectiveness of procedures to respond to events of this nature or to train personnel to respond to extreme external events, tools for the performance of dynamic event tree analysis could be of value.

In this study, a dynamic problem was constructed that would have been very difficult to address with a static event tree. Historically, PRAs gave little or no credit to recovery actions. In the post-Fukushima environment, a flexible approach was developed by the nuclear industry to address the uncertainties that can exist in extreme external events or in accidents involving severe core damage, which involves the provision of FLEX equipment at the plant site or at regional locations. This study provided further evidence of the difficulty posed by static event trees in evaluating the effectiveness of recovery actions.

The approach that was taken was a limited dynamic event tree approach in which analyses with the MELCOR code were performed, prior to undertaking the dynamic portion of the analysis, for typical conditions that could be encountered in a seismic event involving loss of feed-water and recovery actions. It is not clear that the core damage rules developed in this manner can be obtained in general without a true dynamic analysis in which the system analysis model follows the state of the plant as it evolves or branches.[77] As discussed earlier, we also assessed the probability of stuck-open PORVs as a pathway to core damage. It became clear, however, that in order to avoid double counting of core damage, the partial dynamic analysis approach being taken would become complex. A true dynamic analysis can address this type of issue more directly.

SPRA has not typically addressed aftershocks. The logic is that, if an aftershock occurs that is greater than the initial shock, it becomes the main shock. The uncertainties in the seismic hazard curve are so great that a series of shocks smaller than the main shock may be a secondary consideration. Nevertheless, when considering human response and recovery actions realistically, this study indicates that the occurrence of aftershocks could have an important impact.

---

[77] U. Catalyurek, Rutt B., Metzroth K., Hakobyan A., Aldemir T., Dunagan S., and Kunsman D., "Development of a Code Agnostic Computational Infrastructure for the Dynamic Generation of Accident Progression Event Trees," *Reliability Engineering and System Safety*, 95, 278-294 (2010)

# 9. FLOODING MODEL DEVELOPMENT

Although the direct numerical simulation of the Navier-Stokes equations remains impractical in general applications, as the speed and data storage capability of computers have increased, it has become more practical to apply computational fluid dynamics (CFD) models, such as those in the FLUENT code,[78] to the solution of time-dependent fluid flow problems with substantially higher fidelity than the lumped parameter models historically used in reactor safety codes. Nevertheless, in order to support a detailed uncertainty analysis, as in Risk-Informed Safety Margin (RISMC) applications, a very large number of analyses are required. For this reason, a simple but flexible flooding model has been developed to assess the time-dependent, seismically-induced flooding of rooms in a building. This code has been used to address the failure of water tanks, activation of sprinkler systems, or water ingress from external floods. The following section describes the results of sensitivity studies performed in support of Case Study 2, which is described in Section 4.

## 9.1 General Model Characteristics

The model is implemented in MATLAB. The model is currently 1-D in space: no consideration is given to waves or currents within rooms, and each room is represented with a single water level. Thus, the focus is on the flow paths between rooms. The flow paths are purely gravity-driven at this point in development. Flow paths are given a length and hydraulic diameter to account for frictional pressure drop over the length of a flow path.

### 9.1.1 Model Requirements

The flooding model has been created to satisfy the following requirements:

1. An arbitrary number of rooms
2. An arbitrary number of flow paths between rooms
3. An arbitrary number of sources of water characterized by a source rate as a function of time (kg/s)
4. An arbitrary number of sump drains (treated with orifice flow to a virtual volume)
5. Obstructions within a room that reduce the cross sectional area accessible to water as a function of height within the room
6. Characterization of the vulnerability of safety related equipment as a function of water elevation in the room
7. Identification of which rooms contain safety related equipment (but not their specific location within a room)
8. Treatment of rooms as effective parallelepipeds

### 9.1.2 Flow Regimes

Flow paths are critical to the model. There are two basic flow regimes currently implemented: orifice and sluice. Both are derived from Bernoulli’s equation. The transition between these regimes is smoothed by a combination of the two.

---

[78] Fluent, A. N. S. Y. S. "User’s Guide, 2014." (15).

#### 9.1.2.1 Orifice Flow (Regime 1)

Figure 9.1 illustrates two rooms in the plant separated by a wall with an aperture, e.g. door. In orifice flow, the flow path is submerged on both sides of the opening, as indicated in the figure. The flow is described in Equation 9.1.

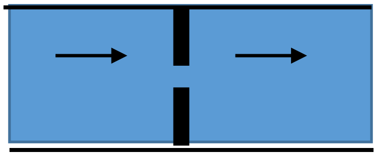

Figure 9.1: Orifice Flow

$$Q_O = c_d A \sqrt{\frac{2(P_1 - P_2)}{\rho}} \tag{9.1}$$

where $Q_O$ is the volumetric flow rate ($m^3/s$), $c_d$ is the discharge coefficient, $P_1$ is the pressure of the source room (P1), $P_2$ is the pressure of the sink room (Pa), $A$ is the area of the flow path ($m^2$), and $\rho$ is the density of the water ($kg/m^3$). The discharge coefficient is currently treated as a constant with value 0.6. In reality it is experimentally-determined and dependent on the ratio of diameters of the general flow and the orifice, as well as the Reynolds number through the orifice. For most applications, 0.6 is a standard approximation. Currently, the pressure difference is driven only by a difference in water level between the rooms.

#### 9.1.2.2 Sluice Flow (Regime 2)

Sluice flow, in which the higher-level side reaches above the top of the flow path and the lower-level side does not, is a form of open-channel flow as shown in Figure 9.2 and described in Equation 9.2.

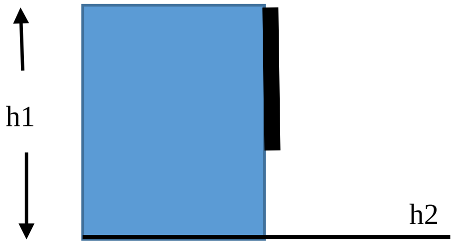

Figure 9.2: Sluice Flow

$$Q_S = c_d h_2 b \sqrt{2 g h_1} \tag{9.2}$$

where $Q_S$ is the volumetric flow rate ($m^3/s$), $c_d$ is the discharge coefficient, $h_1$ is the height of the source water (m), $h_2$ is the height of the sink water (m), $g$ is the gravitational constant 9.8 $m/s^2$, and $b$ is the width of the flow path (m). The discharge coefficient is again estimated as 0.6.

#### 9.1.2.3 Mixed Flow

Most situations involving room flooding will fall in between the two preceding flow regimes. For these cases, a hybrid regime is used. Two such situations are shown in Figures 9.3 and 9.4. For the portion of the flow path that is submerged on both sides, orifice flow is used. This region is depicted in Figures 9.3 and 9.4 with red arrows. The total heights are used in the pressure difference calculation, but the flow path area used is only the portion that is submerged in both rooms. The remaining portion of the flow path is modeled using sluice flow, where $h_2$ is the height difference between the higher water level or the top of the flow path (whichever is lower) and the lower water level. The total flow is the sum of orifice and sluice flow.

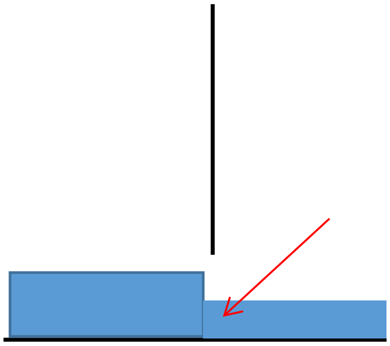

Figure 9.3: Flow Regime 3 (red arrow indicates region of orifice flow)

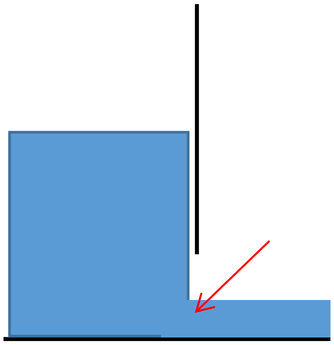

Figure 9.4: Flow Regime 4 (red arrow indicates region of orifice flow)

### 9.1.3 Model Calculation Process

In order to accommodate an arbitrary number of rooms, flow paths, obstructions and water sources, these parameters are entered by the user as matrices. Heights are relative to a reference point, such as ground level. For example, a 10 m tall room with a floor at ground level would have a minimum height of 0 m and maximum height of 10 m, where a 10 m tall room with a floor at 3 m above ground would have a minimum height of 3 m and a maximum height of 13 m.

### 9.1.3.1 Scenario Parameter Population

The Room, Obstruction, Flow Path, Source Information, and Source Rate matrices are defined in Tables 9.1 through 9.5, respectively. Each entity represented in a matrix occupies one line of that matrix. The Room matrix (Table 9.1) allows for an initial water level in each room. Rooms and obstructions are assumed to have the same area at all heights. Large obstructions (Table 9.2) may occupy some of the room, causing the water level to rise more quickly. The “From” and “To” rooms in the Flow Path matrix (Table 9.3) represent an arbitrary flow direction. The model checks to see which room is higher and will reverse flow if appropriate. It was desired to accommodate a wide variety of water source profiles, including step, ramp, exponential, or a user-entered vector.

To enable this, the water sources are defined by two matrices: one containing general information (Table 9.4), and the other with the rate by time (Table 9.5).

Table 9.1: Room Matrix Definition

| **Parameter** | **Units** |
|---|---|
| Room Number | # |
| Minimum Height | m |
| Maximum Height | m |
| Area | $m^2$ |
| Initial Water Level | m |

Table 9.2: Obstruction Matrix Definition

| **Parameter** | **Units** |
|---|---|
| Obstruction Number | # |
| Room | # |
| Minimum Height | m |
| Maximum Height | m |
| Area | $m^2$ |

Table 9.3: Flow Path Matrix Definition

| **Parameter** | **Units** |
|---|---|
| Flow Path Number | # |
| From Room | # |
| To Room | # |
| Area | $m^2$ |
| Hydraulic Diameter | m |
| Length | m |
| From Elevation | m |
| To Elevation | m |

Table 9.4: Source Information Matrix Definition

| **Parameter** | **Units** |
|---|---|
| Source Number | # |
| Water Density | $kg/m^3$ |
| Room Number | # |

Table 9.5: Source Rate Matrix Definition

| **Parameter** | **Units** |
|---|---|
| Source Number | # |
| A. Step Input #1 Rate | kg/s |
| B. Step Input #1 Start Time | s |
| C. Step Input #2 Rate | kg/s |
| D. Step Input #2 Start Time | s |

| | |
|---|---|
| F. Ramp Input #1 Rate | kg/s |
| G. Ramp Input #1 Start Time | s |
| H. Ramp Input #2 Rate | kg/s |
| K. Ramp Input #2 Start Time | s |
| L. Exponential Coefficient | kg/s |
| M. Exponential Decay Constant | 1/s |

#### 9.1.3.2 Running Cases

Using the 5 matrices and a problem end time as inputs, the room height at time is solved simultaneously for each room as determined by solving Equation 9.3.

$$\frac{dH(i,t)}{dt} = \frac{Flow(i,t)+Source(i,t)}{Area(i,t)} \tag{9.3}$$

Where $H(i,t)$ is the height (m) of water in room $i$ at time $t$, $Flow(i,t)$ is the net flow (m$^3$/s) into the room as calculated from a combination of Equations 9.1 and 9.2, $Source(i,t)$ is the flow (m$^3$/s) from outside sources, and $Area(i,t)$ is the surface area (m$^2$) corrected for obstructions.

The flooding model currently uses a 4th-order Runge-Kutta differential equation solver to solve Equation 9.3 for each room. MATLAB's ode45[79]adaptive general purpose differential equation solver was previously used, as it was found to have the best blend of stable results and fast run time for simple cases. Adaptive differential equation solvers (such as ode45) are not generally well-suited to solving problems with discontinuities, such as flow paths abruptly opening and closing.

## 9.2 Recent Flooding Model Improvements

Recent work beyond the initial construction of the model has focused on improving its applicability to likely nuclear power plant flooding scenarios. This has been accomplished in two areas: dynamically opening and closing flow paths, and friction effects over pipe length.

### 9.2.1 Dynamic Flow Paths

As originally written, the flooding model was static in terms of the opened and closed states of the flow paths between rooms. An example of the results of a static scenario is shown in Figure 9.5. In this case water drains continuously from a CST and a larger backup CST through a series of rooms in a nuclear power plant auxiliary building. The rooms are as described in Table 9.6, and will be used throughout this document. The flow paths between the rooms are described in Table 9.7. These may be approximately visualized using Figure 9.13. The water levels in Figure 9.5 are referenced globally, and so the level in each room must be calculated using the minimum elevation specified in Table 9.6. It is assumed that sensitive equipment resides in the basement rooms (4 and 5 in Figure 9.5 and Table 9.6) and will fail if the water level in those rooms rises above 0.61m (2 ft) above the floor. In this case the water level in the basement rooms reaches a maximum of 7 cm above the floor, and the equipment is deemed to have survived.

---

[79] MathWorks, R. "Solve nonstiff differential equations; medium order method–MATLAB ode45 (2013)."

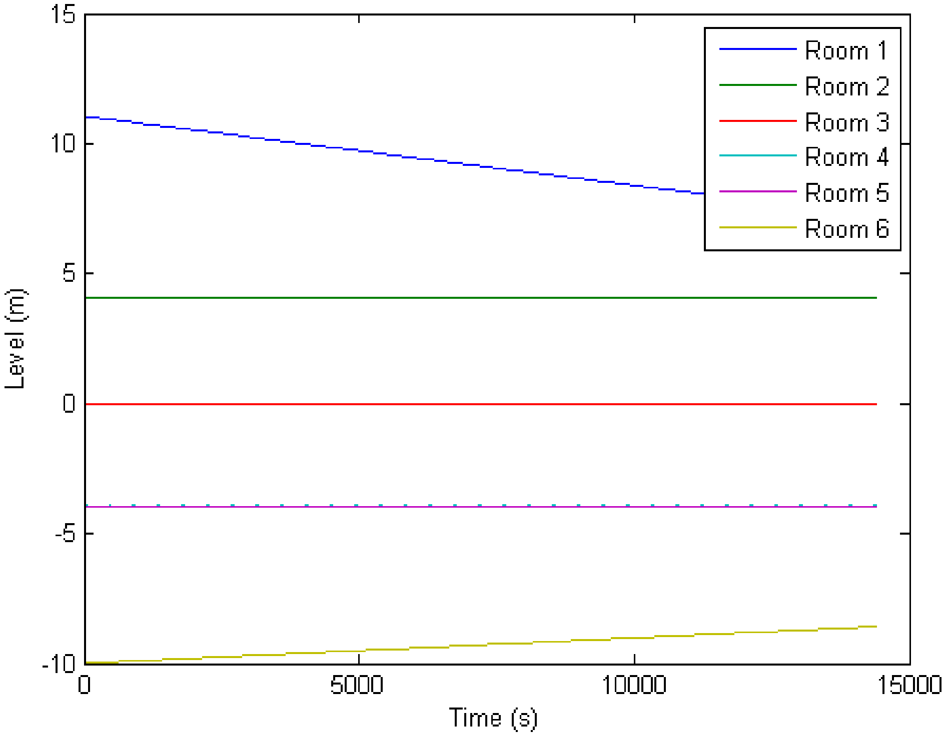

Figure 9.5: Static Flooding Analysis, No Friction

Table 9.6: Room Information

| Room | Name | Area ($m^2$) | Max. Elev (m) | Min. Elev (m) | Initial Level (m) |
|---|---|---|---|---|---|
| 1 | Backup CST | 102.6 | 11.07 | 0 | 11.07 |
| 2 | Main CST | 102.6 | 4.06 | 0 | 4.06 |
| 3 | Aux. Building | 278.71 | 4 | 0 | 0 |
| 4 | Aux. Basement 1 | 139.36 | 0 | -4 | -4 |
| 5 | Aux. Basement 2 | 139.36 | 0 | -4 | -4 |
| 6 | Aux. Sump | 278.71 | -4 | -10 | -10 |

Table 9.7: Flow Path Information

| Flow Path | From Room | To Room | Area ($m^2$) | Diameter (m) | Length (m) | From Elevation (m) | To Elevation (m) |
|---|---|---|---|---|---|---|---|
| 1 | 1 | 2 | 0.2827 | 0.6 | 2 | 0.3 | 0.3 |
| 2 | 2 | 3 | 0.005 | 0.138 | 2 | 0.3 | 0.3 |
| 3 | 3 | 4 | 6.0 | 2.4 | 0.1 | 0.0 | 0.0 |
| 4 | 4 | 5 | 2.2 | 1.375 | 0.1 | -3.3125 | -3.3125 |
| 5 | 4 | 6 | 0.00456 | 0.0762 | 9.144 | -4.0 | -4.0 |
| 6 | 5 | 6 | 0.00456 | 0.0762 | 9.144 | -4.0 | -4.0 |

Two means for modifying flow paths have been provided: pressure-dependent and time-dependent. Time-dependent operations simply open and close flow paths at given problem times. In Figure

9.6, a case is shown where the backup CST is not opened until 1 hr into the simulation. This may occur if an operator realizes that a leak is occurring but still needs to maintain flow from the main CST. A flow path could similarly be closed at a given time. Whichever operation has occurred most recently takes precedent, so a path could be opened and later closed if desired. In this case, the water level in the basement rooms reaches a maximum of 7 cm above the floor, and the equipment is again assumed to have survived.

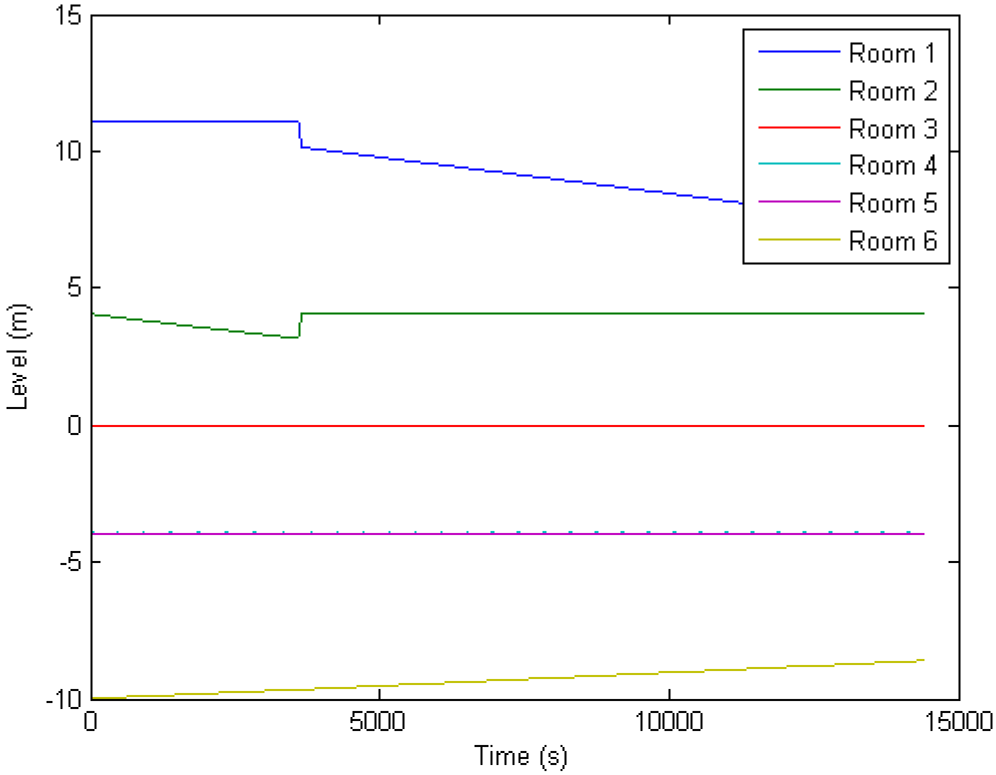

Figure 9.6: Dynamic Flooding Analysis (Backup CST Opens at 1hr), No Friction

Pressure-dependent operations can only open flow paths, and may be used to represent a door bursting due to a difference in water levels on either side. A door bursting is an irreversible process, and so any time-dependent command to close the flow path after a pressure-dependent opening is ignored. Figure 9.7 shows a case where a door between the two basement rooms bursts when the difference in water level is 1.52 m (5 ft). In this case the level in Room 4 reaches 11 cm above the floor, while the door to Room 5 never bursts, and equipment is assumed to have survived in both rooms.

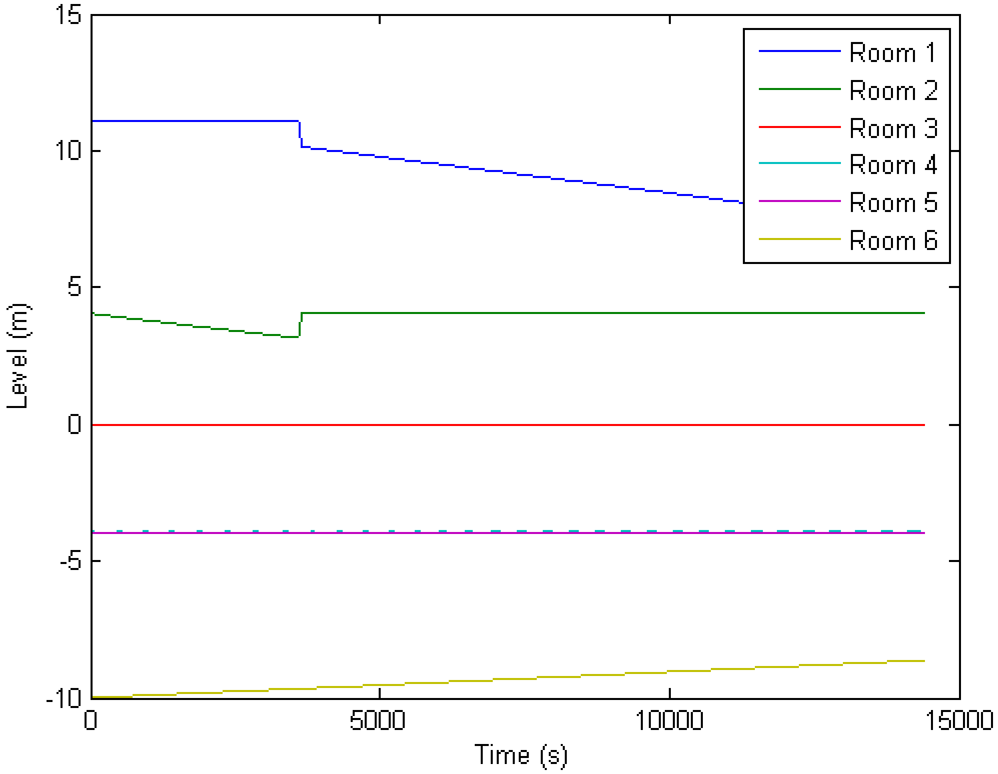

Figure 9.7: Dynamic Flooding Analysis (Backup CST Opens at 1 hr & Basement Door Opens at 5 ft Difference), No Friction

### 9.2.2 Friction

As originally written, the flooding model accounted for shape change losses in flow paths through the use of a discharge coefficient. This did not account for losses in long or narrow pipes, which may exist in nuclear power plants. Loss of pressure through the length of a flow path has been added using the Blasius correlation[80]. Multiple assumptions are required for this treatment of friction, including that the flow path is completely full, the flow path walls are smooth, the flow is turbulent, and the fluid is completely water (with the density of water at approximately 0°C.

The head loss due to pipe friction is given by Equation 9.4, where $f$ is the friction factor, $L$ is the length of the flow path (m), $V$ is the flow velocity (m/s), $D$ is the flow path hydraulic diameter (m), and $g$ is the gravitational constant 9.8 m/s$^2$. The Blasius correlation is given as Equation 9.5, where $Re$ is the Reynolds number (Equation 9.6). In Equation 9.6, $v$ is the kinematic viscosity, $8.9 \times 10^{-4}$ (m$^2$/s).

$$h = f\frac{L}{D}\frac{V^2}{2g} \tag{9.4}$$

$$f = 0.316Re^{-0.25} \tag{9.5}$$

---

[80] K. T. Trinh, "On the Blasius correlation for friction factors." *arXiv preprint arXiv:1007.2466* (2010).

$$Re = \frac{VD}{v} \tag{9.6}$$

The flow velocity is first calculated without pipe friction, using the water level difference on each side of the flow path as the driving head (Equations 9.1 and 9.2). The velocity is used to calculate the head loss, which is subtracted from the initial gravity head to calculate a new velocity. This process iterates until the difference between the old and new velocity is below a convergence criteria, for example 10%.

Figure 9.8 repeats the case of Figure 9.7 with friction applied. The difference is most clear in the sump water level. The drains from the basement rooms are very long and small in diameter, and so frictional losses are large. This results in much higher levels in the basement rooms, as Room 4 reaches a water level of 1.6 m and Room 5 reaches 0.8 m, both failing the equipment within.

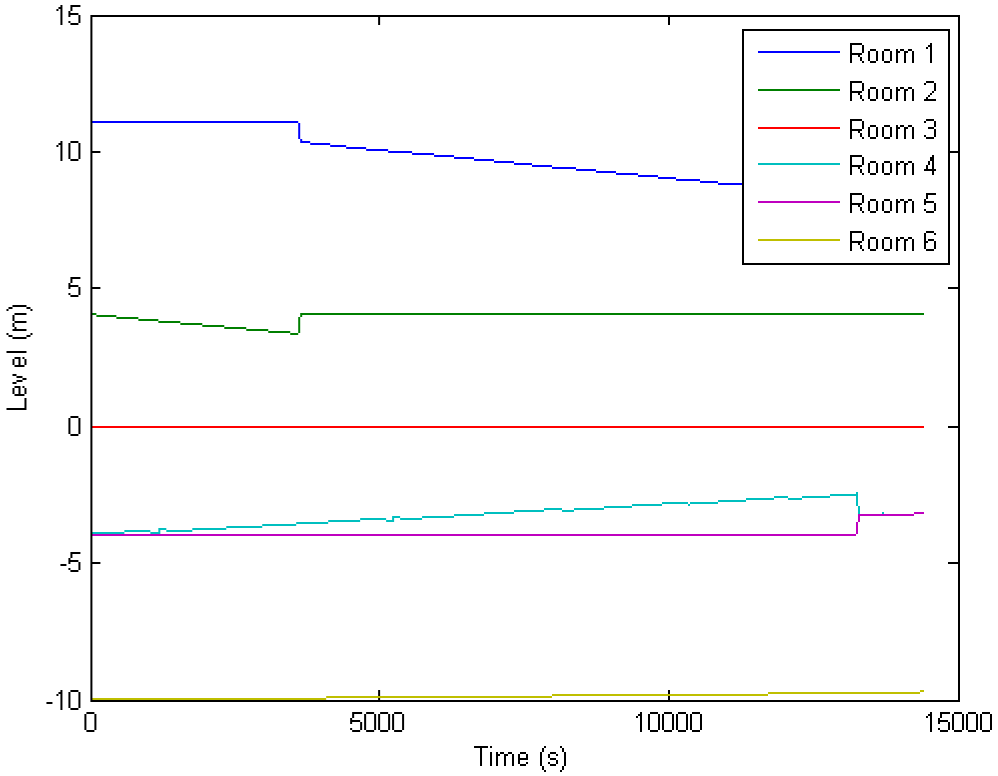

Figure 9.8: Dynamic Flooding Analysis (Backup CST Opens at 1 hr & Basement Door Opens at 1.52 m Difference), Friction Enabled

## 9.3 Test Cases

### 9.3.1 Effect of Leak Size

The effect of the size of the leak into the auxiliary building is examined by varying the area of the leak and corresponding hydraulic diameter. The leak is assumed circular, as in a guillotine pipe break. The above case is repeated for 20 cm$^2$, 30 cm$^2$, 40 cm$^2$, and 50 cm$^2$ leak sizes. Figure 9.9 shows the water levels in each room as a function of leak size. The maximum water level in each basement room is given in Table 9.8.

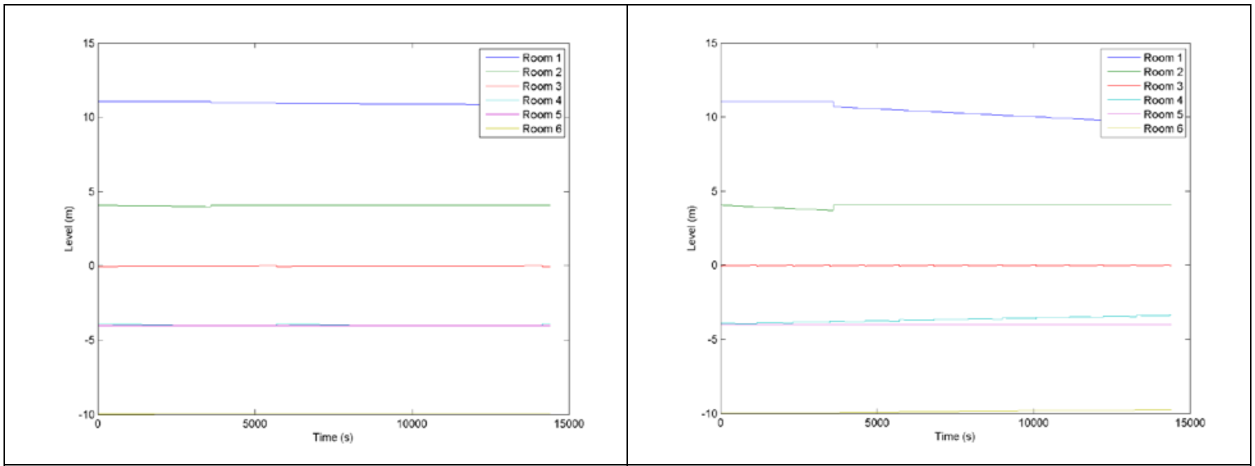

(a) Leak Size 20 cm$^2$

(b) Leak Size 30 cm$^2$

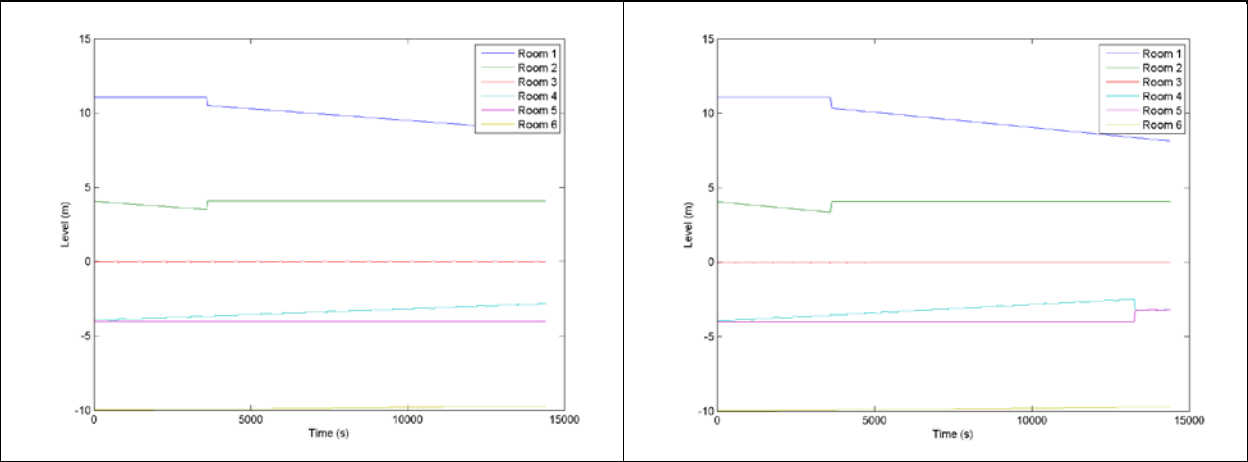

(c) Leak Size 40 cm$^2$

(d) Leak Size 50 cm$^2$

Figure 9.9: Dynamic Flooding Analysis, Variable Leak Size

Table 9.8: Effect of Leak Size on Basement Water Level

| Break Size | Max Room 4 Level (m) | Max Room 5 Level (m) |
|---|---|---|
| 20 cm$^2$ | 0.09 | 0 |
| 30 cm$^2$ | 0.7 | 0 |
| 40 cm$^2$ | 1.2 | 0 |
| 50 cm$^2$ | 1.6 | 0.8 |

It can be seen in Figure 9.9 (a-c) that for smaller leaks, the basement door never bursts. In the case of 30 cm$^2$ and 40 cm$^2$ leaks (Figure 9.9 (b-c)), it is possible to fail equipment in one room without affecting the other.

### 9.3.2 Effect of Drain Size

The case of a 50 cm$^2$ leak is further explored by varying the drain size in the basement rooms. Room 6 represents a semi-infinite water sink that is not a part of the auxiliary building. This is reflected by the drain length of 9.1 m from each basement room. Due to their location on the floor and the difficulty in cleaning long pipes, these drains may become clogged with debris. This could be modeled by varying the area and diameter of the drain.

Figure 9.10 shows the effect of drain diameter of 3.8 cm, 5.1 cm, 6.4 cm, and 7.6 cm. The difference is not dramatic, but it is still significant. The maximum level in Room 5 varies 18 cm from one extreme case (Figure 9.10 (a), 3.8 cm diameter) to the other (Figure 9.10 (d), 7.6 cm diameter). In the nominal case of 7.6 cm diameter (Figure 9.10 (d)) the equipment still fails under the criteria used in this report, but the margin of failure is clearly affected by the drain size.

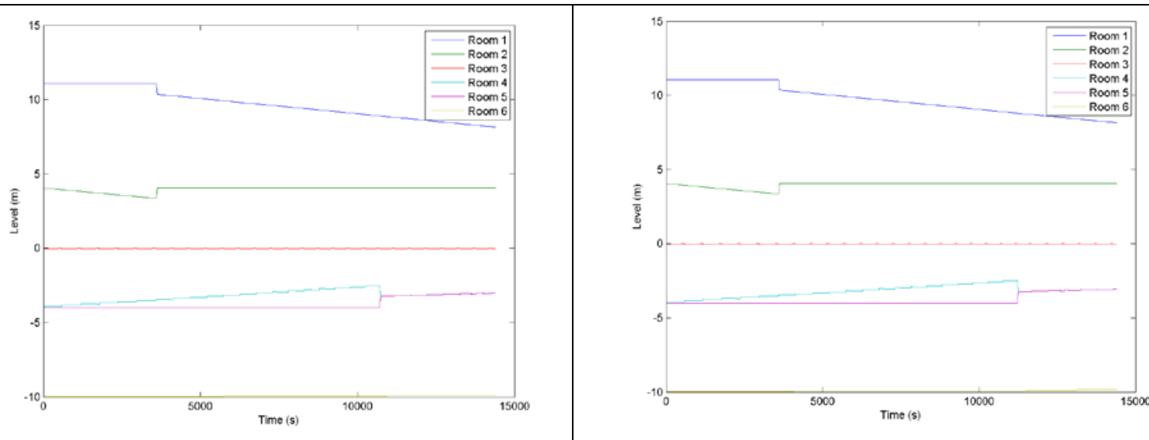

(a) Drain Diameter 3.8 cm

(b) Drain Diameter 5.1 cm

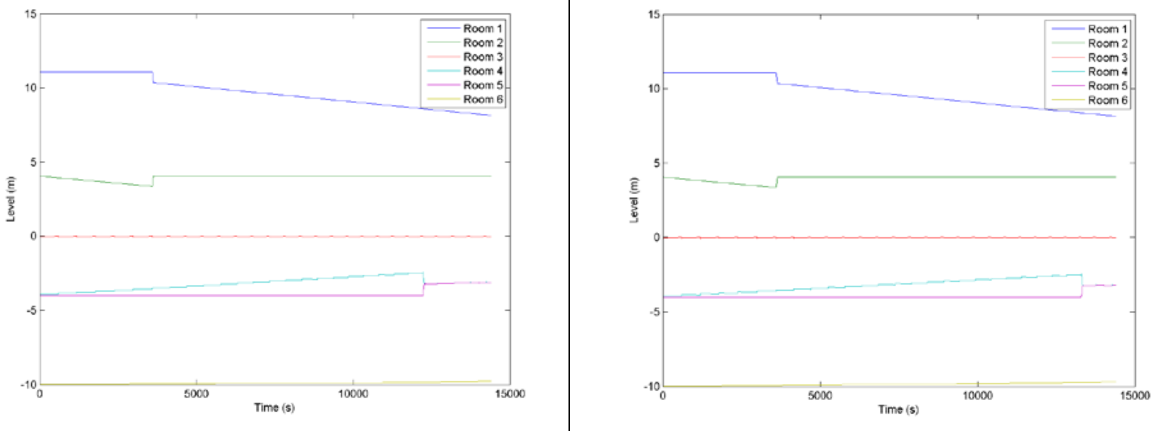

(c) Drain Diameter 6.4 cm

(d) Drain Diameter 7.6 cm

Figure 9.10: Dynamic Flooding Analysis, Variable Basement Drain Size

## 9.4 Benchmarking

A benchmarking of the model against established codes has been initiated. This is being accomplished in two phases. First, the results from the model for a test case are compared against a similarly-detailed thermal hydraulic code (Section 9.4.1). The second method of benchmarking is to simulate the test case in a full computational fluid dynamics (CFD) analysis (Section 9.4.2).

### 9.4.1 MELCOR

The similarly-detailed code used for this comparison is MELCOR[81]. MELCOR is a system-level severe nuclear accident simulator code used by the Nuclear Regulatory Commission for safety analyses. Its general thermal hydraulic model comprises control volumes with flow paths between them, and largely one-dimensional flow. Flow is modeled with more detail in certain areas of interest, including when two-phase flow exists. Control volumes and flow paths are defined with similar parameters to the flooding model under study, as in Tables 9.6 and 9.7, respectively.

This benchmarking was performed with similar values to Tables 9.6 and 9.7. A major difference was that the simulated pipe break was larger, meant to represent a large rupture of the main CST. In this case, Flow Path 2 was assumed to be circular with a diameter of 0.6 m. A comparison of results is shown in Figure 9.10, where water levels from the simplified flooding model are dashed lines corresponding to the same color solid lines representing MELCOR results. The levels can be seen to agree fairly well overall, with some key differences early in the simulation. While the model under study transitions smoothly between sluice and orifice flow using a combined regime, MELCOR transitions abruptly. Therefore, the emptying of a tank in MELCOR (such as the solid blue line in Figure 9.11) proceeds very slowly at first, and then switches to a faster regime.

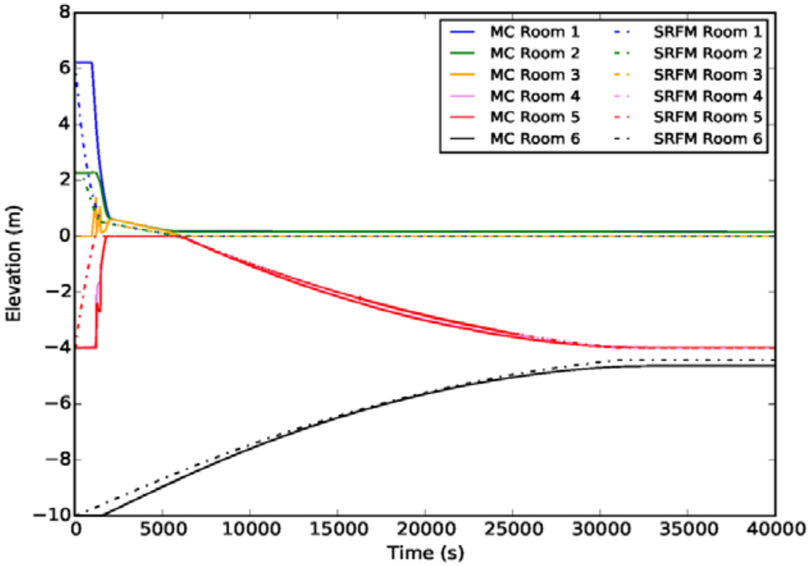

Figure 9.11: Simplified flooding model Benchmarked against MELCOR for Case Study 2 Large CST Tank Rupture

---

[81] R. K. Cole, et al. *MELCOR computer code manuals*. Division of Systems Technology, Office of Nuclear Regulatory Research, US Nuclear Regulatory Commission (1998)

### 9.4.2 Fluent

For this analysis, the Volume of Fluid[82] (VOF) method is used in Ansys Fluent.[94] The VOF method is used with immiscible fluids, such as air and water. A single set of momentum equations is solved, and the volume fraction in each element is tracked. First, the geometry is specified and meshed as shown in Figure 9.12.

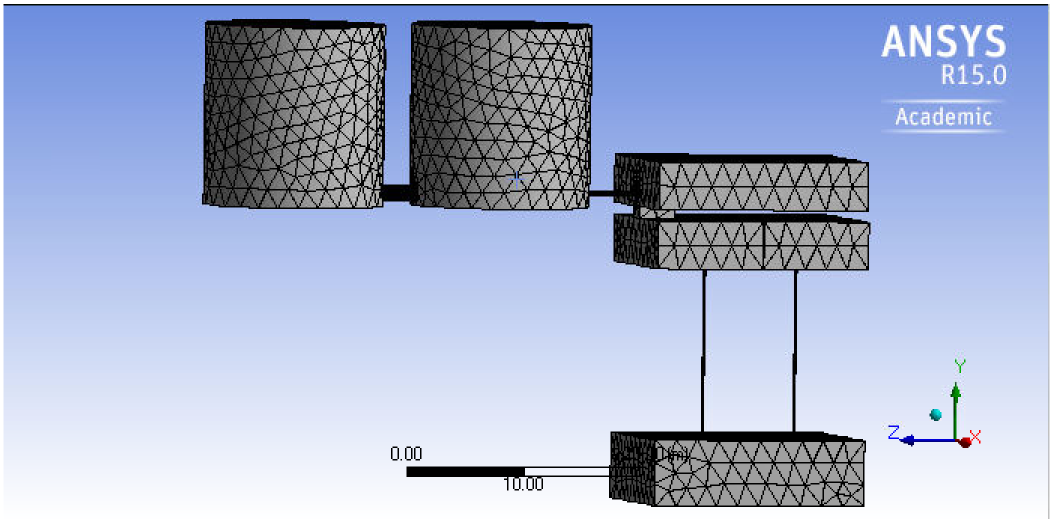

Figure 9.12: Case Study 2 Fluent Mesh

The unstructured mesh generated in ANSYS is coarse far away from flow paths, and much finer near and within flow paths. A balance must be struck on the overall granularity of the mesh. If the mesh is too coarse, the simulation will tend to fail convergence criteria and results will be less accurate. For example, with this geometry and set of initial conditions, a mesh with roughly 351,000 elements and 133,000 nodes will fail almost immediately. If the mesh is too fine, on the other hand, the simulation will proceed very slowly. Using default settings, this geometry is meshed with roughly 680,000 elements and 253,000 nodes. As a basis for comparison, this CFD analysis required approximately 12 hours on 14 processor cores to advance 7 seconds into the problem.

For a first analysis, the boundary conditions are set as walls and the flow is assumed laminar. In reality, the CSTs are vented and the flow path to the auxiliary building is not likely to be airtight. The effects of various boundary conditions will be explored once the model is otherwise well-established. Various turbulent effects will also be explored, as water driven by a large gravity head may reach transitional or turbulent Reynolds numbers.

A case is shown with its conditions just after the start of the analysis in Figure 9.13. It can be seen that the tanks were only partly filled with water (blue), and water is just starting to flow into the pipe that simulates a rupture. This is seen in greater detail in Figure 9.14. An effect of the wall boundary condition is that water moves into the pipe in “gulps”, as it is resisted by air pressure. This will be carefully examined as the model develops, as it has the potential to significantly affect

---

[82] C. W. Hirt, and B. D. Nichols, "Volume of fluid (VOF) method for the dynamics of free boundaries." *Journal of computational physics* 39.1: 201-225 (1981)

the results of the analysis. The sump room may also be replaced with a constant pressure outlet boundary condition, but is retained here for ease of visualization.

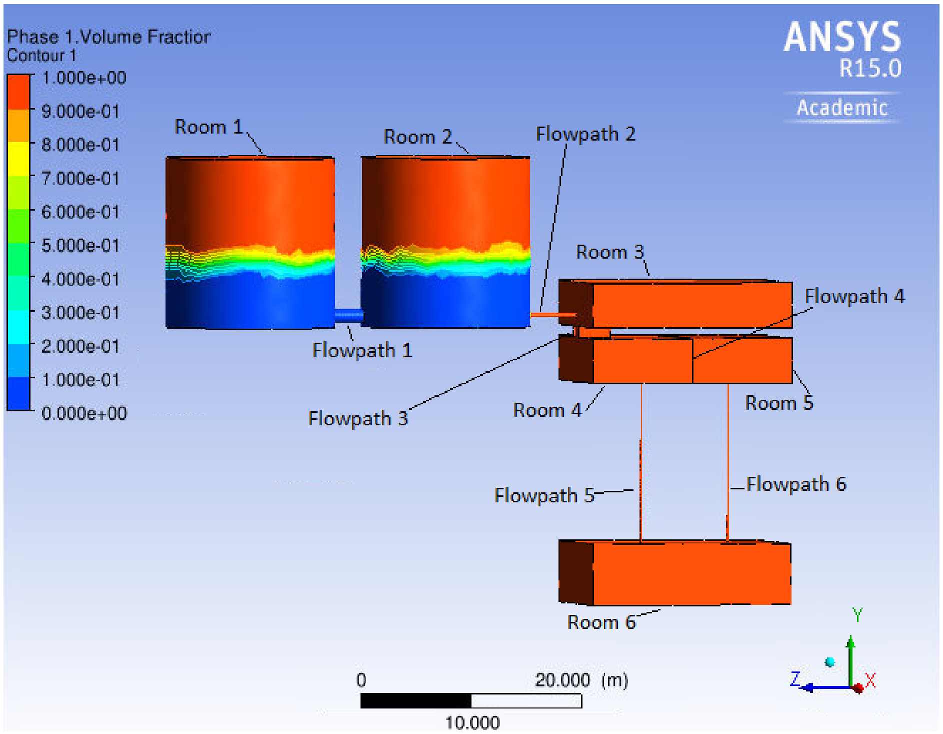

Figure 9.13: Case Study 2 Fluent Volume Fractions at t=0.5 s

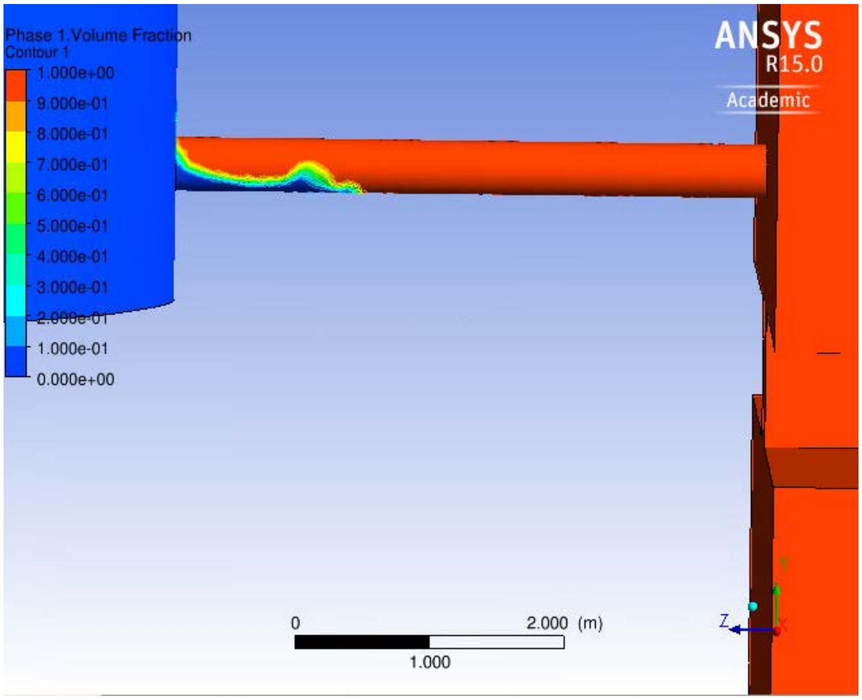

Figure 9.14: Case Study 2 Fluent Volume Fractions at CST Rupture at t=0.5 s

## 10. CASE STUDY 3: CONDENSATE STORAGE TANK STRUCTURAL MODELING

As indicated earlier, the CST supplies water to several key systems including the high pressure coolant injection (HPCI) and reactor core isolation cooling (RCIC) systems. If water is emptied from this tank or other large storage tanks due to structural failure, one of the systems that depends on the CST could fail and potentially lead to radioactive release from the NPP.

The modeling of liquid-filled storage tanks provides difficulties due to the high nonlinearity introduced by the fluid-structure interaction. Therefore, 3D finite element (FE) models that characterize the nonlinear fluid-structure interaction are needed to appropriately model the dynamic response. Due to the complexities involved in appropriately modeling fluid-structure interaction, past researchers have developed simplistic 2D models to characterize dynamic properties of liquid-filled storage tanks. Several of these simplified models were developed using SAP2000[83] based off properties from a representative CST found in literature[84]. These models were analyzed to determine their dynamic properties, and the results were compared to a 3D FE model, created by another researcher on this project, to investigate the limitations of simplified liquid-filled storage tank models during SPRA.

### 10.1 Condensate Storage Tank Structure Model

The realistic CST structure used in this study was a slight modification of the CST structure discussed in Section 2.3 from Nie et al. The tank was a cylindrical steel storage tank filled almost completely with water. Geometric and material properties of the CST structure used in this research are shown in Table 10.1.

Table 10.1 Geometric and material properties of realstic CST structure

| Geometric Properties | | |
|---|---|---|
| Tank height to dome (ft) | $h_t$ | 37.5 |
| Height of stored liquid (ft) | $h_w$ | 35 |
| Radius of circular tank (ft) | $r_t$ | 25 |
| Thickness of tank wall (in.) | $t_s$ | 0.5 |
| Thickness of dome (in.) | $t_d$ | 0.5 |
| **Material Properties** | | |
| Elastic modulus of steel (psf) | $E_s$ | 4,176,000,000 |
| Density of steel (pcf) | $\rho_s$ | 489.4 |
| Density of water (pcf) | $\rho_w$ | 62.4 |

---

[83] SAP2000, Version 18. Computers and Structures, Inc., Berkeley, CA. www.csiberkeley.com (2016).

[84] Nie, J.R., Braverman, J.I., Hofmayer, C.H., Choun, Y. S., Hahm, D., and Choi, I. K. *A Procedure for Determination of Degradation Acceptance Criteria for Structures and Passive Components in Nuclear Power Plants*. Upton, NY: Brookhaven National Lab. (2012).

### 10.2 Description of Structural Models

Simplified 2D liquid-filled storage tank models were investigated in this research and compared to a 3D FE model that was developed by fellow researcher. While 3D FE models are able to appropriately characterize the complex fluid-structure interaction, past researchers have developed simplified 2D models that estimate the dynamic forces imparted on storage tank walls during seismic events. In derivation of the simplified 2D models, an important assumption is made to differentiate the model into one of two distinct categories of simplified storage tank models. This assumption is whether the tank wall behaves rigidly or flexibly during seismic events. Typically, concrete storage tanks are assumed to have rigid wall behavior, whereas steel tanks are assumed to have flexible wall behavior. However, this assumption presents further uncertainty in the dynamic analysis results of simplified 2D models compared to 3D FE models.

Modern evaluation of liquid-filled storage tanks at NPPs includes determining forces acting on tank walls that result in hoop stress, sliding at the base, and overturning moments. From experience, researchers point to sliding and overturning moments as the most common failures modes (Nie et al. 2012). For both simplified 2D and detailed 3D FE models, these two common failure modes can be evaluated by the base shear and overturning moment captured by each model during dynamic analysis.

#### 10.2.1 Simplified 2D Models

Four separate simplified liquid-filled storage tank models were created for the CST using SAP2000. In each model, the fluid-structure interaction is mimicked by a series of masses connected to two vertical beams representing the tank wall. The masses are connected to the vertical beams with either a rigid link or spring. Masses connected by a rigid link are called “impulsive” and represent fluid weight and movement with the steel tank. Masses connected by a spring are called “convective” and represent sloshing effect of fluid near the top of the fluid surface.

Two of the models, Housner[85] and ACI 350.3[86], were developed with one impulsive mass and one convective mass. The other two models, Bauer[87] and Haroun and Housner[88], were developed with one impulsive mass and two convective masses. For the rigid links, beam elements with infinitely large stiffnesses were used. For convective springs, linear spring elements were used. The stiffness of each linear spring element was calculated using equations for the respective model being analyzed. In each model, beam elements were used to mimic the structural properties of the 3D tank wall and dome. Two vertical beam elements were used for the tank wall and were connected at the top with a horizontal beam element spanning the diameter of the tank. The structural properties of the vertical and horizontal beam elements are shown in Table 10.2.

---

[85] Housner, G. W. “The Dynamic Behavior of Water Tanks,” *Bulletin of the Seismological Society of America* Vol. 53, No. 2: 381-387. (1963).

[86] ACI 350.3 “Seismic Design of Liquid-Containing Concrete Structures (ACI 350.3-01) and Commentary (ACI 350.3R-01).” Farmington Hills, MI: American Concrete Institute. (2001).

[87] Bauer, H. F. *Fluid Oscillations in the Containers of a Space Vehicle and their Influence Upon Stability*. Washington, D.C.: National Aeronautics and Space Administration. (1964).

[88] Haroun, M. A. and Housner G. W. (1981). “Seismic Design of Liquid Storage Tanks,” *Journal of the Technical Councils of ASCE* Vol. 107, No. 1: 191-207. (1981).

Specific modeling details are shown in Althoff[89] and can be used to create each of the simplified 2D CST models.

Table 10.2 Properties of frame elements for tank wall and dome

| | | |
|---|---|---|
| Moment of inertia of each tank wall beam ($ft^4$) | $I_{wb}$ | 1025.2 |
| Cross-sectional area of each tank wall beam ($ft^2$) | $A_{wb}$ | 3.3 |
| Moment of inertia of tank dome beam ($ft^4$) | $I_{db}$ | $3.0 \times 10^{-4}$ |
| Cross-sectional area of tank dome beam ($ft^2$) | $A_{db}$ | 2.1 |

For each model, parameters for impulsive and convective masses, stiffness of convective springs, and heights from the base to the impulsive and convective masses were determined using empirical equations and graphs developed by each of the researchers and summarized by Althoff. The parameters used to develop the simplified 2D systems are summarized in Tables 10.3 through 10.6. In total, four simplified 2D CST models were developed. A visual representation of each model is shown in Figure 10.1. The final SAP2000 model of each is shown in Figure 10.2.

Table 10.3 Parameters for simplified tank model using Housner model

| | | |
|---|---|---|
| Equivalent mass of impulsive component (slugs) | $m_i$ | 92,003.1 |
| Height to center of gravity of impulsive mass (ft) | $h_i$ | 13.1 |
| Equivalent mass of convective component (slugs) | $m_c$ | 31,334.8 |
| Height to center of gravity of convective mass (ft) | $h_c$ | 24.4 |
| Total stiffness of convective spring (slugs/ft) | $k_c$ | 71,712.1 |
| Stiffness of each convective spring (slugs/ft) | $k_c/2$ | 35,856.1 |

Table 10.4 Parameters for simplified tank model using ACI 350.3 model

| | | |
|---|---|---|
| Equivalent mass of impulsive component (slugs) | $m_i$ | 91,022.9 |
| Height to center of gravity of impulsive mass (ft) | $h_i$ | 13.1 |
| Equivalent mass of convective component (slugs) | $m_c$ | 43,301.4 |
| Height to center of gravity of convective mass (ft) | $h_c$ | 23.3 |
| Total stiffness of convective spring (slugs/ft) | $k_c$ | 101,439.8 |
| Stiffness of each convective spring (slugs/ft) | $k_c/2$ | 50,719.9 |

---

[89] Althoff, E. "Detailed and Simplified Structural Modeling and Dynamic Analysis of Nuclear Power Plant Structures." Master's Thesis, The Ohio State University, Columbus, Ohio (2017).

Table 10.5 Parameters for simplified tank model using Bauer model

| | | |
|---|---|---|
| Equivalent mass of impulsive component (slugs) | $m_i$ | 129,126.5 |
| Height to center of gravity of impulsive mass (ft) | $h_i$ | 17.3 |
| Equivalent mass of bottom convective component (slugs) | $m_{c1}$ | 3,631.9 |
| Height to center of gravity of bottom convective mass (ft) | $h_{c1}$ | 22.1 |
| Total stiffness of bottom convective spring (slugs/ft) | $k_{c1}$ | 17,925.0 |
| Stiffness of each bottom convective spring (slugs/ft) | $k_{c1}/2$ | 8,962.5 |
| Equivalent mass of top convective component (slugs) | $m_{c2}$ | 562.9 |
| Height to center of gravity of top convective mass (ft) | $h_{c2}$ | 27.9 |
| Total stiffness of top convective spring (slugs/ft) | $k_{c2}$ | 5,086.9 |
| Stiffness of each top convective spring (slugs/ft) | $k_{c2}/2$ | 2,543.4 |

Table 10.6 Parameters for simplified tank model using Haroun and Housner model

| | | |
|---|---|---|
| Equivalent mass of impulsive component (slugs) | $m_i$ | 90,658.5 |
| Height to center of gravity of impulsive mass (ft) | $h_i$ | 14.5 |
| Equivalent mass of bottom convective component (slugs) | $m_{c1}$ | 86,658.8 |
| Height to center of gravity of bot. convective mass (ft) | $h_{c1}$ | 15.8 |
| Total stiffness of bottom convective mass spring (slugs/ft) | $k_{c1}$ | 270,618,728.3 |
| Stiffness of each bottom convective mass spring (slugs/ft) | $k_{c1}/2$ | 135,309,364.2 |
| Equivalent mass of top convective component (slugs) | $m_{c2}$ | 42,830.8 |
| Height to center of gravity of top convective mass (ft) | $h_{c2}$ | 23.3 |
| Total stiffness of convective mass spring (slugs/ft) | $k_{c2}$ | 96,121.3 |
| Stiffness of each top convective mass spring (slugs/ft) | $k_{c2}/2$ | 48,060.6 |

### 10.2.2 Detailed 3D Model

To accurately capture the complex and nonlinear behavior of fluid-structure interaction in the CST during seismic events, a 3D FE model was developed by another researcher on this project. The original development of the 3D FE model was discussed in Hur et al.[90]. Since then, several improvements have been made to the model, and the results in this chapter come from the most current version of the 3D FE model.

---

[90] Hur, J., Althoff, E., Sezen, H., Denning, R., and Aldemir, T. "Seismic Assessment and Performance of Nonstructural Components Affected by Structural Modeling," *Nuclear Engineering and Technology* Vol. 49, No. 2: 387-394. (2016).

For the 3D FE model, ANSYS[91] was used for modeling. Shell elements were used to model the steel tank structure, and fluid elements were used to model the stored liquid. Typical material properties were assigned to shell and fluid elements for steel and water, respectively. The complex fluid-structure interaction was modeled using contact elements between shell elements and fluid elements. Once the geometry of the model was created, a mesh convergence study was completed to determine the final model's optimum number of elements for run-time efficiency during dynamic analysis.

### 10.3 Modal Analysis of Simplified 2D Models

Modal analysis was completed to capture and compare general dynamic behavior of each simplified 2D CST model. The effects of significant dynamic properties including natural frequencies and mass participation ratios for significant modes were investigated. Due to the simplified nature of the 2D models, only dynamic characteristics in the singular transverse direction of the models were investigated. Importantly, due to the symmetrical geometry of the tank, the 2D models developed in this research replicated any potential horizontal direction of loading and dynamic behavior of the structure.

Due to the lumped-mass nature of the simplified 2D models, each model has either two or three significant modes corresponding to either two or three lumped-masses. Tables 10.7 and 10.8 summarize significant modal information such as natural frequencies, mass participation ratios, and cumulative mass participation ratios for each simplified model. Mode shapes for each model's significant modes are shown in Figures 10.3 through 10.6.

Table 10.7 Modal information for Housner, and ACI 350.3 models

| Mode number | Natural frequency (Hz) | Mass participation ratio | Cumulative mass participation ratio |
|---|---|---|---|
| Housner model | | | |
| 1 | 0.24 | 24.5% | 24.5% |
| 2 | 7.90 | 75.4% | 100% |
| ACI 350.3 model | | | |
| 1 | 0.24 | 31.2% | 31.2% |
| 2 | 7.94 | 68.8% | 100% |

The Housner and ACI 350.3 models were each developed as a two-mass system. Correspondingly, each had two significant transverse modes. The natural frequencies and mass participation ratios of each mode were very similar comparing modal information in Table 10.7. The natural frequencies of the second mode for the Housner and ACI 350.3 models were 7.90 Hz and 7.94 Hz, respectively. The corresponding mass participation ratios of the second mode were 75% and 69% for the Housner and ACI 350.3 models, respectively. This information signified that the second mode dominates the total dynamic response of the Housner and ACI 350.3 models. Figures 10.3 and 10.4 show the second mode's shape for each model.

---

[91] ANSYS Mechanical, Version 17. ANSYS Software Solutions, ANSYS Inc., Canonsburg, Pennsylvania; http://www.ansys.com/ (2016).

Table 10.8 Modal information for Bauer, and Haroun and Housner models

| Mode number | Natural frequency (Hz) | Mass participation ratio | Cumulative mass participation ratio |
|---|---|---|---|
| Bauer model | | | |
| 1 | 0.35 | 2.7% | 2.7% |
| 2 | 0.48 | 0.4% | 3.1% |
| 3 | 5.81 | 96.9% | 100% |
| Haroun and Housner model | | | |
| 1 | 0.24 | 19.1% | 19.1% |
| 2 | 4.90 | 77.7% | 96.8% |
| 3 | 13.08 | 3.2% | 100% |

Since the Bauer, and Haroun and Housner models were each developed as a three-mass system, each had three significant transverse modes. Unlike the Housner and ACI 350.3 models, the mode that dominated the total dynamic response of each was different. Surveying Table 10.8, the third mode of the Bauer model had a natural frequency of 5.81 Hz and mass participation ratio of 97% indicating that the third mode dominates the total dynamic response for the Bauer model. Meanwhile, the second mode of the Haroun and Housner model had a natural frequency of 4.9 Hz and mass participation ratio of 78% according to Table 10.8. This shows that the second mode dominates the total dynamic response for the Haroun and Housner model. While the modes that dominate the total dynamic response of the Bauer and Haroun and Housner models were not the same, the dynamic properties of the dominating modes were very similar. For the Bauer, and Haroun and Housner models, the respective natural frequencies of the modes dominating total dynamic response were 5.81 Hz and 4.9 Hz with corresponding mass participation ratios of 97% and 78%, respectively. Unlike the simplified tank models, dynamic response of an empty tank or cantilever beam would normally be dominated by the first mode. Therefore, this analysis shows that higher mode effects are much more critical for liquid-filled tanks.

Comparison of the natural frequencies for the modes dominating response of each model revealed important stiffness differences between models. For the Housner, and ACI 350.3 models, the natural frequencies for the mode dominating total dynamic response were 7.9 Hz and 7.94 Hz, respectively (Table 10.7). Contrarily, the natural frequencies for the mode dominating total dynamic response of the Bauer, and Haroun and Housner models were 5.81 Hz and 4.9 Hz, respectively (Table 10.8). These natural frequency results indicated decreased stiffness for the Bauer and Haroun and Housner models compared to the Housner and ACI 350.3 models.

## 10.4 Time History Analysis of Simplified 2D Models

General dynamic behavior characteristics of all four simplified CST models were evaluated and compared using modal analysis. However, time history analysis is necessary for SPRA to determine maximum response during seismic events. To evaluate the dynamic response to seismic events, El Centro ground motion (Section 2.6) was applied to each model in the transverse direction. Maximum base shear and overturning moment are typically calculated and compared with specific failure limits during SPRA due to the common failure modes associated with them.

Similarly, maximum displacement and acceleration of NPP structures are also often commonly evaluated during SPRA.

Due to the simplified nature of the 2D CST models, maximum total base shears and overturning moments were easily obtained from the maximum response at the base of each vertical beam during time history analysis. Maximum displacements and accelerations were obtained at the top of the vertical beams for each model due to the simplified models behaving similar to a cantilever beam. Values of maximum displacement, acceleration, base shear, and overturning moment are summarized in Table 10.9 for each simplified 2D CST model. The corresponding response histories at the locations of maximum response are shown in Figures 10.7 through 10.10.

Table 10.9 Maximum dynamic response comparison of all simplified 2D CST models

| Model | Displacement (in.) | Acceleration (ft/s$^2$) | Base shear (kip) | Overturning moment (kip-ft) |
|---|---|---|---|---|
| Housner | 0.139 | 24.71 | 1240 | 17110 |
| ACI 350.3 | 0.136 | 24.49 | 1212 | 16713 |
| Bauer | 0.239 | 24.43 | 1631 | 28915 |
| Haroun and Housner | 0.225 | 20.22 | 1779 | 27468 |

Results from time history analysis revealed similar dynamic response properties as modal analysis results. Maximum displacements and accelerations of the Housner and ACI 350.3 models were very similar. Maximum displacements were recorded as 0.139 in. and 0.136 in. for the Housner and ACI 350.3 models, respectively (Table 10.9). Similarly, maximum accelerations for the Housner and ACI 350.3 models were 24.71 ft/s$^2$ and 24.59 ft/s$^2$, respectively. The maximum displacements for the Bauer, and Haroun and Housner models were also very similar. The maximum displacements for the Bauer and Haroun and Housner models were 0.239 in. and 0.225 in., respectively (Table 10.9). The larger maximum displacements for the Bauer and Haroun and Housner models verified the decreased stiffness compared to the Housner and ACI 350.3 models that was shown in modal analysis. Figures 10.7 and 10.8 show the displacement and acceleration response histories for all simplified 2D CST models. The displacement and acceleration response histories for the Housner and ACI 350.3 models were nearly identical. However, the displacement and acceleration response histories for the Bauer and Haroun and Housner models were not similar.

The maximum base shears and overturning moments from time history analyses followed the same tendencies as the maximum displacements and accelerations for all simplified 2D CST models. For the Housner and ACI 350.3 models, the maximum base shears and overturning moments were very similar. The maximum base shears were recorded as 1240 kips and 1212 kips, respectively, in Table 10.9 for the Housner and ACI 350.3 models. The maximum overturning moments for the Housner and ACI 350.3 models 17,110 kip-ft and 16,713 kip-ft. Likewise, the Bauer, and Haroun and Housner models had similar maximum base shear and overturning moment responses. According to Table 10.9, the maximum base shear for the Bauer, and Haroun and Housner models were 1631 kips and 1779 kips, respectively, whereas the maximum overturning moments were 28,915 kip-ft and 27,468 kip-ft, respectively. Similar to the displacement and acceleration response histories, response histories for base shear and overturning moment (Figures 10.9 and

10.10) were very similar for the Housner and ACI 350.3 models but significantly different for the Bauer, and Haroun and Housner models.

As shown by the dynamic analysis of the simplified 2D CST models, models with one convective mass and one impulsive mass, Housner and ACI 30.3, were nearly equivalent. The dynamic properties and responses of the simplified models with two convective masses and one impulsive mass, Bauer, and Haroun and Housner models were similar but not identical. For this reason, only the Housner, Bauer, and Haroun and Housner models were used for comparison against the 3D FE model.

### 10.5 Comparison of 2D and 3D Models

To evaluate the limitations of the 2D CST models, a comparison of the dynamic properties and responses of the simplified 2D and detailed 3D models was completed. Modal analysis results were used to evaluate and compare the general dynamic properties of each model while time history analysis results were used to evaluate and compare the dynamic response of each model when subjected to seismic events.

The detailed 3D model was developed using FEs in ANSYS by another researcher on this project. Initial modeling and analysis results showed encouraging comparison of 2D and 3D modal analysis results in Hur et al. Another researcher on this project has since developed new modeling and analysis techniques subsequent to the Hur et al. paper. These improvements focused on a more appropriate comparison to the simplified models that focused on evaluating forces that were imparted on the tank wall during seismic events. The most recent 3D FE model results produced by the fellow researcher are used in this chapter.

#### 10.5.1 Modal Analysis

The simplified 2D CST models can only capture either two or three significant mode shapes. However, due to the 3D FE model having significantly many more degrees-of-freedom (DOFs) compared to the simplified 2D models, the 3D FE model captures significantly many more modes. A significant number of the extra mode shapes correspond to different modes of liquid sloshing in the tank. For simplified models, each model either had only one or two modes of liquid sloshing, also called convective modes, due to the mass they were associated with. The 3D FE model also captures many more modes associate with the portion of water that deformed with the tank structure whereas each simplified model either captures one or two. These modes can also be called impulsive modes due to the mass they were associated with in simplified models.

For comparison purposes, only a few significant modes were retrieved from the 3D FE model’s results. These modes included two convective modes and one significant impulsive mode. The natural frequencies of these three modes are summarized in Table 10.10. Corresponding mode shapes for the 3D FE model are shown in Figure 10.11. Due to the symmetrical nature of the tank and water in both transverse directions in the 3D FE model, only natural frequencies and mode shapes for one transverse direction are shown in Table 10.10 and Figure 10.11. Modal information in both transverse directions is the same for this 3D FE model due to its symmetrical nature.

Table 10.10 Comparison of natural frequencies for significant modes in simplifed 2D and detailed 3D CST models

| Mode | Natural frequency (Hz) | | | |
|---|---|---|---|---|
| | Housner | Bauer | Haroun and Housner | 3D model |
| Convective | 0.24 | 0.35 | 0.24 | 0.24 (mode 1) |
| | | | | 0.31 (mode 3) |
| Impulsive | 7.90 | 5.81 | 4.90 | 6.56 (mode 55) |

The significant convective mode captured by both 2D and 3D models had very similar natural frequencies in Table 10.10. The natural frequencies of the Housner, Haroun and Housner, and 3D FE model were all 0.24 Hz while the Bauer model's significant convective mode had a natural frequency of 0.35 Hz. The mode shape captured by the 3D FE model for this mode (Figure 10.11) was also similar to the liquid sloshing behavior discussed in Section 2.3 that the developers of the simplified models wished to capture by the convective mass. However, the 3D FE model also captured many other sloshing modes and corresponding shapes. For example, the second convective mode for the 3D FE model is shown in Table 10.10 and its corresponding shape in Figure 10.11. Many more convective modes were captured but are not shown.

The significant impulsive mode captured by the 3D FE model was also similar to the impulsive modes captured by simplified models. According to Table 10.10, the natural frequency of the 3D FE model's impulsive mode was 6.56 Hz. Comparing this to the corresponding natural frequencies of simplified models in Table 10.10, the natural frequency of the 3D FE model was between that of the Housner model; and the Bauer, and Haroun and Housner models. Recalling from Section 10.3 that the impulsive mode dominated the total dynamic response of the simplified models, the modal analysis results indicated that the 3D FE model had more stiffness than the Bauer and Haroun and Housner models, but less stiffness than the Housner model.

### 10.5.2 Time History Analysis

For dynamic response of simplified models, displacements, accelerations, base shears, and overturning moments resulting from time history analyses were investigated. However, to compare simplified models to the 3D FE model, only base shears and overturning moments were investigated. From the derivation of the simplified models in Section 2.3, only these two parameters corresponded to the original intention of the simplified models.

Similar to simplified 2D models, El Centro ground motion (Section 2.6) was applied in a transverse direction to the 3D FE model for time history analysis. As SPRA typically focuses on the maximum response of a structure during seismic events, maximum responses from time history analysis were the focus of comparison. Table 10.11 summarizes the maximum base shears and overturning moments of 2D and 3D models. The response histories for base shear and overturning moment are shown in Figures 10.12 and 10.13.

Maximum dynamic response results in Table 10.11 indicated similar dynamic behavior as modal analysis. For the 3D FE model, the maximum base shear and overturning moment from time history analysis were 1373 kips and 22,035 kip-ft according to Table 10.11. These values for maximum dynamic response of the 3D FE model were between those in Table 10.11 for the

Housner, Bauer, and Haroun and Housner models. These results confirmed the conclusions from comparison of 2D and 3D models during modal analysis, i.e., the rigidity and dynamic properties of the 3D FE model is somewhere between Housner model and the other two 2D models. The larger maximum base shears and overturning moments in the Bauer and Haroun and Housner models signified these models had less stiffness than the 3D FE model. Similarly, the smaller base shears and overturning moments in the Housner model implied this simplified model had a larger stiffness than the 3D FE model.

Table 10.11 Maximum dynamic response comparison of 2D and 3D CST models

| Model | Base shear (kip) | Overturning moment (kip-ft) |
|---|---|---|
| Housner | 1240 | 17,110 |
| Bauer | 1631 | 28,915 |
| Haroun and Housner | 1779 | 27,468 |
| 3D FE Model | 1373 | 22,035 |

The response histories of 2D and 3D models for base shear and overturning moment (Figures 10.12 and 10.13) showed the same general properties as modal analysis results and maximum dynamic response results. In general, the Bauer, and Haroun and Housner models overestimated the base shear and overturning moment of the 3D FE model throughout the entire history. Interestingly, the response histories for the Housner and 3D FE models were similar throughout the entire history except at a few points of peak response.

### 10.6 Failure Analysis of Simplified 2D Models

The adequacy of the CST for a site in the Central and Eastern United States (CEUS) was evaluated using the ground motions developed by RIZZO Associates, Inc. (Section 2.6). To determine its adequacy, two scenarios for the anchorage of the CST to its foundation were investigated. The first scenario used twelve anchors to connect the CST to its foundation. The second scenario used 78 anchors to connect the CST to its foundation. Project collaborators at RIZZO Associates, Inc. calculated base shear and overturning moment capacities for the CST using the steel tank's material properties. Capacities were calculated based on methods from several current standards (EPRI 6041 1991, EPRI TR-103959 1994) for liquid-filled storage tanks to prevent sliding and buckling of the tank walls during seismic behavior. For the CST with twelve anchors, the overturning moment capacity of the tank was as 30,707 kip-ft. For the CST with 78 anchors, the base shear capacity was 2584 kips.

In total, project collaborators from RIZZO Associates, Inc. developed 25 three-dimensional CEUS ground motion sets. However, due to the 2D nature of the simplified CST models, the two horizontal directions from each ground motion set were separated into a total of 50 CEUS ground motion sets for the analysis of the simplified CST models. Furthermore, to be consistent with the derivation of the simplified models, the vertical ground motions were neglected, and only the horizontal ground motions were applied to 2D CST models.

An analysis of each simplified model with the CEUS ground motions was completed. Results revealed that the maximum dynamic responses were not large enough to exceed the limit states for base shear and overturning moments. In order to exceed the limit states, the time histories of all 50 CEUS ground motions were linearly scaled to investigate the linearity of the simplified system. Results verified each simplified system captured linear responses to the scaled ground motions. The maximum dynamic responses from the original CEUS ground motions were then linearly scaled (1, 1.1, 1.2,…, 8) for the maximum dynamic responses from all 50 ground motions to reach the limit states for base shear and overturning moment (Figures 10.14 and 10.15). For each CEUS ground motion scale factor (1, 1.1, 1.2,…, 8), a "fail" or "no fail" criteria for each limit state was evaluated for all 50 ground motions. The total number of "fails" was then calculated for each scale factor and divided by the total number of ground motions per scale factor (50) to determine the failure percentage of each CEUS ground motion scale factor. This analysis was completed for all four simplified CST models.

It is important to note that linearly scaling ground motions similar to this extent is not appropriate for a true seismic risk analysis. Development of ground motions for different response spectrums should realistically be done. However, linearly scaling the ground motions to illustrate the basic seismic response characteristics of the simplified CST models was perceived as suitable. In that respect, the results from Figures 10.14 and 10.15 reinforce results from analysis in Sections 10.3 and 10.4 while also giving some insight into the seismic capacity of each simplified CST model. The Housner and ACI 350.3 models had nearly identical failure percentages for all CEUS ground motion scale factors for both base shear and overturning moment. The scale factor at which all 50 ground motions exceeded the overturning moment limit state was 5.3, which equated to peak ground acceleration (PGA) values around 1.1g. The Bauer, and Haroun and Housner models also had comparable failure percentages for all scale factors for overturning moment. The scale factor where all 50 ground motions exceeded the overturning moment limit state was 3.4 for the Bauer and Haroun and Housner models. This scale factor equated to PGA values around 0.7g for each ground motion. The Bauer, and Haroun and Housner models did not result in similar failure percentages for base shear. Figure 10.14 illustrates how the Bauer model required larger scale factors to reach 100% of responses beyond the base shear limit state.

### 10.7 Summary and Conclusions

To evaluate the dynamic characteristics of liquid-filled storage tanks at NPPs, structural properties for a CST were retrieved from literature and used to develop models for a realistic CST. Four simplified 2D CST models were developed based on models developed by previous researchers discussed in Althoff. Modal and time history analyses were completed for all four simplified models to evaluate and compare the dynamic characteristics and response of each. Finally, to evaluate the limitations of the simplified models, their modal and time history analysis results were compared to those from a detailed 3D FE model developed in Hur et al. that incorporated the fluid-structure interaction that was neglected in simplified models.

Since SPRA is typically concerned with the maximum responses of structures during seismic events, the dynamic analysis results of simplified models created two distinct groups of simplified CST models. The Housner and ACI 350.3 models were shown to be nearly equivalent models with similar modal analysis results in Table 10.7 and maximum dynamic response results in Table 10.9. The Bauer, and Haroun and Housner models were also shown to be nearly equivalent models with similar modal analysis results in Table 10.8 and maximum dynamic response results in Table

10.9. Smaller maximum displacements in Table 10.9 for the Housner and ACI 350.3 models indicated more rigid models, whereas the larger displacements in Bauer and Haroun and Housner models indicated more flexibility. The increased flexibility introduced in the Bauer and Haroun and Housner models corresponded to larger maximum base shears and overturning moments during time history analysis. Shown in Table 10.9, the maximum base shears and overturning moments for the Bauer and Haroun and Housner models were approximately 1700 kips and 28,190 kip-ft, whereas the maximum base shears and overturning moments for the Housner and ACI 350.3 models were around 1225 kips and 16,900 kip-ft.

A comparison of the dynamic properties of simplified 2D and detailed 3D models showed that the dynamic response of the detailed 3D model was between that of the two groups of simplified models. Modal analysis results for the simplified 2D model (Tables 10.7 and 10.8) showed the natural frequencies of the modes dominating total dynamic response were 7.9 Hz, 5.81 Hz, 4.9 Hz, and 9.56 Hz for the Housner, Bauer, Haroun and Housner, and 3D FE models, respectively. Similarly, maximum base shear and overturning moment from time history analysis for the 3D FE model were 1373 kips and 22,035 kip-ft in Table 10.11. These values for the 3D FE model were almost exactly halfway between the corresponding values for the two groups of simplified models. As shown, the total dynamic behavior of all models indicated that the more rigid simplified models underestimated dynamic response of the 3D FE model, whereas the more flexible models overestimated dynamic response of the 3D FE model.

A failure analysis of the simplified CST models was also completed to evaluate the adequacy of the CST investigated for a Central and Eastern United States (CEUS) site. A total of 50 ground motions developed for a CEUS response spectra were applied to all four simplified models, and the maximum base shear and overturning moment responses from each were compared to limit states. Results indicated that a minimum linear scale factor of 3 for the ground motions was needed for any response from the 50 ground motions to reach the limit states. This scale factor corresponded an approximate PGA of 0.6g. Scale factors of up to 6 were needed for some ground motions to reach the base shear limit state, which equated to a PGA around 1.2g. These results indicated that the CST was reasonably safe for a CEUS site.

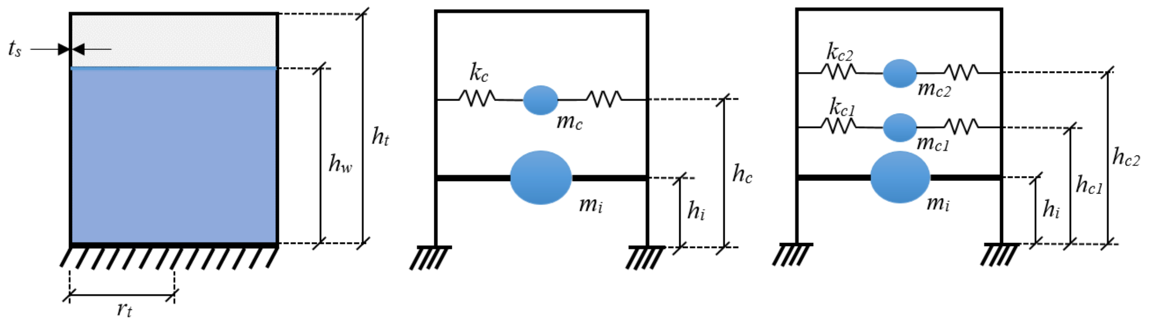

(a) (b) (c)

Figure 10.1 Simplified 2D liquid-filled storage tank models: (a) 2D elevation of original CST, (b) Housner or ACI 350.3, and (c) Bauer, or Haroun and Housner

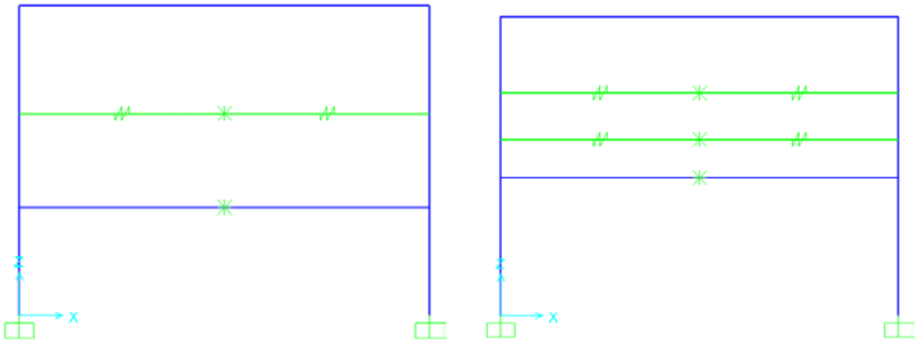

(a) (b)

Figure 10.2 SAP2000 models of simplified 2D liquid-filled storage tanks: (a) Housner or ACI 350.3, and (b) Bauer, or Haroun and Housner

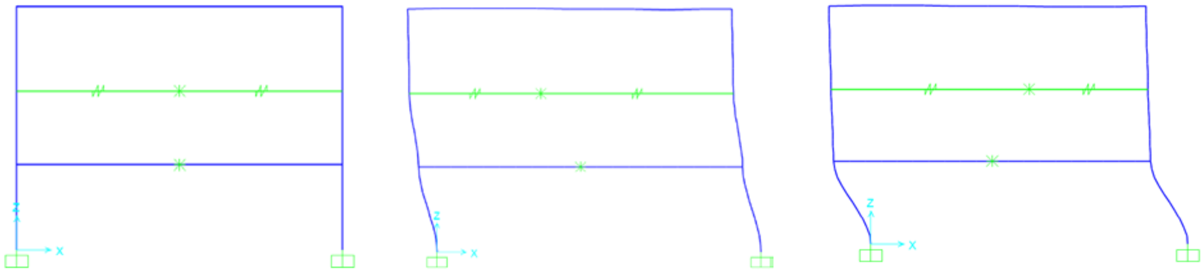

(a) (b) (c)

Figure 10.3 Mode shapes for Housner model: (a) undeformed shape, (b) mode 1, and (c) mode 2

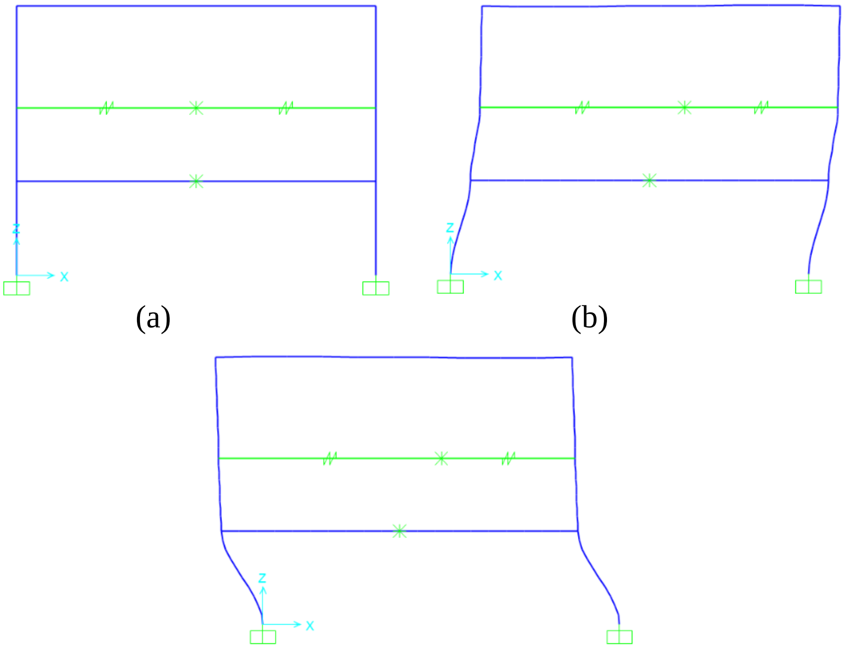

(a) (b)

(c)

Figure 10.4 Mode shapes for ACI 350.3 model: (a) undeformed shape, (b) mode 1, and (c) mode 2

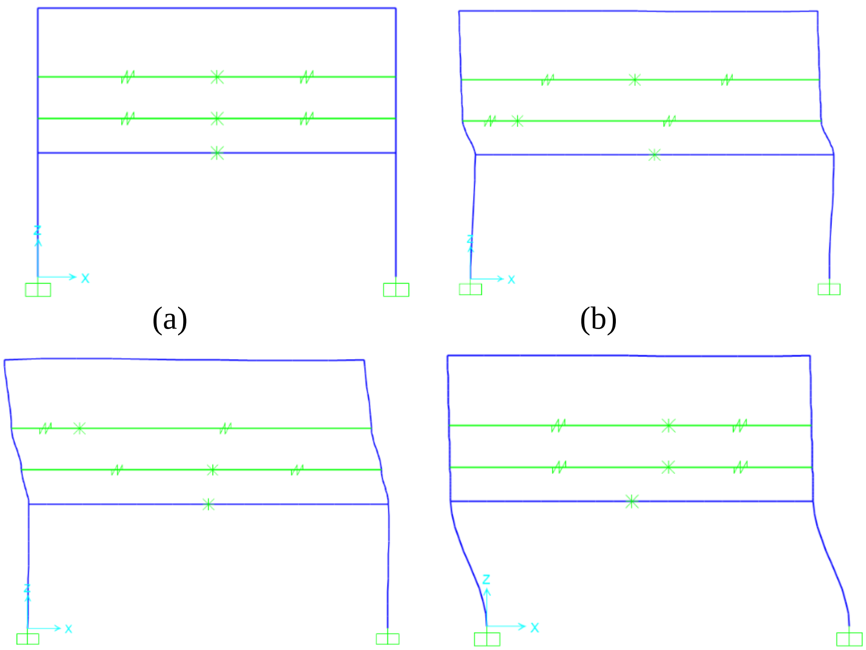

(a) (b)

(c) (d)

Figure 10.5 Mode shapes for the Bauer model: (a) undeformed shape, (b) mode 1, (c) mode 2, and (d) mode 3

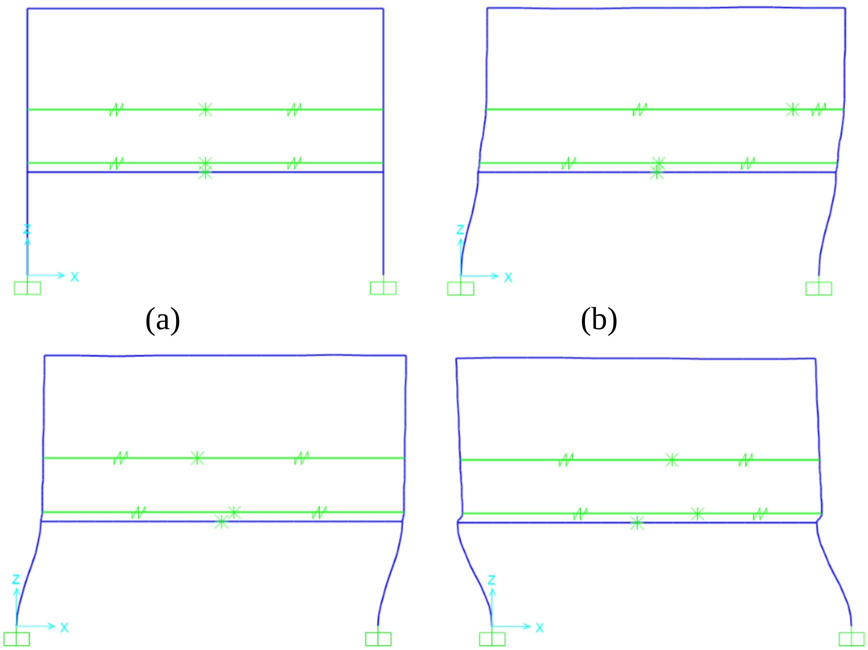

(a) (b)

(c) (d)

Figure 10.6 Mode shapes for the Haroun and Housner model: (a) undeformed shape, (b) mode 1, (c) mode 2, and (d) mode 3

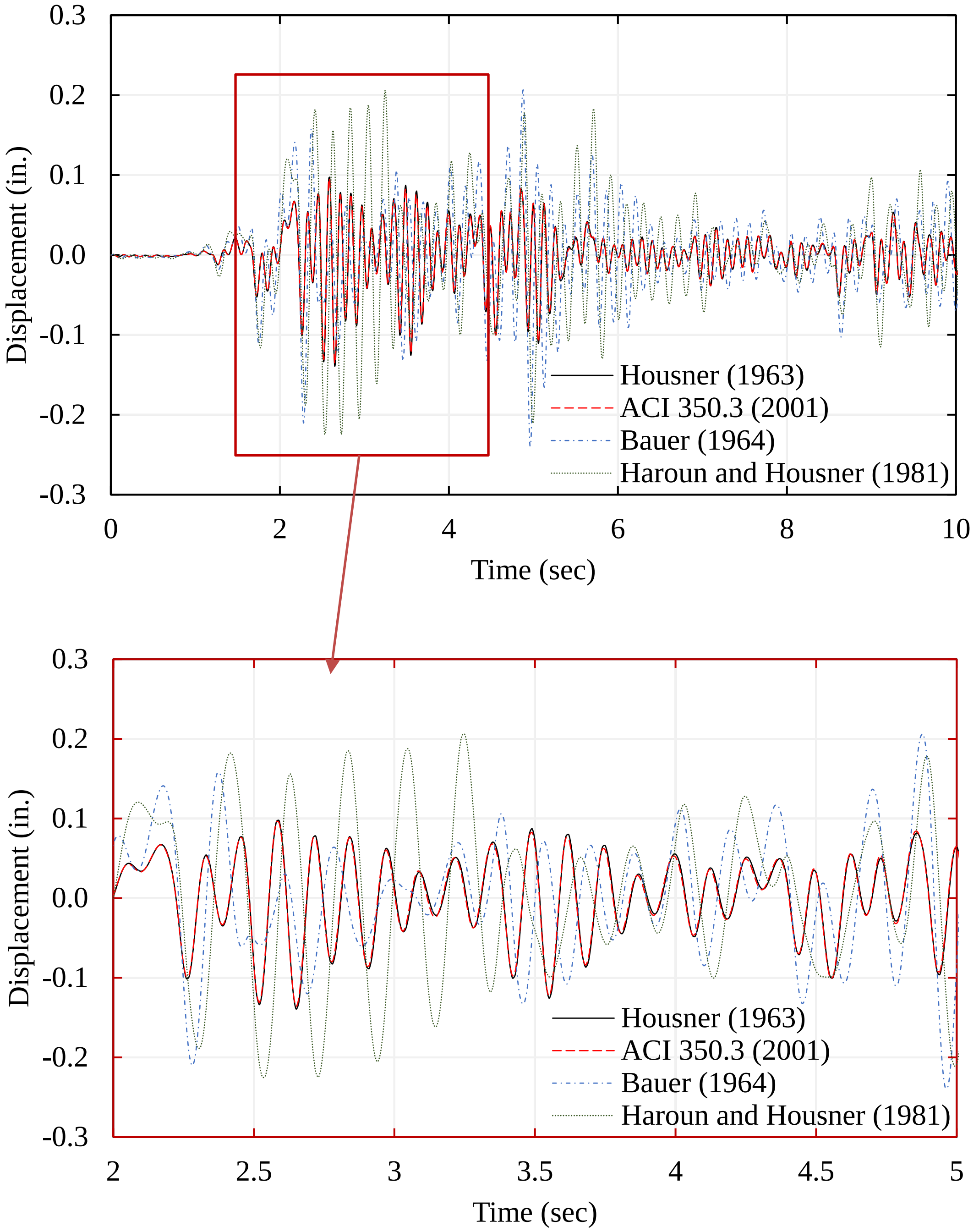

Figure 10.7 Displacement response history comparison of simplified 2D CST models

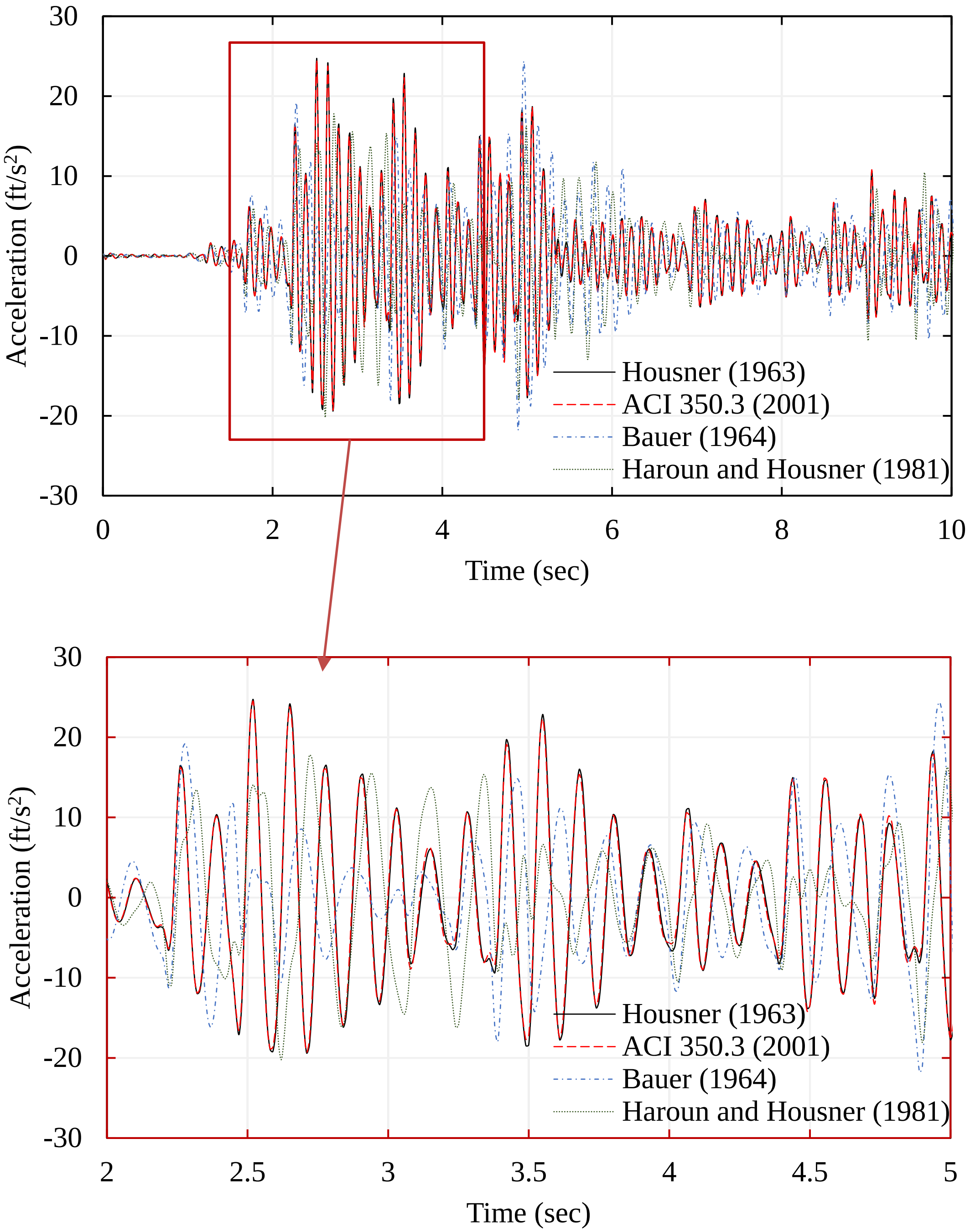

Figure 10.8 Acceleration response history comparison of simplified 2D CST models

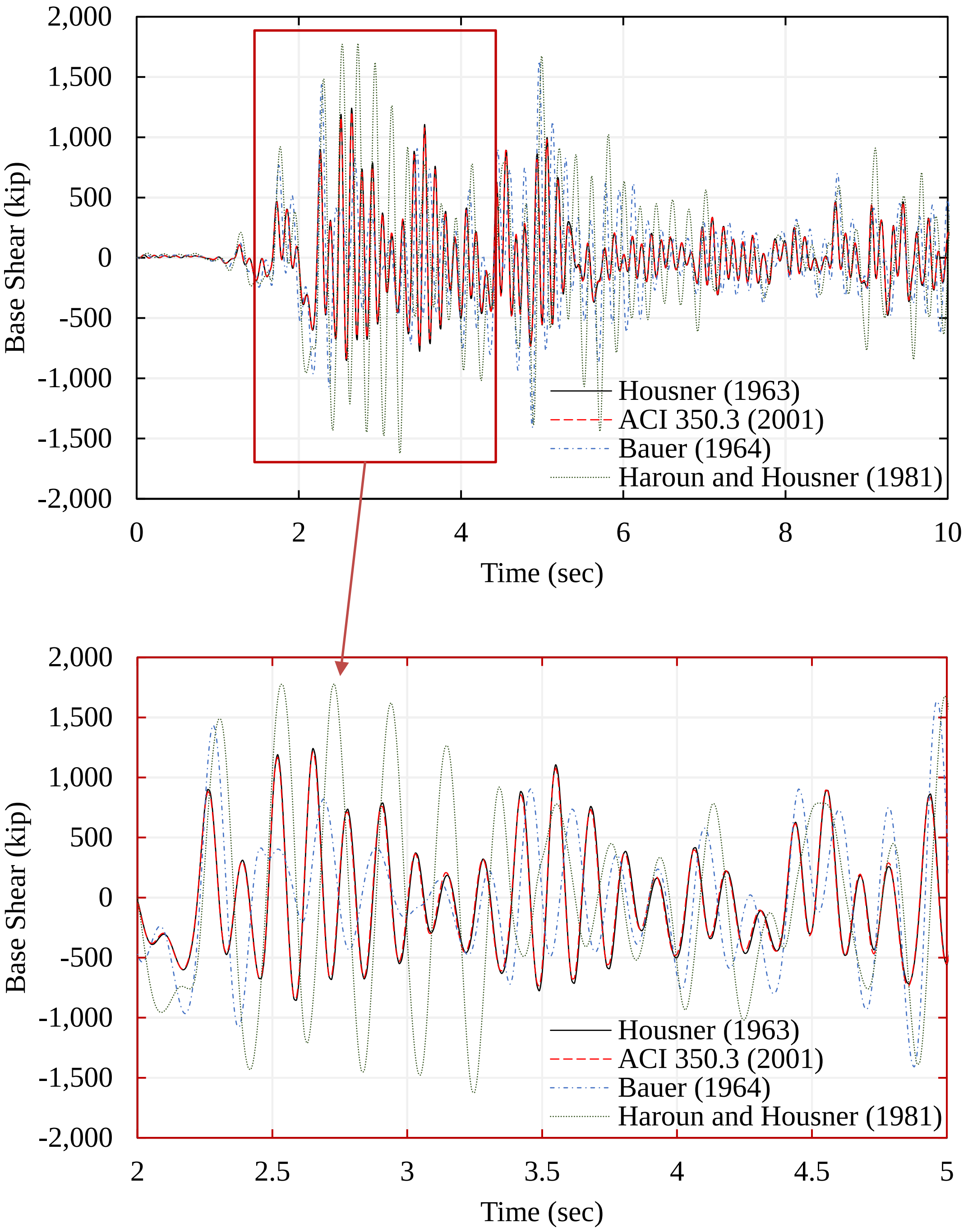

Figure 10.9 Base shear response history comparison of simplified 2D CST models

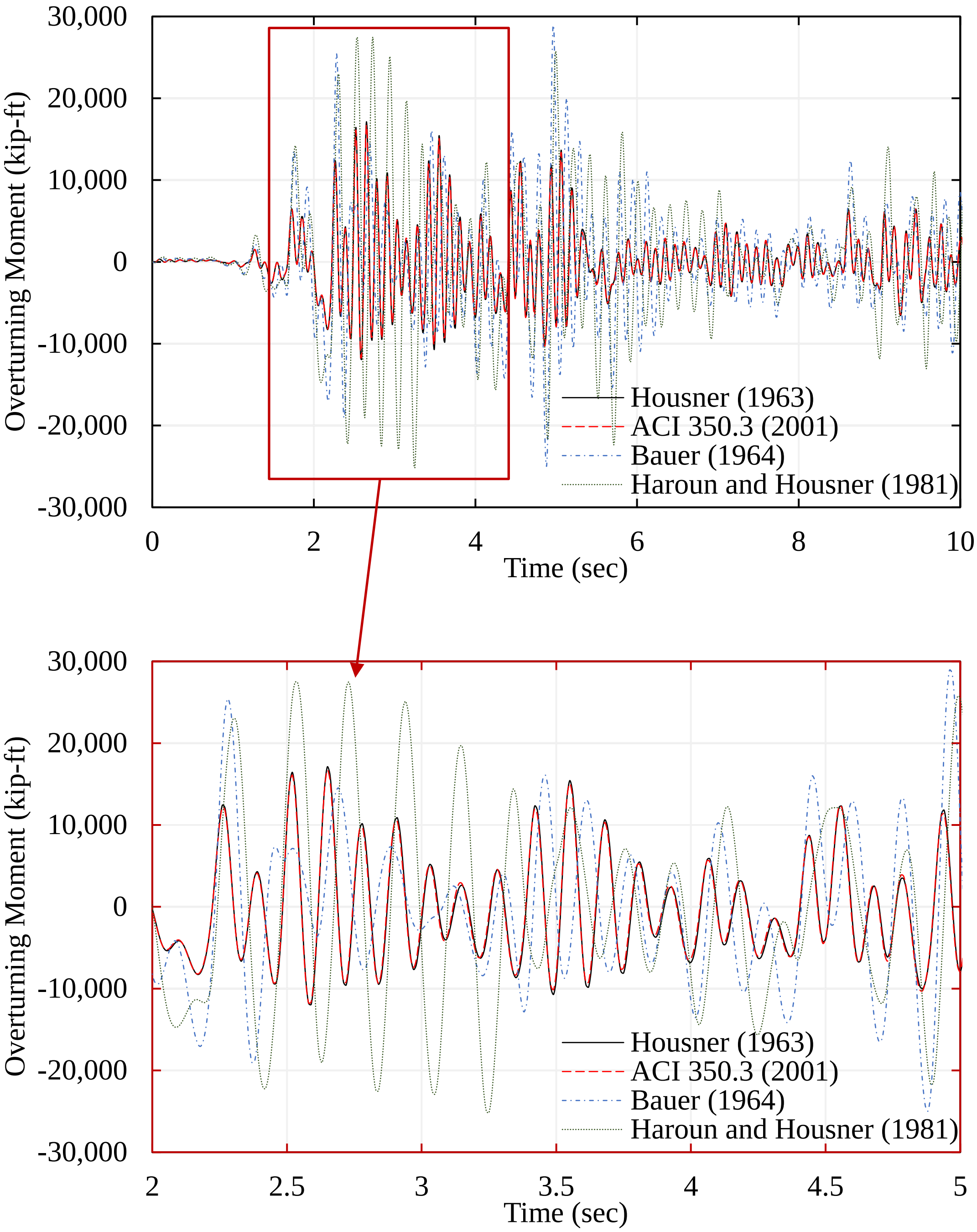

Figure 10.10 Overturning moment response history comparison of simplified 2D CST models

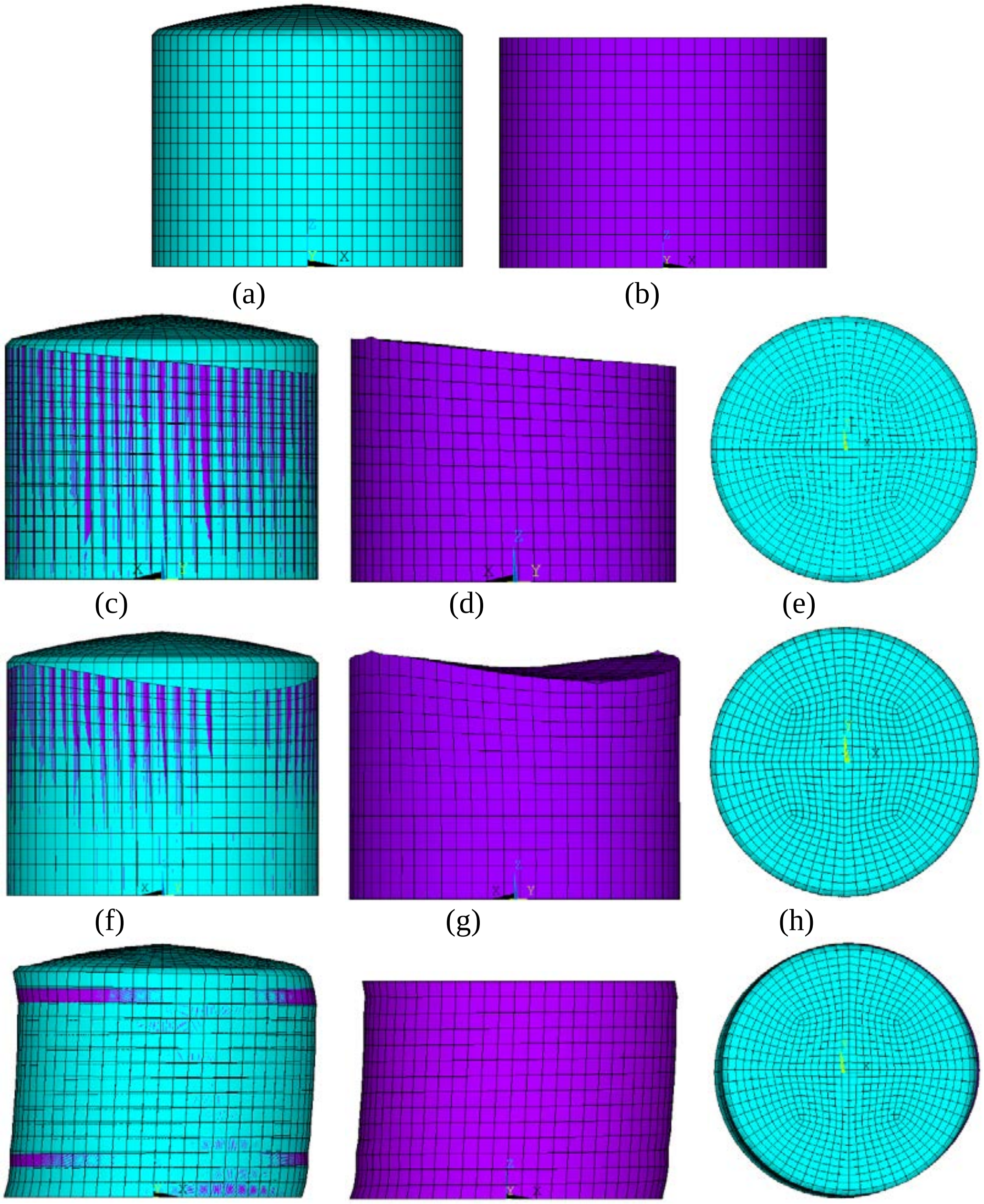

(a) (b)

(c) (d) (e)

(f) (g) (h)

(i) (j) (k)

Figure 10.11 Mode shapes for the 3D FE model: (a) undeformed shape of tank, (b) undeformed shape of water, (c) tank and water side view of first convective mode, (d) water side view of first convective mode, (e) top view of first convective mode, (f) tank and water side view of second convective mode, (g) water side view of second convective mode, (h) top view of second convective mode, (i) tank and water side view of impulsive mode, (j) water side view of impulsive mode, and (k) top view of impulsive mode

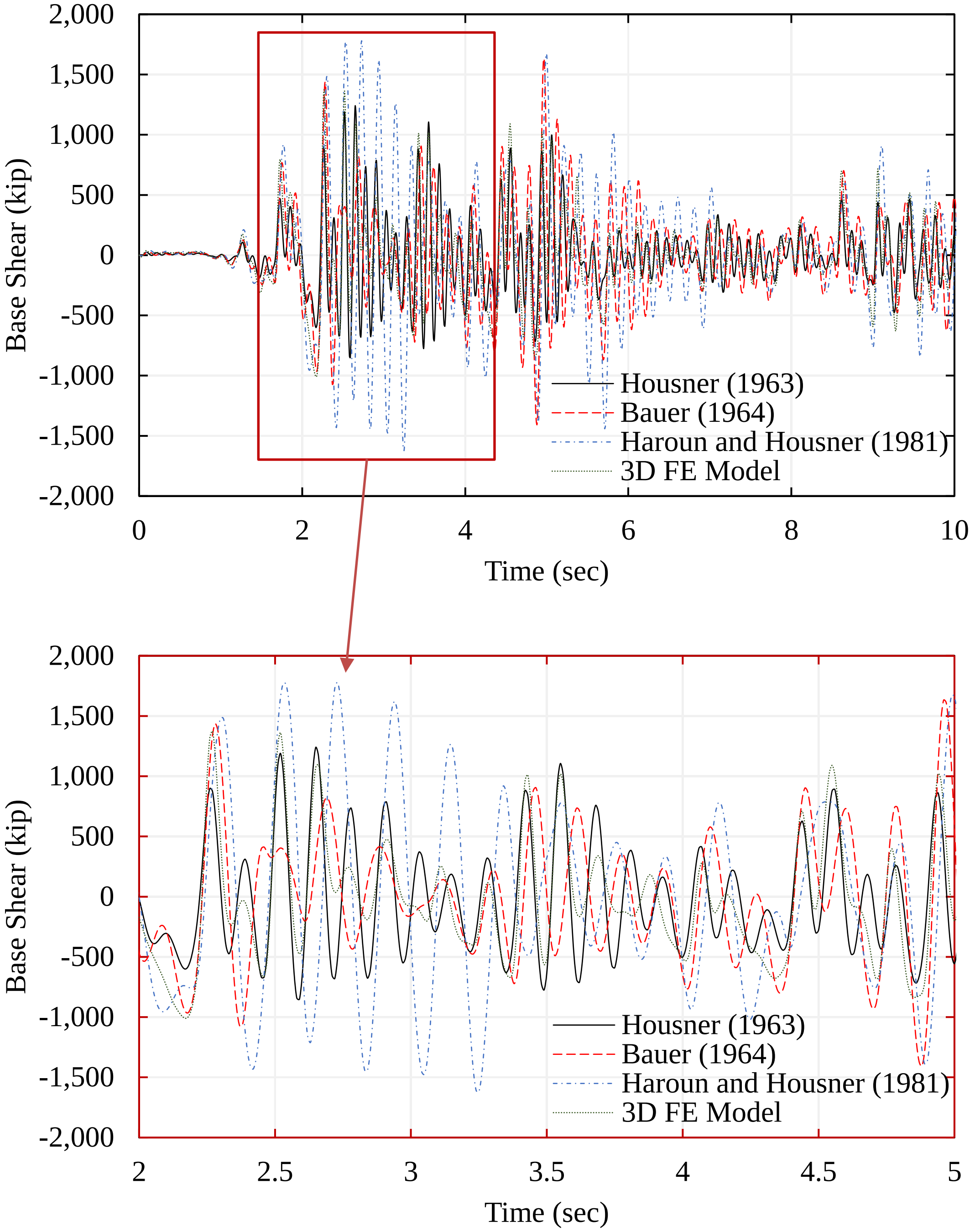

Figure 10.12 Base shear response history comparison of 2D and 3D CST models

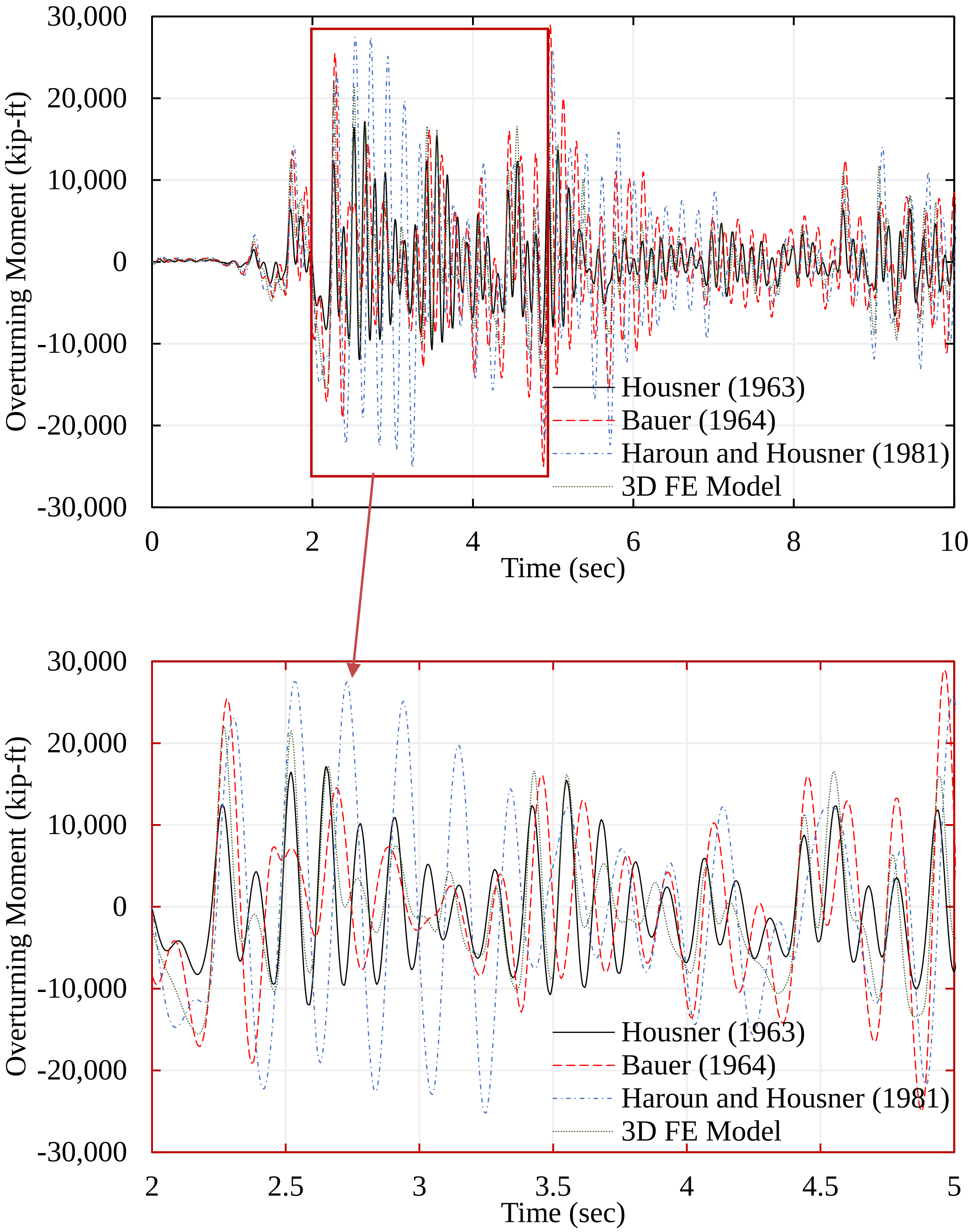

Figure 10.13 Overturning moment response history comparison of 2D and 3D CST models

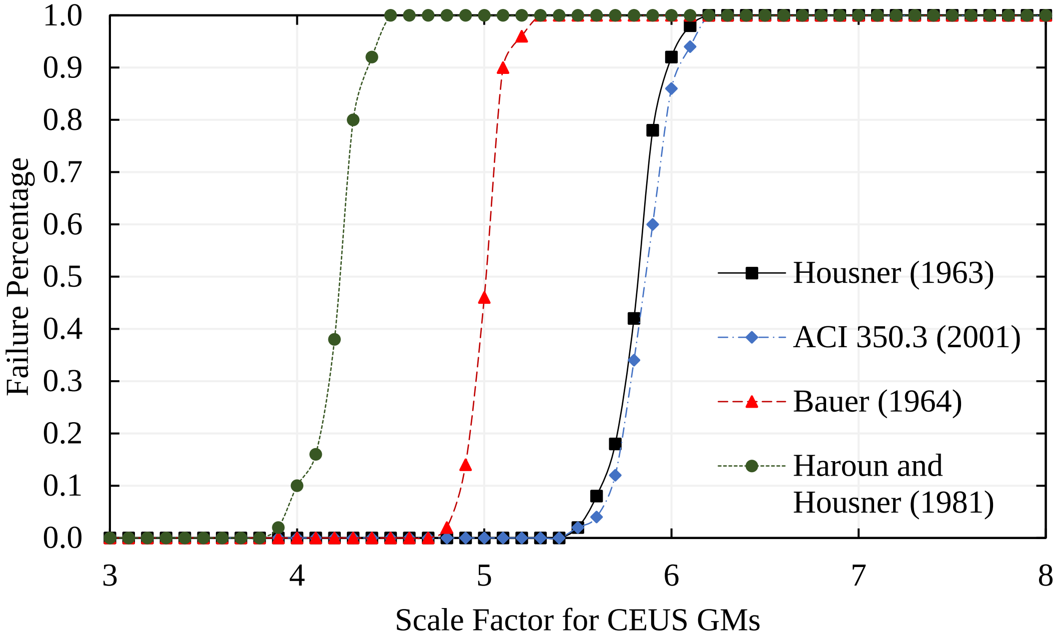

Figure 10.14 Base shear failure analysis of simplified CST models

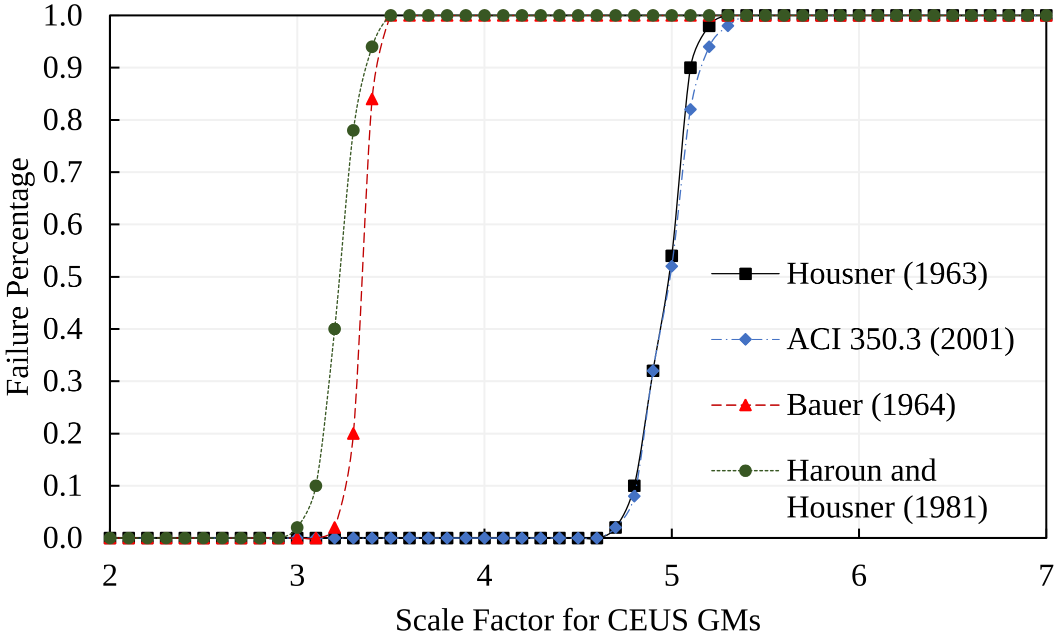

Figure 10.15 Overturning moment failure analysis of simplified CST models

# 11. CASE STUDY 4: CONTAINMENT STRUCTURE AND POLAR CRANE ANALYSIS

## 11.1 Background

In order to perform SPRA of NPPs, seismic analysis of critical NPP structures must be conducted. The seismic analysis of structures requires development of realistic and accurate physical and theoretical models to accurately determine their response, which is significantly influenced by both the ground motion characteristics and dynamic properties of the structures. Thus comparion of the the simplified stick models and detailed 3D FE model development is one of the steps to be performed in the seismic probabilistic risk assessment.

In the following sections, assumptions and procedures for modeling of a containment building structure are described. Three-dimensional FE and simplified models, including lumped and distributed mass stick models, of the containment structure are developed and analyzed. Then, the results are compared. Lumped mass stick model is the commonly used method in the industry due to its simplicity and ability to quickly determine the approximate dynamic response. Modal and time history analyses are more accurate and are performed using different structural analysis programs including SAP2000[92] and ANSYS[93].

Although it is not a real existing NPP structure, a PWR example problem found in the SASSI Manual[94] provides enough details for the containment model used in this research. Structural models of the containment building are developed using the data given in the SASSI Manual.

## 11.2 Description of Containment Structure

Perhaps the most critical structure for SPRA at a NPP is the containment structure. According to the United States Nuclear Regulatory Commission (NRC), the containment structure's primary purpose is to contain radioactivity from the reactor vessel that could otherwise be released from the plant during an accident scenario. Most containment structures are heavily reinforced concrete or post-tensioned concrete structures with a cylindrical lower part and dome-shaped upper section (NRC 2017).

Besides the nuclear reactor stored within the containment structure, another piece of equipment of particular importance is the polar crane. According to NuCrane Manufacturing, polar cranes are used during refueling to lift heavy equipment such as the reactor heads, reactor internals, and other miscellaneous loads (NuCrane Manufacturing 2017). Due to the high rigidity of the containment structure, structural failure during seismic events is less likely than failure of nonstructural components (NCs). Failure of the polar crane during seismic events, for example, could also lead to radioactive release. The polar crane is of particular interest due to its high location, and therefore dynamic response, and the consequences its failure would have on the overall risk to a plant. To investigate the safety of NCs in the containment structure, a case study using the polar crane is completed and presented in this chapter.

---

[92] SAP2000, Computers and Structures, Inc., Berkeley, CA, www.csiberkeley.com (2016).

[93] ANSYS Mechanical, Version 17. ANSYS Software Solutions, ANSYS Inc., Canonsburg, Pennsylvania; http://www.ansys.com/ (2016).

[94] SASSI, Structural Analysis Software System Interface, http://www.dnfsb.gov/sites/default/files/Board%20Activities/Letters/2011/ltr_20111227_18206.pdf

Although structural failure of the containment structure is less likely than NCs, a model to predict its dynamic response is needed to determine the dynamic response of NCs inside or attached to the containment structure. Both 2D and 3D models using SAP2000 and ANSYS were created for the containment structure. Finite elements were used for 3D models. For simplified 2D models, a lumped-mass stick model was adopted. Containment structure models were formulated based on a realistic containment structure found in literature (Figure 11.a, Ostadan 2000). A realistic polar crane was later added to the 3D FE model in SAP2000. The stresses and deflections that the crane girders undergo during seismic events were investigated, and failure analyses were completed as part of a case study.

## 11.1 Containment Structure Model

A realistic containment structure (Ostadan 2000) was chosen in this study (Figure 11.a). The containment structure was designed as a reinforced concrete structure with a cylindrical lower part and dome-shaped upper section. Its geometric and material properties are shown in Tables 11.1

Table 11.1 Geometric and material properties of containment structure

| Geometric properties | |
|---|---|
| Height to top of cylindrical section (ft) | 143.8 |
| Height to top of dome section (ft) | 208.3 |
| Thickness of cylindrical section (ft) | 3.5 |
| Thickness of dome section (ft) | 2.5 |
| Radius to interior face of cylindrical section (ft) | 62 |
| Material properties | |
| Elastic Modulus of Concrete (ksf) | 690,000 |
| Shear Modulus of Concrete (ksf) | 270,000 |
| Density of Concrete (kcf) | 0.15 |

After the simplified and detailed models for the containment structure were developed, a polar crane was added to the SAP2000 3D FE model. The geometric and material properties for the polar crane system are shown in Table 11.2. A particular difficulty of the polar crane was the details of the connection between the crane girders and the concrete wall of the containment structure. In reality, the crane girders are connected to the main structure of the containment building by a rail system. However, it was assumed for modeling simplicity that the crane girders were either pinned or fixed to the containment structure walls to allow no translation in any direction. The crane girders themselves were a rectangular steel tube section with two 2 in. thick horizontal plates and two 1 in. thick vertical plates.

Table 11.2 Geometric and material properties of the polar crane

| Geometric properties | |
|---|---|
| Girder span (ft) | 120 |
| Girder spacing (ft) | 28 |
| Outer width of tube girder (ft) | 5 |
| Inner width of tube girder (ft) | 4.83 |
| Outer height of tube girder (ft) | 11.67 |
| Inner height of tube girder(ft) | 11.33 |
| Material properties | |
| Weight of trolley (kips) | 200 |
| Elastic modulus of crane steel (ksf) | 4,176,000 |
| Poisson's ratio for crane girder steel | 0.3 |
| Density of crane steel (kcf) | 0.49 |

## 11.2 Description of Structural Model

Both simplified 2D and detailed 3D models were developed for the containment structure to investigate the capabilities and limitations of each for SPRA. For 2D models, a lumped-mass stick model was adopted. Due to the simplicity and symmetrical nature of the actual structure, simplified models are able to mimic any transverse direction of the structure with just one 2D stick model. For this reason, simplified models are more suitable for a simple symmetrical structure compared to a structure with significant mass, stiffness, or geometric irregularity. Finite elements (FEs) were used to develop a detailed 3D model. Modeling and investigation of 2D stick models was completed in SAP2000, whereas 3D FE models were created in both SAP2000 and ANSYS.

### 11.2.1 Simplified 2D Model

In this research, simplified 2D lumped-mass stick models were used. In addition to the geometric and material properties provided by Ostadan[95] for a realistic containment structure, structural properties for the vertical beams and lumped-masses for a 2D stick model were provided above. This information included properties such as weight for each lumped-mass, shear area for each vertical beam, and moment of inertia for each vertical beam. Slight modifications were made from the 2D stick model provided by Ostadan to be consistent with the actual geometry of the 3D containment structure. The structural properties used for the 2D lumped-mass stick model in this research are shown in Tables 11.3 and 11.4. The final SAP2000 model of the 2D stick model is shown in Figure 11.1.

---

[95] Ostadan, F. *SASSI 2000: A System for Analysis of Soil-Structure Interaction* User's Manual. Berkeley, CA: University of California, Berkeley. (2000).

Table 11.3 Lumped-mass values and location for 2D stick model of containment structure

| Mass number | Height from base, $h_i$ (ft) | Mass, $m_i$ (kip-s/ft$^2$) |
|---|---|---|
| 1 | 0 | 77.716 |
| 2 | 23.8 | 143.024 |
| 3 | 43.8 | 130.615 |
| 4 | 63.8 | 130.615 |
| 5 | 83.8 | 130.615 |
| 6 | 103.8 | 130.615 |
| 7 | 123.8 | 130.615 |
| 8 | 143.8 | 115.122 |
| 9 | 165.3 | 94.013 |
| 10 | 184.4 | 76.795 |
| 11 | 198.5 | 55.285 |
| 12 | 208.3 | 22.688 |

Table 11.4 Structural properties of vertical beams for 2D stick model of containment structure

| Beam number | Area, $A_i$ (ft$^2$) | Shear area, $V_i$ (ft$^2$) | Moment of inertia, $M_i$ (ft$^4$ x10$^6$) |
|---|---|---|---|
| 1 | 1401.9 | 701.0 | 2.85 |
| 2 | 1401.9 | 701.0 | 2.85 |
| 3 | 1401.9 | 701.0 | 2.85 |
| 4 | 1401.9 | 701.0 | 2.85 |
| 5 | 1401.9 | 701.0 | 2.85 |
| 6 | 1401.9 | 701.0. | 2.85 |
| 7 | 1401.9 | 701.0 | 2.85 |
| 8 | 994.7 | 497.4 | 1.93 |
| 9 | 993.5 | 496.8 | 1.51 |
| 10 | 992.5 | 496.3 | 0.859 |
| 11 | 994 | 497.0 | 0.224 |

### 11.2.2 Detailed 3D Models

Detailed 3D finite element (FE) models of the containment structure were developed using the geometric and material properties outlined in Table 11.1. FE models of the containment structure were developed in both SAP2000 and ANSYS. For the containment structure, the only structural components were the heavily-reinforced concrete walls. Due to the large thickness of these walls, solid elements were chosen for modeling both the cylindrical and dome sections. The SAP2000 model was developed with the only solid element option (Solid). The solid elements in SAP2000 were linear hexahedral elements with eight nodes. Several solid elements options are available in ANSYS. Linear hexahedral (SOLID186) elements were chosen due to their favorable mesh convergence properties. The solid elements used in ANSYS had 20 nodes as opposed to the 8 node solid elements used SAP2000.

In addition to the main structure of the containment building, a polar crane was later added to the 3D FE model in SAP2000 to perform a failure analysis. For the polar crane system, beam elements were used for the crane girders and connecting trolley. A concentrated mass was added to account for the total mass of the trolley.

## 11.3 Modal Analysis

To evaluate and compare the general dynamic properties of all models, modal analysis was completed for both simplified 2D and detailed 3D models. Due to the symmetric nature of the containment structure, modal information in any transverse direction is equivalent to that produced by the singular transverse direction in the 2D stick model. Also due to the simplified nature of 2D stick models, only modes in the transverse direction are obtained. However, 3D FE models capture all potential mode shapes of the actual structure. Many of these modes are insignificant modes with very low mass participation in dynamic analysis. Modal analysis results obtained from the 3D FE models focused on the significant mode shapes. However, a few insignificant modes are selected and shown for the 3D structure to illustrate this phenomenon.

Significant modal information for 2D stick models included natural frequencies for the first several transverse modes and the corresponding mass participation and cumulative mass participation ratios. Table 11.5 summarizes the significant modal information for the 2D stick model. Corresponding mode shapes for the significant transverse modes of the 2D stick model are shown in Figure 11.2.

Table 11.5 Modal information for 2D stick model

| Mode number | Natural frequency (Hz) | Mass participation | Cumulative mass participation |
|---|---|---|---|
| 1 | 5.33 | 76.0% | 76.0% |
| 2 | 16.06 | 16.9% | 92.9% |
| 3 | 29.33 | 4.3% | 97.3% |
| 4 | 42.18 | 1.7% | 98.9% |

Modal analysis results for the 2D stick model (Table 11.5) revealed that the first mode dominates the total dynamic response of the structure. This corresponded to a mass participation ratio of 76% and natural frequency of 5.33 Hz for the first mode. After the first mode, mass participation ratios of subsequent modes dropped significantly. According to Table 11.5, the natural frequency, mass participation ratio, and cumulative mass participations ratio of the second mode were 16.06 Hz, 17%, and 93%, respectively. All subsequent modes had mass participation ratios of less than 5%

in the transverse direction. The 93% cumulative mass participation ratio for the first two modes indicates that these two modes dominate the total dynamic response. Mode shapes for the first two modes of the 2D stick model are shown in Figure 11.2.

For 3D FE models, modal information for several transverse modes was obtained in terms of natural frequency, mass participation, and cumulative mass participation. Due to the complexity of the 3D FE model, significantly more transverse modes were captured compared to the 2D stick model. Shown in Table 11.6, modal information for the first several significant transverse modes and two insignificant modes was obtained from modal analysis. Mode shapes for all modes captured by both SAP2000 and ANSYS and summarized in Table 11.6 are shown in Figures 11.3 through 11.12. Due to the symmetrical nature of the 3D FE models, alternating modes had the same natural frequency as the preceding mode. This was due to consecutive modes having the same mass and stiffness properties about both transverse directions. For this reason, Table 11.6 summarizes each transverse mode about each direction as just one mode.

Table 11.6 shows that the modal information for 3D FE models in SAP2000 and ANSYS was nearly identical. For example, the natural frequencies of modes 1 (and 2), 16, and 37 were 5.23 Hz, 14.88 Hz, and 24.51 Hz, respectively, for the ANSYS model. The natural frequencies of these three modes in the SAP2000 model were recorded as 5.24 Hz, 14.87 Hz, and 24.22 Hz, respectively. According to the SAP2000 results in Table 11.6, the first mode accounts for 71% of the mass participation about one of the transverse directions. This corresponds to the first mode being the mode that dominates the total dynamic response of the structure. The mass participation ratio and cumulative mass participation ratio of mode 16 is 19% and 90%. This indicates that the total dynamic response of the structure is captured by modes 1 and 16 (Figures 11.3 and 11.6).

Table 11.6 Modal information for 3D FE models

| Mode number | ANSYS | SAP2000 | | |
|---|---|---|---|---|
| | Natural frequency (Hz) | Natural frequency (Hz) | Mass participation | Cumulative mass participation |
| 1/2 | 5.23 | 5.24 | 71.5% | 71.5% |
| 3/4 | 6.87 | 6.92 | 4E-14% | 71.5% |
| 5/6 | 7.90 | 7.94 | 4E-14% | 71.5% |
| 16/17 | 14.88 | 14.87 | 18.8% | 90.3% |
| 37/38 | 24.51 | 24.22 | 2.8% | 93.1% |

A characteristic of the 3D FE models not captured by the 2D stick model is the transverse modes with little mass participation. According to Table 11.6, the first (and second) mode for the 3D FE models each had a mass participation ratio of 71% in a transverse direction. However, the third through sixth modes had virtually no mass participation in any direction. Figures 11.4 and 11.5 show how these corresponding mode shapes in SAP2000 capture local deformation of the walls and not global deformation of the structure.

To compare general dynamic properties of the 2D stick and 3D FE models, the natural frequencies of the first three significant transverse modes of each model were summarized in Table 11.7. As expected for the 2D stick model, the first three significant transverse modes were the first three modes. However, for the 3D FE models, the first three significant transverse modes were determined by the first three modes with the largest mass participation in one transverse direction. Table 11.6 shows that the first three significant modes in one transverse direction for 3D FE models were modes 1, 16, and 37.

Table 11.7 Significant transverse mode comparison for 2D stick and 3D FE models

| Mode number | Natural frequency (Hz) | | |
|---|---|---|---|
| | 2D SAP2000 | 3D SAP2000 | 3D ANSYS |
| 1 | 5.33 | 5.24 | 5.23 |
| 2 | 16.06 | 14.87 | 14.88 |
| 3 | 29.33 | 24.22 | 24.51 |

Comparing the natural frequencies of the first three significant transverse modes of 2D stick and 3D FE models in Table 11.7, it was observed that the first two modes matched well between all models. The natural frequencies of the first significant transverse mode were 5.33 Hz, 5.14 Hz, and 5.23 Hz, respectively, for the 2D stick model, 3D FE model in SAP2000, and 3D FE model in ANSYS. Similarly, the natural frequencies of the second significant transverse mode were 16.06 Hz, 14.86 Hz, and 14.88 Hz, respectively, for the same models. These two modes captured more than 90% of the total dynamic response of the structure based on their mass participation ratios (Tables 11.5 and 11.6). Therefore, the 2D stick model, 3D FE model in SAP2000, and 3D FE model in ANSYS all shared the same general dynamic properties for transverse loading scenarios.

### 11.4 Time History Analysis

The general dynamic properties of simplified 2D and detailed 3D models were evaluated and compared for the containment structure as part of modal analysis. For SPRA, time history analysis of each model was completed to evaluate and compare the dynamic response of each model when subjected to seismic events. For analysis and comparison purposes, El Centro ground motion (Section 2.6) was applied to 2D stick and 3D FE models. Since SPRA typically focuses on the maximum response of a structure during seismic events, the maximum responses at two critical locations were evaluated. The first location was the highest location on the containment structure, which corresponded to the location of maximum global displacement and acceleration response. The second location was the connection of the cylindrical section to the dome section. This location corresponded to the typical location of a polar crane.

The maximum displacements and accelerations at the two critical locations are summarized in Table 11.8. The maximum responses at these locations is typically more critical, but the response histories are also important when comparing simplified and detailed models. For each location, the initial ten seconds of the displacement and acceleration response histories of 2D stick and 3D FE models are shown in Figures 11.13 through 11.16.

Table 11.8 Comparison of maximum responses for simplified 2D and detailed 3D models at the top of the containment structure (location 1) and at the top of the cylindrical section (location 2)

| Model | Location 1 (top of dome) | Location 2 (top of cylinder) |
|---|---|---|
| Displacement (in.) | | |
| 2D stick | 0.328 | 0.236 |
| 3D FE SAP2000 | 0.323 | 0.242 |
| 3D FE ANSYS | 0.323 | 0.242 |
| Acceleration (ft/s$^2$) | | |
| 2D stick | 33.72 | 24.79 |
| 3D FE SAP2000 | 32.90 | 23.21 |
| 3D FE ANSYS | 32.25 | 22.02 |

The maximum displacement and acceleration responses at both locations were very similar for all models. For example, the maximum displacement at location 1 was 0.328 in. for the 2D stick model and 0.323 in. for the 3D FE models in SAP2000 and ANSYS as reported in Table 11.8. Maximum accelerations of each model also matched very well. According to Table 11.8, the maximum accelerations at location 2 were 24.79 ft/s$^2$, 23.21 ft/s$^2$, and 22.02 ft/s$^2$, respectively, for the 2D stick model, 3D FE model in SAP2000, and 3D FE model in ANSYS.

Similar to the maximum responses at the two locations, the response histories at the two locations matched fairly well throughout the duration of the time history. Figures 11.13 through 11.16 show how the response histories for the 2D stick model and 3D FE models in SAP2000 and ANSYS were very similar. Figures 11.13 through 11.16 do show that several of the peak responses from all models occur at slightly different time-steps, but the difference is almost negligible.

### 11.5 Polar Crane Analysis

A particularly important piece of equipment in the containment structure is the polar crane. As such, Schukin and Vayndrakh[96] investigated the seismic fragility of the polar crane to assess the associated risks. Schukin and Vayndrakh state that the main uses of the polar crane are for refueling and lifting operations during shutdown. However, the polar crane stays in place when not in use. To perform a seismic fragility analysis, a FE model was created for a typical polar crane and support system, similar to the one shown in Figure 11.17. The model included two large steel girders, a lateral load-resisting steel frame called the seismic restraining system (SRS), a trolley that supported the actual crane, and the containment structure itself, which they called the supporting ring wall.

Using their FE model, several scenarios for the polar crane were investigated by Schukin and Vayndrakh. These scenarios included the polar crane carrying just its own weight and carrying its own weight and its load-carrying capacity of 180 tons, varying friction parameters between the trolley wheels and supporting rails, and varying trolley positions along the bridge beams. Fragility

---

[96] Schukin, A. and Vayndrakh, M. "Seismic Non-linear Analysis of Polar Crane," Paper presented at the 19th International Conference on Structural Mechanics in Reactor Technology, Toronto, Canada. (2007).

curves were developed from uncertainty analysis of the aforementioned parameters. Schukin and Vayndrakh concluded that two of the more important parameters that affect the seismic performance of the polar crane are the friction between the trolley and supporting rail and position of the trolley on the girders. Using the information from Schukin and Vayndrakh, a polar crane case study was developed to evaluate its potential failure modes. The main parameters evaluated in the case study were the location of the trolley on the girders and the connection of the girders to the containment structure.

## 11.6 Polar Crane Case Study

To assess the seismic performance of the polar crane's structural system for a typical CEUS site, six scenarios were developed and investigated for the crane girders. These scenarios included two trolley locations along the crane girders and possible connections for the crane girder to the containment structure wall. In each scenario, each end of the 120-ft long crane girders were either fixed or pinned. For example, a crane girder with the first connection fixed and the second connection pinned would have "fixed-pinned" connections. In each scenario, the location of the trolley was either 60 ft or 2 ft away from the first connection. Each scenario for the polar crane was numbered and is summarized in Table 11.9.

Table 11.9 Summary of six polar crane scenarios for dynamic analysis

| Scenario | Girder support | Trolley distance to first support (ft) |
|---|---|---|
| 1 | Fixed-fixed | 60 |
| 2 | Fixed-fixed | 2 |
| 3 | Fixed-pinned | 60 |
| 4 | Fixed-pinned | 2 |
| 5 | Pinned-pinned | 60 |
| 6 | Pinned-pinned | 2 |

During seismic events, two critical limit states are typically checked to determine the seismic performance of the crane girders. These two limit states include the allowable compressive stress in the crane girders, and the allowable total deflection of the crane girders. The allowable limit states for stress and deflection were recommended by engineers at RIZZO Associates, Inc. and are summarized in Table 11.10.

Table 11.10 Summary of limit states for the polar crane girders

| | |
|---|---|
| Allowable compressive stress (ksi) | 32.5 |
| Allowable deflection (in.) | $\frac{\mathrm{L}}{1000} = \frac{(120\ \mathrm{ft})(12\ \frac{\mathrm{in.}}{\mathrm{ft}})}{1000} = 1.44$ |

To evaluate the adequacy of the crane girders at a typical CEUS site, each crane girder scenario from Table 11.9 was added to the containment structure's 3D FE model in SAP2000. The ground motions developed by RIZZO Associates, Inc. (Section 2.6) were then used to determine the maximum dynamic responses of the crane girders. In total, 25 three-dimensional CEUS ground motions were developed. However, the two horizontal directions from each set were separated to create 50 two-dimensional (one horizontal and one vertical) ground motion sets. This was done to increase the total number of ground motions and to be more consistent with the analyses in Sections 11.3 and 11.4 that simply used one horizontal ground motion.

All 50 CEUS ground motion sets were applied to each 3D containment structure model with a crane girder scenario. The crane girders' maximum stresses and deflections resulting from the dynamic response of the containment structure were significantly lower than the limit state values in Table 11.10. This indicated that the ground motions would need to be significantly higher to reach the failure limit states. In order to reach the stresses and deflections in Table 11.10, the time histories for all 50 CEUS ground motions were linearly scaled to determine if the crane girders' response was linear. Responses from a few large CEUS ground motion scale factors (10 and 20) verified the linearity of the crane girders' response. The maximum stresses and deflections resulting from the unscaled CEUS ground motions were then linearly scaled (1, 2, …, 75) to exceed the limits states in Table 11.10. For each CEUS ground motion scale factor, a "fail" or "no fail" criteria was evaluated for each of the 50 ground motion sets against each of the limit states for stress and deflection in Table 11.10. The total number of "fails" was calculated for each independent scale factor, and each total number of "fails" was divided by the total number of ground motions sets (50). This resulted in a failure percentage for each CEUS ground motion scale factor for each scenario. Using the results from analysis, Figures 11.17 and 11.18 were developed to illustrate the failure percentages versus CEUS ground motion scale factors for each scenario.

Importantly, it should be noted that linearly scaling ground motions to the extent done here is not appropriate for a true risk analysis. Ground motions developed for higher seismicity areas should realistically be done. Linearly scaling the ground motions in this study was done simply to illustrate the extreme accelerations needed to reach the stress and deflection limit states. For instance, the smallest CEUS ground motion scale factors needed for several scenarios to exceed the limit states were equivalent to peak ground acceleration (PGA) around 8g. In reality, PGAs that large have not been recorded, and the mechanics of the soil-structure interaction at that PGA level would be significantly different from the assumed fixed-base connection in these models.

The analysis results do indicate that the deflection limit state is the most critical in every scenario. Comparing results from Figures 11.18 and 11.19, the CEUS ground motion scale factors needed to exceed the deflection limit state are smaller than scale factors for the compressive stress limit state. For example, scenario 6 required CEUS ground motion scale factor of 26 to reach 100% exceedance of the deflection limit state, whereas a scale factor of 74 was needed to reach 100% exceedance of the compressive stress limit state. Not all scenarios had such large difference between the two limit states. Scenario 4 had the smallest difference between the deflection and compressive stress limit states. For scenario 4, CEUS ground motion scale factor of 27 was needed to reach 100% exceedance of the deflection limit state, whereas a scale factor of 36 was needed to reach 100% exceedance of the compressive stress limit state.

### 11.7 Summary and Conclusions

The dynamic behavior and response of a NPP containment structure were investigated to determine the suitability for using simplified versus detailed models. Geometric and material properties of a realistic containment structure were obtained through literature (Ostadan 2000), and detailed 3D FE models in both SAP2000 and ANSYS were developed. A simplified stick model was also developed in SAP2000 for the containment structure based off mechanical properties for a lumped-mass stick model from Ostadan that were slightly modified to be consistent with detailed 3D models that were developed. Modal and time history analyses were then completed to evaluate the dynamic response of all models.

The symmetrical nature of the containment structure meant that each transverse direction of the structure had the same dynamic characteristics. As such, modal analysis of detailed 3D models revealed that all transverse modes were equal and opposite for consecutive modes as shown in Table 11.6. Similarly, modal analysis results of each 3D FE model revealed that each model was very comparable to the other. Table 11.6 shows that the natural frequencies of all corresponding modes were within 2% of each other for 3D FE models. Results show the simplified model of the containment structure was able to capture the transverse modes that dominated the dynamic response of the structure. Tables 11.5 and 11.7 show that the simplified stick model's modes that dominate the dynamic response of the structure (modes 1 and 2) had natural frequencies within 10% of the 3D FE models.

Time history analysis was performed using both 2D and 3D containment structure models for SPRA. Results from time history analysis show that each 3D FE model captured approximately the same maximum dynamic response at two critical locations. At each location, corresponding maximum displacements and accelerations of each 3D FE model were within 5% of each other (Table 11.8). Figures 11.13 through 11.16 also show how the response histories for each 3D FE model were nearly identical throughout the histories. Similar to the modal analysis results, the time history analysis results of the simplified stick model matched those of each 3D FE model well. Table 11.8 shows that maximum displacements and accelerations at each critical location were all less than 15% different than the corresponding results from 3D FE models. Figures 11.13 through 11.16 illustrate how the response histories of the simplified stick model also matched very well throughout the histories except at a few locations of peak response.

A polar crane was later added to the 3D FE model in SAP2000. Six loading and connection scenarios were considered to evaluate the adequacy of the crane girders at a CEUS site. A total of 50 CEUS ground motion sets were applied to a 3D containment structure model with each scenario, and results showed stresses and deflections in the crane girders were significantly lower than the limit states (Table 11.10). Responses from the ground motions were linearly increased until responses from all 50 ground motions exceeded the compressive stress and deflection limits states. Results indicated that higher peak ground acceleration (PGA) than ever recorded was needed for each failure state to be exceeded (Figures 11.18 and 11.19). At PGA this large, the failure probability contributions from this system to the overall risk of the plant are virtually inconsequential. Furthermore, these results also imply that other scenarios such as dropping of heavy equipment from the polar crane onto an uncovered reactor core or dropping of fuel from a cladding failure are more likely than failure of the crane girder itself.

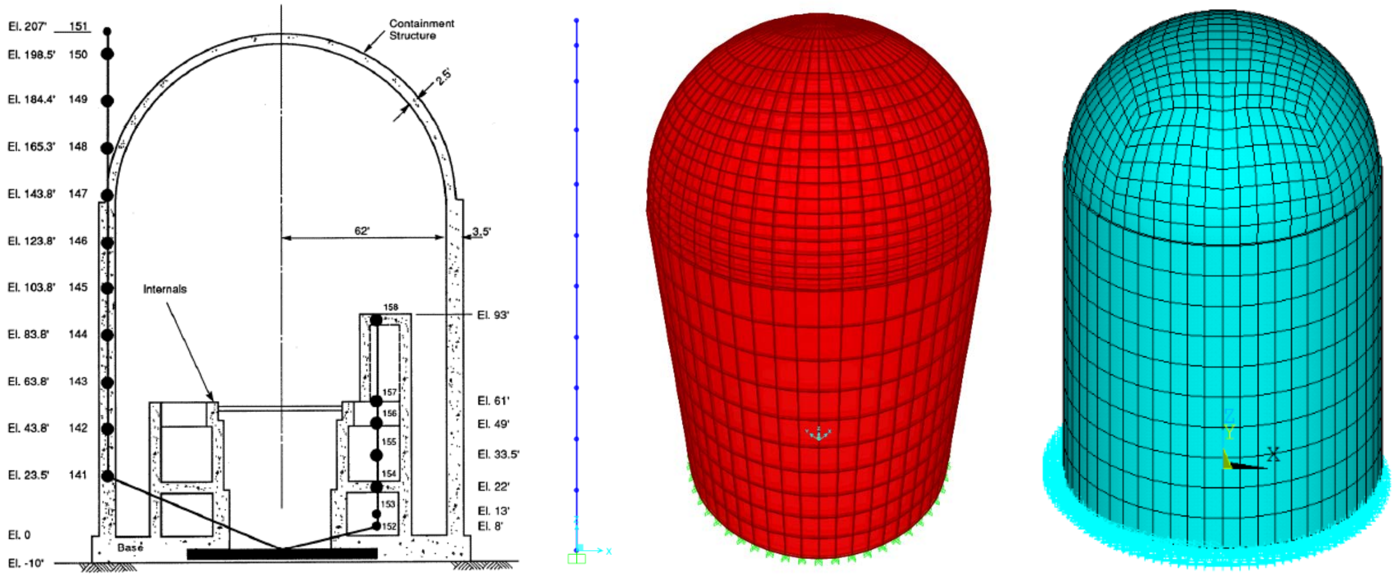

(a) (b) (c) (d)

Figure 11.1 Containment structure and final models: b) 2D stick model in SAP2000, c) 3D FE model in SAP2000, and) 3D FE model in ANSYS

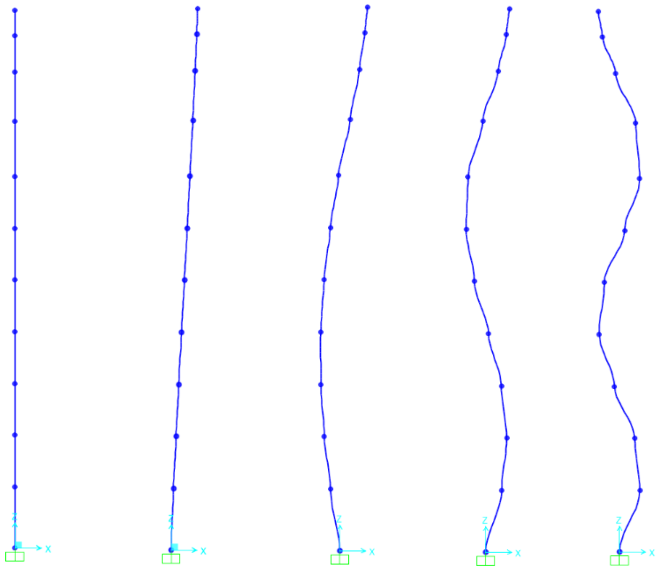

(a) (b) (d) (e) (f)

Figure 11.2 Mode shapes for 2D stick model: a) undeformed shape, b) mode 1, c) mode 2, d) mode 3, and e) mode 4

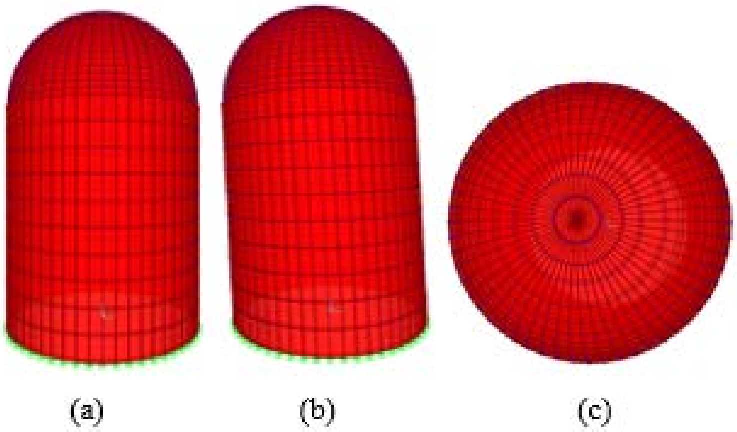

(a) (b) (c)

Figure 7.3 Mode shape for modes 1 and 2 of 3D SAP2000 model: a) undeformed shape, b) elevation, and c) top view

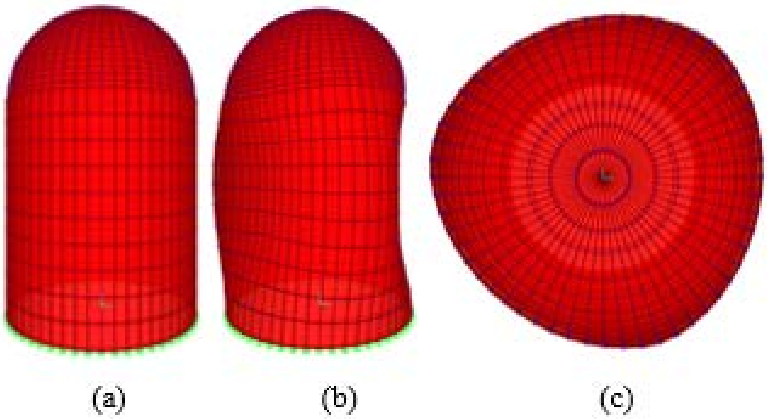

(a) (b) (c)

Figure 7.4 Mode shape for modes 3 and 4 of 3D SAP2000 model: a) undeformed shape, b) elevation, and c) top view

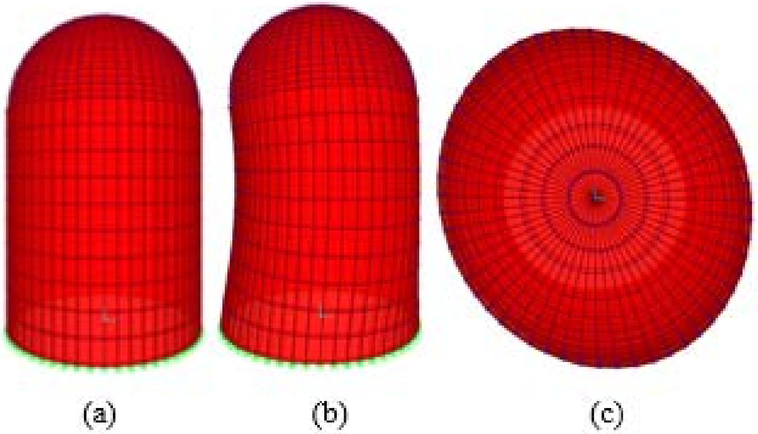

(a) (b) (c)

Figure 7.5 Mode shape for modes 5 and 6 of 3D SAP2000 model: a) undeformed shape, b) elevation, and c) top view

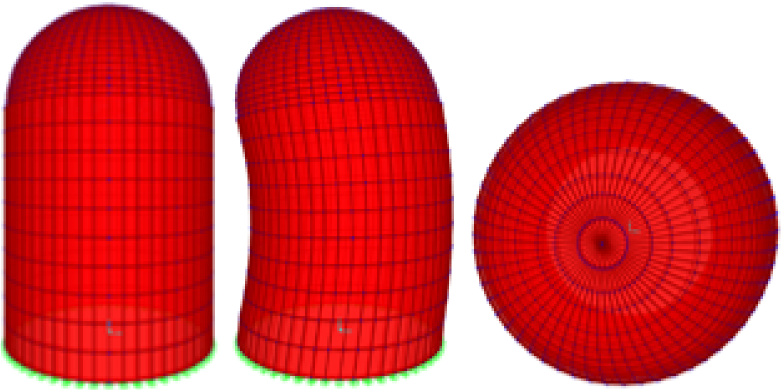
(a) (b) (c)

Figure 7.6 Mode shape for modes 16 and 17 of 3D SAP2000 model: a) undeformed shape, b) elevation, and c) top view

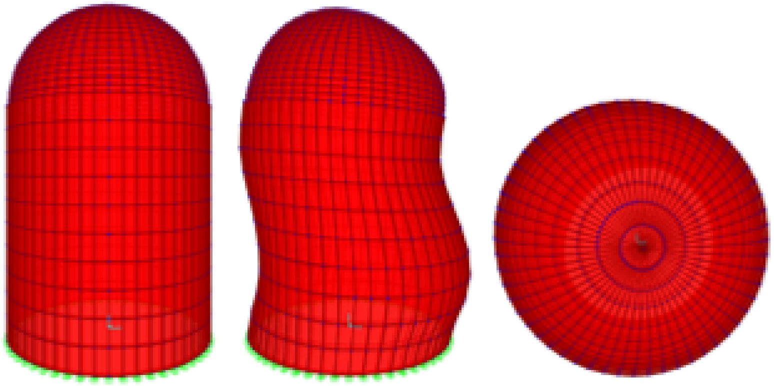
(a) (b) (c)

Figure 7.7 Mode shape for modes 37 and 38 of 3D SAP2000 model: a) undeformed shape, b) elevation, and c) top view

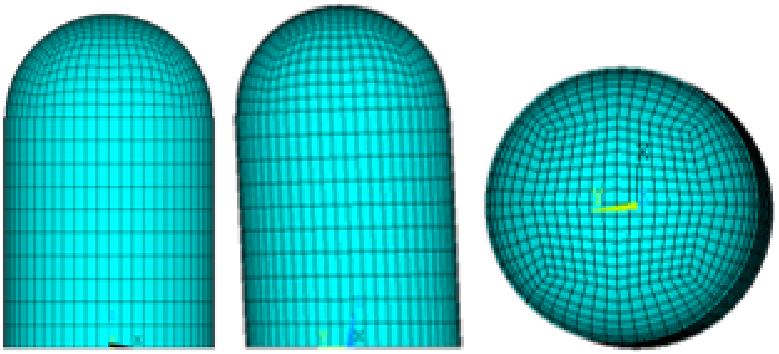
(a) (b) (c)

Figure 7.8 Mode shape for modes 1 and 2 of 3D ANSYS Mechanical model: a) undeformed shape, b) elevation, and c) top view

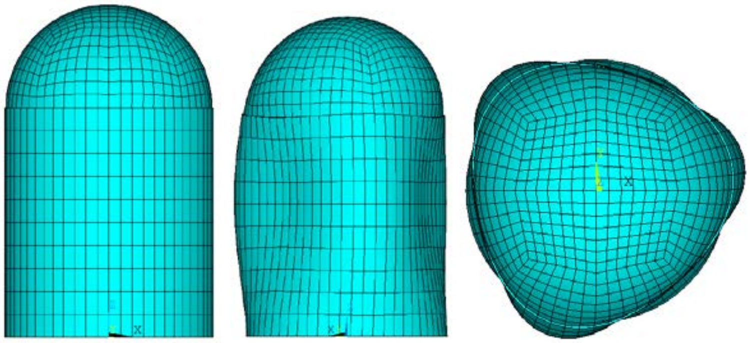

(a) (b) (c)

Figure 11.9 Mode shape for modes 3 and 4 of 3D ANSYS model: a) undeformed shape, b) elevation, and c) top view

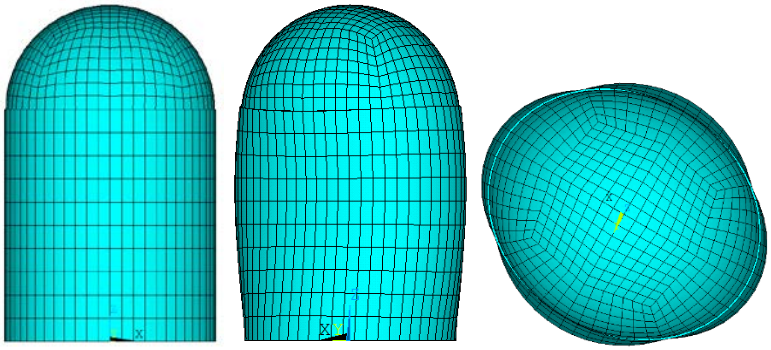

(a) (b) (c)

Figure 11.10 Mode shape for modes 5 and 6 of 3D ANSYS model: a) undeformed shape, b) elevation, and c) top view

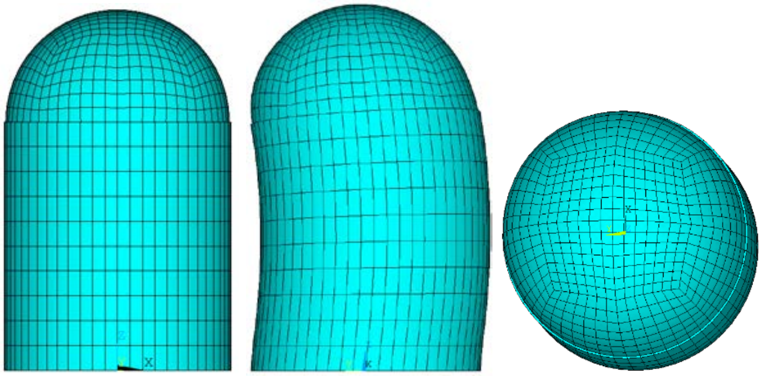

(a) (b) (c)

Figure 11.11 Mode shape for modes 16 and 17 of 3D ANSYS model: a) undeformed shape, b) elevation, and c) top view

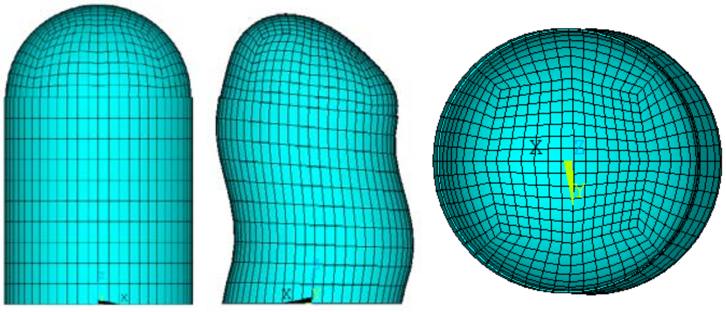

(a) (b) (c)

Figure 11.12 Mode shape for modes 37 and 38 of 3D ANSYS model: a) undeformed shape, b) elevation, and c) top view

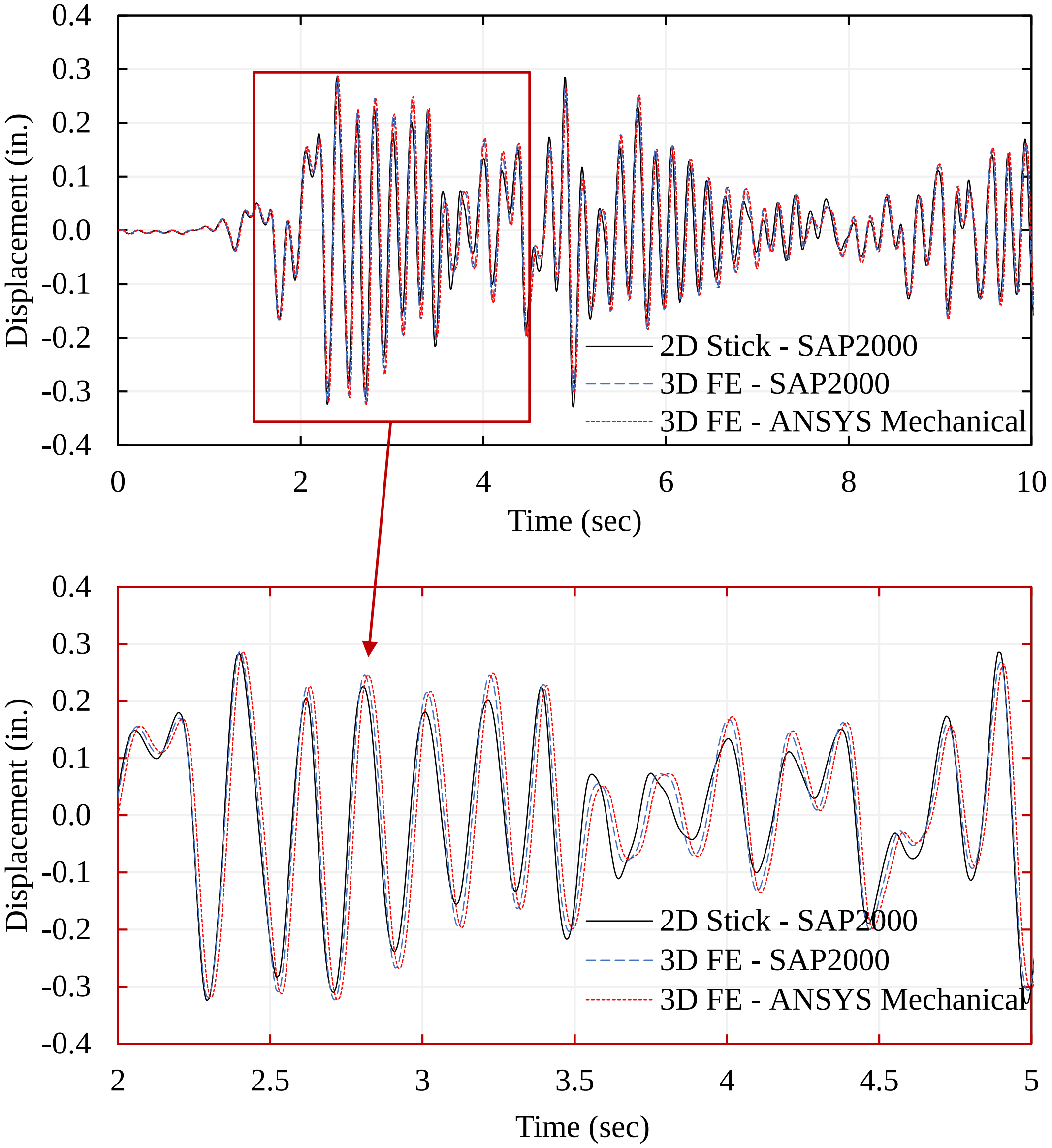

Figure 11.13 Displacement response history comparison at top of dome (location 1) for 2D stick and 3D FE models

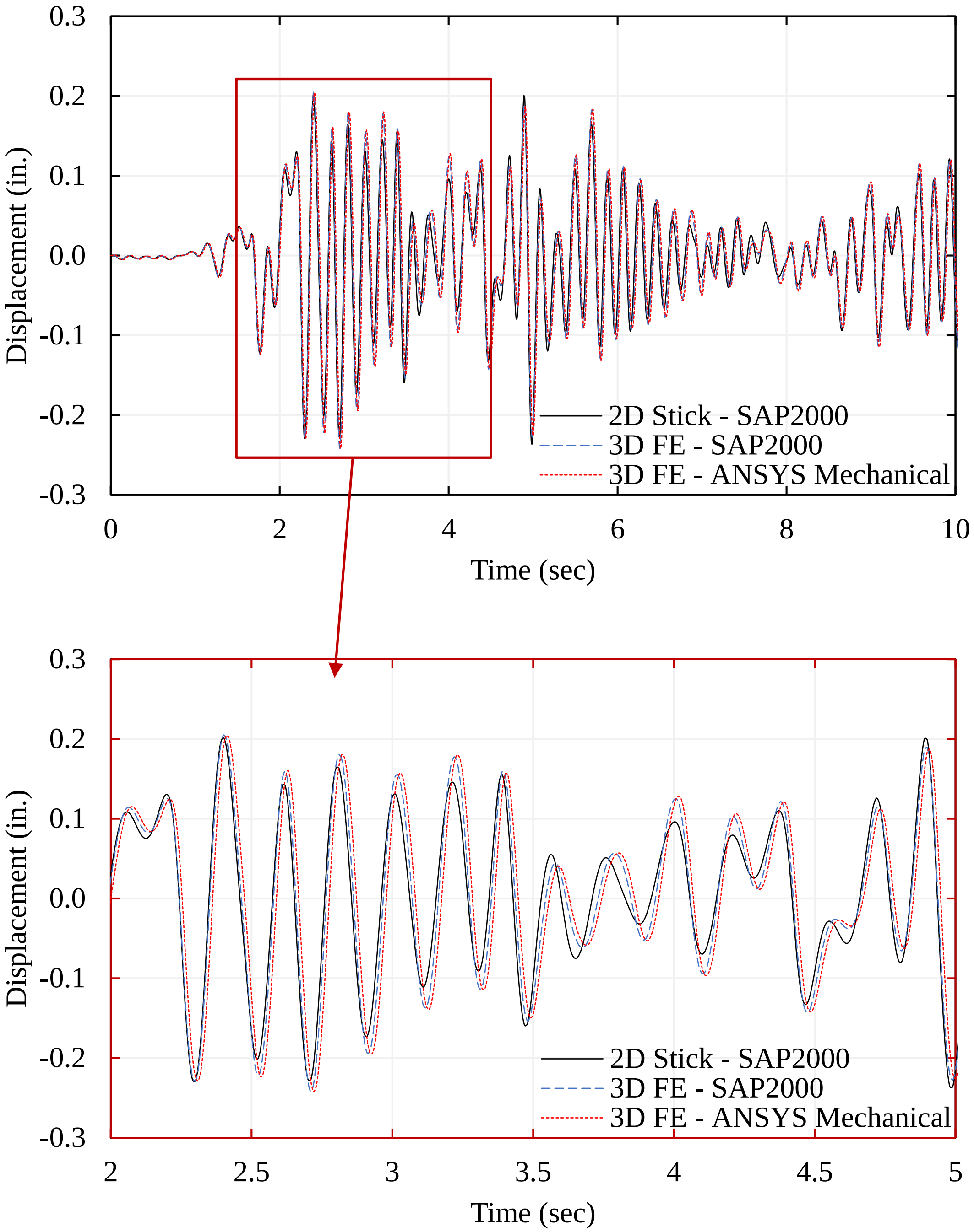

Figure 11.14 Displacement response history comparison at top of cylinder (location 2) for 2D stick and 3D FE models

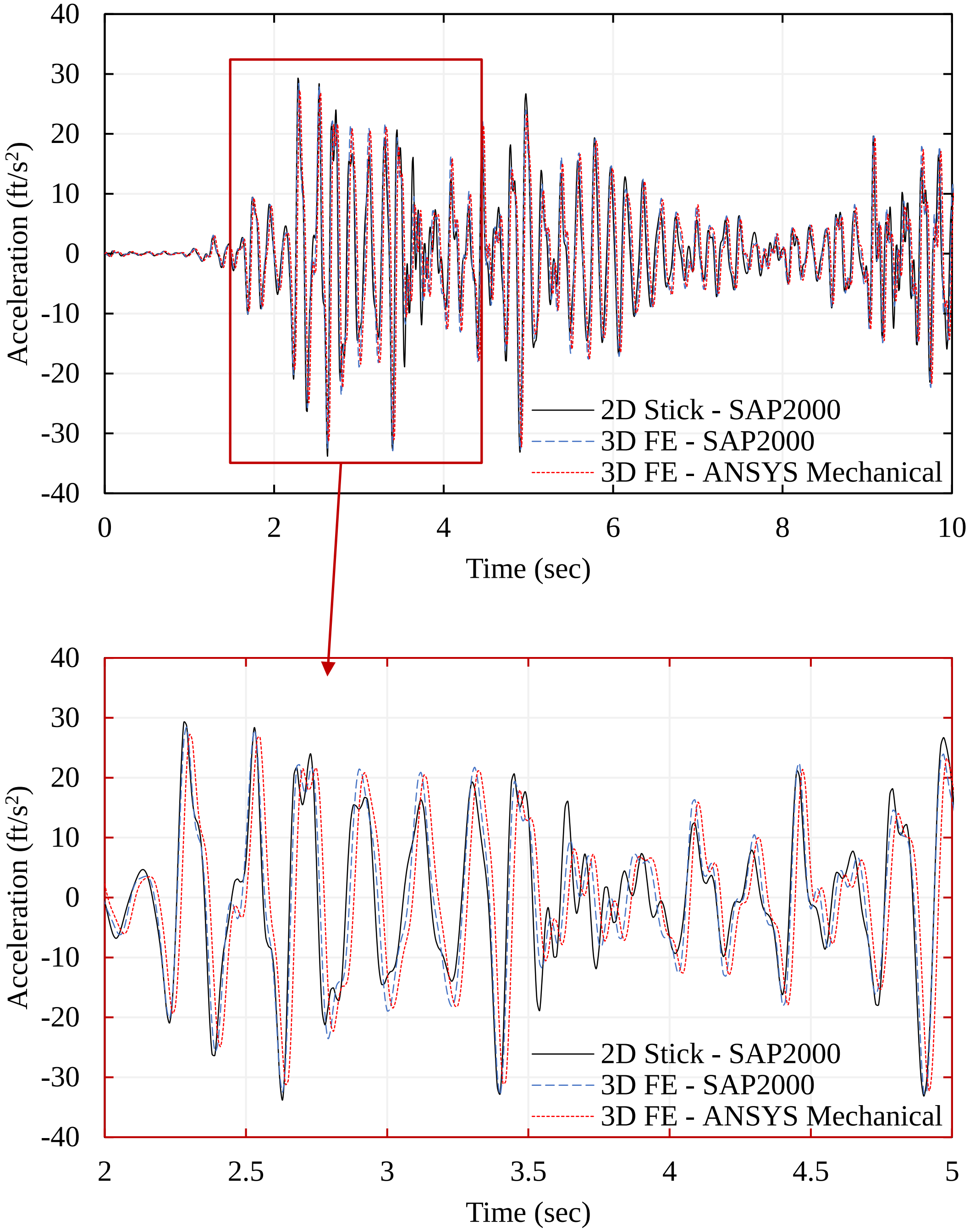

Figure 11.15 Acceleration response history comparison at top of dome (location 1) for 2D stick and 3D FE models

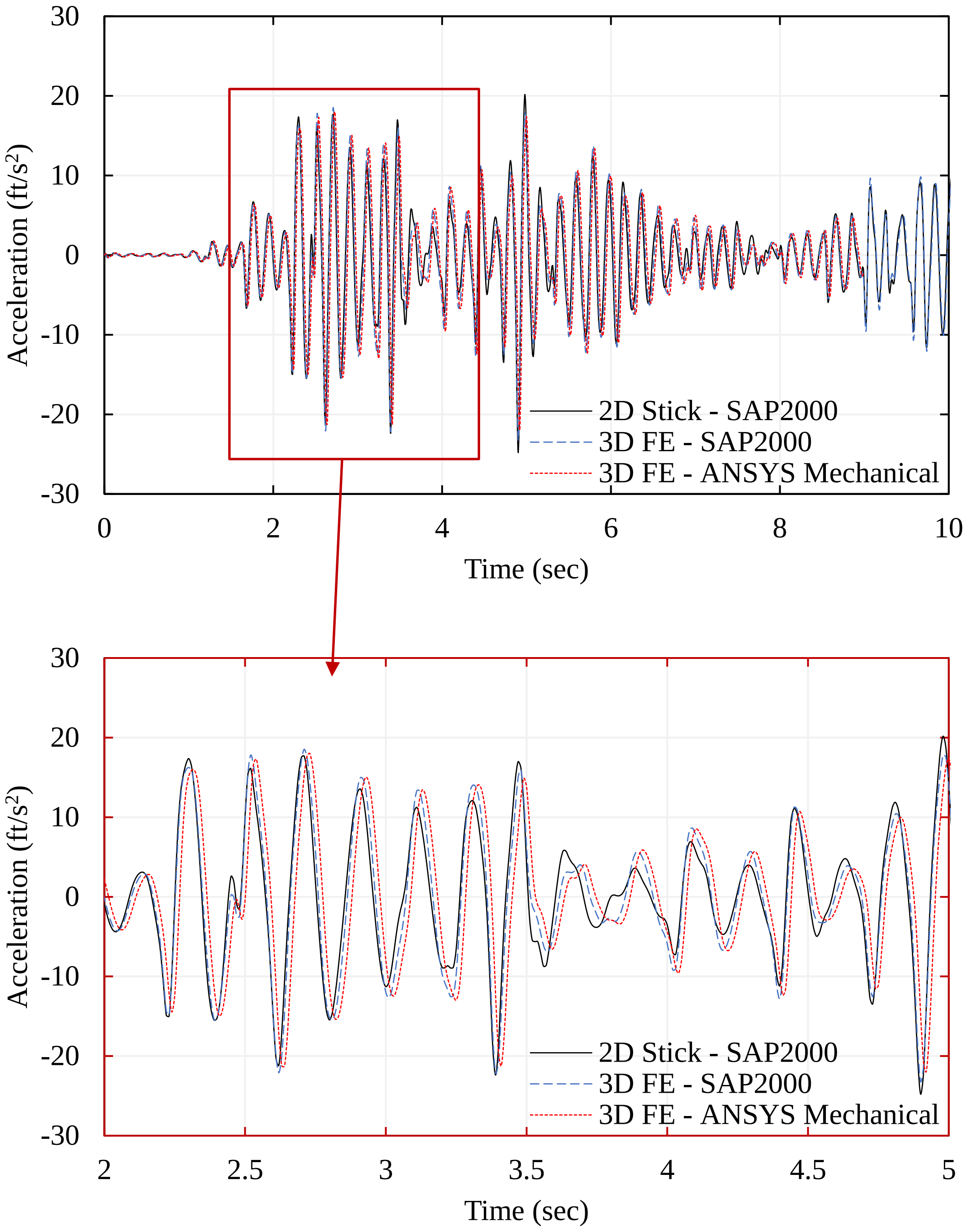

Figure 11.16 Acceleration response history comparison at top of cylinder (location 2) for 2D stick and 3D FE models

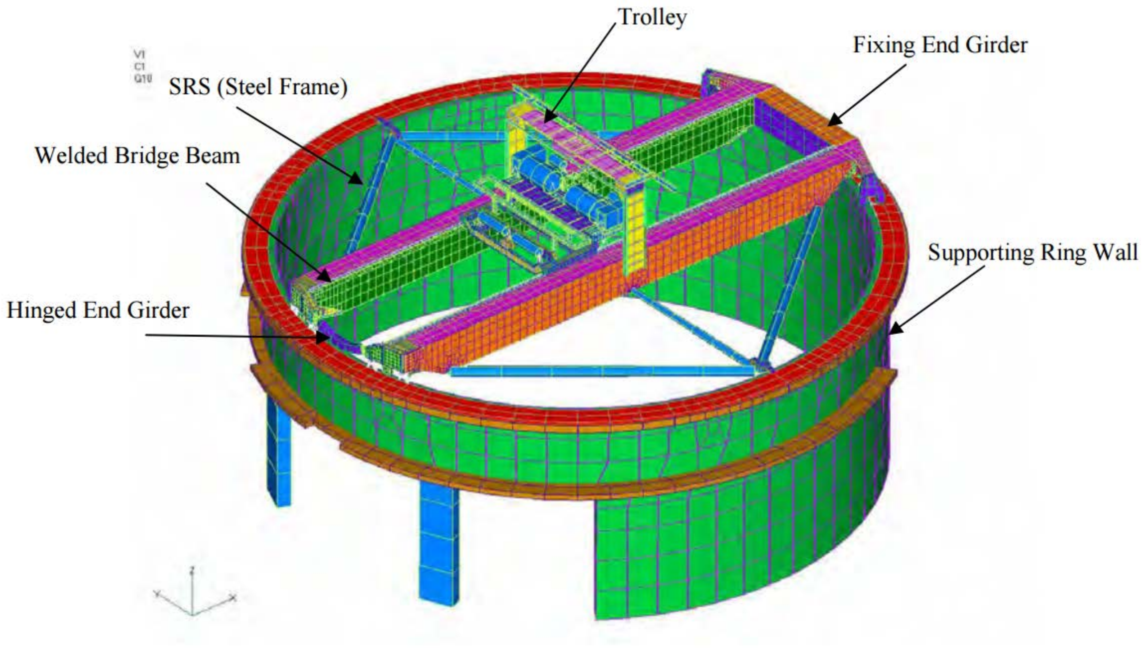

Figure 11.17 FE model of polar crane and supporting structure (Schukin and Vayndrakh 2007)

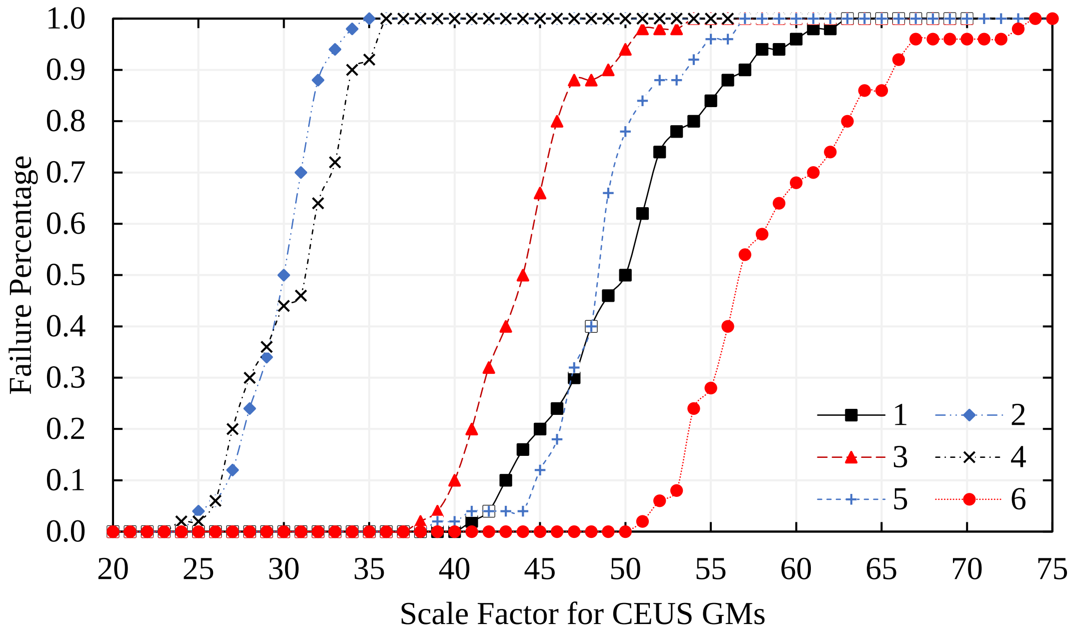

Figure 11.18 Compressive stress failure analysis for polar crane girders for the six scenarios considered

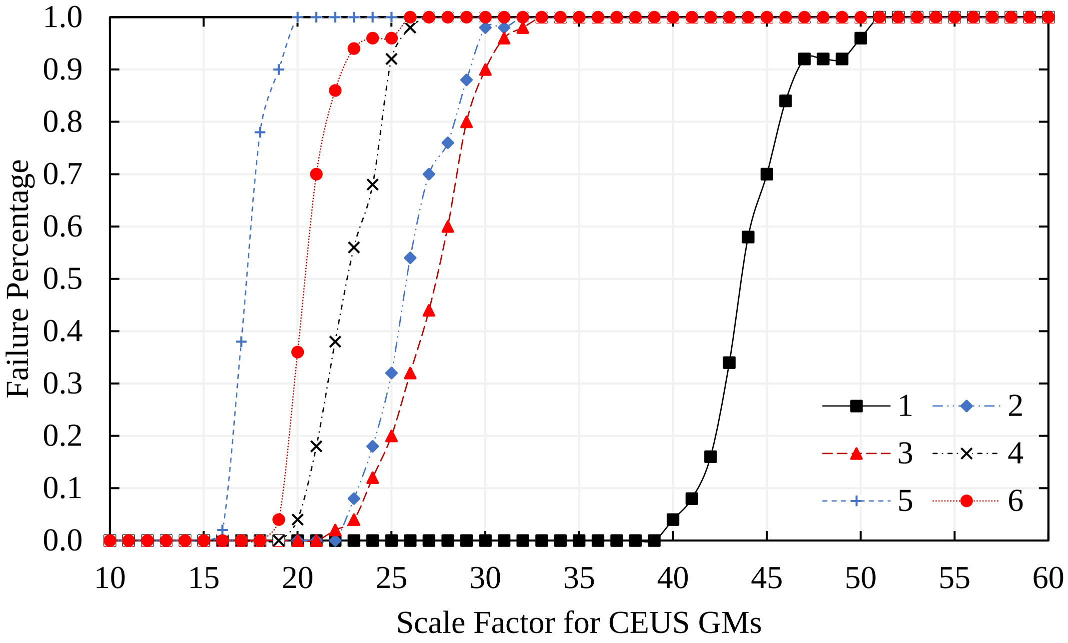

Figure 11.19 Deflection failure analysis for polar crane girders for the six scenarios considered

# 12. DYNAMIC TREATMENT OF AFTERSHOCKS IN SPRA

## 12.1 Background

Historically, SPRA has focused on damage incurred as the result of a main seismic shock rather than on the effects of aftershocks. One of the many lessons from the Fukushima accident was that aftershocks can play an important role in affecting human performance[97]. Although in current SPRAs human error probabilities are modified with performance shaping factors to account for the emotional stress associated with aftershocks, a dynamic analysis would be required to incorporate cognitive models of human performance, which accounted for the operator's current perception of both the threat of severe core damage and the operator's personal risk, into an SPRA.

By definition, the main shock has the highest acceleration among the series of shock events that occur associated with a seismic event. However, the main shock is not necessarily the first in the cascade of shocks. When the first shock wave is not the largest in the series it is referred to as a foreshock. As discussed below foreshocks occur in approximately 7% of earthquakes. The probabilities of aftershocks that are similar in magnitude to the main shock are not negligible. Thus, to the extent that the main shock causes inelastic structural damage in the plant, the potential exists for further damage associated with aftershocks.

The March 11, 2011 Tohoku earthquake (the earthquake triggering the tsunami that damaged the Fukushima reactors) which was a magnitude 9 event was preceded by one minute by a 7.3 magnitude foreshock.[98] There have subsequently been more than 900 aftershocks associated with this event, 60 of which were higher than magnitude 6. On the same day as the main shock there were aftershocks of magnitudes 7.9, 7.7 and 7.4. Each of these is a major seismic event in its own right. The potential for aftershocks was a consideration that limited staff entry to potentially hazardous areas during attempts to prevent core meltdown. On April 7, a 7.1 magnitude aftershock resulted in a loss of all ac power to the site.[99]

An objective of the DSPRA framework being formulated within this project is to develop an approach to the dynamic treatment of aftershocks in an SPRA. There is a cost associated with DET analysis. The conditions under which a complete DET analysis within an SPRA would be warranted is unclear at this point but should be explored. At a minimum a capability is required to perform a pseudo-dynamic analysis of the effects of aftershocks as they affect a best-estimate scenario of accident progression, system response, and human performance.

## 12.2 Characteristics of Aftershocks

Characteristics of aftershocks are identified in a tutorial by Feltzer of USGS.[100] Some of those characteristics are repeated in the following:

- Aftershocks are often seen as small unimportant earthquakes. For example, the National Hazard Map and engineering codes ignore them.

---

[97] National Research Council, "Lessons Learned from the Fukushima Nuclear Accident for Improving Safety of U.S. Nuclear Plants," National Academies Press, Washington, DC (2014)

[98] USGS, https://en.wikipedia.org/wiki/List_of_foreshocks_and_aftershocks_of_the_2011_T%C5%8Dhoku_earthquake.

[99] National Research Council, "Lessons Learned from the Fukushima Nuclear Accident for Improving Safety of U.S. Nuclear Plants," National Academies Press, Washington, D.C. (2014)

[100] K. Felzer, "The Wonderful World of Aftershocks," http://pasadena.wr.usgs.gov/office/kfelzer/SeisLabTalk.pdf

- But aftershocks are important! They are the majority of all earthquakes. They have some amazing statistical properties
- Amazing aftershock Statistic #1, Omori's Law: Decrease in the rate of aftershocks as a function of time

  $$\mathrm{R(t)} = \frac{\mathrm{K}}{\mathrm{(t+c)^p}} \qquad (12.1)$$

  where, $t$ = time and $K$, $c$ and $p$ are constants.
  Aftershocks can follow Omori's Law for hundreds of years. There is no known derivation for Omori's Law but there is substantial experience verifying its form.
- Amazing aftershock Statistic #2: The magnitude of each individual aftershock is independent of the magnitude of its main shock. Larger earthquakes have larger aftershocks only because they have more aftershocks. All foreshocks can be explained as earthquakes with aftershocks that are larger than themselves.
- Foreshock rates can be accurately predicted from the rate of aftershocks smaller than the main shock. Based on the Gutenberg-Richter distribution

  $$\mathrm{N(M)} = \mathrm{A} \cdot 10^{-\mathrm{bM}} \qquad (12.2)$$

  Predicted rate that an earthquake will produce an aftershock larger than itself $\approx 0.05$.

- The timing or "clock advance" of an aftershock is independent of the amount of stress applied by the main shock.

### 12.3 Assessment of the Probability of Aftershocks

Reasenberg and Jones[101] have developed an expression for the rate of aftershocks with magnitude M or larger at time t following a main shock of magnitude $M_m$ based on the combination of the Omori[102] and the Gutenberg-Richter laws.

$$\lambda(t, M) = 10^{a+b(M_m-M)}(t+c)^{-p} \qquad (12.3)$$

where $a$, $b$, $c$ and $p$ are constants. Treating the aftershock process as a nonhomogeneous Poisson process in time, the probability of exceeding a given magnitude of earthquake is

$$P = 1 - \exp(-\int_S^T \lambda(t, M)dt) \qquad (12.4)$$

Based on integration of Equation 12.4 (as corrected in Reference 7), Reasenberg and Jones[5] produced the following tables of probability of one or more events exceeding $M_m$ in different time intervals for the following values of $a$ = -1.67, $b$ = 0.91, $c$ = 0.05 and $p$ = 1.08.

$$P = 1 - \exp\{\left(10^{a+b(M_m-M)}\right)\left(\frac{1}{1-p}\right)\left[(T+c)^{1-p} - (S+c)^{1-p]}\right]\} \qquad (12.5)$$

---

[101] P.A. Reasenberg and L.M. Jones, "Earthquake Hazard after a Mainshock in California," Science, Vol. 243, pp 1173-1176 (1989)

[102] T. Utsu, Y. Ogata and R.S. Matsuura, "The Centenary of the Omori Formula for a Decay Law of Aftershock Activity," J. Phys. Earth, 43, 1-33 (1995)

Table 12.1. Probability of $M>M_m$ as a Function of Start Time and Duration

| Duration (T-S) (days) | Start Time (days) | | | |
|---|---|---|---|---|
| | 0.01 | 0.5 | 1 | 3 |
| 1 | 0.066 | 0.022 | 0.014 | 0.005 |
| 3 | 0.086 | 0.038 | 0.027 | 0.013 |
| 7 | 0.101 | 0.052 | 0.039 | 0.022 |
| 30 | 0.123 | 0.074 | 0.061 | 0.042 |

Based on this model, the probability of exceeding any value of earthquake magnitude can be calculated based on the magnitude of the main shock. Earthquake magnitude is a measure of the total energy release associated with the earthquake. From the viewpoint of SPRA, the measure of interest is not earthquake magnitude but the level of *acceleration* at the basemat of the plant. In an SPRA, a standard spectrum (Uniform Hazard Curve or Ground Motion Response Spectrum) is used to characterize the exceedance frequency of ground acceleration as a function of the frequency of vibration. The seismic hazard curve is used to determine the exceedance frequency of a characteristic vibrational frequency, such as the 100 Hz value. At a plant site, the equipment is designed to withstand a given level of peak ground acceleration (safe shutdown earthquake). The relationship between earthquake magnitude and the ground acceleration typically is described by the form of Equation 12.6[103] but the values of the parameters are site dependent.

$$M = \alpha \cdot \log(PGA) + \beta \tag{12.6}$$

Typical values for a plant in California are α = 2.3, β = 0.92 [8]. For this example,

$$P = 1 - \exp\{\left(10^{\alpha}(\frac{PGAm}{PGA})^{2.3b}\right)\left(\frac{1}{1-p}\right)\left[(T+c)^{1-p} - (S+c)^{1-p]}\right]\} \tag{12.7}$$

Given a design basis earthquake with the value PGAm, or a magnitude of Mm, the probability of an aftershock exceeding either a peak ground acceleration of PGAm or a Modified Mercalli magnitude of Mm is the same, regardless of whether Equation 12.5 or Equation 12.7 is used. However, as the PGA varies, the probability of containment failure does not change in direct proportion to the ratio of PGA to earthquake magnitude. For example, the exceedance probability of an aftershock of 0.5 PGAm is not the same as the exceedance probability of an aftershock of 0.5 Mm. Figure 12.1 was developed using Equation 12.7 for a specified short duration of 0.1 days at different times after the occurrence of an initial shock with acceleration, PGAm.

---

[103] L. Linkimer, "Relationship Between Peak Ground Acceleration and Modified Mercalli Intensity in Costa Rica," Revista Geologica de America Central, 38: 81-94 (2008)

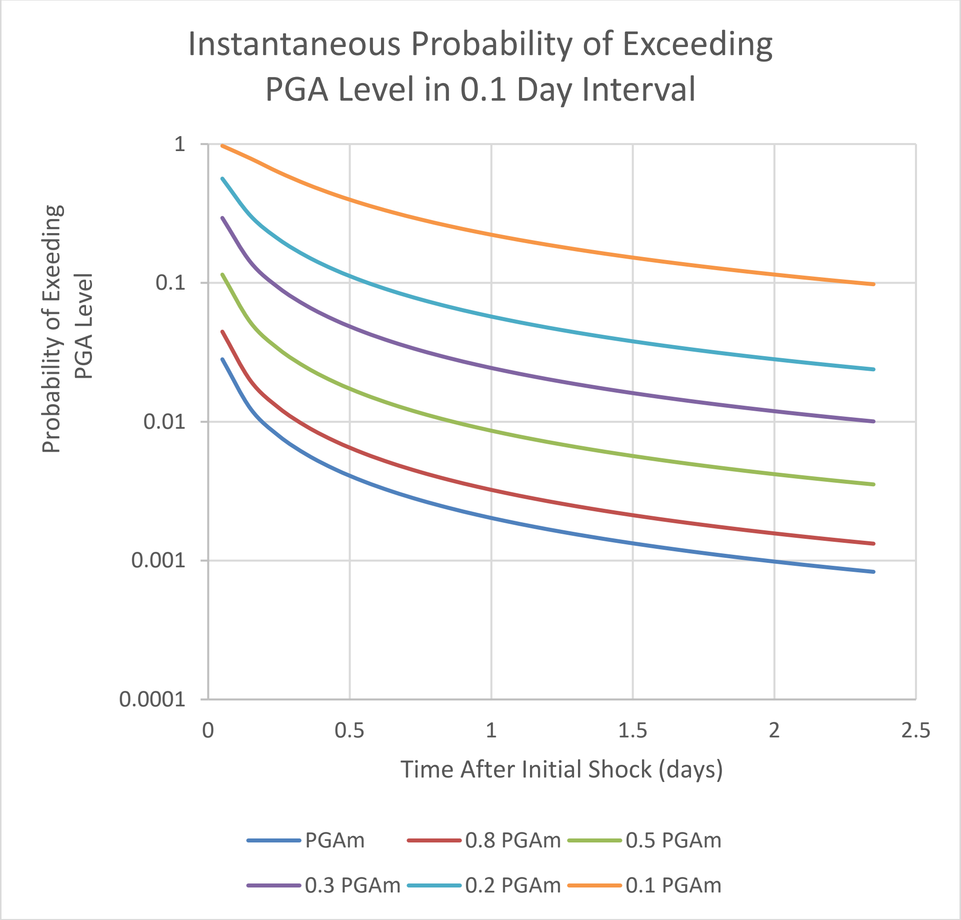

Figure 12.1. Probability of Exceeding PGA Level in a Period of 0.1 Days

A similar model for aftershocks has been developed by Tsutsumi et al.[104] in which consideration is given to the relative locations of foreshocks and aftershocks as they would affect the loads on a plant. The additional amount of knowledge required associated with determining the locations of faults in the neighborhood of the plant does not appear to be warranted relative to the uncertainty in the analysis.

## 12.4 Treatment in Dynamic Analysis

In the current approach to SPRA, a static approach is used to quantify the probabilities of different scenarios associated with the success or failure of SSC. A level of earthquake, PGA, is determined based on an associated exceedance frequency, such as 1E-4 per yr, 1E-5 per yr or 1E-6 per yr as determined by the local seismic hazard characterization. For the specified PGA, conditional failure probabilities are assessed for the different SSCs. Different combinations of system failures can lead to severe core damage as described by system event trees. In the static approach to PRA, the probabilities of the different branches of the event tree are determined using fault trees. For a Level 1 PRA, success (no core damage) or failure (core damage) is determined by transient

---

[104] H. Tsutsumi, H. Nanba, S. Motohashi and K. Ebisawa, “Development of Seismic PSA Methodology Considering Aftershock,” Specialist Meeting on the Seismic Probabilistic Safety Assessment of Nuclear Facilities, NEA/CSNI/R14 (2007)

thermal-hydraulic analyses that are performed prior to the quantification of core damage frequency. Design basis analysis codes like TRACE[105] or RELAP5[106] (or its planned successor RELAP7[107]) provide realistic assessments of core conditions up to the point of incipient core damage. The MELCOR 2[108] (or industry alternative MAAP[109]) codes are used to analyze conditions beyond the point of severe core damage including assessing the likelihood of successful recovery actions. The thermal-hydraulic analyses are performed separate from the Boolean analysis associated with determining core damage probability. Similarly, in SPRA analysis, the structural response of structures and components is performed separate from a transient thermal-hydraulic analysis of the accident scenario.

The DET approach was developed to primarily address two issues with static event trees[110] [111]: a) ability to model process/hardware/software/human interactions under changing conditions, and, b) in the Level 2 portion of a PRA, the ability to treat multiple events that have high associated modeling uncertainty in a manner that is phenomenologically consistent with the models in the severe accident analysis code. Traditionally, DET has not been performed to support SPRA. However, seismic events are inherently dynamic events, particularly because of the potential for aftershocks. The damage caused by the main shock largely establishes a set of pathways that could potentially lead to core damage. Aftershocks are capable of altering accident sequences in a manner that could lead to entirely different end states than those that would result from system failures resulting from the initial shock wave.

An approach to performing DET analysis that includes aftershocks looks very much like a Level 2 DET analysis. The MELCOR 2 computer code would be used to perform the dynamic thermal-hydraulic analysis under the control of the RAVEN[112] computer code (in a manner analogous to the use of the ADAPT code to control the branching of a Level 1/2 DET). Branching rules would be developed in advance of the analysis. For example, structural analyses could be performed and the conditional probabilities of components assessed involving different levels of acceleration. From the human reliability analysis perspective, rules would be developed to determine the extent of delay in a recovery action associated with a given level of aftershock. From the perspective of structural failure, consideration will be given to the progression of inelastic damage to structural components due to different combinations of main and aftershocks. Consideration will also be given to scenarios that are initiated by a foreshock with a subsequent main shock of higher

---

[105] US NRC, "TRACE V5.0 Assessment Manual, Main Report," (March 2010)

[106] US NRC, "RELAP5/MOD3.3 Code Manual, NUREG/CR-5535 (2001)

[107] H. Zhang et al., "RELAP-7: Demonstrating the Integration of Two-Phase Flow Components for an Ideal BWR Loop," INL/EXT-13-29514, Rev. 0 (2013)

[108] R. O. Gauntt, "MELCOR Computer Code Manual, Version 1.8.5, Vol. 2, Rev.2," NUREG/CR-6119, Sandia National Laboratory, Albuquerque, NM (2006)

[109] Fauske & Associate, Inc., "MAAP4 - Modular Accident Analysis Program for LWR Power Plants, Vol.2, Part 1: Code Structure and Theory," Electric Power Research Institute, Palo Alto, CA (1994)

[110] A. Hakobyan, T. Aldemir, R. Denning, S. Dunagan, D. Kunsman, B. Rutt and U. Catalyurek, "Dynamic Generation of Accident Progression Event Trees," Nuclear Engineering and Design, 238: 3457-3467 (2008)

[111] K. Hsueh and A. Mosleh, "The Development and Application of the Accident Dynamic Simulator for Dynamic Probabilistic Risk Assessment of Nuclear Power Plants," Reliability Engineering and System Safety, 52: 279-296 (1996)

[112] A. Alfonsi, C. Rabiti, D. Mandelli, J. Cogliati, and R. Kinoshita, "Raven as a Tool for Dynamic Probabilistic Risk Assessment: Software Overview,' Proceedings of M&C 2013 International Topical Meeting on Mathematics and Commputation, DC-ROM, American Nuclear Society, LaGrange Park, IL (2013)

acceleration. The DET analysis would also consider branching probabilities associated with phenomenological events, such as the occurrence of hydrogen explosions.

Typically, the response of the nuclear power plant systems during the first few hours of the event is critical to the outcome. There are some seismic scenarios in which there is an extended period of time before core damage is threatened, such as the time required to exhaust the station batteries (approximately eight hours) in a long-term station blackout event. In a short term station blackout event in which DC power is unavailable, the critical period is on the order of 1-2 hours. In a station blackout event in which not only the core melts but the containment pressure cannot be controlled, containment failure might not occur until 48 hours. Thus, for the dynamic analysis that considers the effects of aftershocks, we would expect to interrupt the transient thermal-hydraulic analysis at pre-defined intervals to determine the variety of potential outcomes from after-shocks during that interval of time.

Time zero in the analysis is defined by the occurrence of the first shock experienced by the plant. That could be either a foreshock or the main shock. In the analysis, the main shock has a PGA of PGAm. The probability of a foreshock is assessed in Table 12.1 to have a probability of 0.07. If there is a foreshock it is assumed that the main shock will occur essentially immediately. Although it is possible to consider different possible magnitudes of foreshocks, for the purpose of this example, we assume that the existence of a foreshock does not significantly affect the results and that the accident scenario is initiated by a main shock of magnitude PGAm. At this point, it is necessary to determine the different plant states that can exist after experiencing the PGA of the main shock, i.e., what SSCs have been failed as the result of the event and their impact on accident progression. For example, the plant will have lost offsite power. With some probability the plant will also have lost availability of diesel generators and possibly other systems that affect the transient behavior of the scenario. Thus, based on structural analyses and fragility analyses that have been performed pre-transient analysis, immediately following the main shock there will be multiple analysis pathways (threads) each with an associated probability to be tracked on different computer cores.

The analyses will proceed for a specified duration to consider the impact of aftershocks. Each branch could also be interrupted by achieving some other branching condition, such as the occurrence of a hydrogen burn. Assume for this example that the transient progression is interrupted at 0.1 day (2.4 hr intervals). In the first interval the conditional probabilities of one or more shock waves exceeding different levels of acceleration from Figure 12.1 are shown in Table 12.2, which was derived from Figure 12.1. Thus, each existing thread in the analysis could at this point give rise to six new threads associated with different magnitudes of aftershocks, as well as the continuation of the old thread associated with no aftershocks of significance in that time period. Before continuing the analysis, it is necessary to determine how the state of the plant has been altered by the occurrence of an aftershock with the acceleration associated with that branch. This could require the analyst to perform new structural analyses prior to continuing the analysis. The impact on operator performance must also be evaluated. If a crew member was in the process of performing some critical action at the time of the aftershock, it will be necessary to assess the impact of the aftershock on the success or failure to complete that critical action successfully. The analysis is then restarted with different probabilities and plant conditions for the various threads being followed. At the end of the next defined time interval, all of the analyses are again halted.

At this new time, e.g. 0.2 days (4.8 hr), the analysis must consider a new table similar to Table 12.2, based on Figure 12.1. In this case, the branching probabilities will be changed.

Table 12.2. Probability of One or More Aftershocks in the First 2.4 Hr

| Acceleration | Exceedance Probability | Interval | Probability within 2.4 hr Period |
|---|---|---|---|
| | | >1 PGAm | 0.028 |
| PGAm | 0.028 | 0.8-1 PGAm | 0.017 |
| 0.8 PGAm | 0.045 | 0.5-0.8 PGAm | 0.055 |
| 0.5 PGAm | 0.11 | 0.3-0.5 PGAm | 0.18 |
| 0.3 PGAm | 0.29 | 0.2-0.3 PGAm | 0.27 |
| 0.2 PGAm | 0.56 | 0.1-0.2 PGAm | 0.41 |
| 0.1 PGAm | 0.97 | <0.1 PGAm | 0.03 |

Although the analysis approach described above is doable in concept, the number of threads that have to be followed in a separate computer core grows very rapidly. One way to reduce the growth is to consider only a limited number of branching possibilities in Table 12.2. Another possibility is to eliminate very low probability threads and a third approach is to combine threads that represent essentially identical scenarios. Clustering techniques could be used for this purpose.

Thus, in concept we know how a dynamic analysis including the effects of aftershocks can be performed. However, before going to the effort of developing the associated branching rules and support information, it makes sense to undertake simple approximate examples to determine those conditions under which a dynamic analysis is warranted. The approach to do that is to develop a set of base scenarios with MELCOR that account for the various plant states associated with the initial shock. At various times in the scenarios, we would look to see what the potential impacts would be of shocks of different magnitudes. In this sense, we would perform a pseudo-dynamic analysis.

As described in Sections 7 and 8, two case studies have been defined to look at: a) the effects of performing an uncertainty analysis for the structural response of an auxiliary building on the joint failure probability of two essentially identical components at two locations in the building when the fragility of those components is determined by experiment (Case 1), and, b) common cause failure resulting from seismically induced flooding in combination with random failure probabilities of components (Case 2). Case 2 study includes the potential for a technician to close a valve between two tanks from which condensate water is spilling and thus to decrease the potential for flooding a basement room to the point of failing HPI pumps. A third case study will be defined that examines the impact of aftershocks on Case 2 study with regard to human error probability and the potential failure of a structural wall in the auxiliary building.

# 13. SOFTWARE AND TOOLS USED TO SUPPORT PERFORMANCE OF SPRA

## 13.1 Introduction

This document contains the computer codes that were used for uncertainty quantification. Sections 13.2 and 13.3 describe the MATLAB codes used for the structural analysis and flooding analysis, respectively. Sections A, B and C describe the software input used for condensate storage tank modeling, auxiliary building modeling, and containment structure modeling, respectively. Usage of the codes are illustrated by sample inputs and outputs.

## 13.2 Description of 2D Stick Model Codes in Matlab and Workflow

The seismic performance of simplified buildings and attached nonstructural components are analytically computed using MATLAB codes, and their results are compared to the simulation results using 3D finite element models in the project. For the simplified models, a second floor building is assumed as a 2-degree of freedom (2DOF), and the nonstructural components are assumed as a single-degree of freedom (SDOF) and attached to the each floor of the building. Considering the variation of stiffness and mass distributions of the building and the nonstructural components, a large numbers of samples are generated using the Latin Hypercube Sampling (LHS) method, and the seismic performance of each sample is computed solving the following equation:

$$\boldsymbol{M}\begin{Bmatrix}\ddot{u}_1\\ \ddot{u}_2\end{Bmatrix}+\boldsymbol{C}\begin{Bmatrix}\dot{u}_1\\ \dot{u}_2\end{Bmatrix}+\boldsymbol{K}\begin{Bmatrix}u_1\\ u_2\end{Bmatrix}=-\boldsymbol{M}l\ddot{u}_g$$

where $\boldsymbol{M}=\begin{bmatrix}m1 & 0\\ 0 & m2\end{bmatrix}$ is the mass matrix, $\boldsymbol{K}=\begin{bmatrix}k1+k2 & -k2\\ -k2 & k2\end{bmatrix}$ is the stiffness matrix, $\boldsymbol{C}=a_0M+a_0K$ is the damping matrix with $a_0=\frac{2\zeta\omega_1\omega_2}{\omega_1+\omega_2}$ and $a_1=\frac{2\zeta}{\omega_1+\omega_2}$.

In order to solve this partial differential equation, the Bogachi-Shampine method is used, which is implemented in the function, *ode 23,* in MATLAB. It is a Runge–Kutta method of order three with four stages with the First Same As Last (FSAL) property, so that it uses approximately three function evaluations per time step. The solution of the equation provides: (1) the absolute floor accelerations FA1 ($\ddot{u}_1$) and FA2 ($\ddot{u}_2$), and (2) floor displacemens FD1 ($u_1$) and FD2 ($u_2$). Using these histories of FA1 and FA2, fundamental frequencies of non-structural components (NSCs), $T_n$, and a constant damping ratio of 5% for the NSC, absolute acceleration histories of NSCs are computed.

As the result of the analysis above, the dynamic performance of nonstructural components under seismic shaking are compared to their limit states (capacities) to judge the operational failures. The conditional failure probabilities are computed using the equations below. $\boldsymbol{P_f}$ is the conditional failure probability of a NCS. The Resistance (capacity) model ($\boldsymbol{R}$) is a log-normal function based on the literature review. The Stress (demand/response) model ($\boldsymbol{S}$) is determined by the simulation result of samples. $S_1$ and $S_2$ present the peak acceleration response of NSC1 and NSC2 from the previous analysis result.

$$\boldsymbol{P_f}=\boldsymbol{P}[(\boldsymbol{R_1}-\boldsymbol{S_1}<\boldsymbol{0})\cap(\boldsymbol{R_2}-\boldsymbol{S_2}<\boldsymbol{0})]$$

$$=\int_{-\infty}^{\infty}\int_{-\infty}^{\infty}\int_{r_2}^{\infty}\int_{r_1}^{\infty}\boldsymbol{f_{R_1,R_2,S_1,S_2}(r_1,r_2,s_1,s_2)ds_1ds_2dr_1dr_2}$$

### 13.2.1 Joint Failure Probability Calculations – Case Study 1

```
close all
clear all
% clc

format long g

NSamp = 1e4;

load('Peak_2500.mat');
Peak_Accel = Peak_accel; Peak_Disp = Peak_disp; PFF = PF;
load('Peak_5000.mat');
Peak_Accel = [Peak_Accel; Peak_accel(2501:end,:)]; Peak_Disp = [Peak_disp;
Peak_disp(2501:end,:)]; PFF = [PF; PF(2501:end,:)];
load('Peak_7500.mat');
Peak_Accel = [Peak_Accel; Peak_accel(5001:end,:)]; Peak_Disp = [Peak_disp;
Peak_disp(5001:end,:)]; PFF = [PF; PF(5001:end,:)];
load('Peak10000.mat');
Peak_Accel = [Peak_Accel; Peak_accel(7501:end,:)]; Peak_Disp = [Peak_disp;
Peak_disp(7501:end,:)]; PFF = [PF; PF(7501:end,:)];
load('Sampling_LHS3.mat');

GM = PF(:,1);   % Peak Ground Acceleration (PGA)
FA1 = PF(:,2); % Peak Floor Acceleration (PFA1)
FA2 = PF(:,3); % Peak Floor Acceleration (PFA2)
u1 = PF(:,4);  % Peak Floor Displacement (PFD1)
u2 = PF(:,5);  % Peak Floor Displacement (PFD2)

NC_D1 = Peak_Disp(:,2);
NC_D2 = Peak_Disp(:,1);
NC_A1 = Peak_Accel(:,2); %NC's response Acceleration 1  ! Load !!!!!!!!!!!
NC_A2 = Peak_Accel(:,1); %NC's response Acceleration 2  ! Load !!!!!!!!!!!

% NC_A1 = normrnd(0.2,0.25,10000,1); NC_A1 = NC_A1-min(NC_A1); NC_A1 =
NC_A1/max(NC_A1)*1.4;
% NC_A2 = normrnd(-0.5,0.1,10000,1); NC_A2 = NC_A2-min(NC_A2); NC_A2 =
NC_A2/max(NC_A2)*1.4;

% Tn_lhs = Buildings' Natural Period (second)
% zeta_lhs = Buildings' damping ratio (Unitless)
% Freq_n_lhs = Natural Periods of Nonstructural components (Hz)
% GM_n =  number of GM among LA ground motions

% 125V DC batteries, racks mean = mr=1.01 betaR = 0.28 betaU =0.63
mr = 1.01; betaR=0.28;betaU=0.63;  beta = sqrt(betaR^2+betaU^2);
mu = log(mr^2)/sqrt(beta^2+mr^2);
sigma = sqrt(log(beta^2/(mr^2)+1));
```

```
F_accel = lognrnd(mu,sigma, 1,NSamp);

for i =1:NSamp;
%     i
    if F_accel(i) > NC_A1(i);
        PF1(i)=0;
    else PF1(i)=1;
    end
    if F_accel(i) > NC_A2(i);
        PF2(i)=0;
    else PF2(i)=1;
    end
    PFF(i) = PF1(i)*PF2(i);
end

pf1 = sum(PF1)/NSamp;
pf2 = sum(PF2)/NSamp;
pff = sum(PFF)/NSamp;

% % % [Fs1,x1]= ecdf(NC_A1);
smin = 0; smax = max(NC_A1)*5;
x1 = smin:(smax-smin)/100000:smax; x1 = x1';
Fs1 = zeros(length(x1),1);
for i = 1:length(x1);
    Fs1(i,1) = length(NC_A1(NC_A1<=x1(i)))/length(NC_A1);
end
fr1 = lognpdf(x1,mu,sigma);
pf1_integ = trapz(x1,(1-Fs1).*fr1);

% % % [Fs2,x2]= ecdf(NC_A2);
smin = 0; smax = max(NC_A2)*5;
x2 = smin:(smax-smin)/100000:smax; x2 = x2';
Fs2 = zeros(length(x2),1);
for i = 1:length(x2);
    Fs2(i,1) = length(NC_A2(NC_A2<=x2(i)))/length(NC_A2);
end
fr2 = lognpdf(x2,mu,sigma);
pf2_integ = trapz(x2,(1-Fs2).*fr2);

[pf1_integ pf1; pf2_integ pf2]

S = [NC_A1, NC_A2];
s_max = min(S,[],2);
smin = min([NC_A1; NC_A2])/2; smax = max([NC_A1; NC_A2])*2;
% smin = 0; smax = max([NC_A1; NC_A2])*100;
x12 = smin:(smax-smin)/100000:smax;
Gs12 = zeros(length(x12),1);
for i = 1:length(x12);
    Gs12(i,1) = length(s_max(s_max>=x12(i)))/length(s_max);
end
fr12 = lognpdf(x12',mu,sigma);
pf12_integ = trapz(x12,Gs12.*fr12)

figure;
plot(x1,1-Fs1,'r',x2,1-Fs2,':m','linewidth', 2); hold on;
```

```
plot(x2,fr2,'b', 'linewidth', 1)
xlabel('Peak Acceleration', 'FontSize',11,'FontName','times');
ylabel('Probability Density', 'FontSize',11,'FontName','times');
legend('Peak Accel. of NC1','Peak Accel. of
NC2','Capacity','FontSize',11,'FontName','times','Location','northeast');
xlim([0 8]);

% % Hz_building = 1./Tn_lhs;
% %
figure;
plot(Freq_n_lhs,NC_A2,'bo',Freq_n_lhs,NC_A1,'ro')
xlabel('Fundamental Frequencies of Axillary Building(Hz)',
'FontSize',11,'FontName','times');
ylabel('Peak Acceleration(g)', 'FontSize',11,'FontName','times');
legend('Peak Accel. of NC1','Peak Accel. of
NC2','FontSize',11,'FontName','times','Location','northwest');

figure;
semilog(Freq_n_lhs,NC_D2,'bo',Freq_n_lhs,NC_D1,'ro')
xlabel('Fundamental Frequencies of Axillary Building(Hz)',
'FontSize',11,'FontName','times');
ylabel('Peak Displacement(inch)', 'FontSize',11,'FontName','times');
legend('Peak Disp. of NC1','Peak Disp. of
NC2','FontSize',11,'FontName','times','Location','northwest');
```

### 13.2.2 Sampling and Analysis of 2D Stick Model of Auxiliary Building: Case Study 1

```
%% 2DOF model sampling and confirming their Eigen values and vectors
% clear all;
% close all;

pi = pi();

% % % M_m =  Mass matrix M_m(1) =  first floor
% % % S_m =  Stiffness matrix S_m(1) =  first floor
% % % zeta = Buildings' damping ratio (Unitless)  --> Rayleigh damping
% % % Freq_n = Natural Periods of Nonstructural components (Hz)
% % % GM_n =  number of GM among LA ground motions
% n_sample = length(Tn_lhs);

g = 9.8; % unit: m/sec^2

TimeStep=load('LAGMs/LaTimeStep.TSTEP');

%load('Sampling_20000_RAVEN.mat')

 for i=1:1;
     tic
     i
    %%%%%%%%%%%%%%%%%%%%%%%%%%%%%%%%%%%%%%%%%%%%%%%%%%%%%%%%%%%%%%%%%%%%%%%%
```

```
    % Input data %%%%%%%%%%%%%%%%%%%%%%%%%%%%%%%%%%%%%%%%%%%%%%%%%%%%%%%%%%
    %%%%%%%%%%%%%%%%%%%%%%%%%%%%%%%%%%%%%%%%%%%%%%%%%%%%%%%%%%%%%%%%%%%%%%%
    %   Generating Linear Structures #######################################

    % Main Building Structures (2DOF)
    M_m = [m1(i) 0; 0 m2(i)];
    S_m = [s1(i)+s2(i) -s2(i); -s2(i) s2(i)];

    [V,D] = eig(inv(M_m)*S_m);
    [diagD,ordD] = sort(diag(D));
    omega = sqrt(diag(diagD));
    freq = omega/(2*pi);

    % The damping ratio of structure (we need to choose the distribution
    aa0 = zeta(i)*2*omega(1,1)*omega(2,2)/(omega(1,1)+omega(2,2));
    aa1 = zeta(i)*2/(omega(1,1)+omega(2,2));

    C_m = aa0*M_m+aa1*S_m;
    ML = M_m*ones(2,1);

    % NC components
    zeta1 = 0.02;  %damping ratio
    NC_fq = Freq_n(i); %Fundamental Frequency of NC, unit : Hz!!!!

    % Loading
################################################################
    n_GM=GM_n(i);

    GM = load(['LAGMs/Mla',num2str(n_GM),'.dat']);
    dt_e = TimeStep(n_GM,2);
    %  Solving PDE
######################################################################
    T_end = length(GM)*dt_e;
    dt_a = 0.0001;
    dt_o = dt_a;
    %%% Run GM
    t = 0:dt_e:(length(GM)-1)*dt_e;
    scale_Factor = 1.0;
    accel=g*GM*scale_Factor;

    % Start Solving 0 FL
##################################################
    sim('ODE_MDOF_SA_val.mdl');

    Peak_GM(i) = max(abs(accel_GM/g));

    PF_A1(i) = max(abs(a1/g));  %% the first floor acceleration
    PF_A2(i) = max(abs(a2/g));  %% the second floor acceleration

    PF_D1(i) = max(abs(u1));  %% the first floor displacement
    PF_D2(i) = max(abs(u2));  %% the first floor displacement

    N_D1(i) = max(abs(disp_NC1));    %% Displacement of NC1 on the first
floor
    N_D2(i) = max(abs(disp_NC2));    %% Displacement of NC2 on the second
floor
```

```
    N_A1(i) = max(abs(accel_NC1/g));    %% Acceleration of NC1 on the first
floor
    N_A2(i) = max(abs(accel_NC2/g));    %% Acceleration of NC2 on the second
floor

        toc
 end

%save(['test'], 'Peak_GM', 'PF_A1', 'PF_A2', 'PF_D1', 'PF_D2', 'N_D1',
'N_D2','N_A1', 'N_A2');
csvwrite(['Sample_out.csv'], [Peak_GM, PF_A1, PF_A2, PF_D1, PF_D2, N_D1,
N_D2,N_A1, N_A2]);
```

### 13.3 Description of Reduced-Order Room Flooding Model

The reduced-order room flooding model (RORFM) calculates the flow of water between rooms assuming purely gravity-driven flow and using a simplified Bernoulli equation:

$$\frac{V_1^2}{2} + g * z_1 = \frac{V_2^2}{2} + g * z_2$$

where $V_1$ represents fluid velocity in room *1*, $g=9.8m/s^2$, and $z_1$ is the water level in room *1*. The subscripts are used similarly for room *2*. The choice of this equation causes changes in flow to take place instantly, as static head does not result in increased pressure but is immediately translated to kinetic energy. Relevant flows in the CFD calculation using FLUENT were found to reach a quasi-steady state within 3s, suggesting that this is an acceptable design choice for the purposes of the RORFM.

The RORFM is built around Rooms, which have a uniform water level, and Flowpaths, which do not hold-up water. The following matrices are created by the RORFM, and may be of arbitrary length:

Rooms: maximum and minimum elevation, initial water level, and area

Flowpaths: connecting Rooms, elevation at either end, hydraulic diameter, length, area, and discharge coefficient

Obstructions: affected Room, maximum and minimum elevation, and area

The discharge coefficient is a multiplier on the Bernoulli flow through each Flowpath, and represents the effects of the narrowing and expansion of the flow through a constriction. It is a tunable parameter, which must be found through experimentation. The changes in Room water levels at each time step are calculated as a set of the differential equation:

$$\frac{dH(i,t)}{dt} = \frac{Flow(i,t)}{Area(i,t)}$$

where $Flow(i,t)$ represents the net flow into Room $i$ at time $t$ through all Flowpaths, and $Area(i,t)$ represents the Room's surface area at the current water level $H$, which may be reduced by large obstructions such as pumps or cabinets. The outputs of the RORFM are volumetric flow rates through Flowpaths and water levels in Rooms for each time step of the calculation.

### 13.3.1 Tuning and Verification of the RORFM

In order to tune the discharge coefficient in the RORFM, simple cases are built in both the RORFM and FLUENT that represent a similar scenario. An example of a FLUENT mesh of such a case is shown as Figure 13.1. Both of the rooms and the flow path are initially filled with stationary water. One room is put under a steady inlet pressure condition representative of the static pressure at the bottom of a 10m tall CST (98 kPa). The other room uses a pressure outlet condition at atmospheric pressure.

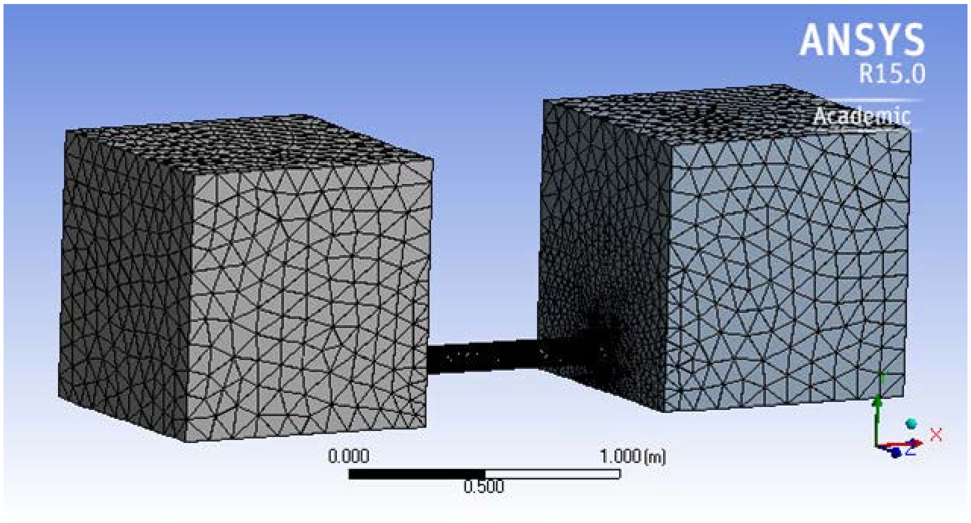

Figure 1: FLUENT Mesh for Steady-State RORFM Tuning

The ratio of flow path size to room size is preserved to that of the auxiliary building flood scenario to capture the effects of the narrowing and expansion of flow. The model was run and the steady-state flow across the flow path was recorded. The analysis was repeated for a number of circular flow paths as well as a large rectangular path 2m high and 3m wide that represents an equipment door, as seen in Table 13.1. The Reynolds number was recorded in each case to confirm that the flow requires the use of a FLUENT turbulence model. It was also repeated for a static pressure of 9.8kPa, representing a 1m column of water. Each steady-state case took approximately 15 minutes to run.

The results of the steady-state FLUENT cases are shown in Table 13.1. Similar cases were run in the RORFM using very large Rooms to simulate steady-state conditions. The discharge coefficient in the RORFM was initially set at 0.6 for each Flowpath, and was adjusted iteratively in small steps until the steady-state flow matched that of FLUENT within 1%. The large rectangular flow path resulted in a high discharge coefficient in both cases. This is expected, as regime with no restriction of flow would have a coefficient of 1.

Table 1: Tuning of RORFM against FLUENT Steady-State Results

| | | **Fluent Results** | | **RORFM Tuning** | |
|---|---|---|---|---|---|
| **Shape** | **Size (m)** | **Re (1m)** | **Re (10m)** | **$C_d$ (1m)** | **$C_d$ (10m)** |
| Circular | 0.05 | 8.6E4 | 2.8E5 | 0.68 | 0.70 |
| Circular | 0.1 | 1.8E5 | 5.9E5 | 0.72 | 0.74 |
| Circular | 0.5 | 9.2E5 | 2.9E6 | 0.67 | 0.74 |
| Circular | 1.0 | 1.8E6 | 5.7E6 | 0.62 | 0.72 |
| Rectangular | 3*2 | 4.3E6 | 1.4E7 | 0.83 | 0.81 |

The goal of the RORFM is a transient model of flooding. However, a full-scale verification with FLUENT is not computationally feasible. Therefore, the transient behavior of each flow path is compared in a reduced-size transient case. As seen in Figure 2, a tall and narrow room is used to represent a CST. The small volume of the tall room causes it to empty more quickly than in the full scenario, but with an equal flow rate at a given water level. It is connected via a flow path to a room that is sized to preserve the narrowing and expansion of the flow. The back of the small room is a pressure outlet condition at atmospheric pressure.

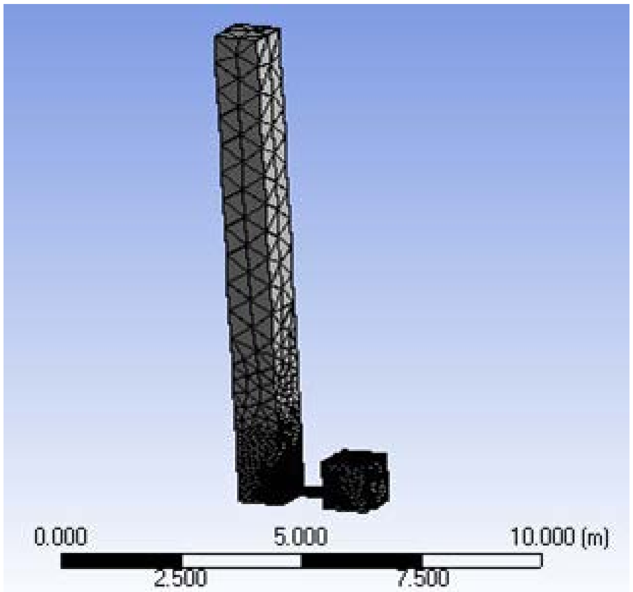

Figure 2: FLUENT Mesh for Transient RORFM Verification

The transient case is started with the tall room filled with water and the rest of the problem space filled with air. The top of the tall room is a pressure outlet boundary condition that allows reverse flow, representing the vent on CSTs. This transient scenario requires approximately 30 minutes to run.

Verification

The transient behavior of the tuned RORFM was verified against the transient FLUENT case of a 20cm (8 inch) diameter pipe (see Figure 2), which represents the AFW supply pipes out of the CST. The flow rates of both models for the approximately 70s the room representing the CST took to empty are shown in Figure 3. It can be seen that the rates differ somewhat at the start, as the RORFM instantly establishes flow, while FLUENT must fill the flow path and then establish flow. A change in flow regime may be seen for both models when the flow path is no longer full, around 59s. The flow rates also diverge as the tank drops below half-full, suggesting that the RORFM slightly overpredicts flow in lower-head conditions.

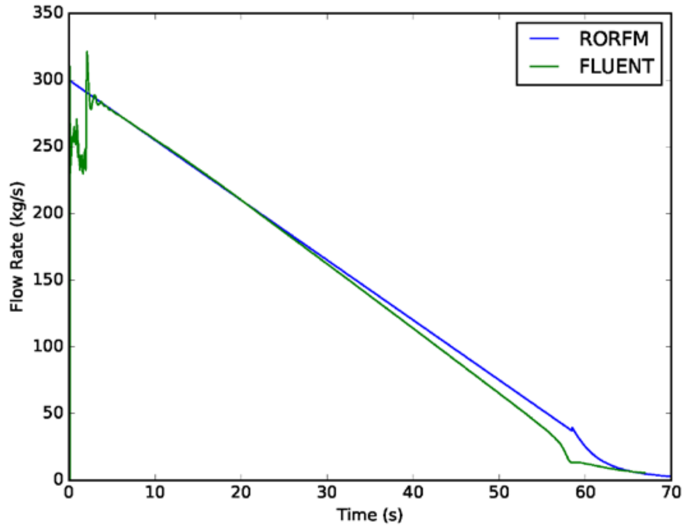

Figure 3: Flow Rates for Transient Verification, 20cm Pipe

Figure 4 shows the cumulative flow across the flow path over time, which is a measure of the general usefulness of the RORFM for measuring changes in water levels. At 60s after the start of the transient, the cumulative flow in the RORFM was 4% higher than the cumulative flow in FLUENT. This process may be repeated for a variety of flow paths and initial static heads.

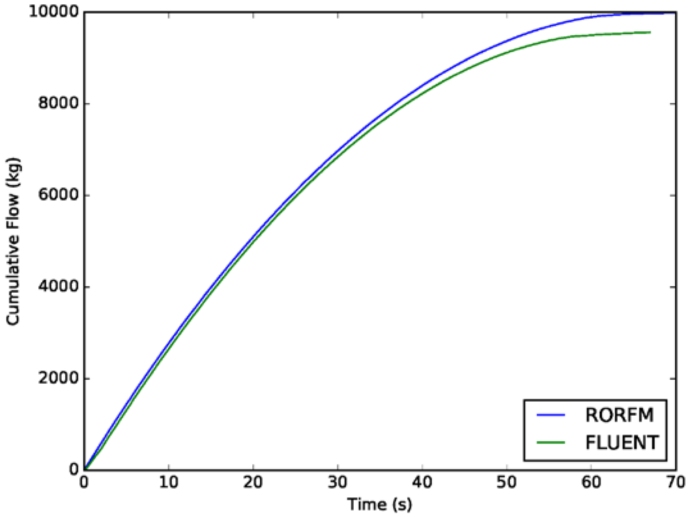

Figure 4: Cumulative Flow for Transient Verification, 20cm Pipe

### 13.3.2 Reduced Order Flooding Model - MATLAB Code

```
function srfm_ode_master(input_file_name)
Rooms=table2array(readtable('Rooms.dat'));
```

```
Obstruct=table2array(readtable('Obstruct.dat'));
FlowPaths=table2array(readtable('FlowPaths.dat'));
FlowPathFractions=table2array(readtable('FlowPathFractions.dat'));
Source_Info=table2array(readtable('Source_Info.dat'));
Source_Rate=table2array(readtable('Source_Rate.dat'));
t_end=table2array(readtable('t_end.dat'));
t_step=table2array(readtable('t_step.dat'));
Friction_Enable=table2array(readtable('Friction_Enable.dat'));
tic
[t,H]=srfm_ode(FlowPaths,Obstruct,Rooms,Source_Info,Source_Rate,FlowPathFractions,t_e
nd,Friction_Enable,t_step);
t_exec=toc;
t=t';
save(strcat(num2str(FlowPathFractions(1,2)),'t.txt'),'t','-ascii')
save(strcat(num2str(FlowPathFractions(1,2)),'H.txt'),'H','-ascii')
save(strcat(num2str(FlowPathFractions(1,2)),'t_exec.txt'),'t_exec','-ascii')
save(strcat(num2str(FlowPathFractions(1,2)),'out_mat.mat'))
end

function
[t,H]=srfm_ode(FlowPaths,Obstruct,Rooms,Source_Info,Source_Rate,FlowPathFractions,t_e
nd,Friction_Enable,t_step)
if size(Rooms,1)==2
    ff = @(t,H)[...

(sum(srfm_flow(H,1,FlowPaths,Rooms,Friction_Enable)*srfm_flow_fraction(t,H,1,FlowPath
Fractions,FlowPaths))+(srfm_water_source(t,1,Source_Info,Source_Rate)/1000))/srfm_sur
f_area(1,H(1),Rooms,Obstruct);...

(sum(srfm_flow(H,2,FlowPaths,Rooms,Friction_Enable)*srfm_flow_fraction(t,H,2,FlowPath
Fractions,FlowPaths))+(srfm_water_source(t,2,Source_Info,Source_Rate)/1000))/srfm_sur
f_area(2,H(2),Rooms,Obstruct)...
        ];
elseif size(Rooms,1)==3
    ff = @(t,H)[...

(sum(srfm_flow(H,1,FlowPaths,Rooms,Friction_Enable)*srfm_flow_fraction(t,H,1,FlowPath
Fractions,FlowPaths))+(srfm_water_source(t,1,Source_Info,Source_Rate)/1000))/srfm_sur
f_area(1,H(1),Rooms,Obstruct);...

(sum(srfm_flow(H,2,FlowPaths,Rooms,Friction_Enable)*srfm_flow_fraction(t,H,2,FlowPath
Fractions,FlowPaths))+(srfm_water_source(t,2,Source_Info,Source_Rate)/1000))/srfm_sur
f_area(2,H(2),Rooms,Obstruct);...

(sum(srfm_flow(H,3,FlowPaths,Rooms,Friction_Enable)*srfm_flow_fraction(t,H,3,FlowPath
Fractions,FlowPaths))+(srfm_water_source(t,3,Source_Info,Source_Rate)/1000))/srfm_sur
f_area(3,H(3),Rooms,Obstruct)...
        ];
elseif size(Rooms,1)==4
    ff = @(t,H)[...

(sum(srfm_flow(H,1,FlowPaths,Rooms,Friction_Enable)*srfm_flow_fraction(t,H,1,FlowPath
Fractions,FlowPaths))+(srfm_water_source(t,1,Source_Info,Source_Rate)/1000))/srfm_sur
f_area(1,H(1),Rooms,Obstruct);...
```

```
(sum(srfm_flow(H,2,FlowPaths,Rooms,Friction_Enable)*srfm_flow_fraction(t,H,2,FlowPath
Fractions,FlowPaths))+(srfm_water_source(t,2,Source_Info,Source_Rate)/1000))/srfm_sur
f_area(2,H(2),Rooms,Obstruct);...

(sum(srfm_flow(H,3,FlowPaths,Rooms,Friction_Enable)*srfm_flow_fraction(t,H,3,FlowPath
Fractions,FlowPaths))+(srfm_water_source(t,3,Source_Info,Source_Rate)/1000))/srfm_sur
f_area(3,H(3),Rooms,Obstruct);...

(sum(srfm_flow(H,4,FlowPaths,Rooms,Friction_Enable)*srfm_flow_fraction(t,H,4,FlowPath
Fractions,FlowPaths))+(srfm_water_source(t,4,Source_Info,Source_Rate)/1000))/srfm_sur
f_area(4,H(4),Rooms,Obstruct)...
        ];
elseif size(Rooms,1)==5
    ff = @(t,H)[...

(sum(srfm_flow(H,1,FlowPaths,Rooms,Friction_Enable)*srfm_flow_fraction(t,H,1,FlowPath
Fractions,FlowPaths))+(srfm_water_source(t,1,Source_Info,Source_Rate)/1000))/srfm_sur
f_area(1,H(1),Rooms,Obstruct);...

(sum(srfm_flow(H,2,FlowPaths,Rooms,Friction_Enable)*srfm_flow_fraction(t,H,2,FlowPath
Fractions,FlowPaths))+(srfm_water_source(t,2,Source_Info,Source_Rate)/1000))/srfm_sur
f_area(2,H(2),Rooms,Obstruct);...

(sum(srfm_flow(H,3,FlowPaths,Rooms,Friction_Enable)*srfm_flow_fraction(t,H,3,FlowPath
Fractions,FlowPaths))+(srfm_water_source(t,3,Source_Info,Source_Rate)/1000))/srfm_sur
f_area(3,H(3),Rooms,Obstruct);...

(sum(srfm_flow(H,4,FlowPaths,Rooms,Friction_Enable)*srfm_flow_fraction(t,H,4,FlowPath
Fractions,FlowPaths))+(srfm_water_source(t,4,Source_Info,Source_Rate)/1000))/srfm_sur
f_area(4,H(4),Rooms,Obstruct);...

(sum(srfm_flow(H,5,FlowPaths,Rooms,Friction_Enable)*srfm_flow_fraction(t,H,5,FlowPath
Fractions,FlowPaths))+(srfm_water_source(t,5,Source_Info,Source_Rate)/1000))/srfm_sur
f_area(5,H(5),Rooms,Obstruct)...
        ];
elseif size(Rooms,1)==6
    ff = @(t,H)[...

(sum(srfm_flow(H,1,FlowPaths,Rooms,Friction_Enable)*srfm_flow_fraction(t,H,1,FlowPath
Fractions,FlowPaths))+(srfm_water_source(t,1,Source_Info,Source_Rate)/1000))/srfm_sur
f_area(1,H(1),Rooms,Obstruct);...

(sum(srfm_flow(H,2,FlowPaths,Rooms,Friction_Enable)*srfm_flow_fraction(t,H,2,FlowPath
Fractions,FlowPaths))+(srfm_water_source(t,2,Source_Info,Source_Rate)/1000))/srfm_sur
f_area(2,H(2),Rooms,Obstruct);...

(sum(srfm_flow(H,3,FlowPaths,Rooms,Friction_Enable)*srfm_flow_fraction(t,H,3,FlowPath
Fractions,FlowPaths))+(srfm_water_source(t,3,Source_Info,Source_Rate)/1000))/srfm_sur
f_area(3,H(3),Rooms,Obstruct);...

(sum(srfm_flow(H,4,FlowPaths,Rooms,Friction_Enable)*srfm_flow_fraction(t,H,4,FlowPath
Fractions,FlowPaths))+(srfm_water_source(t,4,Source_Info,Source_Rate)/1000))/srfm_sur
f_area(4,H(4),Rooms,Obstruct);...
```

```
(sum(srfm_flow(H,5,FlowPaths,Rooms,Friction_Enable)*srfm_flow_fraction(t,H,5,FlowPath
Fractions,FlowPaths))+(srfm_water_source(t,5,Source_Info,Source_Rate)/1000))/srfm_sur
f_area(5,H(5),Rooms,Obstruct);...

(sum(srfm_flow(H,6,FlowPaths,Rooms,Friction_Enable)*srfm_flow_fraction(t,H,6,FlowPath
Fractions,FlowPaths))+(srfm_water_source(t,6,Source_Info,Source_Rate)/1000))/srfm_sur
f_area(6,H(6),Rooms,Obstruct)...
        ];
elseif size(Rooms,1)==7
    ff = @(t,H)[...

(sum(srfm_flow(H,1,FlowPaths,Rooms,Friction_Enable)*srfm_flow_fraction(t,H,1,FlowPath
Fractions,FlowPaths))+(srfm_water_source(t,1,Source_Info,Source_Rate)/1000))/srfm_sur
f_area(1,H(1),Rooms,Obstruct);...

(sum(srfm_flow(H,2,FlowPaths,Rooms,Friction_Enable)*srfm_flow_fraction(t,H,2,FlowPath
Fractions,FlowPaths))+(srfm_water_source(t,2,Source_Info,Source_Rate)/1000))/srfm_sur
f_area(2,H(2),Rooms,Obstruct);...

(sum(srfm_flow(H,3,FlowPaths,Rooms,Friction_Enable)*srfm_flow_fraction(t,H,3,FlowPath
Fractions,FlowPaths))+(srfm_water_source(t,3,Source_Info,Source_Rate)/1000))/srfm_sur
f_area(3,H(3),Rooms,Obstruct);...

(sum(srfm_flow(H,4,FlowPaths,Rooms,Friction_Enable)*srfm_flow_fraction(t,H,4,FlowPath
Fractions,FlowPaths))+(srfm_water_source(t,4,Source_Info,Source_Rate)/1000))/srfm_sur
f_area(4,H(4),Rooms,Obstruct);...

(sum(srfm_flow(H,5,FlowPaths,Rooms,Friction_Enable)*srfm_flow_fraction(t,H,5,FlowPath
Fractions,FlowPaths))+(srfm_water_source(t,5,Source_Info,Source_Rate)/1000))/srfm_sur
f_area(5,H(5),Rooms,Obstruct);...

(sum(srfm_flow(H,6,FlowPaths,Rooms,Friction_Enable)*srfm_flow_fraction(t,H,6,FlowPath
Fractions,FlowPaths))+(srfm_water_source(t,6,Source_Info,Source_Rate)/1000))/srfm_sur
f_area(6,H(6),Rooms,Obstruct);...

(sum(srfm_flow(H,7,FlowPaths,Rooms,Friction_Enable)*srfm_flow_fraction(t,H,7,FlowPath
Fractions,FlowPaths))+(srfm_water_source(t,7,Source_Info,Source_Rate)/1000))/srfm_sur
f_area(7,H(7),Rooms,Obstruct)...
        ];
elseif size(Rooms,1)==8
    ff = @(t,H)[...

(sum(srfm_flow(H,1,FlowPaths,Rooms,Friction_Enable)*srfm_flow_fraction(t,H,1,FlowPath
Fractions,FlowPaths))+(srfm_water_source(t,1,Source_Info,Source_Rate)/1000))/srfm_sur
f_area(1,H(1),Rooms,Obstruct);...

(sum(srfm_flow(H,2,FlowPaths,Rooms,Friction_Enable)*srfm_flow_fraction(t,H,2,FlowPath
Fractions,FlowPaths))+(srfm_water_source(t,2,Source_Info,Source_Rate)/1000))/srfm_sur
f_area(2,H(2),Rooms,Obstruct);...

(sum(srfm_flow(H,3,FlowPaths,Rooms,Friction_Enable)*srfm_flow_fraction(t,H,3,FlowPath
Fractions,FlowPaths))+(srfm_water_source(t,3,Source_Info,Source_Rate)/1000))/srfm_sur
f_area(3,H(3),Rooms,Obstruct);...
```

```
(sum(srfm_flow(H,4,FlowPaths,Rooms,Friction_Enable)*srfm_flow_fraction(t,H,4,FlowPath
Fractions,FlowPaths))+(srfm_water_source(t,4,Source_Info,Source_Rate)/1000))/srfm_sur
f_area(4,H(4),Rooms,Obstruct);...

(sum(srfm_flow(H,5,FlowPaths,Rooms,Friction_Enable)*srfm_flow_fraction(t,H,5,FlowPath
Fractions,FlowPaths))+(srfm_water_source(t,5,Source_Info,Source_Rate)/1000))/srfm_sur
f_area(5,H(5),Rooms,Obstruct);...

(sum(srfm_flow(H,6,FlowPaths,Rooms,Friction_Enable)*srfm_flow_fraction(t,H,6,FlowPath
Fractions,FlowPaths))+(srfm_water_source(t,6,Source_Info,Source_Rate)/1000))/srfm_sur
f_area(6,H(6),Rooms,Obstruct);...

(sum(srfm_flow(H,7,FlowPaths,Rooms,Friction_Enable)*srfm_flow_fraction(t,H,7,FlowPath
Fractions,FlowPaths))+(srfm_water_source(t,7,Source_Info,Source_Rate)/1000))/srfm_sur
f_area(7,H(7),Rooms,Obstruct);...

(sum(srfm_flow(H,8,FlowPaths,Rooms,Friction_Enable)*srfm_flow_fraction(t,H,8,FlowPath
Fractions,FlowPaths))+(srfm_water_source(t,8,Source_Info,Source_Rate)/1000))/srfm_sur
f_area(8,H(8),Rooms,Obstruct)...
        ];
elseif size(Rooms,1)==9
    ff = @(t,H)[...

(sum(srfm_flow(H,1,FlowPaths,Rooms,Friction_Enable)*srfm_flow_fraction(t,H,1,FlowPath
Fractions,FlowPaths))+(srfm_water_source(t,1,Source_Info,Source_Rate)/1000))/srfm_sur
f_area(1,H(1),Rooms,Obstruct);...

(sum(srfm_flow(H,2,FlowPaths,Rooms,Friction_Enable)*srfm_flow_fraction(t,H,2,FlowPath
Fractions,FlowPaths))+(srfm_water_source(t,2,Source_Info,Source_Rate)/1000))/srfm_sur
f_area(2,H(2),Rooms,Obstruct);...

(sum(srfm_flow(H,3,FlowPaths,Rooms,Friction_Enable)*srfm_flow_fraction(t,H,3,FlowPath
Fractions,FlowPaths))+(srfm_water_source(t,3,Source_Info,Source_Rate)/1000))/srfm_sur
f_area(3,H(3),Rooms,Obstruct);...

(sum(srfm_flow(H,4,FlowPaths,Rooms,Friction_Enable)*srfm_flow_fraction(t,H,4,FlowPath
Fractions,FlowPaths))+(srfm_water_source(t,4,Source_Info,Source_Rate)/1000))/srfm_sur
f_area(4,H(4),Rooms,Obstruct);...

(sum(srfm_flow(H,5,FlowPaths,Rooms,Friction_Enable)*srfm_flow_fraction(t,H,5,FlowPath
Fractions,FlowPaths))+(srfm_water_source(t,5,Source_Info,Source_Rate)/1000))/srfm_sur
f_area(5,H(5),Rooms,Obstruct);...

(sum(srfm_flow(H,6,FlowPaths,Rooms,Friction_Enable)*srfm_flow_fraction(t,H,6,FlowPath
Fractions,FlowPaths))+(srfm_water_source(t,6,Source_Info,Source_Rate)/1000))/srfm_sur
f_area(6,H(6),Rooms,Obstruct);...

(sum(srfm_flow(H,7,FlowPaths,Rooms,Friction_Enable)*srfm_flow_fraction(t,H,7,FlowPath
Fractions,FlowPaths))+(srfm_water_source(t,7,Source_Info,Source_Rate)/1000))/srfm_sur
f_area(7,H(7),Rooms,Obstruct);...

(sum(srfm_flow(H,8,FlowPaths,Rooms,Friction_Enable)*srfm_flow_fraction(t,H,8,FlowPath
Fractions,FlowPaths))+(srfm_water_source(t,8,Source_Info,Source_Rate)/1000))/srfm_sur
f_area(8,H(8),Rooms,Obstruct);...
```

```
(sum(srfm_flow(H,9,FlowPaths,Rooms,Friction_Enable)*srfm_flow_fraction(t,H,9,FlowPath
Fractions,FlowPaths))+(srfm_water_source(t,9,Source_Info,Source_Rate)/1000))/srfm_sur
f_area(9,H(9),Rooms,Obstruct)...
        ];
end
t=0:t_step:t_end;
H = ode4(ff,t,(Rooms(:,5)));
clear srfm_flow_fraction
end

function qdot=srfm_flow(H,room,FlowPaths,Rooms,Friction_Enable)
g=9.8;
visc=8.9e-4;
r_flowpaths=(FlowPaths(:,7)==room) | (FlowPaths(:,8)==room);
r_flowpaths=find(r_flowpaths);
qdot=zeros(1,length(r_flowpaths));
qdot_headloss=zeros(1,length(r_flowpaths));
qdot_headloss_old=zeros(1,length(r_flowpaths));
deltaH=zeros(1,length(r_flowpaths));
qdot_V=zeros(1,length(r_flowpaths));
qdot_Re=zeros(1,length(r_flowpaths));
qdot_f=zeros(1,length(r_flowpaths));
FricError=ones(1,length(r_flowpaths));
fric_iterations=zeros(1,length(r_flowpaths));
ReductionFactor=zeros(1,length(r_flowpaths));

for i=1:length(r_flowpaths)
    while fric_iterations(i)<5
        deltaH(i)=ReductionFactor(i)*abs(H(FlowPaths(r_flowpaths(i),7))-
H(FlowPaths(r_flowpaths(i),8)));
        if                  (FlowPaths(r_flowpaths(i),7)==room)                  &
(H(FlowPaths(r_flowpaths(i),7))>H(FlowPaths(r_flowpaths(i),8)))                  &
(H(FlowPaths(r_flowpaths(i),7))>(FlowPaths(r_flowpaths(i),5)-
(FlowPaths(r_flowpaths(i),3)/2)))         &         (H(room)>Rooms(room,2))         &
(H(FlowPaths(r_flowpaths(i),8))<Rooms(FlowPaths(r_flowpaths(i),8),3))
            if
H(FlowPaths(r_flowpaths(i),7))>(FlowPaths(r_flowpaths(i),5)+(FlowPaths(r_flowpaths(i)
,3)/2))
                qdot(i)=-
(FlowPaths(r_flowpaths(i),9)*FlowPaths(r_flowpaths(i),2)*sqrt(abs(2*g*(deltaH(i)))));
            else
                qdot(i)=-
(FlowPaths(r_flowpaths(i),9)*(((4*((H(FlowPaths(r_flowpaths(i),7))-
(FlowPaths(r_flowpaths(i),5)-
(FlowPaths(r_flowpaths(i),3)/2)))^2))/3)*sqrt(abs(((2*(FlowPaths(r_flowpaths(i),3)/2)
)/(H(FlowPaths(r_flowpaths(i),7))-(FlowPaths(r_flowpaths(i),5)-
(FlowPaths(r_flowpaths(i),3)/2))))-0.605)))*sqrt(abs(2*g*deltaH(i))));
            end
        end
        if                  (FlowPaths(r_flowpaths(i),8)==room)                  &
(H(FlowPaths(r_flowpaths(i),8))>H(FlowPaths(r_flowpaths(i),7)))                  &
(H(FlowPaths(r_flowpaths(i),8))>(FlowPaths(r_flowpaths(i),6)-
(FlowPaths(r_flowpaths(i),3)/2)))         &         (H(room)>Rooms(room,2))         &
(H(FlowPaths(r_flowpaths(i),7))<Rooms(FlowPaths(r_flowpaths(i),7),3))
```

```
            if
H(FlowPaths(r_flowpaths(i),8))>(FlowPaths(r_flowpaths(i),6)+(FlowPaths(r_flowpaths(i)
,3)/2))
                qdot(i)=-
(FlowPaths(r_flowpaths(i),9)*FlowPaths(r_flowpaths(i),2)*sqrt(abs(2*g*deltaH(i))));
            else
                qdot(i)=-
(FlowPaths(r_flowpaths(i),9)*(((4*((H(FlowPaths(r_flowpaths(i),8))-
(FlowPaths(r_flowpaths(i),6)-
(FlowPaths(r_flowpaths(i),3)/2)))^2))/3)*sqrt(abs(((2*(FlowPaths(r_flowpaths(i),3)/2)
)/(H(FlowPaths(r_flowpaths(i),8))-(FlowPaths(r_flowpaths(i),6)-
(FlowPaths(r_flowpaths(i),3)/2))))-0.605)))*sqrt(abs(2*g*deltaH(i))));
            end
        end
        if                   (FlowPaths(r_flowpaths(i),7)==room)                  &
(H(FlowPaths(r_flowpaths(i),7))<H(FlowPaths(r_flowpaths(i),8)))                   &
(H(FlowPaths(r_flowpaths(i),8))>(FlowPaths(r_flowpaths(i),6)-
(FlowPaths(r_flowpaths(i),3)/2)))         &         (H(room)<Rooms(room,3))         &
(H(FlowPaths(r_flowpaths(i),8))>Rooms(FlowPaths(r_flowpaths(i),8),2))
            if
H(FlowPaths(r_flowpaths(i),8))>(FlowPaths(r_flowpaths(i),6)+(FlowPaths(r_flowpaths(i)
,3)/2))

qdot(i)=(FlowPaths(r_flowpaths(i),9)*FlowPaths(r_flowpaths(i),2)*sqrt(abs(2*g*deltaH(
i))));
            else

qdot(i)=(FlowPaths(r_flowpaths(i),9)*(((4*((H(FlowPaths(r_flowpaths(i),8))-
(FlowPaths(r_flowpaths(i),6)-
(FlowPaths(r_flowpaths(i),3)/2)))^2))/3)*sqrt(abs(((2*(FlowPaths(r_flowpaths(i),3)/2)
)/(H(FlowPaths(r_flowpaths(i),8))-(FlowPaths(r_flowpaths(i),6)-
(FlowPaths(r_flowpaths(i),3)/2))))-0.605)))*sqrt(abs(2*g*deltaH(i))));
            end
        end
        if                   (FlowPaths(r_flowpaths(i),8)==room)                  &
(H(FlowPaths(r_flowpaths(i),8))<H(FlowPaths(r_flowpaths(i),7)))                   &
(H(FlowPaths(r_flowpaths(i),7))>(FlowPaths(r_flowpaths(i),5)-
(FlowPaths(r_flowpaths(i),3)/2)))         &         (H(room)<Rooms(room,3))         &
(H(FlowPaths(r_flowpaths(i),7))>Rooms(FlowPaths(r_flowpaths(i),7),2))
            if
H(FlowPaths(r_flowpaths(i),7))>(FlowPaths(r_flowpaths(i),5)+(FlowPaths(r_flowpaths(i)
,3)/2))

qdot(i)=(FlowPaths(r_flowpaths(i),9)*FlowPaths(r_flowpaths(i),2)*sqrt(abs(2*g*deltaH(
i))));
            else

qdot(i)=(FlowPaths(r_flowpaths(i),9)*(((4*((H(FlowPaths(r_flowpaths(i),7))-
(FlowPaths(r_flowpaths(i),5)-
(FlowPaths(r_flowpaths(i),3)/2)))^2))/3)*sqrt(abs(((2*(FlowPaths(r_flowpaths(i),3)/2)
)/(H(FlowPaths(r_flowpaths(i),7))-(FlowPaths(r_flowpaths(i),5)-
(FlowPaths(r_flowpaths(i),3)/2))))-0.605)))*sqrt(abs(2*g*deltaH(i))));
            end
        end
        qdot_V(i)=abs(qdot(i)/FlowPaths(r_flowpaths(i),2));
```

```
        qdot_Re(i)=(qdot_V(i)*FlowPaths(r_flowpaths(i),3))/visc;
        if qdot_Re(i)>2300
            qdot_f(i)=0.316*(qdot_Re(i)^(-0.25));
        elseif qdot_Re(i)>0 & qdot_Re(i)<=2300
            qdot_f(i)=64/qdot_Re(i);
             elseif qdot_Re(i)==0
                   qdot_f(i)=0;
        end
        qdot_headloss_old(i)=qdot_headloss(i);

qdot_headloss(i)=abs((qdot_f(i)*FlowPaths(r_flowpaths(i),4)*((qdot_V(i))^2))/(2*g*Flo
wPaths(r_flowpaths(i),3)));
        FricError(i)=(qdot_headloss(i)-qdot_headloss_old(i))/(qdot_headloss(i));
        FricError(isinf(FricError)) = 0 ;
        FricError(isnan(FricError)) = 0 ;
        if Friction_Enable==0
            FricError(i)=0;
            fric_iterations(i)=5;
        end
        fric_iterations(i)=fric_iterations(i)+1;
        if FricError(i)>0.1
            ReductionFactor(i)=0.75;
             elseif FricError(i)<=-0.1
                   ReductionFactor(i)=1.25;
        else
            ReductionFactor(i)=1.0;
        end
    end
end
end

function [FlowFrac]=srfm_flow_fraction(t,H,room,FlowPathFractions,FlowPaths)
persistent BurstHTrigTime
r_flowpaths=(FlowPaths(:,7)==room) | (FlowPaths(:,8)==room);
r_flowpaths=find(r_flowpaths);
for i=1:length(r_flowpaths)
    FlowFrac(i)=FlowPathFractions(r_flowpaths(i),2);
end
for i=1:length(r_flowpaths)
    if isempty(BurstHTrigTime)
        BurstHTrigTime=zeros(2,size(FlowPaths,1));
    end
    if                  ((FlowPathFractions(r_flowpaths(i),5)~=0)                 &
(BurstHTrigTime(1,r_flowpaths(i))==0)       &       (H(FlowPaths(r_flowpaths(i),7))-
H(FlowPaths(r_flowpaths(i),8))) >= (FlowPathFractions(r_flowpaths(i),5)))
        BurstHTrigTime(1,r_flowpaths(i))=t;
    end
    if                  ((FlowPathFractions(r_flowpaths(i),6)~=0)                 &
(BurstHTrigTime(2,r_flowpaths(i))==0)       &       (H(FlowPaths(r_flowpaths(i),8))-
H(FlowPaths(r_flowpaths(i),7))) >= (FlowPathFractions(r_flowpaths(i),6)))
        BurstHTrigTime(1,r_flowpaths(i))=t;
    end
    if                   (FlowPathFractions(r_flowpaths(i),3)==0                 |
t<FlowPathFractions(r_flowpaths(i),3))  &  (FlowPathFractions(r_flowpaths(i),4)==0  |
```

```
t<FlowPathFractions(r_flowpaths(i),4)) & (sum(sum(BurstHTrigTime))==0 |
((not(any(any(t>BurstHTrigTime)))) & sum(sum(BurstHTrigTime))>0))
        FlowFrac(i)=FlowPathFractions(r_flowpaths(i),2);
    end
    if (FlowPathFractions(r_flowpaths(i),4)==0 |
t<FlowPathFractions(r_flowpaths(i),4)) & ((FlowPathFractions(r_flowpaths(i),3)~=0 &
t>=FlowPathFractions(r_flowpaths(i),3)) | ((BurstHTrigTime(1,r_flowpaths(i))<t) &
(BurstHTrigTime(1,r_flowpaths(i))>0)) | ((BurstHTrigTime(2,r_flowpaths(i))<t) &
(BurstHTrigTime(2,r_flowpaths(i))>0)))
        FlowFrac(i)=1;
    end
    if (FlowPathFractions(r_flowpaths(i),4)~=0 &
t>=FlowPathFractions(r_flowpaths(i),4)) & ((FlowPathFractions(r_flowpaths(i),3)==0) |
(FlowPathFractions(r_flowpaths(i),3)~=0 & t<FlowPathFractions(r_flowpaths(i),3))) &
((BurstHTrigTime(1,r_flowpaths(i))==0) | ((BurstHTrigTime(1,r_flowpaths(i))>t) &
(BurstHTrigTime(1,r_flowpaths(i))>0))) & ((BurstHTrigTime(2,r_flowpaths(i))==0) |
((BurstHTrigTime(2,r_flowpaths(i))>t) & (BurstHTrigTime(2,r_flowpaths(i))>0)))
        FlowFrac(i)=0;
    end
    if (FlowPathFractions(r_flowpaths(i),4)~=0 &
t>=FlowPathFractions(r_flowpaths(i),4)) & ((FlowPathFractions(r_flowpaths(i),3)~=0 &
t>=FlowPathFractions(r_flowpaths(i),3))|(FlowPathFractions(r_flowpaths(i),5)~=0 &
any((H(FlowPaths(r_flowpaths(i),7),:)-
H(FlowPaths(r_flowpaths(i),8),:))>=FlowPathFractions(r_flowpaths(i),5)))|(FlowPathFra
ctions(r_flowpaths(i),6)~=0 & any((H(FlowPaths(r_flowpaths(i),8),:)-
H(FlowPaths(r_flowpaths(i),7),:))>=FlowPathFractions(r_flowpaths(i),6))))
        if ((FlowPathFractions(r_flowpaths(i),4)) >
(FlowPathFractions(r_flowpaths(i),3))) &
((FlowPathFractions(r_flowpaths(i),4))>((BurstHTrigTime(1,r_flowpaths(i))>0) &
BurstHTrigTime(1,r_flowpaths(i)))) &
((FlowPathFractions(r_flowpaths(i),4))>((BurstHTrigTime(2,r_flowpaths(i))>0) &
BurstHTrigTime(2,r_flowpaths(i))))
            FlowFrac(i)=0;
        else
            FlowFrac(i)=1;
        end
    end
end
for i=1:length(r_flowpaths)
    if FlowFrac(i)>1
        FlowFrac(i)=1;
    elseif FlowFrac(i)<0
        FlowFrac(i)=0;
    end
end
FlowFrac=FlowFrac';
End

function A=srfm_surf_area(r,H,Rooms,Obstruct)
if isempty(Obstruct)
    A=Rooms(r,4);
else
    obs=Obstruct(Obstruct(:,2)==r);
    A=Rooms(r,4)-sum(Obstruct(obs,5).*(Obstruct(obs,4)>=H & H>=Obstruct(obs,3)));
end
```

```
end

function Q_in=srfm_water_source(t,r,Source_Info,Source_Rate)
if isempty(Source_Info)
    Q_in=0;
else
    n=Source_Info(:,3)==r;
    Q_in=sum((Source_Rate(n,2).*(t>=Source_Rate(n,3)))+
(Source_Rate(n,4).*(t>=Source_Rate(n,5)))+                    ((Source_Rate(n,6).*(t-
Source_Rate(n,7))).*(t>=Source_Rate(n,7)))+                   ((Source_Rate(n,8).*(t-
Source_Rate(n,9))).*(t>=Source_Rate(n,9)))+                 (Source_Rate(n,10).*exp(-
(Source_Rate(n,11)*t))));
end
end
```

### 13.3.3 Reduced Order Flooding Model - Sample Input

```
%   Number  Zmin    Zmax    Area    LInitial    Rho
Rooms=...
  [1      0.0     6.23    45.60   6.23        1000;
   2      0.0     6.23    45.60   6.23        1000;
   3      0.0     1.524   167.23  0.00        1000;
   4      0.0     4.0     278.71  0.00        1000;
   5      -4.0    0.0     139.36  -4.0        1000;
   6      -4.0    0.0     139.36  -4.0        1000;
   7      -10.0   -4      2000.0  -10.0       1000;
 ];
%   Number  Room    Zmin    Zmax    Area
Obstruct=...
   [1     3      0.0     1.5     91.2];
%   Number      Area    Dh      L       FromZ   ToZ     From    To   Discharge Coefficient
FlowPaths=...
  [1          0.0324  0.2032  1.0     0.1     0.1     1       3    0.43;
   2          0.0324  0.2032  1.0     0.1     0.1     1       3    0.43;
   3          0.0324  0.2032  1.0     0.1     0.1     2       3    0.43;
   4          0.0324  0.2032  1.0     0.1     0.1     2       3    0.43;
   5          0.00456 0.0762  1.5     0.0     0.0     3       7    0.43;
   6          1.0000  0.5     1.5     0.0     0.0     3       4    0.43;
   7          0.00456 0.0762  1.5     -4.0    -4.0    4       7    0.43;
   8          6.0     2.4     1.0     0.0     0.0     4       5    0.43;
   9          2.2     1.375   0.1     -3.3125 -3.3125 5       6    0.43;
   10         0.00456 0.0762  1.5     -4.0    -4.0    5       7    0.43;
   11         0.00456 0.0762  1.5     -4.0    -4.0    6       7    0.43
 ];
%    #   FFt0    burstT   closeT    burstHfrom  burstHto
FlowPathFractions=...
   [1   1.0     0       0         0          0;
    2   0.0     0       0         0          0;
    3   0.0     0       0         0          0;
    4   0.0     0       0         0          0;
```

```
    5   0.0     0       0         0          0;
    6   1.0     0       0         0          0;
    7   0.0     0       0         0          0;
    8   1.0     0       0         0          0;
    9   0.0     0       0         1.524      0;
    10  1.0     0       0         0          0;
    11  1.0     0       0         0          0;
    ];
%   Number  Density   Room
Source_Info=[];%...
%    [1      1000      1];
%   Number A B C D F G H K L M
Source_Rate=[];%...
%    [1 0 0 0 0 0 0 0 0 0 0];
t_end=14400;
t_step=5.0;
Friction_Enable=1;
```

### 13.3.4 Reduced Order Flooding Model - Sample Output

```
%       t (s)    Rm 1 lev (m)    Rm 2 lev (m)    Rm 3 lev (m)    Rm 4 lev (m)    Rm 5 lev (m)    Rm 6 lev (m)
Rm 7 lev (m)
0.0000000e+00   6.2300000e+00   6.2300000e+00   0.0000000e+00   0.0000000e+00  -4.0000000e+00  -
4.0000000e+00  -1.0000000e+01
5.0000000e+00   6.2153943e+00   6.2300000e+00   7.5936833e-03  -4.4400921e-02  -3.9106776e+00  -
4.0000000e+00  -9.9999922e+00
1.0000000e+01   6.2008135e+00   6.2300000e+00   1.3705780e-02  -4.3682667e-02  -3.9113432e+00  -
4.0000000e+00  -9.9999458e+00
1.5000000e+01   6.1862568e+00   6.2300000e+00   1.9599204e-02  -4.2908723e-02  -3.9120087e+00  -
4.0000000e+00  -9.9998994e+00
2.0000000e+01   6.1717242e+00   6.2300000e+00   2.5281815e-02  -4.2081194e-02  -3.9126742e+00  -
4.0000000e+00  -9.9998530e+00
2.5000000e+01   6.1572152e+00   6.2300000e+00   3.0761088e-02  -4.1202081e-02  -3.9133397e+00  -
4.0000000e+00  -9.9998067e+00
3.0000000e+01   6.1427298e+00   6.2300000e+00   3.6044216e-02  -4.0273308e-02  -3.9140051e+00  -
4.0000000e+00  -9.9997603e+00
3.5000000e+01   6.1282677e+00   6.2300000e+00   4.1138179e-02  -3.9296745e-02  -3.9146705e+00  -
4.0000000e+00  -9.9997139e+00
4.0000000e+01   6.1138287e+00   6.2300000e+00   4.6049776e-02  -3.8274212e-02  -3.9153358e+00  -
4.0000000e+00  -9.9996676e+00
4.5000000e+01   6.0994126e+00   6.2300000e+00   5.0785649e-02  -3.7207487e-02  -3.9160011e+00  -
4.0000000e+00  -9.9996212e+00
5.0000000e+01   6.0850192e+00   6.2300000e+00   5.5352293e-02  -3.6098310e-02  -3.9166664e+00  -
4.0000000e+00  -9.9995749e+00
5.5000000e+01   6.0706482e+00   6.2300000e+00   5.9756060e-02  -3.4948383e-02  -3.9173316e+00  -
4.0000000e+00  -9.9995285e+00
6.0000000e+01   6.0562996e+00   6.2300000e+00   6.4003159e-02  -3.3759369e-02  -3.9179968e+00  -
4.0000000e+00  -9.9994822e+00
```

```
6.5000000e+01   6.0419731e+00   6.2300000e+00   6.8099656e-02  -3.2532895e-02  -3.9186619e+00  -
4.0000000e+00  -9.9994358e+00
7.0000000e+01   6.0276686e+00   6.2300000e+00   7.2051466e-02  -3.1270547e-02  -3.9193270e+00  -
4.0000000e+00  -9.9993895e+00
```